Low-Carbon Biofuels: Optical and Numerical Analysis of Combustion Performance

By:

Abdallah Yousef Subhi Abu Saleh

Supervisors:

Dr Ruoyang Yuan

Dr Kevin J. Hughes

A thesis submitted in partial fulfilment of the requirements for the degree of Doctor of Philosophy

The University of Sheffield
Faculty of Engineering
Department of Mechanical Engineering

June 2023

Acknowledgments

During my PhD journey, I came across many people for whom I am very thankful for their guidance, support, and encouragement. Firstly, I would like to express my gratitude and appreciation to my first supervisor, Dr Ruoyang Yuan, for the great support and guidance and for providing me with the opportunity to do this PhD. I am thankful to Dr Ruoyang Yuan for her patience, knowledge, ideas, vision, and motivation that I have received from her during this PhD. This work would not have been possible without her constant guidance and support.

I would like to express my sincere thanks to my second supervisor, Dr Kevin Hughes, for his great guidance and support. I want to thank him for the knowledge, ideas, and lab support I received from him during my PhD. I want to thank my personal tutor Professor Derek Ingham for his guidance and support in the weekly group meetings and during my PhD journey. I would also like to extend my sincere appreciation to my PhD second supervisor during my first year at Loughborough University, Professor Graham Hargrave, for his support and guidance.

I want to thank all my friends and colleagues in the Energy 2050 group at the University of Sheffield who have supported me throughout this PhD journey. Your presence has made my PhD journey more pleasurable. A special thanks to the workshop support provided by M Kirkland, G Barker, D Webster, and C Todd. I would also like to thank all the postgraduate research officers in the Mechanical Engineering department at the University of Sheffield for their support.

I want to express my deepest sincere gratitude and thanks to my parents. Your prayers, unceasing support, encouragement, and love are the main reasons for my success. I also want to thank my brothers and sisters for their constant encouragement and support.

Finally, I would like to acknowledge EPSRC David Clarke Fellowship for the funding support of the research project [Grant Ref: EP/S017259/2].

Publications

Journal publication

Chapter 5 contained the following publication:

A. Abu Saleh, K. J. Hughes, and R. Yuan, “Reaction zone characteristics of iso-pentanol swirl spray flames using OH-PLIF and 2C-LII,” *Proc. Combust. Inst.*, vol. 39, no. 2, pp. 2663–2672, Jan. 2023, doi: 10.1016/j.proci.2022.07.232.

Chapters 3 and 4 contained the following publication:

Journal publication on the “Feasibility on equivalence ratio measurement via OH*, CH*, C2* chemiluminescence and effect from soot emissions in coflow non-premixed DME / C1-C2 hydrocarbon flames.” This paper was submitted to the 'Frontiers in Fuels Journal.' The paper was accepted with minor corrections but has not been published as of the date of thesis submission.

Planned journal publications

Journal publication on the “The Impact of Dilution Air Strategy on the N-heptane Turbulent Swirl Spray Flames,” including results from Chapter 7 will be submitted to the 40th International Symposium on Combustion.

Conference publications

Chapter 6 contained the following publication:

A. Abu Saleh, T. Knight, and R. Yuan, “Application of Planar Time-Resolved 2C-LII for Soot Emission Measurements in Diffusion Flames of DME Blends and in Swirl Spray Flames,” *AIAA Sci. Technol. Forum Expo. AIAA SciTech Forum 2022*, doi: 10.2514/6.2022-1942.

Chapter 5 contained the following publication:

A. Abu Saleh, K. J. Hughes, and R. Yuan, “NO emission charateristics of iso-pentanol swirl spray flames using NO-PLIF, ” *AIAA Sci. Technol. Forum Expo. AIAA SciTech Forum 2023*, doi: 10.2514/6.2023-0990.

Results of following publication not included in this thesis:

A. Abu Saleh, S. Siouris, K. J. Hughes, R. Yuan, M. Pourkashanian, "Assessment of mixtures of iso-pentanol and Jet A-1 for use in aviation gas turbine engines, " *AIAA Sci. Technol. Forum Expo. AIAA SciTech Forum 2023*, doi: 10.2514/6.2023-2341.

Talks and presentations

I delivered a presentation at the Low-Carbon Combustion conference. Saleh, A.A., Hargrave, G. and Yuan, R., Characteristics of flame heat release and soot emissions of methane and ethylene laminar diffusion flames with dimethyl ether addition. In *Book of abstracts* (p. 53). https://lowcarbon.sciencesconf.org/data/pages/book_of_abstracts_lowcarboncombustion_2.pdf#page=54.

Another presentation was delivered at the Supergen Bioenergy Hub Researchers' Day Meeting: Introduction & Case Study 1 (Hydrogen Fuel Cell) Session on the "Renewable gas production through in-situ biogas upgrading: process evaluation and fuel combustion characteristics." Dr. Davide Poggio and I delivered this presentation.

Declaration

I, Abdallah Yousef Subhi Abu Saleh, confirm that the Thesis is my own work. I am aware of the University's Guidance on the Use of Unfair Means (www.sheffield.ac.uk/ssid/unfair-means). This work has not been previously been presented for an award at this, or any other, university.

Abstract

This thesis describes experimental and numerical studies of the combustion and emission characteristics of two biofuels (DME and iso-pentanol) and their blend in different non-premixed flame types (laminar co-flow flame and bluff-body swirl spray flame) and conditions.

The first part of this thesis present 1D chemical kinetic simulations of DME/ hydrocarbon mixtures, n-heptane, and iso-pentanol fuels in a non-premixed counter flow flame configuration. The aim of these simulations is to study and provide new understandings of the characteristics of soot emission, flame chemiluminescence and HRR. In addition, to study the flame structures and species profiles including OH*, OH, CH*, CH, HRR, CH_3, C_3H_3, C_2H_2 and flame temperature of various fuel mixtures and mixing ratios. Results suggest that the addition of DME to hydrocarbon fuels overall reduces the concentration of soot precursors and peak values of heat release rate (HRR), and increases the strain rate value required for quenching. The pure iso-pentanol flame showed a lower flame temperature than pure n-heptane flame. Also, pure iso-pentanol was found to contribute less to C_2H_4 production than pure n-heptane.

In the second part of this thesis, the effects of adding DME to methane and ethylene laminar co-flow flames on HRR and reaction zone were experimentally investigated using CH*, OH*, and C_2* chemiluminescence across a full range of DME mixing ratios. In addition, the results of a feasibility about mapping chemiluminescence pair ratios (OH*/CH*, OH*/C_2*) to local equivalency ratios were described. The burner used for these investigations is the laminar co-flow diffusion burner. The soot radiation appearance in C_2* chemiluminescence for methane flames became initially stronger with little addition of DME (25%). Nevertheless, the soot radiation appearance became weaker when the DME mixture ratio was increased by more than 25%, indicating either less soot concentration or reduced soot temperature. In the DME cases, the OH*/CH* ratio does not have an ideal monotonic function of equivalence ratio. Nonetheless, mapping the numerical to experimental results for OH*/CH* ratios conditional on the OH* profiles could provide useful information on the equivalence ratio values.

Next, the reaction zone and stability characteristics of bluff-body swirl spray flames of pure iso-pentanol, n-heptane, ethanol, a 50:50 volume ratio mixture of iso-pentanol/n-heptane, and a 50:50 volume ratio mixture of ethanol/n-heptane are described. In addition, relative NO

concentrations of pure iso-pentanol, pure n-heptane, and an iso-pentanol/n-heptane blend are presented. The OH-PLIF measurements were used to study the flame sheet characteristics, OH* chemiluminescence was used to represent the heat release distribution, and NO-PLIF measurements were used to measure the relative NO concentrations. In far away from blow-off (sooting) and stable conditions, the addition of pure iso-pentanol reduced the overall lift-off height. Also, an iso-pentanol/n-heptane blend at near blow-off condition exhibited the lowest mean lift-off height amongst all other near blow-off cases. In far away from the blow-off condition, pure iso-pentanol was shown to have fewer local extinctions than n-heptane/iso-pentanol. Whereas in stable and near blow-off conditions, pure iso-pentanol exhibited the highest occurrence of local extinctions amongst all the other tested flames at near blow-off condition. Also, the addition of iso-pentanol to n-heptane increased the OH* chemiluminescence signal, and decreased the relative NO content in the flame.

Next, soot emissions measurements of the laminar diffusion flames of DME and blends, and swirl spray flames of iso-pentanol and blends using calibrated planar time-resolved two-colour Laser-induced incandescence (2C-LII) are described. In addition, the influence of laser energy and acquisition parameters on soot concentration quantification, soot temperatures, and effective primary particle diameters (ePPDs) of different fuels in both flame types are studied. The acquisition delay time have an impact on the measured soot volume fraction (SVF). In DME/C_2H_4/N_2 flame mixtures, the DME addition to the pure ethylene/N_2 flame decreased the SVFs after 20 ns delay, whereas at delay times < 20 ns an opposite conclusion was obtained. An increase in the ePPDs is observed as DME added to C_2H_4/N_2 flame. The addition of iso-pentanol to n-heptane reduced the overall SVF and ePPDs, and increased the peak soot temperature.

The final part of this thesis describes the impact of introducing dilution air downstream the chamber of n-heptane bluff-body swirl spray flame on the stability, HRR and flame structure. In addition, preliminary understanding of the flame structure behaviour and temperature are described with the use of 1D non-premixed laminar counter flow flame simulations. Numerical results exhibited that 10% dilution air addition in the oxidiser side increases the peak temperature, HRR, and OH mole fraction. Experimentally, more efficient spray breakup near the nozzle region detected with the addition of dilution air. The effect of dilution air on the lift-off height is negligible, whereas it increases the occurrence of local extinction event in the flame. Overall, the addition of dilution air also found to enhance the stability of the flame.

Table of Contents

List of Tables

List of Figures

Nomenclature

Roman Letters

a	strain rate
C_s	specific heat of soot
C_p	specific heat capacity at constant pressure
C_α	model constant for soot inception
C_β	model constant for soot coagulation rate
C_γ	model constant for the soot surface growth
C_oxid	model constant for the soot oxidation rate scaling parameter
C_ω	model constant for the soot oxidation
c	speed of light
$d_\mathrm{p,eff}$	effective primary particle diameter
D_f	fuel nozzle diameter
D_a	diameter of the air annular exit
$D_\mathrm{sw\ inner}$	inner diameter of the swirl
$D_\mathrm{sw\ outer}$	outer diameter of the swirl
D	diffusion coefficient of the mixture
E	local chemiluminescence emission
E_activ	activation energy
$E(m)$	soot absorption function
E_tot	total energy
erf	error function
f	Eucken correction of thermal conductivity
Fr	Froude number
F_x	gravitational force in x direction
G	factor of heat transfer
$G_\emptyset$	tangential momentum flux
G_x	axial momentum flux
h	Planck's constant
h_i	constant enthalpy of species i
K_a	thermal conductivity of the surrounding gas
k_p	Boltzmann constant

k_{eff}	thermal conductivity
L_{MFP}	mean free path length
Le	lewis number
M	soot mass concentration
M_{P}	mass of an incipient soot particle
N	soot particle number density
N_{A}	Avogadro number
n	number of species
P	power
p_o	pressure of ambient gas
Q	volumetric flow rate
$\dot{Q}_{\mathrm{conduction}}$	conduction heat loss from the particle to the surrounding gas
R	ideal gas constant
Re	Reynolds number
R_i	net rate production of species i
$R_{\lambda 1,2}$	instrument responsivity at the two wavelengths
S	Projection of chemiluminescence signal
S_i	rate of creation of species i
S_N	swirl number
S_h	volumetric heat source
T	temperature
T_{a}	activation temperature
T_γ	activation temperature for surface growth
T_α	activation temperature for soot inception
T_l	laser-heated temperature
T_o	temperature of the ambient gases
T_{peak}	peak temperature of the soot particle in the cooling regime
T_{s}	soot temperatures
t	time
U_{a}	air velocity
U_{f}	fuel velocity
U_{internal}	internal energy
V	detection volume
v_a	kinematic viscosity of air

v_f	kinematic viscosity of fuel
v_x	velocity in the axial direction
v_r	velocity in radial the direction
We	Weber number
w_b	equivalent width of the laser sheet
w_i	production rate of species i
X_{prec}	soot precursor's mole fraction
X_{sgs}	mole fraction of surface growth species
x	Cartesian coordinate
Y	mass fraction
y	Cartesian coordinate
b^*_{nuc}	normalised radical nuclei concentration

Greek Letters

τ_T	temperature decay rate
ρ	density
ρ_s	soot density
γ	gas's specific heat ratio
α_T	coefficient of thermal accommodation
σ_m	average molecular cross section for air
$\lambda_{1,2}$	measuring wavelengths of 550 nm and 650 nm bandpass filters
λ	detection wavelength
η	detection system calibration constant
ξ	mixture fraction
β	DME mixture ratio
α	fuel mixture ratio
χ	scalar dissipation rate
θ	vane angle of the swirl
ϕ	global equivalence ratio
σ	fuel surface tension
μ_d	dynamic viscosity of the fluid

Subscript

st	stoichiometry
a	air
f	fuel
s	soot
k, j	pixel indices

Abbreviations

A1	benzene and phenyl
CFD	Computational Fluid Dynamics
DME	dimethyl ether
EGR	exhaust gas recirculation
EPA	Environmental Protection Agency
FCU	Frequency Conversion Unit
FWHM	full width-half maximum
GHGs	greenhouse gases
HC	hydrocarbon
HCCI	Homogeneous charge compression ignition
HCN	hydrocarbon radicals
HRR	heat release rate
IAT	Inverse Abel Transform
ICCD	intensified charge-coupled device
ID	inner diameter
IFB	inner flame branch
IRZ	inner recirculation zone
ITHR	intermediate temperature heat release
LBO	lean blow-off
LII	Laser-induced incandescence
MFC	mass flow controller
NO_x	nitrogen oxides
OFB	outer flame branch
PAH	polycyclic aromatic hydrocarbons

PDF	probability density function
PLIF	Planar Laser induced fluorescence
PM	particulate matter
PTU	Programmable Timing Unit
RQL	Rich-Burn, Quick-Mix, Lean-Burn
RTFO	Renewable Transport Fuel Obligation
SCCM	Standard cubic centimeters per minute
SLPM	standard litre per minute
SVF	soot volume fraction
TTL	acquisition duration, ICCD camera intensifier gate width
2C-LII	two-colour laser induced incandescence

Chapter 1: Introduction

1.1 Motivation

Since the successful creation of the first commercial internal combustion engine in the 18th century, the research has been primarily focused on the development of engine design in order to enhance operating performance. Nevertheless, in the last few decades, the focus has shifted to another important aspect which is about producing cleaner emissions from combustion engines. Despite the substantial advancements achieved on substitute energy systems, it is anticipated that burning conventional fuel will continue dominating the energy sector in various domains including transport and power generation across the globe for the near future and the next 40 years [1]. The increased demand on the transportation sector, residential combustion, and various energy industries resulted in increasing the amount of greenhouse gases (GHGs) and different harmful gas emissions, such as nitrogen oxides (NO_x) and particulate matter (PM), released into the environment [2], as shown in Figure 1-1 [3]. According to Public Health England (2018), the poor quality of air due to such emissions is the biggest environmental hazard to the community [3]. In 2019, the World Health Organisation revealed that about 4.2 million deaths around the world are attributed to air pollution due to such emissions [4]. Both brief and prolonged exposure to these different pollutants, including soot and NO_x, can cause health issues including lung cancers, cardiovascular disease and asthma [3]. In the UK alone,

around 28,000-36,000 deaths yearly are associated with the prolonged subjection to "man-made" air pollution [3]. A recent report published by Imperial College London estimated 3,600 to 4,100 deaths in Greater London in 2019 were attributed to particulate matter produced by human-made activities [5]. Consequently, following the rise in the public's general awareness regarding not only the environmental protection, but more importantly the need for alternate energy sources, decreasing the current levels of gas emissions has become the main area of concern, creating a higher demand for relevant research.

The ongoing rise in the demand for some of the sectors mentioned in Figure 1-1 could however, lead to significant energy supply shortage caused by the increase in oil consumption. Due to growing concerns regarding the lack of energy, the need for decreasing gas emissions has caused a higher demand for relevant research. As a result of contemporary biological processes, and contrary to the non-renewable properties of crude oils, biofuels are believed to be the cleaner source of energy [6]. The UK government will compel their fuel suppliers to provide and mix at least 12.4% (by volume) of biofuel by 2032, under the Renewable Transport Fuel Obligation (RTFO) [7].

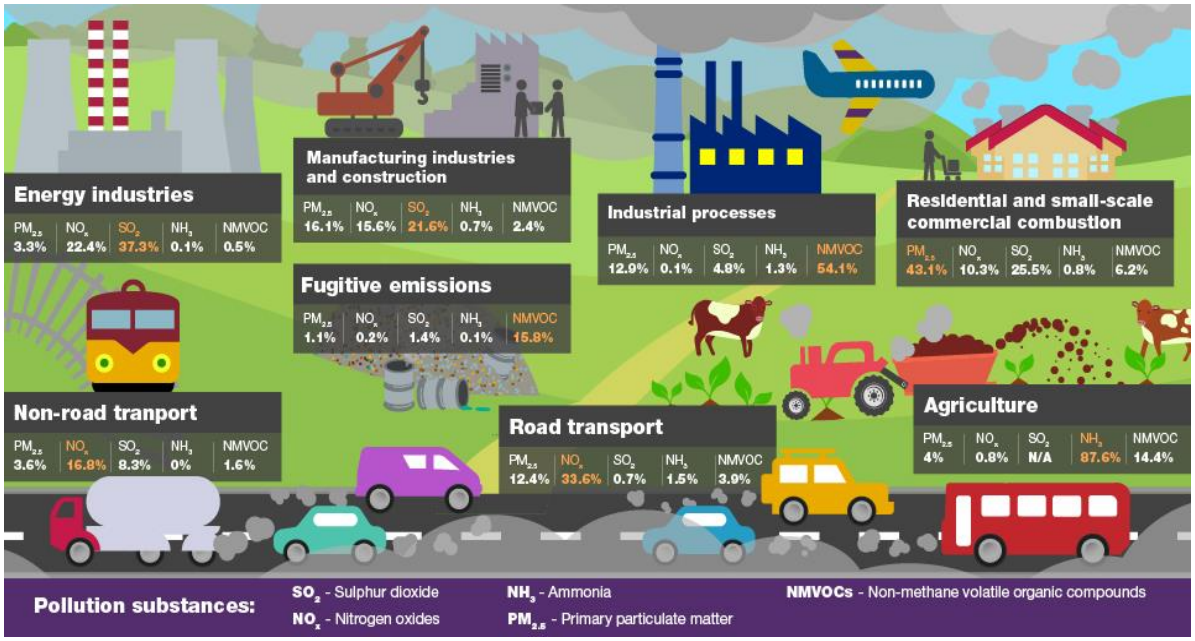

Figure 1-1 The sources of air pollution in the UK in 2018 [3].

The utilization of cleaner fuels, such as biofuels or low carbon fuels, as an alternative to fossil fuels is one of the solutions as it offers similar energy content with less soot, NO_x, and net GHG emissions. Predominantly, ethanol and methanol are the compounds mostly associated with clean fuel term in the science sphere. Although, other oxygenated fuels, for

example, dimethyl ether (DME), iso-pentanol also have renewable properties, which have been shown through previous studies conducted by multiple researchers, showing that they decrease emissions and health problems, as well as enhancing the performance of engine combustion [8]–[10]. Moreover, they can be utilized in a wide range of sectors including transportation, electricity generation, and residential combustion applications. Therefore, the targeted biofuels in this thesis are DME, iso-pentanol and their blends with hydrocarbon fuels. DME is an oxygenated ether fuel and considered to be a promising alternative clean fuel; it can be obtained from a range of sources including biomass [11] and natural gas. DME can be utilized not only in compression ignition engines, but also in gas turbines. Iso-pentanol is an oxygenated alcoholic fuel, which could potentially reduce the level of emissions, especially NO_x and soot [12].

It has already been demonstrated that both of these important biofuels emit reduced particle pollutants. However, there is not enough experimental and numerical research on them and their mixtures, which impedes the development of the next-generation low-emission sustainable engines. Fundamental understanding of the combustion and emissions characteristics is still required for both targeted fuels candidates. In terms of emissions, experimental data are required to demonstrate how DME and iso-pentanol affects soot and NO_x formation using advanced diagnostic technique. In addition, numerical and computational studies are needed to be developed to predict soot and NO_x emissions of these fuels. Whereas in terms of combustion characteristics, some investigations are required to understand their heat release rate (HRR) and flame stabilization features. These are all important data that will contribute towards the development of future low carbon technologies.

1.2 Physico-chemical properties of the Targeted Bio-fuels: DME & Iso-pentanol

Different oxygenated biofuels are now becoming alternative fuels for different uses. This evidence is beneficial in contributing towards low-carbon transportation. Nevertheless, there are a number of issues and challenges that still need to be looked at before they are applied in real applications. These challenges include for example the sources of feedstock's to produce the biofuels, the production methodologies, and the applications in which they can be used, etc. [13]. Nevertheless, understanding the impact of the physico-chemical properties of biofuels on

the combustion performance and emissions remains important on both economic and environmental aspects. Biofuels are usually characterised by different physico-chemical characteristics including cetane number, density, boiling point, calorific value, viscosity etc. Such properties could provide an indication of the biofuel's suitability for the motor's emissions and performance [14], [15]. Table 1-1 displays the physico-chemical characteristics of the targeted biofuels in this thesis and some of the conventional fuels [16]–[20].

Table 1-1 Physico-chemical properties of the targeted biofuels, ethanol, methane, diesel and gasoline [16]–[20].

Property	**Ethanol**	**DME**	**Iso-pentanol**	**Methane**	**Diesel**	**Gasoline**
Chemical Formula	C_2H_5OH	CH_3OCH_3	$C_5H_{11}OH$	CH_4	C3 to C25	C4 to C12
Molecular Weight	46	46	88.1	16	170	108
Carbon Content mass%	52.2	52.2	68.2	75	86	85-88
Hydrogen Content mass%	13.0	13	13.6	25	14	12-15
Oxygen Content mass%	34.8	34.8	18.2	0	0	0
Air-Fuel Ratio	9	9	11.76	17.2	14.6	14.7
Cetane Number	5-15	55-60		75-80	40-50	5-20
Boiling point (°C)	78.2	-25	131	-161	180-360	39-204
Liquid Density (kg/m^3)	785.3	667	777	0.716	831	710-770
Liquid viscosity (kg/ms)	1.074	0.15			2-4	0.4-0.88
Auto-ignition temperature (°C)	363	235	350	600	250	280-486
Net calorific value (lower heating value) (MJ/kg)	26.8	28.8	35.37	50	42.5	46.7
Latent heat of vaporization (kJ/kg)	896	467.13	631	510	300	

DME is one of the main targeted biofuel in this work. Having been obtained from a range of sources including biomass and natural gas, DME is deemed a possible clean fuel alternative to fossil fuels. In comparison to other biofuels, it possesses no Carbon-Carbon bond, a very low boiling point and high cetane number. This is further complemented by a comparatively low auto ignition temperature. Lower amounts of harmful emissions have also been found present in DME's combustion products [16], making in the better alternative to diesel fuel. The

DME energy density is lower than diesel fuel by about 45%. DME is also an oxygenated compound with a short ignition delay feature [21], thus, it can be utilized as an ignition enhancer [22]. Due to this feature smaller regions of over lean/ rich mixtures are formed throughout the ignition delay time, and hence reduces the hydrocarbon (HC) emissions. Nevertheless, significant quantity of methyl groups (CH_3) can be generated from DME combustion (e.g. $CH_3OCH_3 \leftrightarrow CH_3 + CH_3O$ [23], [24]) which could lead to an increase in the creation of soot due to the suggested reaction pathway of DME $\rightarrow CH_3$ (H) $\rightarrow C_2H_2$ (C_3H_3) $\rightarrow$ C_6H_6 $\rightarrow$ soot [25]. Therefore, detailed understanding of the fundamental combustion performance and emission characteristics of DME and DME blends is required before implementing the fuels in existing systems.

Alcohol fuels are organic molecules that mostly include hydroxyl (chemical formula: −OH) & alkyl (general formula: C_nH_{2n+1}) groups. High alcohols, those with a number of carbon atoms ≥ 4, have recently attracted considerable attention as sustainable biofuels because of their appealing thermodynamic and physico-chemical features. Recently, it has been suggested [20], [26] that long-chain alcohols have some advantages over ethanol, for example greater energy content and lower hygroscopicity [20], [27], that can make them a better alternative to conventional fuels. At the moment, ethanol is the most extensively utilised biofuel. It was pointed out previously [28] that ethanol has several drawbacks, including its poor stability, miscibility and low flash point and Cetane number when mixed with diesel fuel. Iso-pentanol, also known as 3-methyl-1-butanol, is an isoamyl alcohol and categorizes under second-generation biofuels. It is a promising next-generation biofuel for replacing gasoline [27] and diesel [29] because of its high volumetric energy density, better blend stability and is less hygroscopic tendency than methanol and ethanol [30], resulting in better combustion efficiency. In addition, iso-pentanol has a greater flash point in comparison to ethanol. This makes it easier to transport and store. The physico-chemical properties of iso-pentanol are quite similar to ethanol, indicating the feasibility of substituting ethanol when mixing it with hydrocarbon fuels. Iso-pentanol has good potential in reducing soot formation because it increases the amount of oxygen atoms [13], [31]–[33] and also improves air entrainment due to its long ignition delay [34]. The polarity of iso-pentanol decreases quickly due to the longer alkyl chain [31]. As seen in the molecular formula in Table 1-1, iso-pentanol contains five carbon atoms (i.e. increased alcohol carbon chain length) which can improve the ignition [35]. Furthermore, it has the potentiality in reducing NO_x and PM emissions when mixed with hydrocarbon fuels. Iso-pentanol can be generated sustainably from the ligno-cellulosic biomass

feedstocks, starchy and sugary [36]. It can be produced using a variety of developed fermentation techniques including cyanobacteria and clostridium cellulolyticum [37]. Iso-pentanol has been identified as a targeted fuel by the Joint BioEnergy Institute of the US Department of Energy [38]. Iso-pentanol offers various advantages as an alternative fuel, nevertheless it is still in the early phases of development, and further research and development into combustion and emissions is required.

1.3 Introduction on Laminar Diffusion Flame

The fuel and oxidant in diffusion flame are unmixed prior to injection (non-premixed flame). These types of flames are commonly created by injecting the fuel jet to an oxidant flow (co-flow). However, an inverse configuration called counter flow, is also possible [39]. In laminar diffusion flames, the mixing occurs much slower than the rates of chemical reactions, hence the burning rate relies more on the mixing time. Combustion in such flame occurs at the boundary amongst the fuel and oxidant gases (at the reaction zone). Laminar diffusion flame is utilized in several industrial combustion applications such as residential gas appliances diesel and jet engines [40].

Several factors influence the flame structure, these include fuel gas type and its flow rate. One of the simplest examples of the diffusion flame is the candle flame as shown in Fig. 1-2 [40]. At stoichiometric mixture fraction (ξ_{st}), the combustion occurs and hence the fuel and oxidant mass fractions are too small. It can be noticed in Figure 1-2 that there is no soot (yellow region) at the lower part of the flame, even though that this region is very rich. This is because the formation of soot is very slow, however the oxidation process of soot is very fast.

Strain rate of diffusion flames is an essential feature for the mixture of the fuel and air. This parameter is usually determined through using the counter flow burner configuration [41]. The strain rate can be increased in such configuration by increasing the fuel jet flow speed. Increasing the strain rate in counter flow configuration results in reducing the adiabatic flame temperature, and after a certain strain rate value the flame gets extinguished [42]. This is because as the strain rate increases, the residence time reduces. Hence, less of the fuel/ air mixture is transferred to products (diffusive time scale becomes shorter) and eventually the flame becomes extinguished.

The ways that hydrocarbons get generated in diffusion flames are essential to the fundamental knowledge of emissions formation, such as soot. Typically, in diffusion flames, the generated soot particles oxidize mostly to carbon monoxide, however changes to the operating conditions may results in reducing the fuel/ air ratio in the flame oxidative area and hence preventing the completion of oxidation process to carbon dioxide causing big levels of gaseous emissions [43]. As a result, investigating the sooting flames (diffusion flames) stays essential for safety and environmental purposes. Therefore, in this thesis, the combustion and emission characteristics of DME mixture with hydrocarbon fuels, such as methane, and ethylene will be investigated in laminar non-premixed flames configuration.

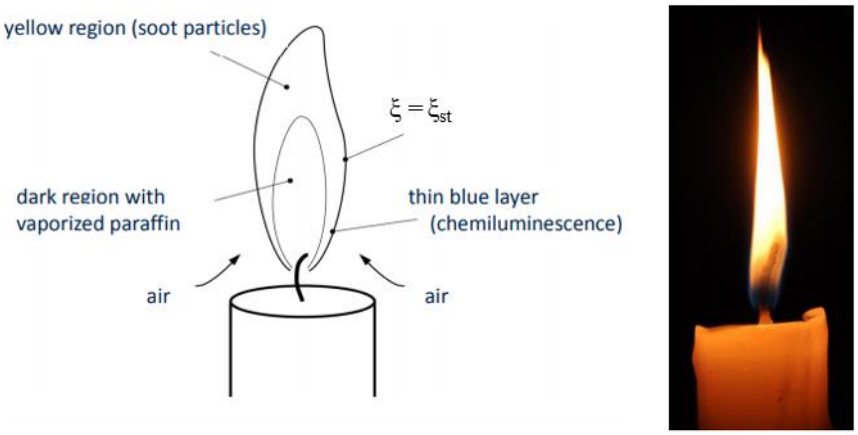

Figure 1-2 Schematic of candle flame identifying the different regions of the flame [40].

1.4 Introduction on Spray Combustion and Flame Stabilisation

Understanding the combustion chemistry characteristics of the liquid fuel sprays is very essential due to its usage in multiple combustion applications such as gas turbines, furnaces and IC engines. According to Presser et al. [44], there are numerous factors that have considerable control on the behavior of the spray fuel and their mixture with air processes - for example, the distribution size of the injected fuel droplets, the relative motion between droplets and the gas surrounding it, type of motion the injected fuel has and the classification of the flow (e.g. laminar or turbulent). In return, these factors depend on the type of the injected fuel and their specific processes, for example, vaporization rate and heat transfer. Thus, a detailed understanding of the way that the biofuels droplets react and mix with the air flow is crucial for studying the emissions released from spray flames. Numerous authors [45]–[47] have

described and investigated the basics of droplet evaporation in spray flames. Another important process in spray droplets formation is atomization. The spray atomization process occurs faster than droplets evaporation which only occurs after atomization is complete and the size of the droplets is sufficiently small. The formation of spray is a very complicated process which involves multiple stages, as described in many previous studies. The surface area covered by droplets increases as the number of small droplets increases and hence, the heat and mass exchange rates increase henceforth.

Any force that is involved in breaking-up the interface between the liquid and gas phases must be bigger than the interfacial tension. The droplet surface breaks up due to the aerodynamic drag force whereas the surface tension force (resistant force) aims to reinstate the initial state of the droplet. The ratio between the aerodynamic force and surface tension force is presented by the Weber number (We), and this is a dimensionless number that can be used to analyse fluid flows when two separate fluids (e.g. liquid fuel and air) meet, and so it is usually used to characterise the atomisation process.

Several studies have investigated the impact of fuel properties (physical and chemical) on the structure of spray flames [48]–[52]. Presser et al. [48] used a range of different fuels including conventional (kerosene), alternative (methanol) and single component (heptane) fuels to study their physical and chemical properties impact on the structure of spray flames such as droplets size and velocity. Their entire experimental studies, implemented with hollow cone fuel spray, were carried out with constant swirl number, fuel/ air ratio, Weber, and Reynolds number (Re is defined as "the ratio of fluid momentum force to viscous shear force" [53], and is used to determine whether the flow is turbulent or laminar). The results revealed a direct proportional relationship between the droplet size and the fuel properties of density and viscosity.

1.4.1 Flame Stabilisation

Running the fuel-air combustion mixture under lean condition is one of the ways that can be implemented to reduce NO_x emissions. Nevertheless, this method increases the possibility of risk in terms of the occurrence of flame global extinction phenomenon (flame blow-off) in which the flow velocity become very high and hence, the flame loses its stability spreading downstream and ultimately extinguishes completely. Consequently, blow-off in lean fuel mixtures has become one of the main topics of research because of the requirement to run the

fuel-air blend under lean conditions and thus, near to their blow-off limits. Subsequently, it is important to investigate the impact of the alternative clean biofuels' properties on the extinction limit to guarantee the safety of using such biofuels in industrial applications. Therefore, flame stabilisation is fundamentally crucial in the effective operation and design of the combustion systems, especially aero-engines. The main aim of flame stabilisation is to prevent the blow-off phenomenon.

The blow-off phenomenon has been widely investigated and a large collection of information about its risks and affects were gathered in the past through different experiments and computational studies [54]–[56]. Raushenbakh and Belyy [57] investigated the impact of a bluff body on the stability of premixed turbulent flames. They reported that when the stream speed of the fuel-air mixture in the recirculation zone continues increasing, a critical value upon which the flame blow-off is reached. The peak speeds of blow-off mostly occur when the mixture ratio is stoichiometric, and as the mixture ratio become richer or leaner the blow-off speeds decrease. Researchers who have conducted investigations on flame stabilization using bluff bodies or swirls agree with the concept that the energy and mass of the hot gases inside the recirculation zone are transported to the unburned gases located outside this zone, and the fast mixing between the hot gasses and the unburned gasses results in blowing-off the flame. However, the blow-off limits and behaviour may differ in different flame categories (for instance gaseous and spray).

Achieving the stability feature rises the flexibility to operate in low emission mode over a wide-ranging load [58]. Different techniques developed to help with flame stabilization depending on the engine type but one commonly used is the bluff-body [59]. The swirl stabilized combustion concept, which provides advantages such as better turbulent mixing and flame stabilization, has been widely used in aero-engines [60]. Swirling flows generate an inner recirculation zone (IRZ) within the flame creating an ideal condition for the hot, recirculated products to keep the new injected reactants into the combustor constantly ignited [61]. The injection of dilution air/ secondary air strategy downstream the combustion chamber, also known as the Rich-Burn, Quick-Mix, Lean-Burn (RQL) combustor, of gas turbine engines was introduced in 1980 to reduce the NO_x emissions [62], [63]. Modern burners use the bluff-body swirling flames along with the dilution air strategy [64].

Swirlers are often used in burners and other combustion applications (including gas turbines) to maintain flame stability [60], [65]–[67]. A swirl burner provides a swirl motion to

the combustion gases, forming a toroidal recirculation zone. This recirculation motion aids keeping the flame ignited through recirculating the heated gases, thus decreasing the velocity needed for flame stabilization and allows for a better burning. The recirculation motion decreases the combustion length through generating fast mixing once the fluid is injected and on the boundaries of the recirculation zone. In addition, it has a considerable impact on pollutant releases, combustion intensity and flame blow-off limits. Manufacturers of gas turbine engines and burners use swirlers to create the required recirculation motion to increase the residence time of the reactant gases inside the recirculation zone, improving the flame stability. One of the most important parameters in characterizing the swirling flow is the swirl number. It is defined as the ratio of the tangential momentum flux ($G_\emptyset$) to the axial momentum flux (G_x) [60]. Sheen et al. [68] introduced another correlation for calculating the swirl number based on the swirl vane angle and Reynolds number. Previous studies showed that the swirl number has a significant effect on the combustion characteristics including gas concentration as well as flame temperature [69], [70]. Ylmaz [69] investigated the impact of Swirl Number on combustion characteristics in diffusion flame. According to Syred and Beér [60], high swirl numbers (>0.6) enhance the flame stability through increasing the mixing rate inside the toroidal recirculation. Therefore, the swirl number can be used to define the swirl intensity. In 1977, Owen et al. [71] investigated the impact of swirl on multiple emissions in non-premixed combustion. They found that an increase in swirl number greatly increased NO_x production. Whereas Ishak and Jaafar [72] results showed a decrease in NO_x emissions with increasing the swirl number. The increase of NO_x from oxygenated fuel combustion could sometimes be attributed to the oxygen atom that exists in their species [73]. Nevertheless, alcohol fuels have a high potential to reduce NO_x emissions because of their high latent heat of evaporation, which helps in reducing the temperature inside the engine's cylinder [73].

Bluff bodies are usually used in jet engines and burners along with swirlers, or by itself, to produce recirculation zone which is important for stabilising the flame. A further benefit of using bluff body includes providing a better turbulent mixing feature. Flame stabilization by bluff body was investigated by several researchers for many years [74]–[77]. The straight cylindrical is the most commonly used shape of bluff body by investigators [78], [79]. Nevertheless, there are different bluff body geometries which were also used in the past by multiple researchers. These geometries include hollow cone, solid cone, and both thin and thick discs [80].

In this thesis, the characteristics of combustion and emission of iso-pentanol fuel and its mixtures will be investigated in a bluff-body swirl spray configuration. In addition, dilution air strategy impact on n-heptane combustion in a swirl spray flame will be investigated.

1.5 Literature Background

1.5.1 Fundamentals of Particulate Matter (Soot) Formation

According to EPA [81], particulate matter (PM) indicates to "the blend of solid and liquid phase materials that are existing in the air". Soot is considered to be the main constituent of the PM. This is because the particles and droplets produced as a result of lubricating oil and unburned fuel are adsorbed on the soot [81]. Carbon is the primary component of soot, which is produced from fuel-rich flames. Soot is usually produced as a result of incomplete combustion at high temperatures in which it turns into a solid phase in fuel-rich area. Guo et al. [82], observed that the maximum soot primary particle diameter is approximately between 25 to 30 nm. Tree and Svensson [83] illustrated the generally-known six steps involved in the formation of soot particles from liquid or vapour phase hydrocarbons as shown schematically in Figure 1-3. The six steps in order are "pyrolysis, nucleation, coalescence, surface growth, agglomeration and oxidation" [83].

The oxidation process is about transforming the hydrocarbons into different combustion products such as carbon monoxide (CO), carbon dioxide (CO_2) and water (H_2O). The oxidation process is not shown in Figure 1-3 due to the fact that it could happen simultaneously with any of the other five steps at any time during the formation processes. It is important to know the oxidation rate because it determines the soot emissions coming out from the flame as well as it can control the concentration of soot in different areas of the flame [84]. The incomplete soot oxidation process is the main reason for soot emissions. Its oxidation rate is mostly dependent on two factors: how high the temperature in the mixture is, and the amount of the oxygen available in the mixture. According to Glassman and Yetter [84], the soot particles start oxidizing once the temperature of the mixture becomes higher than 1300 K. In addition, they have suggested that the high amount of oxygen in the fuel mixture helps in accelerating the soot oxidation process. Fenimore et al. [85], who have calculated the soot oxidation in flame gases mentioned that a significant amount of soot in combustion applications is oxidized through radical species such as OH. The soot oxidation through OH species radical has been

investigated further through various experiments by numerous researchers [86]–[88]. Neoh et al. [86] who have studied the impact of oxidation on soot particles using a two-stage burner suggested that soot particles tend to oxidize by O_2 molecules in the fuel-lean region and through OH radicals in the fuel-rich region. The soot oxidation by the O_2 and OH has also been investigated in laminar diffusion flames by Garo et al. [87]. They found that when O_2 molecules are not high enough to oxidize soot particles, OH becomes the main soot oxidizer in the mixture. Puri et al. [88] found out from their results that OH radicals concentration levels become low as the flames are more sooty. This is because the more soot in the flame, the more OH radicals are consumed in oxidation. Almost all studies carried out confirmed that OH radicals have higher efficiencies of collision than O_2 molecules with soot particles in the flames holding high soot concentrations.

In the pyrolysis stage, changes in the atomic composition of the fuel start to occur. The percentage of soot oxidation process at this stage is low [83]. According to Smith [89], the reactions at this stage requires heat from its surroundings, meaning that its rates are very much reliant on temperature. The increase in pyrolysis temperature results in rising the amount of carbon in soot, as well as decreasing the size of soot particles [90]. In addition, this stage is considered to be highly dependent on the concentrations of some molecules and radicals such as O_2 and OH. The fuel pyrolysis stage results in forming the soot precursors such as C_2H_2, C_3H_3 and PAH as shown in Fig. 1-3. The formation of soot precursors depends on both the oxidation rate and the pyrolysis rate of the fuel. Both of these two rates rely on the temperature as mentioned above. However, the temperature affects the rate of the oxidation more than the pyrolysis rate [36]. This means that if the temperature is high and the oxygen concentration is high (like in pre-mixed flames), the oxidation rate will be higher and hence less soot will be formed.

According to Tree and Svensson [83], the soot particle inception (nucleation) is the process of forming the particles from soot precursors. This stage comprises of both small hydrocarbons precursors as well as aromatic molecules. Nucleation stage generates solid particles of a size smaller than 2nm called nuclei. The total mass of the soot is not affected much by these nuclei. However, these small solid particles pave the way for the evolution of the next stage (surface growth), thus, its impact is indirect. Glassman [84] suggests that there is a congruity in the chemical mechanisms for the generation of soot from both premixed and non-premixed systems. In addition, they suggested that in both systems there is a mechanism that is

fuel-independent and has different pathways to form the soot. The feature of the fuel and the adiabatic flame temperature are considered to be the main factors that impact these routes. This means that the tendency of forming soot by different fuels can be distinguished by the variations in the initial rate of formation of 1st and 2nd ring structures. Therefore, soot particle inception rate is controlled by the formation rate of initial ring formation [83]. Most researchers agree that soot particles are formed through polycyclic aromatic hydrocarbons (PAH). In 2002, Frenklach suggested that soot formation's main pathway is the combination of the surface reaction (formation, growth and oxidation) of particles and PAH [91]. The formation of the initial aromatic ring, (benzene and phenyl (A1)), is the primary stage in this process. There are multiple potential routes for the first stage that have been discussed earlier [91], [92]. One of these routes involve adding C_2H_2 to n-C_4H_3 and n-C_4H_5 - this is called "even-carbon-atom" route [91]. On the other hand, other researchers [93], [94], suggested an additional route for A1 formation, known as "odd-carbon-atom" pathway. This is related to resonantly stable radicals, for example, CH_3, C_5H_5 and C_7H_7. It has been proposed that C_3H_3 is one of the main species resulting in formation of benzene (C_6H_6) [94]–[96].

In the surface growth stage, the incepted soot particles react with the gas-phase species resulting in a mass addition to the surface of the soot particles. This stage persists as the soot particles travel away from the reaction zone into cooler areas [83]. It has been suggested earlier by Frenklach and Wang [97] that the main gas-phase species that reacts with the soot particles and results in a surface growth is C_2H_2. They also suggested that the condensation of PAH on the particles' surface lead to the surface growth.

Agglomeration stage is also called "coagulation." It occurs when the developed soot particles collide with each other because of their random and fast motion, and coalesce as a result. Consequently, this decreases the number of soot particles. No changes in the mass of the soot particles occur during this stage. The formed soot particles have a spherical shape initially, and after the coalesce are processed, the soot particles (that were combined with each other) gain a chain-like structure as shown in Fig. 1-3.

Further study on soot formations of targeted fuels was conducted in this PhD thesis by looking at the reaction pathway analysis of soot precursors through 1D simulations (Chapter 3). In addition, experimental investigations were performed for different flames mixtures to calculate the soot volume fraction and soot temperatures (Chapter 6).

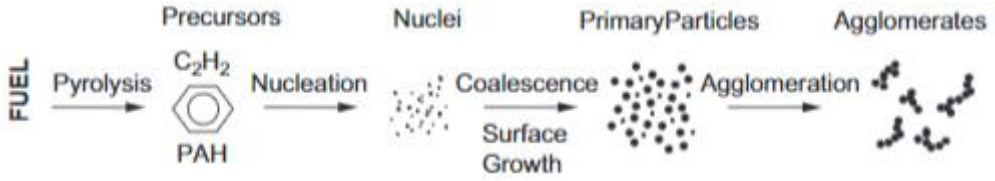

Figure 1-3 Soot production steps from hydrocarbons in the liquid or vapour phase [83].

1.5.1.1 Laser Induced Incandescence Method for Soot Measurement

Laser-induced incandescence (LII) has become a well-known method in combustion science for the soot volume fraction and particle size measurements, and especially in temporally and spatially soot particles resolved measurement [3–5]. LII technique involves heating up the soot particles to a high temperature through a pulsed laser, allowing thermal emissions to be measured during the cooling regime [101]. It is a 'largely selective' technique as it is only related to the non-volatile particles generated as a thermal emission, and the volatile particles are assumed to be completely evaporated during the time scale of the laser pulse [102]. As mentioned earlier in Section 1.5.1, soot particle formation undergoes multiple processes. Solid particles exist in some of these processes. A comprehensive information and understanding of soot particles volume fraction and size is important to investigate the soot emission processes in hydrocarbon/ biofuels flames.

Measurements on the formation characteristics of soot in flames containing DME and iso-pentanol were limited in the literature. Hayashida et al. [103] and Yoon et al. [104] used LII technique to measure the relative concentration of soot in DME laminar co-flow [103] and counter flow [104] diffusion flames, and found negligible concentration of soot in DME flames [104], indicated by the low LII signal intensity compared to methane or propane flames [103]. The latest publication by Ahmed et al. [105] showed that the soot effective particle diameter in the laminar diffusion flame with DME addition is in the range of 18 nm to 35 nm, which on the other hand, was ranging between 5-7 nm at various flame heights in Li et al. [106]. However, those studies used a point-wise approach rather than an imaging method. The latter could provide snapshots of 2-dimensional quantifications of soot emissions, thus beneficial in turbulent conditions. In addition, the effects from detection parameters of the LII signal (i.e. acquisition delay time, duration) and the laser fluence level on the derived soot concentration or particle diameters were not fully-addressed, which could affect the comparative

measurement of DME/hydrocarbon flames, thus requires to be investigated further. This is further investigated in detail in DME/ methane air flames in Chapter 6.

1.5.2 Fundamentals of Oxides of Nitrogen (NOx) Formation

One of the main species that contributes towards polluting the atmosphere by having a significant impact on the ozone balance is NO_x. The main nitrogen oxides that have been found in the atmosphere are nitric oxide (NO), nitrogen dioxide (NO_2) and nitrous oxide (N_2O) [84], [107]. The NO and NO_2 gases collectively are termed as NO_x. NO is considered as one of the primary pollutants, whereas NO_2 falls under both primary and secondary pollutants classifications.

There are three major reaction mechanisms that result in forming NO_x during combustion: thermal NO, fuel NO and prompt NO. The NO that is formed as a result of high temperatures is usually described as "thermal" NO. Thermal NO reaction mechanism, also called the Zeldovich mechanism, has been introduced by Zeldovich and co-workers (as cited in Bowman [108]). Zeldovich et al. (as cited in Bowman [108]) showed that the formation of NO occurs through the oxidation of the atmospheric nitrogen. Zeldovich et al. determined three chemical reactions 1.1-1.3 called the extended Zeldovich mechanism as follows:

$$O + N_2 \leftrightarrow NO + N \quad (1.1)$$

$$N + O_2 \leftrightarrow NO + O \quad (1.2)$$

$$N + OH \leftrightarrow NO + H \quad (1.3)$$

The oxygen atoms are mostly produced from the breakup of the O_2 molecules and subsequently react with the N_2 molecules forming NO, as shown above in reactions 1.1 & 1.2 [84].The thermal NO mechanism refers to the NO that is produced at the high temperature post-flame area. Thus, the formation of nitrogen oxides is controlled mainly through the thermal mechanism in the systems of which the flame contains high temperatures. According to Turns [109], thermal NO contributes mostly near the stoichiometric where both high temperature and high concentrations of O and OH radicals exist. They also suggested that NO_x emissions in both premixed and non-premixed flames can be determined through three factors: temperature, composition of the fuel mixture and the residence time. OH radicals contributes to forming thermal NO as shown above in the reaction 1.3.

Fenimore [110] noticed in their study that there were some NO formation in the fuel rich zone. Therefore, they suggested that there are reactions other than the thermal NO mechanism that contributes to forming NO in the flame region. Furthermore, they suggested that the nitrogen in the air may result in producing small amounts of CN compounds in the flame region. Consequently, the CN compounds generate NO that is referred to as "prompt" NO. The reaction equations that Fenimore [110] proposed for breaking up the N_2 included hydrocarbon radicals (HCN), as follow:

$$CH + N_2 \leftrightarrow HCN + N \quad (1.4)$$

$$C_2 + N_2 \leftrightarrow 2CN \quad (1.5)$$

NO will then be formed from the N atoms through reactions 1.4 and 1.5. Whereas CN needs high concentration of O_2 in order to form NO. Miller & Bowman [111] suggested that prompt mechanism occurs in the flame region when there is a high-level of HCN. In addition, they revealed that prompt mechanism occurs faster than the thermal mechanism.

Another mechanism ("fuel" NO) that contributes to forming NO was discussed by Miller & Bowman [111]. They stated that adding small quantities of N_2 to the fuel can result in increasing the amounts of NO. They also suggested that this mechanism occurs through reactions that include intermediate species, for example NH_2 and NH_3.

The above-mentioned background of the three mechanisms help in analysing the potential causes and routes of NO_x formation of some fuel mixtures in this thesis. Thermal NO reaction mechanism is used for the kinetic study in this PhD. In Chapter 3, the effect of ethanol (oxygenated fuel) addition on NO formation is studied through 1D simulations. In Chapter 5, qualitative NO-PLIF measurement is presented for iso-pentanol/ n-heptane swirl spray flames.

1.5.3 Previous Studies on DME Laminar Non-premixed Flames

Several studies have been conducted utilizing diffusion flames phenomenon to study the characteristics of soot formation [23], [25], [96], [104], [112]–[117]. It has been found from most of these studies that there is a considerable impact of fuel structure on PAH and soot formation. Several researchers have added DME to the combustion of different fuels in non-premixed flames and studied the impact on soot and PAH [23], [25], [96], [104], [105], [112]–[114], [117], [118], however, different trends were concluded in the relationship between DME addition and soot emissions. Details of these previous studies are presented in Table 1-2.

Table 1-2 Previous studies on non-premixed flames.

Authors	Flame configuration	Method	Fuel	Conclusion
Yoon et al. [104]	Counter flow non-premixed	Planer LII* and LIF**	DME/ethylene	Increase in the peak SVF and C_6H_6 with DME addition up to 40%.
Yoon et al. [104]	Counter flow non-premixed	Planer LII and LIF	DME/ methane, ethane and propane	Decrease on soot and PAH formation across all DME mixture ratios.
Choi et al. [117]	Counter flow non-premixed	Laser extinction & 1D simulations	DME/ethylene	In comparison to pure ethylene flame, Soot and PAH were increased for a 5% and 14% DME mixture ratio but decreased when 30% DME was added. It was also noted that the largest sizes of soot particles (50 nm) were obtained in the pure ethylene and soot particle size reduced gradually as more DME was added.
Liu et al. [23]	Co-flow non-premixed	PLIF and 2D LII & 2D computations	DME/ethylene	Both methods agreed that little DME addition to ethylene results in an increased soot and PAH formation.
Bennett et al. [96]	Co-flow non-premixed	Mass spectrometry and thermocouples & 2D computations	DME/ ethylene ethanol/ ethylene	DME addition increased the benzene formation more than the ethanol addition. Their justification was that the carbon-oxygen bond breaks in DME and generates CH_3, which is not the case with ethanol.
McEnally and Pfefferle [114]	Co-flow non-premixed	LII	DME/ethylene	Increase in the peak SVF and C_6H_6 with DME addition up to 10%.
Ahmed et al. [105]	Co-flow non-pemixed	PLIF and LII	DME/ethylene	Small addition of DME (10%) increased soot formation.

*Laser induced incandescence

** Laser induced fluorescence

In 2007, McEnally and Pfefferle [114] studied the influence of DME and ethanol on soot and C_6H_6 in ethylene non-premixed flames. Their results displayed an increase in soot and C_6H_6 by adding DME/ ethanol. They explained the formation of soot and PAH as follows; the added DME/ ethanol broke down into methyl radical (CH_3), which in turn, reacted with C_2 to produce propargyl (C_3H_3), and C_6H_6 was then formed. One year after, Yoon et al. [104] mixed

DME with different biofuels including methane, ethane, propane, and ethylene to investigate the concentration of PAH and soot formation using laser induced incandescence (LII) and laser induced fluorescence (LIF) techniques. Their results proved that no odd carbon species (synergistic effect) is formed from pure ethylene flame. In regards to the addition of DME into ethylene flame, their results were exhibiting in a similar way to those of McEnally and Pfefferle [114] only when the addition of DME was less than 40% in volume. Thereafter, a significant decrease of soot and PAH was obtained. Nevertheless, their results of DME blend with methane, ethane and propane showed a decrease on soot and PAH across all DME mixture ratios. In their experiment, Yoon et al. [104] considered that the maximum intensity of the LII and PAH-LIF signals appears in the regions with highest concentration of soot and PAH. Therefore, they used the peak LII and PAH-LIF signals for all conditions as an indication of soot formation and PAH as shown in Figure 1-4. In 2009, Bennett et al. [96] conducted a computational and experimental study of the impact of DME/ ethanol to non-premixed ethylene/ air flames. They were the first to have modelled 2D computations with detailed chemistry among all past studies which were carried on addition of DME/ ethanol to hydrocarbon flames. Their computational and experimental outcomes showed that temperature and velocity profiles stayed almost unchanged after DME/ ethanol were added by small proportions. Because of this, they considered that the occurrence of any change for any profile in the results would be due to chemistry. The results and explanations of Bennett et al. [96] in terms of benzene (C_6H_6) formation were similar to McEnally and Pfefferle [114]. However, Bennett et al. [96] found that the addition of DME increased the formation of benzene more than the addition of ethanol, which is surprising considering that both generate a small amount of soot. The justification was that the reaction routes which break any of the carbon-oxygen bonds in the DME generate CH_3, which is not the case with ethanol [96], [114]. As pointed out by Liu et al. [23], Bennett et al. [96] failed to take into consideration the formation of soot in their computations. In fact, they believed that this could impact the flame's temperature and species concentration. Accordingly, Liu et al. [23] carried out an experimental and numerical study to further investigate the effect of DME addition to ethylene/ air on soot formation and PAH in non-premixed flame. Their experimental findings were similar to Yoon et al. [104] in terms of adding small amounts of DME to ethylene. On the other hand, Liu et al. [23] numerical results displayed a gradual decrease in the flame temperature where the DME mixture ratio was added to ethylene until the 50% mixture ratio was reached. However, when DME mixture ratio was increased from 50 to 75%, the flame temperature increased significantly. The most

astonishing finding was that the flame temperature reached the lowest point among all the conditions when the DME mixture ratio increased from 75 to 100% (pure DME). Based on their computational findings they justified the early reduction in flame temperature with the small addition of DME as a result of the risen radiation loss via the increase in PAH and soot formation. In 2014, Sirignano et al. [112] examined the effect of DME addition to ethylene in both flames categorizations; premixed and non-premixed. Their non-premixed flame outcomes found to be in a good agreement with the results shown by Yoon et al. [104] and Liu et al. [23]. In 2015, Choi et al. [117] implemented the laser extinction/scattering diagnostic method to study the impact of adding DME to ethylene flames on the soot particles size. Their results displayed that the largest concentrations of soot were noticed when a little amount of DME added to ethylene (5% and 14% DME mixing). Nevertheless, the biggest sizes of soot particles (5.0×10^{-8} m) were obtained in the pure ethylene flame. The sizes of soot particles were then reduced gradually as more DME added [117]. Based on the results presented by Choi et al [117], this means that DME addition to ethylene produces an increase in the soot concentration rather than increasing the sizes of the soot particles.

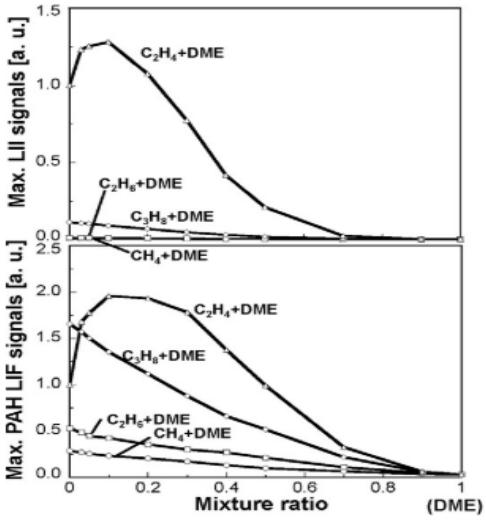

Figure 1-4 The peak LII and PAH LIF signals for DME mixtures with CH_4, C_2H_4, C_3H_8 and C_2H_6 [104].

The majority of the studies [23], [96], [104], [105], [114] were carried out on DME/ethylene mixtures and found a small amount (between 5% to 40%vol) addition of DME to ethylene fuel resulted in an increase in soot formation. This is contrary to the finding of reduced soot emission benefits from DME/diesel blend conducted in a direct injection engine [119] and the finding in DME/alkane blends, where DME blending with methane, ethane and propane showed a decrease in soot and PAH formation across all DME mixture ratios [104]. Hence,

further studies are required to clarify the soot emission benefits from DME additions to the hydrocarbon fuels, and with extended range of fuel compositions and burner configurations. Most of the previous studies have been focused on the DME/ethylene flames and the effect on soot formation. However, there is still a paucity of knowledge regarding flame structure and flame heat release quantification for non-premixed DME/hydrocarbon blend flames.

1.5.4 Previous Studies on Iso-pentanol Combustion

The rising popularity of high chain alcohols as potential alternative fuels and the subsequent demand for their combustion and emissions data motivated the current investigation on iso-pentanol fuel. Iso-pentanol is one of eight isomers of amyl alcohol (pentanol). All of these eight isomers have the same molecular formula $C_5H_{11}OH$. The term "amyl alcohol" alone without additional explanation is usually used for the n-pentanol isomer, which has a straight chain (i.e. molecular structure is linear). Whereas iso-pentanol has a branched-chain alcohol. Iso-pentanol has a lower solubility in water compared to n-pentanol. In recent years, researchers have focused more on C5 family of alcohols; most of the studies have focused on either or both iso-pentanol and n-pentanol. No clear reason has been declared in the previous studies about the choice between n-pentanol and iso-pentanol. Although both of them have characteristics close to each other, as shown by Soo-Young [30], n-pentanol was more investigated. This could be because better heat transfer can be achieved by n-pentanol since it has a straight chain alcohol. In addition, the choice between n-pentanol and iso-pentanol could be linked to their availability or price. Nevertheless, minimal research has been conducted on the iso-pentanol combustion and emissions.

There have only been only a few studies that have investigated the combustion and emission characteristics of iso-pentanol. Investigations carried out on iso-pentanol combustion characteristics and emissions are limited and mostly on ignition delays [120]–[122], laminar flame speeds [121], [123], and the chemical reaction mechanism developments [123]–[125]. In addition, there has been only a few studies that have investigated the impact of iso-pentanol on soot formation. Ying et al. [126] investigated the soot emission of an iso-pentanol/ethylene blend in an inverse diffusion flame. They observed that the addition of iso-pentanol made the soot agglomerates more compact and improved the oxidation reactivity of soot particles [126]. Carniglia [127] studied the soot emission of Jet A-1 mixture with n-pentanol (up to 20% by thermal power), and observed a reduction in soot emission as n-pentanol quantity increased in the blend. Ma et al. [128] investigated the combustion properties of the n-pentanol and diesel

blend utilising a constant-volume bomb. They found that the addition of n-pentanol to diesel fuel speeds up the oxidation process of soot, leading to lower soot emissions. However, there is no study yet reported the soot emission of pure iso-pentanol swirl spray flames. Therefore, this thesis will measure the soot volume fraction of pure iso-pentanol and its mixture with n-heptane fuel using planar time-resolved 2C-LII.

There are a few studies on CI engine applications and chemical kinetics of iso-pentanol/n-pentanol blends carried out to understand its role in low-temperature chemistry and soot reduction. Jin et al. [26] studied the impact of long-chain alcohols (C3-C5) on solubility when mixed with diesel fuel. They found that iso-pentanol (C5) has less solubility on water than C4 alcohols such as iso-butanol. Most of the studies that investigated the NO_x emissions of n-pentanol were conducted on CI engines [32], [34], [129]–[132]. Also, no agreement was found on the effect of NO_x emissions. Wei et al. [129] tested different mixing ratios of n-pentanol (ranging from 0 to 30%) with diesel fuel and found that the n-pentanol addition resulted in increasing NO_x emissions by about 8% (maximum). Li et al. [32] suggested that NO_x and soot emissions produced by n-pentanol can be reduced concurrently using exhaust gas recirculation (EGR). A few studies have investigated the impact of EGR on n-pentanol [130], [133] and iso-pentanol [134] emissions characteristics, and they observed a decrease in NO_x emissions when applying EGR. Nevertheless, some studies did not use EGR and obtained no increase in NO_x emissions when n-pentanol was added to diesel fuel [34], [131], [132]. Li et al. [132] observed that the NO_x emission produced from the mixture of 20% n-pentanol with 80% diesel was almost similar to those of pure diesel fuel in 6 cylinder diesel engine.

Few studies on iso-pentanol were also conducted on HCCI (Homogeneous charge compression ignition) engines. A study carried out on HCCI engines [20] observed that iso-pentanol has more advantages as a fuel for future HCCI engines than currently used ethanol. Yang et al [20] studied the fundamental characteristics of iso-pentanol combustion using HCCI engine. One of their key findings was that the operation-wise of iso-pentanol is similar to ethanol in the HCCI engine in-terms of ignition behaviour. However, they also concluded that the iso-pentanol's reactivity is higher than ethanol and gasoline in HCCI engines. Most of the studies involved on investigating iso-pentanol in HCCI engine conditions agreed that iso-pentanol combustion shows intermediate temperature heat release (ITHR) features [20], [124]. Multiple experimental and modelling studies have also investigated the ignition behaviour of iso-pentanol [120], [135].

1.5.5 Flame Heat Release Measurements

Heat release rate (HRR) is an important aspect of hydrocarbon fuel combustion and a factor to consider when applying alternative fuels in practical applications. The rate of heat release provides information about the thermal energy produced in the combustion. Hence, it can describe how quickly heat is produced in a combustion process. The spatial spread of HRR can identify the reaction zone areas. The heat release rate is important for comprehending and predicting combustion instability [136], [137], as well as combustion noise [138]. Determining the heat release rate through direct measurement techniques is not feasible so far due to difficulties in concurrently monitoring several species and temperatures [139]. Alternatively, researchers use a number of chemical indicators and markers (such as radicals) to mark the rate of heat and its regions.

Multiple combustion investigations have employed the hydroxyl (OH) radical to identify areas of reaction zone [66], [139], [140]. Cavaliere et al. [66] utilised OH Planar Laser Induced Fluorescence (OH-PLIF) diagnostic method to study the flame sheet structure and shape of n-heptane spray flames. Yuan et al. [140] utilised OH-PLIF and CH_2O-PLIF simultaneously to mark the heat release regions of n-heptane spray flames.

Chemiluminescence imaging as a combustion diagnostic has been widely used in premixed flames as a marker for the flame heat release rate (HRR) and equivalence ratio [141]–[145], and as an identification of the reaction zone [145]. The natural existence of chemiluminescence in the flames can be attributed to the excited radicals, for example OH*, CH* and C_2* formed through different chemical reactions during combustion. Hardalupas and Orain [142] demonstrated that CH* and OH* chemiluminescence emission intensities are good markers for HRR in premixed counter flow flames, and the OH*/ CH* intensity ratio with 5% uncertainty can be used to measure the equivalence ratio at lean and stoichiometric conditions. Baumgardner and Harvey [144] also observed that the ratio of OH*/ CH* is well correlated with equivalence ratio for lean conditions, whereas the ratio of C_2*/ CH* exhibits better correlation for the rich conditions. Furthermore, Panoutsos et al. [145] showed that OH* and CH* can be utilized as HRR indicators in both premixed and non-premixed counter flow methane flames. The validity of using CH* or C_2* chemiluminescence in non-premixed flames as an indicator of HRR and equivalence ratio remains questionable due to the likely interference from soot emissions. This thesis will investigate the feasibility of utilising OH*,

CH* or C_2* chemiluminescence as a HRR and equivalence ratio marker in non-premixed flames focusing on DME addition using both experimental and numerical approaches.

Formyl radical (HCO) is essential to the hydrocarbons oxidation in combustion processes. It is created through abstraction and decomposition reactions with CH_2O [146]. HCO was proven in previous studies to be an accurate indicator of HRR [146], [147]. This is due to the fact that HCO exist in the final stage along one of the important routes leading to the formation of CO. In addition, CH_2O interacts with a large amount of HCO generation. Therefore, the availability of the precursor formaldehyde (CH_2O) directly affects the formation of HCO [146]. CH_2O is created via one of the most important heat-releasing reactions, $CH_3 + O \leftrightarrow CH_2O + H$ [136]. Nevertheless, the HCO-PLIF diagnostic method is challenging when used for turbulent flows due to its brief fluorescence lifespan. CH_2O generally forms at low-temperatures and consumes at the high-temperatures. Yuan et al. [140] 1D simulation results showed that the majority of CH_2O mole fractions overlap with the low-temperature HRR region. The product of CH_2O-PLIF and OH-PLIF was used as a substitute for HCO-PLIF to mark the HRR regions [140]. Furthermore, CH_2O-PLIF has been commonly used as an additional methodology in flame structure research.

1.5.6 Local Extinction & Lift-off of Turbulent Spray Flames

The interaction between the flow fields of the fuel spray and the air have a significant impact on the main mechanisms that regulate fuel spray flame behaviour, such as flame stabilization [46]. Flame lift-off and local extinction are important features to investigate and study as they help in understanding the flame stabilization and dynamics of liquid fuels combustion. Verdier et al. [148] described the controlling parameters that may play a big role on the stability mechanism of a spray jet flame. Those parameters include flow dynamics and droplet convection-vaporization. Therefore, there are numerous existing studies that have measured the local extinction and lift-off and demonstrated how they can be affected. However, there is a lack of studies on the flame lift-off and local extinction of iso-pentanol fuel in a bluff-body swirl spray flame. Therefore, this thesis will also focus on how iso-pentanol (the low carbon alternative) would affect the flame structure and including lift-off and local extinction.

1.5.6.1 Local Extinction

The phenomenon of local extinction in the flame is strongly related to lean combustion, as mentioned earlier in Section 1.4.1. This phenomenon occurs when the flow velocity become very high and hence, the flame loses its stability spreading downstream and ultimately extinguishes completely [149]. Previous studies [66], [150], [151] investigated the flame local extinction of different liquid fuels using a spray burner. Yuan et al. [150] used the OH planar laser-induced fluorescence (PLIF) technique to study the influence on local extinctions at conditions close to blow-off by different high and low volatility fuels in swirl spray flames. Their OH-PLIF measurements showed that with increasing airflow velocity less local extinction occurs in the inner reaction zone, notably for the heavier fuels [150]. Cavaliere et al. [66] carried out a comparison study of the blow-off behavior in three different types of flames (non-premixed, premixed and spray), and investigated the location and occurrence of local extinction in each of them. Benajes et al [151] examined the local extinction of the n-heptane spray flame numerically. They concluded that the high level of turbulence and the interaction between the droplets with flame front are the main cause of forming extinctions. Benajes et al [151] also noticed high levels of formaldehyde (CH_2O) and discontinuous concentration of OH in the flame front, of which altogether indicated the occurrence of local extinction.

1.5.6.2 Lift-off

Lift-off phenomenon occurs when the flame separates from the base of the burner and becomes steady somewhere downstream the chamber [84]. The flame will completely blow-off if the velocity continues after the start of lift-off phenomenon. The axial distance between the lowest edge of the flame sheet and the edge of the bluff-body (for burners equipped with bluff-body) is called lift-off height [66]. The flame is less stable as the lift-off height increases because it is much closer to the global blow-off. Recent work conducted by Gimeno et al. [152] studied the flame lift-off height of n-heptane, n-decane, and n-dodecane spray flames in a non-swirled co-flow configuration. According to their findings, the fuel with the greatest droplet size and the lowest volatility has the maximum lift-off height. Additionally, when the lift-off height increases as a result of increasing the co-flow velocity, a less rich reaction zone occurs downstream of the lift-off height leading to less soot formation [152]. Chen et al. [153] investigated the lift-off in non-premixed flames using bluff-body burner. They found that at low fuel velocities, local extinction dominates the lift-off because the jet flame front strongly

interacts with the recirculating air flows. Nishimura et al. [154] further investigated the behaviour of lift-off in bluff-body non-premixed flames at both fuel dominant and air dominant flame conditions. Yuan et al. [150] results showed that with increasing airflow velocity the average lift-off height decreases. Cavaliere et al. [66] measured the heights of lift-off at conditions close to the blow-off and far from blow-off. They found that as the air velocity rises the mean height of lift-off reduces. Mulla and Renou [155] used LII and OH/PAH-PLIF diagnostic methods to investigate soot formation in n-heptane spray flame. One of their findings was that both lift-off and local extinction have no impact on soot behaviour, probably because of the sluggish reaction time of soot.

Most of the previous studies that have investigated lift-off and local extinction in turbulent spray flames have used the OH-PLIF diagnostic technique. This is because OH-PLIF provide a clear insight of the reaction zone, enabling the detection of places where the flame cut off (local extinction) and measuring the height of flame sheet from the base of the injector (lift-off).

1.5.7 Dilution Air Strategy

Dilution air strategy reduces the amount of NO_x emissions significantly as its addition results in more of a lean combustion. In general, lean combustion is associated with an elevated risk of extinction, which can ultimately lead to the global blow-off event [156]. Many studies investigated the impact of different operating parameters including the injection of air dilution on soot emission, oxidation, and particle size distribution of swirl-stabilized flames [64], [157]–[161]. Geigle et al. [159], [160] studied the effect of dilution air at a fixed location on soot emission, oxidation and polycyclic aromatic hydrocarbons (PAH) of ethylene air swirl-stabilized flames using laser-induced incandescence and PAH laser-induced fluorescence. They observed that the addition of dilution air had an impact on the location of soot areas as well as OH distributions in the flames. In addition, they investigated the relationship between soot and OH distributions after the dilution air introduction. Stöhr et al [161] observed that soot accumulates in the rich pockets depending on their residence times, while soot oxidation takes place in the lean zones containing OH. Their findings imply that a suitable modification of dilution air injection creating adequate recirculation of lean burnt gas may further limit the formation of soot. El Helou et al. [157] investigated the influence on soot formation and oxidation by varying the locations and amount of dilution air in C_2H_4 air (gaseous fuel) flames. Their outcomes revealed that dilution air resulted in a faster mixing, and smaller lengths of fuel penetration. In addition, their findings demonstrated that the quantity

and location of injected dilution air affect the soot production. De Falco et al. [158] further investigated the soot formation in a non-premixed ethylene air flames but focusing more on their particle size distribution. El Helou et al. [64] carried out a comparison on the soot formation of synthetic kerosene and conventional fossil liquid fuels in a swirl spray flames along with air dilution injection. Their results showed that the distribution of SVFs is dependent on the quantity of dilution air.

The type of the fuel and its characteristics (i.e. volatility) also play a role in flame stabilization mechanism. Farag et al. [162] evaluated the effect of fuel volatility on lean blow-off (LBO) by using four different fuels, heavy oil was the least volatile and gasoline was the most. According to their findings, the rate of the air stream near the LBO limit increases as the fuel volatility increases, improving combustion stability. Although Yuan et al. [150] used a variety of high and low volatility fuels, their results addressing the effect of fuel volatility on flame stability were in good accord with those of Farag et al. [162]. Numerous studies have investigated the fuel structure of n-heptane both numerically and experimentally in swirl spray flames. The appearance of n-heptane fuel's swirl spray flames is a dual body with a V-shaped shape that has inner and exterior sections [150]. The flame steadily shrinks and both sections get closer to the bluff-body as it approaches the blow-off condition by increasing air stream speed. Davide et al. [66] studied the blow-off behaviour of n-heptane spray flame. They discovered that the loss of flame stability causes the velocity to become independent of fuel flow rate at blow-off. The height of the flame decreased and remained affixed to the bluff-body as the LBO condition approached. Additionally, it was discovered that the chemiluminescence of OH* was lower in the inner flame zone and higher at the outside flame zone. They had a continuous layer of OH in their spray flame structure, which pointed to local blow-off activity. Many studies investigated the n-heptane combustion characteristics in swirl spray flames, however there is no study yet investigated n-heptane combustion, including its stability, in a swirl spray flames with dilution air strategy.

1.5.8 Computational Fluid Dynamics (Modelling) Works on Laminar Diffusion Flames

The use of computation-based techniques to model combustion processes of alternative fuels has increased dramatically in recent years. It has become an essential component of the alternative fuels development process. The combination of experimental and simulation studies play an important role in reducing time and cost of fuels development process through

categorising the aspects that needs additional comprehensive investigations [163]. In latest few years, multiple studies have used 2D CFD modelling to reveal essential mechanisms for different alternative fuels in laminar diffusion flames. DME fuel mixtures has been studied computationally in few studies as mentioned earlier in Section 1.5.3. The key processes in soot production, shown in Figures 1-3, are broadly accepted [164]. Consequently, ongoing work has been done to create soot models that can be used for various flame types along with multiple fuels, including hydrocarbons and oxygenated fuels [23]. However, soot modelling of DME/hydrocarbon fuel mixtures through CFD were not investigated enough. In this work, the CFD model used is the Brookes and Moss model, further details about this soot model is discussed in section 2.4 (Chapter 2).

The modelling study in this thesis primarily concentrated on the soot emissions and combustion characteristics of DME/C_2H_4/N_2 co-flow flame mixtures using a CFD approach. Similar boundary conditions of the experimental study were applied in this computational study to develop a new validated CFD model tailored to DME which is currently missing and unknown. The current soot model used in this thesis was created and validated based on CH_4 flames. The aim of this work is to study the impact of DME fuel on the soot model, and check if this soot model would be still valid to use for DME (oxygenated fuel) flames. Moreover, this thesis visualizes soot volume fraction calculated from the modelling work for the different mixing conditions of DME/ C_2H_4/ N_2 co-flow flames which will be presented and discussed in Chapter 6.

1.6 Research Objectives

The scope of this thesis is to conduct several experimental and numerical studies to provide an in-depth understanding of combustion and emission characteristics for key biofuels (i.e. DME & iso-pentanol) and their mixtures. For DME fuel combustion, the main objective is to understand the impact of DME addition to hydrocarbon fuels, including methane and ethylene, in laminar diffusion flames on soot formation, heat release rate, and flame structure. Whereas for iso-pentanol fuel combustion, the main objective is to understand the impact of iso-pentanol addition to n-heptane turbulent bluff-body swirl spray flames on flame stability, soot formation, NO_x emission, heat release rate, and flame structure. The impact of iso-pentanol on flames stability will be investigated under various flame conditions including cases far from and near blow-off.

The objectives of this thesis are as follows:

- **Understanding flame structure of DME/ hydrocarbons flames**: To investigate DME and its mixtures flame structures and species profiles including OH*, OH, CH*, CH, HRR, CH_3, C_3H_3, C_2H_2 and flame temperature through 1D numerical simulations implemented with a detailed chemical kinetic mechanism (Chapter 3).
- **Understanding flame structure of iso-pentanol and n-heptane flames**: To investigate iso-pentanol and n-heptane flame structures and species profiles including OH, CH, HRR, CH_3, C_3H_3, C_2H_2 and flame temperature through 1D numerical simulations (Chapter 3).
- **Heat release measurements**: To measure and investigate experimentally CH*, OH* and C_2* chemiluminescence of DME/ hydrocarbons flames and iso-pentanol flame mixtures (Chapter 4 and Chapter 5).
- **Understanding the correlation between chemiluminescence and equivalence ratio**: To investigate the feasibility of utilising OH*, CH* or C_2* chemiluminescence as a HRR and equivalence ratio marker in non-premixed flames focusing on DME addition using both experimental and numerical approaches (Chapter 4).
- **Understanding the reaction zone characteristics of turbulent swirl spray flames of iso-pentanol:** To investigate the impact of adding iso-pentanol to n-heptane and ethanol on the flame structure including lift-off and local extinction using OH-PLIF. To measure relative NO formation of pure iso-pentanol and its mixture with n-heptane fuel using NO-PLIF (Chapter 5).
- **Soot measurements of DME/hydrocarbons flames**: To measure and investigate experimentally soot emissions of DME flames and its mixtures using planar time-resolved 2C-LII (Chapter 6).
- **Soot measurements of iso-pentanol/n-heptane flames** To measure the soot volume fraction of pure iso-pentanol and its mixture with n-heptane fuel using planar time-resolved 2C-LII (Chapter 6).
- **Soot modelling of DME/hydrocarbons flames**: To check if the soot model used in this study would be valid to use for DME (oxygenated fuel) flames. In addition, to study the impact of DME fuel on soot volume fraction (Chapter 6).
- **Understanding the impact of dilution air strategy on the stability of swirl spray flames**: To investigate the impact of dilution air strategy on the stability of n-heptane bluff-body swirl spray flames including lift-off and local extinction (Chapter 7).

1.7 Structure of the Thesis

The structure of the thesis are as follow:

Chapter 1

This chapter introduce the problem and explains the motivation of this thesis. In addition, it contains literature background of all topics discussed later in this thesis. At the end on this chapter, research objectives and structures of this thesis are described.

Chapter 2

This chapter describes the experimental, numerical and computational methodologies that were utilised in this thesis.

Chapter 3

This chapter provides new understanding of the characteristics of soot emission, flame chemiluminescence and HRR through 1D chemical kinetic simulations in the non-premixed DME/CH_4 and DME/C_2H_4 flames. The flame structures and species profiles including OH*, OH, CH*, CH, HRR, CH_3, C_3H_3, C_2H_2 and flame temperature were calculated numerically through 1D simulations implemented with a detailed chemical kinetic mechanism (Mech_56.54). Additionally, the impact of adding N_2 as a diluent into DME mixtures with hydrocarbon biofuels was studied numerically. In addition, this chapter investigate iso-pentanol and n-heptane flame structures and species profiles including OH, CH, HRR, CH_3, C_3H_3, C_2H_2 and flame temperature through 1D numerical simulations.

Chapter 4

This chapter investigates experimentally the impact of DME addition to methane and ethylene fuels, across a full range of DME mixing ratios, on flame heat release and reaction zone using CH*, OH* and C_2* chemiluminescence. In addition, the use of species transport model in a computation fluid dynamics (CFD) study to predict the species concentration in 2D as well as to examine if the soot model is validated for DME (oxygenated flames). The CH*, OH* and C_2* were used to locate flame heat release regions as well as to investigate the soot signal's effect on their measurements. The ratios of the chemiluminescence pairs (OH*/CH*, OH*/C_2*) were studied on the feasibility to map local equivalence ratios.

Chapter 5

This chapter delivers new information on how the addition of iso-pentanol to n-heptane swirl spray flame would affect the heat release, flame structure, and flame stabilization including lift-off and local extinction at different operating conditions. In addition, to compare and show the variations between the swirl spray flames of iso-pentanol/ n-heptane blends and ethanol/ n-heptane blends.

Furthermore, relative NO emissions of iso-pentanol swirl spray flames using NO Planar laser-induced fluorescence (NO-PLIF) will be presented and discussed.

Chapter 6

This chapter presents soot particle measurements from self-calibrated planar time-resolved two-colour Laser-induced incandescence (2C-LII) in a range of co-flow laminar diffusion flames of methane and ethylene blended with DME, and in turbulent swirl spray flames of iso-pentanol/ n-heptane blends. In addition, the effects from detection parameters of the LII signal (i.e. acquisition delay time, duration) and the laser fluence level on the derived soot concentration or particle diameters will be discussed. In addition, the soot modelling results for DME flames will be presented in this chapter.

Chapter 7

The impact of dilution air strategy on the stability, HRR and flame structure of n-heptane bluff-body swirl spray flames using OH-PLIF and CH_2O will be investigated in this chapter.

Chapter 8

The chapter contains conclusions of main findings from this thesis, and provide suggestions for future works.

Chapter 2: Experimental and Numerical Methodologies

2.1 Introduction

This chapter describes different numerical and experimental studies used in this thesis. Numerically, 1D simulations of non-premixed laminar flames study were implemented in COSILAB to obtain a preliminary understanding of flame structures and key species profiles. In addition, 2D computational modelling of co-flow laminar diffusion flames was conducted in Ansys Fluent to investigate flame temperature and soot emissions. A co-flow laminar diffusion flame burner was used to examine the impact of DME addition to hydrocarbon fuels on soot formation, heat release rate, and flame structure. Additionally, a bluff-body swirl spray burner was used to study the impact of iso-pentanol addition to n-heptane turbulent bluff-body swirl spray flames on flame stability, soot formation, NOx emission, heat release rate, and flame structure. Figure 2-1 illustrates a flowchart representing this thesis's different numerical and experimental studies.

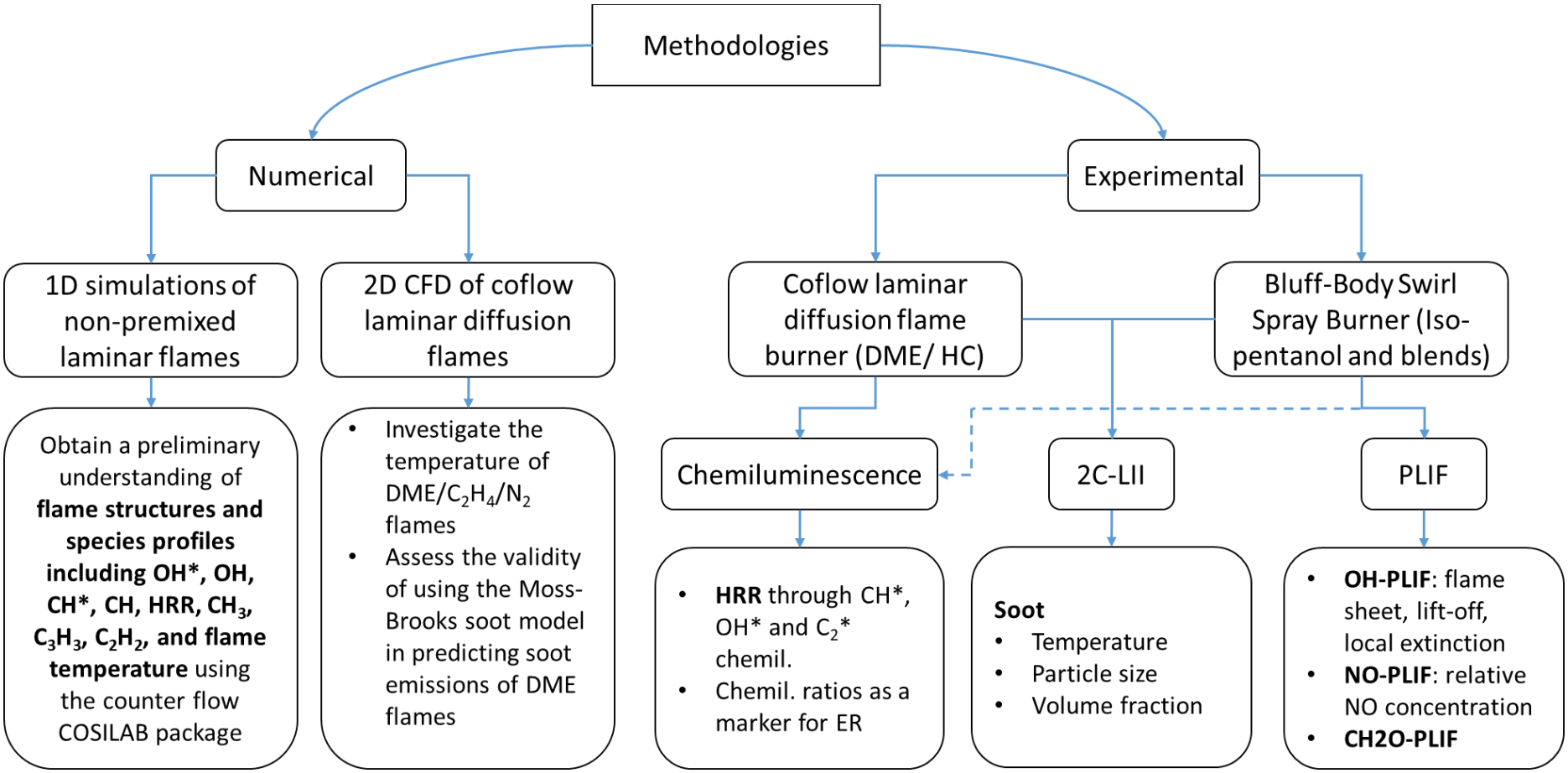

Figure 2-1 Flowchart of different numerical and experimental studies conducted in this thesis.

2.2 1D Numerical Simulations

For the 1D simulations of non-premixed laminar flames, calculations have been conducted using the counter flow COSILAB package [165]. These calculations were carried out at a range of fuel compositions from pure DME to 0% DME blended to $CH_4/C_2H_4/N_2$, pure ethanol to 0% ethanol blended to $CH_4/C_2H_4/C_7H_{16}$, and pure iso-pentanol. The aims of carrying out these calculations are to obtain flame structures and species profiles including OH*, OH, CH*, CH, HRR, CH_3, C_3H_3, C_2H_2 and flame temperature. In addition, to aid in investigating the feasibility of utilising OH*, CH* or C_2* chemiluminescence as a HRR and equivalence ratio marker in non-premixed flames focusing on DME addition. The 1D results will help with the image analysis in the subsequent chapters, in which the key characteristics of OH* and CH* from the simulation will help in explaining the experimental observations, and soot precursors' predictions and formation pathways will help analysing the soot concentration results obtained from 2C-LII.

For DME mixtures, simulations were implemented with a detailed DME chemical kinetic mechanism (Mech_56.54) [166]. Mech_56.54 comprises 113 species and 710 reactions. The Mech_56.54 mechanism has been already validated for DME, CH_4 and their mixtures by Burke et al. [166] using a range of their data and previous literature data. However, in this thesis, the Mech_56.54 mechanism was further validated in a 1D counter flow diffusion C_2H_4 flames with the available results of C_2H_4 in the Yoon et al. [104] study. The output profiles (produced by the Mech_56.54 mechanism) of C_2H_2 and C_3H_3 for C_2H_4 fuel have been compared against the results of Yoon et al. [104] for validation purposes. For ethanol mixtures, 1D simulation were employed with the San Diego mechanism [167], which contains 80 species and 354 reactions. Since these mechanisms do not include reactions for C_6H_6 and higher PAH species, the profiles of C_2H_2 and C_3H_3 were chosen to monitor the characteristics of soot formation for DME mixtures.

The non-premixed flames were modelled in a counter flow configuration. The species mole fraction profile results are expressed in terms of mixture fraction (ξ) space, where ξ represents the fuel stream mass fraction of the mixture, defined by Bilger [168] as $\xi = (Y_F - Y_{F,2})/(Y_{F,1} - Y_{F,2})$, where subscripts 1 and 2 are the streams of fuel and air respectively. The simulated flame cases were set to a fixed strain rate value of 100 s^{-1}, with fixed fuel inlet temperature and pressure of 298K and 1 bar, respectively. Strain rate was also varied to investigate the quenching point for some flame cases. For simplicity, a constant Lewis number (unity) has been used for all species

[169]. The boundary conditions of fuel identified in the left side of the domain whereas the right side was for the oxidiser. The oxidiser stream composition remained similar for all cases in which $Y_{O_2} = 0.21$ and $Y_{N_2} = 0.79$ (standard dry air).

A streamlined set of equations are used in the simulations, where the mixture fraction served as an independent variable [165]. Simulations were performed with a set of governing equations. The energy (2.1) and species (2.2) equations are as follows:

$$\frac{\partial T}{\partial t} = \frac{\chi_{st}}{2}\frac{\partial^2 T}{\partial \xi^2} - \sum_{i=1}^{N}\frac{h_i}{C_p}\frac{w_i}{\rho} \qquad 2.1$$

$$\frac{\partial Y_i}{\partial t} = \frac{\chi_{st}}{2}\frac{1}{Le_i}\frac{\partial^2 Y_i}{\partial \xi^2} + \frac{w_i}{\rho} \qquad 2.2$$

$i = 1, \ldots, I$. In equation 2.1, T is the temperature, h_i is the constant enthalpy of species i, C_p is the specific heat capacity at constant pressure, w_i is the production rate of species i, ρ is the density, the subscript st refers to the stoichiometric conditions. In equation 2.2, Y_i is the mass fraction, Le is the Lewis number. χ_{st} is the scalar dissipation rate that is estimated at stoichiometric conditions. χ is a significant quantity for the description of diffusion flames. Although this quantity is typically specified locally and instantaneously, a global definition can be more related for simplified geometries such as the counter flow geometry used for the 1D simulations in this thesis [165]. Therefore, an average value of the χ of the whole domain is calculated rather than calculating χ value at each specific point. In counter flow diffusion flame geometry, the χ_{st} is directly proportional to the diffusion coefficient D and the spatial derivative of the mixture fraction with respect to the coordinate normal to the flame (y), as follows:

$$\chi_{st} = 2D\left(\frac{\partial \xi}{\partial y}\right)^2_{st} \qquad 2.3$$

Where D can be calculated using Fick's law. Equations (2.1) and (2.2) assume that the scalar dissipation rate is a parameter that requires to be calculated. Nonetheless, the COSILAB software can replace the constant χ_{st} in the above-given equations (2.1 and 2.2) with the corresponding function of the mixture fraction (COSILAB can be calculated as a function of the mixture fraction). The strain rate (a) is related to the scalar dissipation rate (χ) using the following equation (2.4):

$$\chi = \frac{a}{\pi}\exp\left(-2[erf^{-1}(1-2\xi)]^2\right) \quad 2.4$$

The error function is denoted by (erf). Counter flow calculations implemented in COSILAB set the strain rate as an input rather than the scalar dissipation rate [165]. The numerical methods implemented in the computer code of COSILAB are a modified Newton method for steady problems and an extrapolation method for time-dependent problems (Euler method) [165]. Both Newton and Euler methods can be used for all problems in COSILAB [165]. The Newton method was found very robust when applied to unsteady problems. Newton's method usually converges fast if a good estimate for the initial profiles is provided. The weakness occurs when good estimates for the initial profiles do not exist. Therefore, in such situations, the Euler method was solved initially to obtain a converged solution to the problem. Then, the converged solution was input into Newton to get a good, converged solution initial guess for the same problem.

2.3 Experimental Methods

2.3.1 Burners Configuration

Two burners were used in this thesis. A standard co-flow burner [170] was used for the methane and ethylene-air laminar diffusion flames with DME blends. Whereas a bluff-body swirl spray burner with a solid-cone spray configuration was used for the turbulent flames measurements, including iso-pentanol/ n-heptane blends and ethanol/ n-heptane blends.

2.3.1.1 Laminar Diffusion Flame Burner

The experimental apparatus was comprised of a co-flow burner with a fuel blending and flow control system housed in an enclosed, interlocked work bench to allow the application of optical diagnostics. The co-flow burner used in this work had a similar structure to the Yale co-flow burner [170]. The burner had a 4 mm inner diameter (ID) fuel tube centred within a 74 mm ID honeycomb-filled air tube generating an axisymmetric laminar diffusion flame. The honeycomb mesh and glass beads assist in straightening the airflow to generate a constant and uniform co-flow area. A schematic of the co-flow burner and a photograph of the co-flow burner are shown in Figure 2-2.

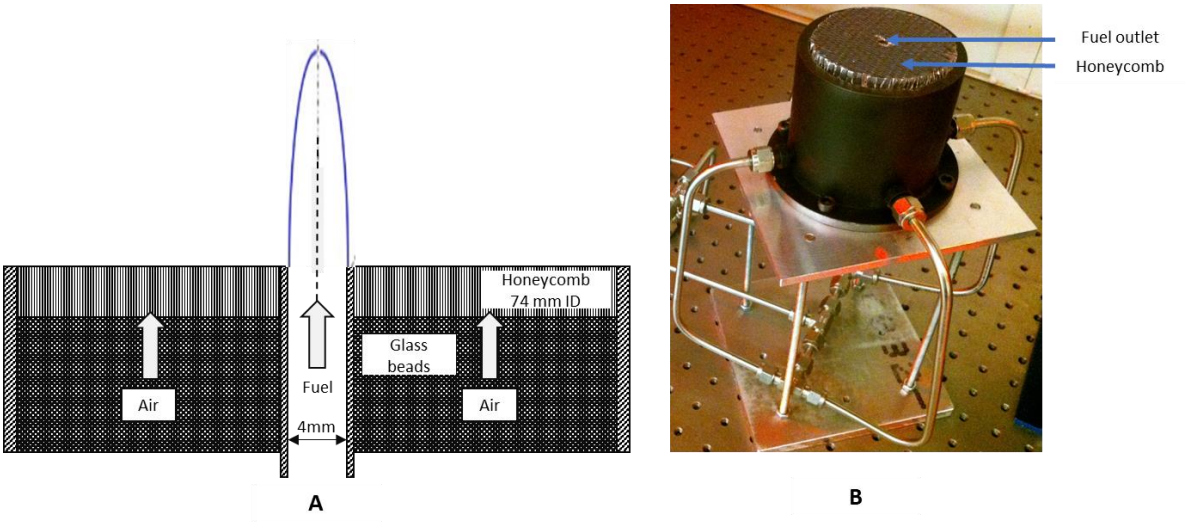

Figure 2-2 (A) schematics of the co-flow burner, and (B) a photograph of the co-flow burner.

2.3.1.2 Bluff-Body Swirl Spray Burner

A bluff-body swirl spray burner with a confined chamber was used for testing the turbulent flames of iso-pentanol/n-heptane blends and ethanol/n-heptane blends. Letty et al. [171], Cavaliere et al. [66] and Yuan et al. [140] have previously used similar burners to investigate the ignition and blow-off in non-premixed heptane spray flames. However, in this work, different fuels and different atomizer (a solid-cone atomizer was used for the first time in this work, in comparison to the previous work which used a hollow-cone atomizer) were used to perform testing under various flow conditions for the targeted fuels. The confined combustion chamber (100 mm Width (W) × 100 mm Length (L) × 150 mm Height (H)) is surrounded by 4 polished quartz plates (supplied from multi-lab Ltd), giving access for the camera and laser. Two of the quartz plates are with dimensions of 100 mm W x 150 mm L x 3 mm Thick, and the other two quartz plates are with dimensions of 106 mm W x 150 mm L x 3 mm. The quartz plates used in this study allowed the laser diagnostic to transmit within the UV-IR range (UV-IR transmittance of the quartz ≥ 92.3% at 320 nm) [172]. A schematic of the bluff-body swirl spray burner is presented in Figure 2-3. Inside the burner, an annular air stream travelled through a six-vane (60° vane angle) swirler prior to its entrance to the confined chamber. This 60° vane angled swirl has a swirl number (S_N) of 1.25 calculated by the equation given by Lefebvre and Ballal [173]:

$$S_N = \frac{2}{3}\frac{1-\left(\frac{D_{\text{sw inner}}}{D_{\text{sw outer}}}\right)^3}{1-\left(\frac{D_{\text{sw inner}}}{D_{\text{sw outer}}}\right)^2} tan\theta \qquad 2.5$$

Where θ is the vane angle of the swirl, $D_{\text{sw inner}}$ is the inner diameter of the swirl, and $D_{\text{sw outer}}$ is the outer diameter of the swirl. Two additional swirls having swirl numbers of 0.36 and 0.63 were only used to study the impact of S_N on the NO formation from iso-pentanol flame. A pressurized atomizer (Delavan) with 0.21 mm orifice diameter was used for all flame conditions, providing a solid cone spray pattern with a cone-angle of 60°. The atomizer was fitted through a bluff-body holder, and both the bottom plate of the burner and the nozzle's outlet were aligned to the same level. The inner diameter of the base of the burner is 40 mm, whereas the outer diameter of the bluff-body is 30 mm. The gap between the bluff-body and the base of the burner is where the annular air enters the confined chamber. Figure 2-3 shows a schematic of the bluff-body swirl spray burner.

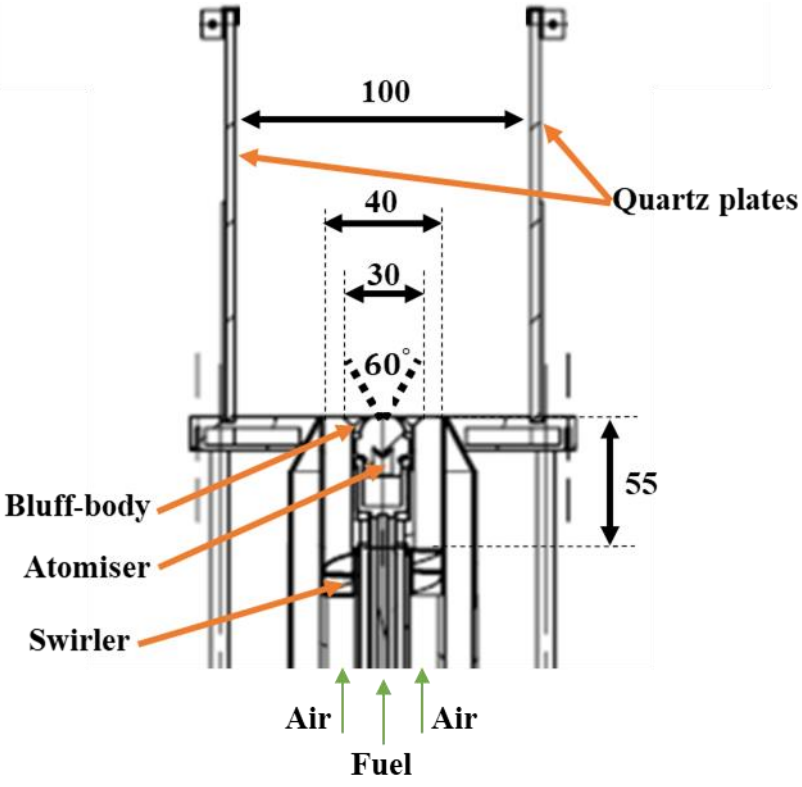

Figure 2-3 Schematic of the bluff-body swirl spray burner.

2.3.2 Flow-rate Measurement & Conditions

2.3.2.1 Laminar Diffusion Flames Conditions

A schematic of the experimental setup of the laminar diffusion flames experiment is shown in Figure 2-4. Separate calibrated mass flow controllers (MRC Alicat MFCs) were used to regulate the flow rates of air and fuels. The air was supplied to the burner from an air compressor and inline air filter. The air flow rate was kept constant at 72 ± 0.2 SLPM (corresponding to an annular air exit velocity of 0.35 m/s) for all tests. The fuels used in this experiment were supplied from individual, single-fuel cylinders and blended within the flow control system. DME was in a liquid state inside its cylinder, hence a Neslab RTE-110 circulator was used to heat DME to 25 ℃ to ensure it was in the gas phase before entering the burner/blender. A constant fuel stream volumetric flow rate of 356 ± 1 SCCM (corresponding to a fuel exit velocity of 0.47 m/s) was maintained throughout all DME/methane mixture cases, and 263 ± 1 SCCM (corresponding to a fuel exit velocity of 0.35 m/s) for all the DME/ethylene cases, to match the condition of the Yale's sooting flame [170]. The experimental conditions are summarised in Table 2-1, where the SCCM values were calculated based on atmospheric conditions (25 °C and 1 bar). In this work, the DME mixture ratio β (ratio of DME in the fuel mixture) is introduced in terms of the ratio of the DME volumetric flow rate to the total fuel volumetric flow rates, i.e., $\beta = Q_{DME}/\sum Q_{fuel}$. Whereas the fuel mixture ratio α (ratio of fuel in the mixture) is defined as the ratio of the total fuel volumetric flow rate to the total volumetric flow rate of the central jet including N_2, i.e., $\alpha = \sum Q_{fuel}/\sum Q_{jet}$. The flames studied in this work are all buoyancy controlled, where the Froude number (Fr) is ranging between 0.461 and 0.499 for the DME/CH_4/N_2 cases and 0.26 for DME/C_2H_4/N_2. The Froude numbers were calculated using the expression provided by Glassman and Yetter [84].

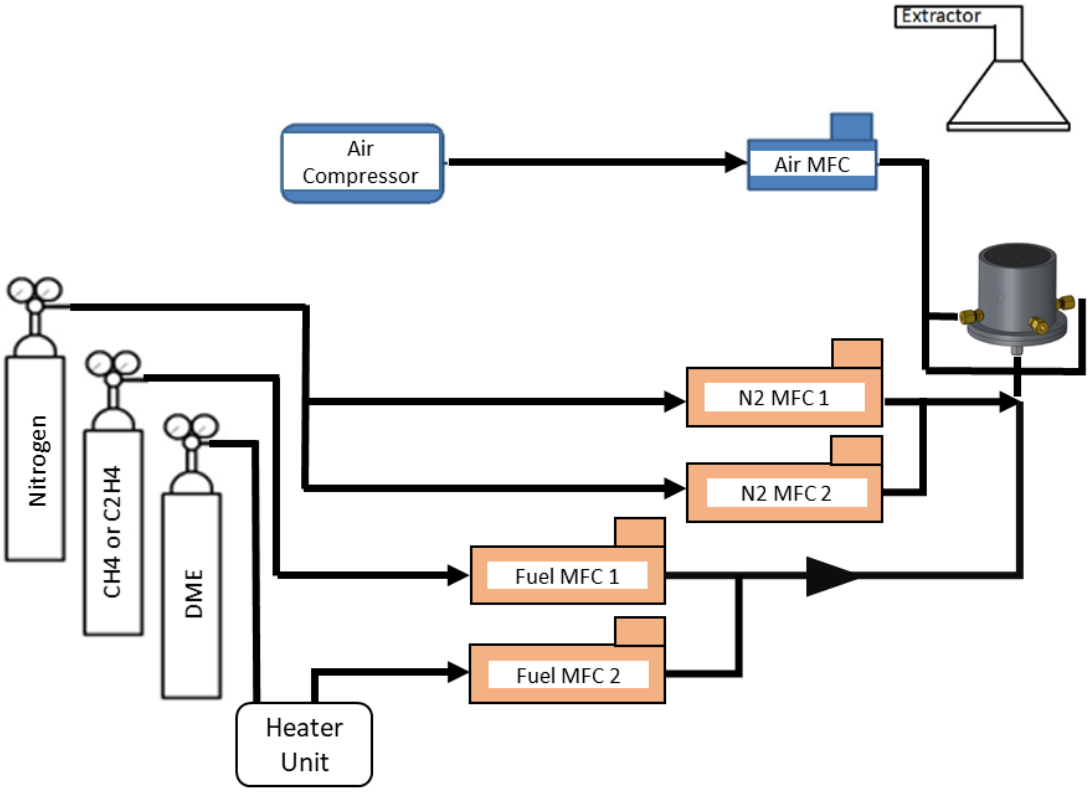

Figure 2-4 Schematic of the experimental setup of the laminar diffusion flames.

Table 2-1 Experimental conditions of the laminar diffusion flames investigated.

Jet component	Case	β	α	Q_{DME} (SCCM)	Q_{Fuel} (SCCM)	Q_{N_2} (SCCM)	Power Output (kW)
DME/CH_4	F1	0	1	0	356.6 CH_4	0	0.195
	F2	0.25	1	89	267.1 CH_4	0	0.229
	F3	0.50	1	177	178.2 CH_4	0	0.261
	F4	0.75	1	267	89.8 CH_4	0	0.296
	F5	1	1	358	0	0	0.331
DME/N_2	F6	1	0.75	267	0	88.8	0.246
	F7	1	0.50	177	0	176.1	0.164
	F8	1	0.25	89	0	246.7	0.082
CH_4/N_2	F9	0	0.75	0	267.1 CH_4	89.8	0.146
	F10	0	0.50	0	178.2 CH_4	177	0.098
	F11	0	0.25	0	89 CH_4	267.1	0.049
$DME/C_2H_4/N_2$	F12	0	0.60	0	158.3 C_2H_4	105.56	0.141
	F13	0.50	0.60	79	79.17 C_2H_4	105.56	0.143
$DME/CH_4/N_2$	F14	0.25	0.85	76	228.1 CH_4	52.4	0.195
	F15	0.50	0.75	132	132.5 CH_4	91.6	0.195
	F16	0.75	0.70	177	58.8 CH_4	121.2	0.195
	F17	1	0.60	211	0	145.5	0.195

2.3.2.2 Turbulent Swirl Spray Flames Conditions

A schematic of the experimental setup of the bluff-body swirl spray flames is shown in Figure 2-5. In Chapter 5, liquid fuels including pure iso-pentanol, n-heptane, ethanol, a 50:50 volume ratio mixture of iso-pentanol/ n-heptane, and a 50:50 volume ratio mixture of ethanol/n-heptane were tested in a bluff-body swirl spray burner to study their reaction zones and stability characteristics. In Chapter 6, pure iso-pentanol, pure n-heptane and a 50:50 volume ratio blend of n-heptane/ iso-pentanol were used as liquid fuels for the bluff-body swirl burner to study soot emissions.

Fuel mass flow rates were in the range of 0.50 - 0.54 g/s. The investigations were mostly carried out on those conditions with a fuel mass flow rate of 0.52 g/s for stable and near blow-off events. Moving from stable to near blow-off condition was achieved by increasing the air flow rate. A lower fuel mass flow rate of 0.506 g/s was applied for studying the soot signal in iso-pentanol, n-heptane and blended flames (these conditions are discussed in Chapter 6). The flow rate of the liquid fuels was controlled by adjusting the nitrogen valve and using a calibrated CODA Coriolis flow meter (accuracy: ± 0.2% of reading) as a monitor. Nitrogen was used to pressurise the liquid fuels inside the pressure vessel.

An air compressor (SXC 4, supplied from HPC compressors) supplied the air flow which was passed through a set of filters including particulate filter, oil and dust filter, and oil vapor and hydrocarbon filter. The air flow was controlled using a calibrated Alicat mass flow controller (MCR-1000 SLPM, accuracy of ± (0.8% of reading + 0.2% of full scale); repeatability of ± (0.2% of reading + 0.02% of full scale)). The flow conditions and fuel properties are shown in Table 2-2. The non-dimensional parameters shown in Table 2-2 were calculated using different equations, all shown in Table 2-3 [150]. S denotes to the stable conditions, and NB as conditions nearer to blow-off. Flame stabilisation in terms of the local extinction and lift-off was investigated in both stable condition pairs (S1, NB, with varying air flow rates) and the far from blow-off (S0) condition (a richer flame with lower fuel and air flow rates used to study soot emissions). Air volumetric flow rates were in the range of 350 - 950 SLPM, which corresponded to an air velocity amongst 10.6 and 28.4 m/s. An air volumetric flowrate of 600 SLPM was used for stable conditions (S1), and 350 SLPM was used for the S0 conditions. At standard temperatures and pressures of 25 °C and 1 psi, measurements were calculated and expressed.

2.3.2.2.1 Identification of near blow-off point

Moving from stable to near blow-off condition was achieved by only increasing the air flow rate without changing the fuel mass flow rate. Prior to that, the global blow-off point was identified for each condition (blow-off limits will be shown in Chapter 5) to help determine the near blow-off condition. This was done by gradually increasing the airflow rate in steps of around 5% every 1 minute until blow-off occurred. The air flow rate for the near blow-off condition was selected at between 9-15% lower than the air flow rate of the global blow-off (quenching) point. The air flow rate for the near blow-off condition was not selected based on a specific percentage difference from the air flow rate of the global blow-off. The air flow rate for the near blow-off condition was selected at that closest rate to the air flow rate of the global blow-off, in which the flame can sustain for at least 4 minutes.

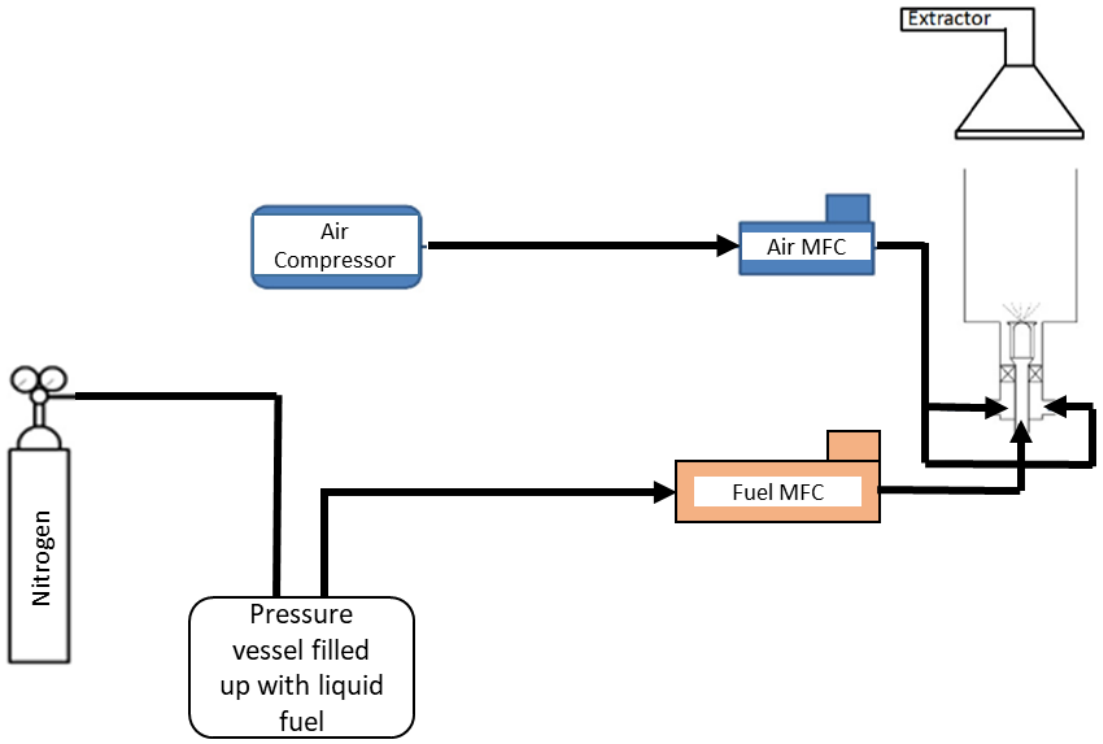

Figure 2-5 Schematic of the experimental setup of the bluff-body swirl spray flames.

Table 2-2 Fuel Properties.

Fuel	**n-heptane (H)**			**iso-pentanol (P)**		
Name	**HS0**	**HS1**	**HNB**	**PS0**	**PS1**	**PNB**
Air velocity, U_a (m/s)	10.6	18.2	28.8	10.6	18.2	28.8
Fuel velocity, U_f (m/s)	20.6	22.8		18.8	23.3	
Global equivalence ratio, ϕ	1.0	0.7	0.4	1.0	0.6	0.4
Fuel density, ρ_f (kg/m^3)	663			777		
Surface tension, σ (N/m)	2.21×10^{-2}			2.47×10^{-2} [32]		
Mixture viscosity, v_f (m^2/s)	6.10×10^{-7}			4.67×10^{-6}		
Power, P (kW)	22.8	25.8	24.8	19.1	22.7	24.9
Fuel Reynold number, Re_f	7.11×10^{3}	7.88×10^{3}		8.46×10^{3}	1.05×10^{3}	
Air Reynold number, Re_a	6.96×10^{3}	1.19×10^{4}	1.89×10^{4}	6.96×10^{3}	1.19×10^{4}	1.89×10^{4}
Fuel Weber number, We_f	2.68×10^{3}	3.30×10^{3}		2.34×10^{3}	3.61×10^{3}	
Air Weber number, We_a	1.14	2.48×10^{-1}	3.96×10^{-1}	6.80×10^{-1}	2.71×10^{-1}	2.98×10^{-1}

Fuel	**50:50 iso-pentanol/n-heptane (HP)**			**ethanol (E)**		**50:50 n-heptane/ethanol (HE)**	
Name	**HPS0**	**HPS1**	**HPNB**	**ES1**	**ENB**	**HES1**	**HENB**
U_a (m/s)	10.6	18.2	28.8	18.2	24.3	18.2	25.2
U_f (m/s)	18.6	20.9		21.4	21.4	20.9	
ϕ	1.0	0.6	0.4	0.43	0.32	0.59	0.39
ρ_f (kg/m^3)	722			759		699	
σ (N/m)	2.34×10^{-2}			2.01×10^{-2}		2.11×10^{-2}	
v_f (m^2/s)	1.68×10^{-6}			1.42×10^{-6}		9.45×10^{-7}	
P (kW)	20.2	22.5	22.9	16.9	16.6	22.3	20.8
Re_f	2.33×10^{3}	2.62×10^{3}		3.17×10^{3}		4.66×10^{3}	
Re_a	6.96×10^{3}	1.19×10^{4}	1.89×10^{4}	1.19×10^{4}	1.59×10^{4}	1.19×10^{4}	1.65×10^{4}
We_f	2.24×10^{3}	2.85×10^{3}		3.64×10^{3}		3.06×10^{3}	
We_a	6.82×10^{-1}	8.24×10^{-2}	6.54×10^{-1}	1.29×10^{-1}	1.00×10^{-1}	9.14×10^{-2}	2.08×10^{-1}

Table 2-3 Non-dimensional parameters equations.

Eq. (2.6)	$Re_f = \frac{U_f D_f}{v_f}$	D_f is the fuel nozzle diameter
Eq. (2.7)	$Re_a = \frac{U_a D_a}{v_a}$	D_a is the diameter of the air annular exit
Eq. (2.8)	$We_f = \frac{\rho_f U_f^2 D_f}{\sigma}$	ρ_f is the density of the fuel
Eq. (2.9)	$We_a = \frac{\rho_a (U_a - U_f)^2 D_f}{\sigma}$	ρ_a is the density of air

2.3.2.3 Turbulent Swirl Spray Flames with a Dilution Air Strategy

In Chapter 7, liquid fuel of pure n-heptane was tested in a bluff-body swirl spray burner with and without dilution air to study the impact of dilution air on flame stability, HRR, and reaction zone. Annular air and fuel flow rates were controlled in the same way as described in Section 2.3.2.2. The same air compressor that supplies the annular air was also used for the dilution air. A separate calibrated Alicat mass flow controller (MCRS-100 SLPM, accuracy of ± (0.8% of reading + 0.2% of full scale); repeatability of ± (0.2% of full scale)) was used to control the dilution air stream. Investigations were carried out on conditions with a fuel mass flow rate of 0.175 g/s and 0.194 g/s. Data were collected at the quenching point (global blow-off), near blow-off, and stable conditions. The global blow-off point for each of the two conditions (without air dilution) identified in the same way as described in Section 2.3.2.2.1. After that, dilution air was added with 5% of the annular air flow rate to study its impact on various characteristics. For example, if 790 SLPM is the annular air flow rate, the dilution air is 39.5 (5%). The impact of dilution air with different percentages including 2%, 5%, and 10% was also tested on one condition.

The flow conditions and fuel properties are shown in Table 2-4. For the first letter of the case name, Q denotes to the quenching (global blow-off) conditions, N as conditions nearer to blow-off, and S as stable conditions. For the second letter of the case name, N denotes to the cases with no air dilution, and D as conditions with air dilution. For the third letter of the case name, L denotes to the cases with low fuel flow rate of 0.175 g/s, whereas H denotes to the cases with higher fuel flow rate of 0.194 g/s.

Table 2-4 Turbulent Swirl Spray Flames with and without Dilution Air Strategy conditions.

Case Name	**Fuel flow rate (g/s)**	**Annular Air flow rate (SLPM)**	**Dilution Air flow rate (SLPM)**	$\boldsymbol{\phi}$	$\boldsymbol{P}$ **(kW)**	$\boldsymbol{Re_f}$	$\boldsymbol{Re_a}$	$\boldsymbol{We_f}$	$\boldsymbol{We_a}$
QN_L	0.175	790	0	0.167	8.4	2.62×10^3	1.57×10^4	3.66×10^2	3.01
QD_L		790	39.5 (5%)	0.162			1.65×10^4		3.47
NN_L		700	0	0.192			1.39×10^4		2.09
ND_L		700	35 (5%)	0.183			1.46×10^4		2.43
SN_L		600	0	0.223			1.19×10^4		1.26
SD_L		600	30 (5%)	0.213			1.25×10^4		1.49

QN_H	0.194	880	0	0.169	9.36	2.92×10^3	1.75×10^4	4.52×10^2	3.75
QD_H		880	44 (5%)	0.161			1.84×10^4		4.32
SN_H		790	0	0.188			1.57×10^4		2.71
SD1_H		790	15.8 (2%)	0.185			1.60×10^4		2.88
SD2_H		790	39.5 (5%)	0.179			1.65×10^4		3.14
SD3_H		790	79 (10%)	0.171			1.73×10^4		3.61

2.3.3 Diagnostic Methods

2.3.3.1 Chemiluminescence Measurements

For laminar diffusion flames, the HRR was measured and approximated using the technique of CH*, OH* and C_2* chemiluminescence imaging. The central wavelength of the narrow bandpass filters used for OH*, CH* and C_2* chemiluminescence measurements are 310 nm, 431.5 nm, and 516.5 nm, respectively, with a full width-half maximum (FWHM) of 10 nm. An intensified CCD camera (Andor iStar CCD 334) coupled with a UV lens was used as the detector. The resolution of the chemiluminescence measurements was 11.7 pixel/mm and between 100 to 200 images were taken to obtain an ensemble mean image. The inverse Abel transform (IAT) was used on the average chemiluminescence images to get 2D chemiluminescence results. The same intensifier gain setting was applied for all cases, however, different exposure duration (10 – 200 ms) were used due to the signal strength.

For turbulent swirl spray flames, OH* chemiluminescence imaging was detected in the wavelength range of 300-320 nm to mark the heat release region. An intensified CCD camera (M-lite from LaVision) was used for the detection system. The same intensifier gain and exposure duration settings, of 65 and 20000 ns respectively, were applied for all turbulent flames cases. The IAT was used on the average chemiluminescence images to get 2D chemiluminescence results. A simple schematic of the chemiluminescence setup for both of the flames type is shown in Figure 2-6.

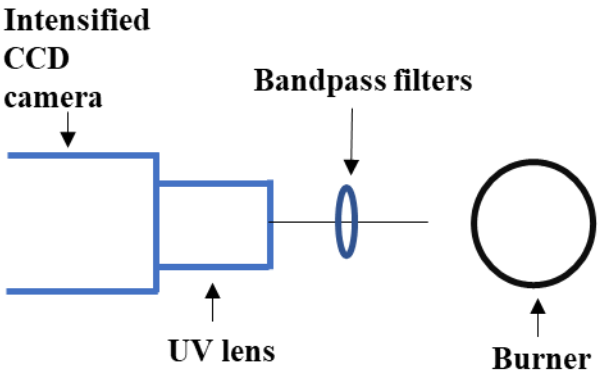

Figure 2-6 A simple schematic of the chemiluminescence setup.

2.3.3.2 Laser Induced Incandescence (LII) Measurements

The LII technique employs a pulsed laser to incandescent and heats the soot particles in a flame to a high temperature, which then enables the measurement of thermal emissions during the cooling phase [101]. The heated soot particles can reach a temperature between 2500 K to 4500 K [174], thus producing broad-spectrum incandescence radiation. The detection system then captures the light discharged by the incandescent soot particles after passing by a set of optics and filters, and this signal is used to calculate the soot temperature and SVF. The LII method is based on the principle that the LII signal observed is proportionate to the SVF in the flame [175]. Nevertheless, quantitative measurement of soot particles remains challenging because of the dependence on the proportionality relationship amongst the SVF and LII signal on various experimental parameters including the laser energy and intensity, optics etc. It is a 'largely selective' technique as it is only related to the non-volatile particles generated as a thermal emission, and the volatile particles are assumed to be completely evaporated during the time scale of the laser pulse [102]. This technique has gained great popularity as a technique of calculating SVF in flame because of its simple principle and non-intrusive nature (meaning does not disturb the properties of particles) [88].

The time-resolved laser induced incandescence method was introduced by Will et al. [176] and Roth et al. [177] to measure the soot particles size. This technique allows recording the soot emission over different acquisition delay times after the end of the laser heating period (cooling regime). Will et al. [176] evaluated the temporal decay by recording the incandescence signal at 2 different delay times within the cooling phase. After that, they computed the signal ratio that is directly proportional to the diameter of soot particle. Hadef et al. [178] obtained the decay curve during the cooling phase by shifting the camera gate at regular intervals. This

method showed its capability to estimate the size of soot particles in a typical sooting laminar diffusion flame.

Self-calibrated planar time-resolved two-colour laser induced incandescence (2C-LII) technique was implemented to measure the soot temperature, soot volume fraction and size of soot particles. This part of the thesis was applied on laminar diffusion flames and bluff-body swirl spray flames (only on the cases far away from blow-off, including n-heptane, iso-pentanol, and their blend). The schematic of the diagnostic setup is shown in Figure 2-7. The light source used was the Nd:YAG laser second harmonic (532 nm) passing through expansion optics, and forming a laser sheet to heat up the soot particles. For laminar diffusion flames, the detector system used was an intensified camera (Andor iStar ICCD 334T) coupled with Nikon UV lens (Sigma 105 mm F2.8 Lens). Whereas for turbulent swirl spray flames, an intensified CCD camera (M-lite from LaVision) was used for the detection system. Soot emissions were filtered through two narrow bandpass filters centred at 550 nm and 650 nm with a FWHM of 10 nm before being projected onto the ICCD camera as shown in Figure 2-7. Mirrors were used to split and project two images into one camera. The transmission coefficients of the detection system at the two wavelengths were measured via a series of calibration measurements with a standard spectral irradiance lamp. The lamp type used for the laminar diffusion flames was the Newport QTH light source and constant power supply unit. Whereas the lamp type used for turbulent swirl spray flames was the Ocean Optics HL-3 plus VIS-NIR. Soot volume fractions and soot temperatures were quantified from the ratio and transmission coefficients of the two filtered radiation images after processing with the Inverse Abel Transform (IAT).

The optical layout, shown in Figure 2-7, allows simultaneous acquisitions of the two images, and thus reduces measurements uncertainties. The achromatic lenses were used in the optical setup to ensure that the emitted light from soot particles does not diverge before passing through the two narrow bandpass filters, enhancing the performance of the filters. In addition, the use of these specific lenses helps in focusing different wavelengths into one focal point, which is essential because only one camera was used and hence reduces the uncertainties. The measurements uncertainties were reduced by achieving no time gap amongst the two images captured. The 2C -LII signals were captured after the end of the laser pulse thus avoiding Mie scattering, additionally with a narrow bandpass filter (550 ± 10 nm) to minimise interference from PAH-LIF.

In the 2C-LII measurement, soot temperature is affected by the laser energy and laser beam profiles, rather than directly reflecting the local gas temperature. The effects from laser fluences, detection delay and duration on the calculated soot temperature were investigated in detail and will be addressed in Chapter 6. The soot temperature is indeed useful information. It may have an indication on the difference in soot properties among different fuels. However, in this thesis, the focus was mainly on the comparison of relative soot concentrations between different fuels.

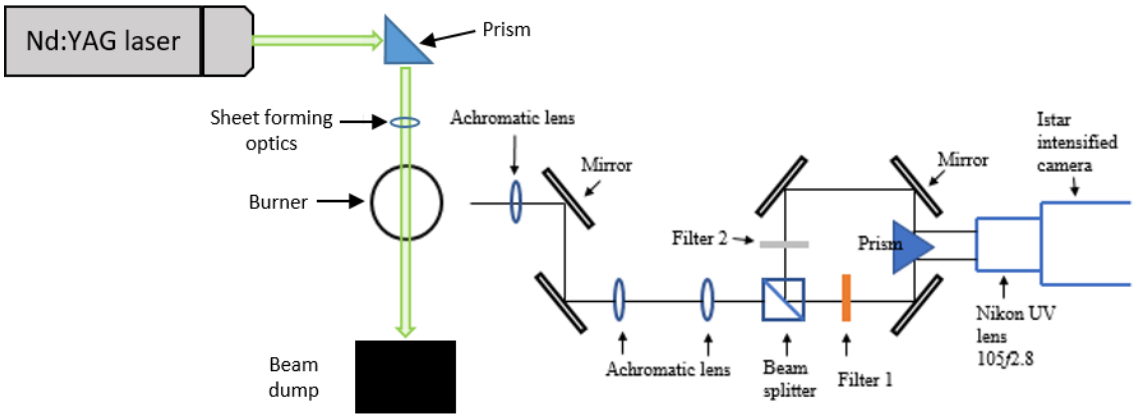

Figure 2-7 Schematic of the LII diagnostic setup and the detection system.

Prior to the start of the experiments, timings between laser Q-switch, camera intensifier gate, and laser emission output were identified, and a range of acquisition delays (0 – 2000 ns, relative to the time corresponding to the end of the laser pulse) and acquisition delay durations (TTLs, i.e. 10, 20, and 40 ns in laminar flames; 20, 40 and 100 ns in turbulence cases) were set in the LII signal detection from the ICCD camera. Pyroelectric energy sensor with ceramic coating was used to measure the laser energy output. Figure 2-8 shows a schematic of the soot temperature profile and laser pulse along with arrows clarifying the terms used in the following discussion in this thesis such as; delay time, camera acquisition duration time, and location of 0 ns delay time in relation to the laser pulse and peak temperature of the heated particle.

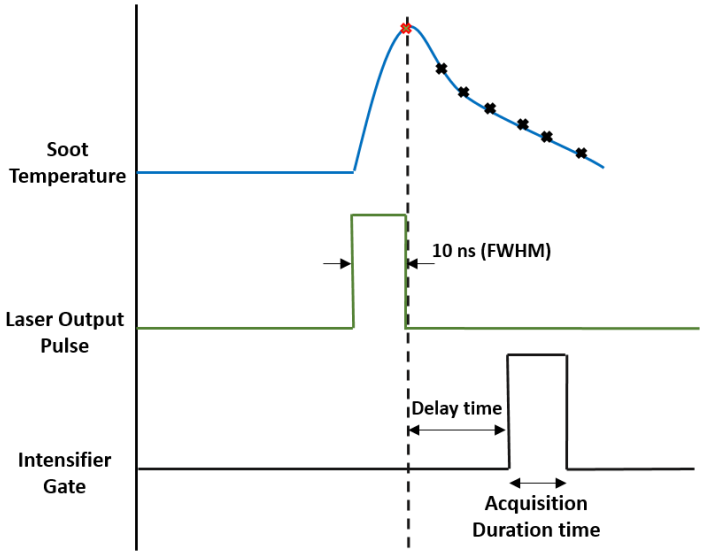

Figure 2-8 Schematic of timing signals with terms used in this paper. The dashed line corresponds to the 0 ns delay time that is at the end of the laser pulse.

2.3.3.2.1 The Planar Two-Colour Soot Pyrometry Measurement

The two-colour soot pyrometry technique was also implemented to measure the soot concentration and temperature (assuming thermal equilibrium where the soot temperature approximates the temperature of surrounding combustion gases) for laminar diffusion flames. This technique has a similar setup to the 2C-LII technique but without using a laser. The resolution of the two-colour measurements was 9.0 pixel/mm. The two-color soot pyrometry technique was used to estimate the soot temperature, which was calculated through an equation derived from Planck's law (further in details in Section 2.3.4.2). The soot temperature was then used to calculate the soot volume fraction.

2.3.3.3 Planer Laser Induced Fluorescence (PLIF) Measurements

Several researchers have utilized the Laser-Induced Fluorescence (LIF) technique to measure concentrations and distributions of some molecules in flames including OH, NO, and CH_2O. This method involves using a laser beam of a selected wavelength to excite chemical species in the flame. This results in moving the chemical species from the ground state to a high-energy state (known also as excited state). The excitation of the chemical species takes place when the wavelength of the laser is adjusted to excite a specific transition in which the difference of energy level between the ground state and the excitation state of the chemical species is matched by the energy of the laser light photons. More details about the method of selecting transitions is presented later in this chapter. The excited species can lose energy by collisional quenching, rotational and vibrational energy transfer processes, and also by the spontaneous

emission of a photon in transferring back to the ground state. The emission of a photon is termed fluorescence and can be at a variety of wavelengths, either longer wavelengths than the exiting laser photon, or at the same wavelength. The fluorescence is detected via an image intensifier and CCD camera, and provides a measure of the relative species concentration. A narrow bandpass filter centred on a specific wavelength (can be either for OH, NO, or CH_2O) needs to be used in order to distinguish the fluorescence emitted from the chemical species in the flame of characteristic wavelength. The narrow bandpass filter is usually attached to the camera without a gap between them to avoid any interference from the surrounding lights. The PLIF technique is based on the fact that the relationship is proportional between the concentration of the chemical species of interest in the flame and the fluorescence intensity produced from the same excited chemical species. The PLIF does not disturb the properties and flow in the flame, and this makes it preferable than using analysers and probes for measuring the concentration of molecules, which can disturb the dynamic flow in the flame. Nevertheless, obtaining quantitative measurements from PLIF is more challenging.

2.3.3.3.1 OH-PLIF

The OH-PLIF diagnostic technique was implemented to investigate the impact of fuels on the flame sheet structure including lift-off and local extinction. Yuan et al. [150] employed this diagnostic technique previously for swirl spray flame of different fuels featuring a hollow-cone spray. The OH-PLIF diagnostic system in this thesis comprised of a dye laser (Sirah Cobra-Stretch) pumped by a pulsed 10 Hz Nd:YAG laser (Quantel Q-smart 850), providing laser radiation around 283 nm wavelength for OH measurements, allowing the excitement of the Q1(6) (282.9274 nm) line in the $A^2\sum - X^2\prod(1,0)$ band. A further off resonance frequency signal denoted as B(Q) at 282.8 nm near the Q1(6) transition was recorded for all the cases to investigate the fuel fluorescence signal of each fuel type. This provides an indication on fuel atomization, and locations of remaining fuels, both liquid and vapour.

The LIFBASE [179] software utilized for simulating the LIF spectra and transition of the chemical species in this study including NO as well as OH. The laser wavelength inserted in the Sirah software may change from day to day. Therefore, the calibration process for the laser wavelength was done every time the laser solution and/or dye laser changed in order to determine its exact wavelength. Figure 2-9 shows the laser wavelength calibration for the OH species. The calibration process was done by scanning a broad range of laser wavelength passing through a laminar flame and recorded the fluorescence signal as a function of

wavelength. During the scan, several peaks in the fluorescence appear which correspond to different transitions of the targeted chemical species. The wavelengths at these peaks were noted and compared to the spectra that was simulated in LIFBASE. The offset value between the LIFBASE spectra and the wavelength peaks from the laser scanning was obtained. This offset was used to alter the wavelength reading of the laser in the Sirah software to correspond with the actual wavelength.

The OH intensity simulated in LIFBASE showed that moving the OH peak intensity Q1(6) by ±0.001 nm could drop the intensity by up to 21.5%. However, the intensity discrepancy of the OH fluorescence signal observed from the camera is marginal with a wavelength shift of ±0.001 nm (minimum step size of the scan). This observation was noticed during the broad-range scanning of laser wavelength passing through a laminar flame. LIFBASE simulated intensity of OH at Q1(6) wavelength (±0.001 nm) and temperature of 1500 K is shown in Table 2-5.

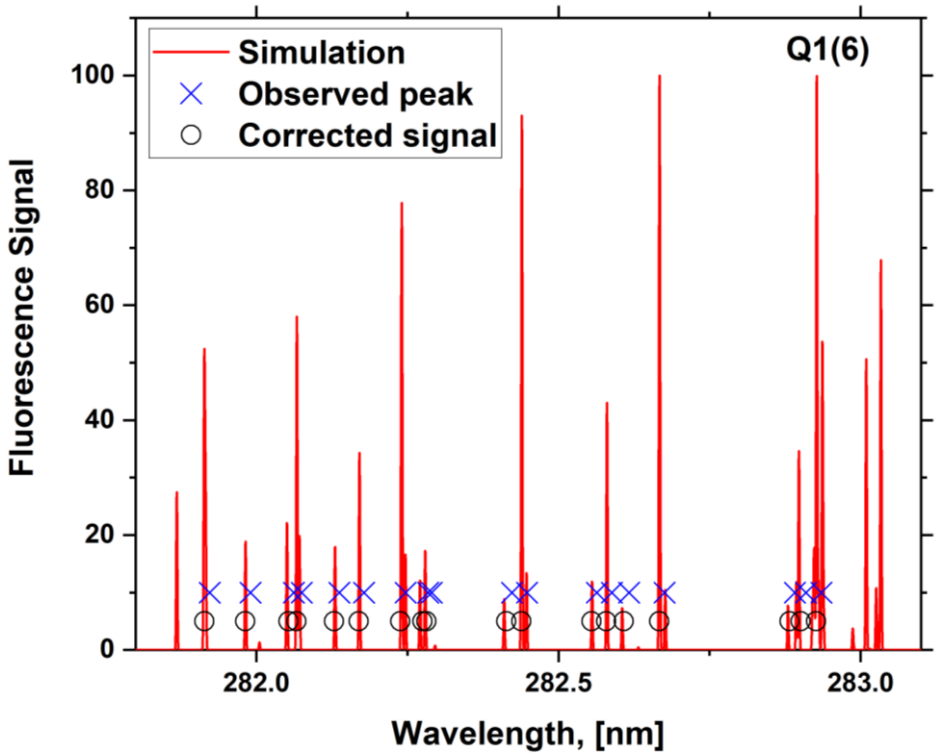

Figure 2-9 The laser wavelength calibration for the OH measurement.

Table 2-5 LIFBASE OH simulated intensities within ±0.001nm of Q1(6) and temperature of 1500 K.

	Wavelength (nm)	OH intensity	Discrepancy (%)
Peak of Q1(6)	282.9274	100.0	
Shift of -0.001 nm	282.9264	85.53	14.4
Shift of +0.001 nm	282.9284	78.49	21.5

A schematic of the OH-PLIF diagnostic setup is shown in Figure 2-10. The laser output from Nd:YAG was produced at a wavelength of 1064 nm and then travelled through a harmonic generator (2ω) (without 3ω) to produce a doubled frequency (532 nm) for the OH measurement. After that, the laser beam entered the Sirah Cobra-Stretch and passed into the dye cells, thus generating a dye laser output of about 566 nm. The dye laser used in this study had the ability to alter the laser beam's wavelength as required. It comprises two cells (resonator and amplifier) and the dye solution keeps circulating through them while operating the system. The dye solution used for the OH measurements consisted of about 0.09 g/L of Rhodamine 6G in methanol for the resonator. Whereas for the amplifier, the solution was further diluted by a factor of one-third, as per the manual recommendation. Therefore, the dye concentration in the amplifier was about 0.03 g/L of Rhodamine 6G in methanol. The output dye laser passed through the doubling crystal to generate UV light around 283 nm, and the Pellin-Broca prism system separated this from the undoubled light. The UV light was then coupled with a set of expansion optics to form a laser light sheet that was passed through the flame. An intensified CCD LaVision camera coupled with a narrow band wavelength filter at 308 nm comprised the fluorescence detection system.

The background signal of Q1(6), B(Q), provided the opportunity to measure the fuel-PLIF of all cases. The measurement of the fuels fluorescence signal is important as it gives indications of the fuel spray distribution and trajectory.

2.3.3.3.2 NO-PLIF

The NO-PLIF diagnostic technique was implemented to measure the relative NO concentrations in the turbulent swirl spray flames. The schematic of the NO-PLIF diagnostic setup is also shown in Figure 2-10. The pulsed 10 Hz Nd:YAG laser passed through a triple frequency (3ω) that was added to the harmonic generator set for the NO measurements, generating a laser beam with a wavelength of 355 nm. The optics setup inside the Sirah Cobra-Stretch is similar to the OH-PLIF, however the dye solution used for NO measurements consisted of about 0.23 g/L of Coumarin 2 in methanol for the resonator and 0.068 g/L for the amplifier. The dye laser in this case provided an output wavelength of about 452 nm, which after passing through the doubling crystal generated UV light around 226 nm allowing the excitement of the Q1(12) (226.0326 nm) line in the $A^2\sum - X^2\prod(0,0)$ band of NO. In this case the fluorescence was detected at the same wavelength as the laser, and a narrowband filter centred at 226 nm was attached to an intensified camera (CCD LaVision) and used to capture

images. To correct the images from background noise, extra off-resonance images were recorded for all conditions. The laser sheet height was 2 cm, and this is limited by the energy density and the signal-to-noise ratios of the imaging system of the current work. Hence the data presented correspond to the area of the upper region of the flame (up to 2 cm above the nozzle). The relative NO concentration was obtained by conducting a laser sheet intensity correction to the mean images of NO-PLIF. This has been achieved by collecting images for a cuvette filled with deionised water placed on the centre of the burner (above the centre of the nozzle) while the laser is firing. After that, the NO signal of the mean images were divided by the laser signal of the cuvette.

The NO intensity simulated in LIFBASE showed that $\pm$0.001 nm from the peak wavelength at Q1(12) transition could decrease the intensity by up to 23.3%. However, similar to OH-PLIF, the intensity discrepancy of the NO fluorescence signal observed from the camera is marginal with a wavelength shift of $\pm$0.001 nm. LIFBASE simulated intensity of NO at Q1(12) wavelength ($\pm$0.001 nm) and temperature of 1500 K is shown in Table 2-6.

Table 2-6 LIFBASE NO simulated intensities within ±0.001nm of Q1(12) and temperature of 1500 K.

	Wavelength (nm)	**NO intensity**	**Discrepancy (%)**
Peak of Q1(12)	226.0326	100	
Shift of -0.001 nm	226.0316	82.3434	17.6%
Shift of +0.001 nm	226.0336	76.6242	23.3%

2.3.3.3.3 CH_2O-PLIF

The combined measurement of CH_2O-PLIF and OH-PLIF is normally used as a substitute for HCO-PLIF to mark the HRR regions [140]. However, in this study, measuring CH_2O-PLIF and OH-PLIF simultaneously was impossible, so they were used separately as a reference of heat release regions. The CH_2O-PLIF diagnostic technique was implemented to study the impact of adding dilution air to the swirl spray flames on the low-temperature HRR regions in the flame. This technique involved a pulsed 10 Hz Nd:YAG laser passing through triple frequency (3ω) generating a laser beam with a wavelength of 355 nm. The laser beam passed through a set of expansion optics (75 and 1000 focusing lenses), forming a laser sheet with a height of 5 cm to excite the CH_2O radicals. The excitation of CH_2O-PLIF occurred at 355 nm, and the fluorescence was captured using an intensified CCD LaVision camera coupled with a narrow band wavelength filter at 433 nm. The CH_2O fluorescence decays very fast after the laser heating period. The lifetime of CH_2O fluorescence is about 5 ns at 1 bar and flame

temperature of 1000 K [180]. Therefore, a zero nanosecond delay was applied among the end of the laser pulse and the camera which is correlated to a 3610 ns delay time. The camera gate was ensured to open as close as to when the laser pulse hits the baseline. The duration of the camera gate used was 200 ns.

2.3.3.3.4 Pulsed Dye Laser System

A clear schematic of the optical layout inside the Sirah Cobra-Stretch is shown in Figure 2-10. The dye cells coloured with yellow are the main components inside the Sirah Cobra-Stretch. The 20 mm dye cell was used for both the resonator and the pre-amplifier, and the 40 mm dye cell was used for the main amplifier.

The performance of the output laser beam is highly dependent on the alignment of the optical, crystals and dye cells components in the Sirah Cobra-Stretch. A poor alignment of these components could produce a laser beam with less intensity and hence cause a reduction in the fluorescence signal of the detected chemical species in the flame. Therefore, the alignment of these components was checked daily before starting the experiment to make sure all the optics are in the correct positions. Another reason that could also have a major impact on the laser intensity is the degradation of the dye solvent. This is considered to be one of the big issues when carrying out NO-PLIF measurements, and hence the dye laser was replaced almost every week. However, the dye solvent for OH-PLIF lasts for a very long time. In addition, according to the manual of the laser system, some other factors could play a role in the efficiency of the laser beam such as the coolant water and the filter cartridges, which need to be replaced every six months to maintain the efficiency of laser performance and intensity.

The Sirah Frequency Conversion Unit (FCU), denoted as the internal SHG in Figure 2-10, is a unit that it is attached to the Sirah Cobra-Stretch to double the frequency of the dye laser beam. The FCU unit comprises of a doubling crystal which contributes in doubling the frequency. Inside the crystal, the phase matching is achieved by fine-tuning the angle of the crystal. This was achieved by creating a new FCU table every time the dye laser and/or dye solution were changed. This table records and modifies all the data that is required to properly calibrate an FCU. A range of wavelengths (in the case of OH the range is 562 nm to 566 nm, and for NO the range is 448 nm to 456 nm) was selected based on the targeted chemical species and monitored at 10 to 15 points that were pre-defined within the range. Recoding a new table dataset was then done by manually adjusting the position of the crystal. The laser output was monitored at each point using a power meter to reach the maximum reading. After picking up

the points that had the maximum readings, the AutoCalculate function in the Sirah software was used to fit the recorded points and displays a new fit result in the graph in the Table window. Improper phase matching of the crystal could reflect a reduction in the laser energy.

The camera's exposure was timed to coincide with the moment when the laser light pulse illuminated the targeted species in the flame; this timing is known as the “Reference Time”. The camera and the laser were both triggered in advance of the light's emission. The laser triggers both the Flash Lamp and the Q-switch. Flash lamp firing occurs before the light emission to pump the laser, and the Q-Switch occurs at the time of the light emission. A schematic (example) of the triggering pulses with the Reference Time is shown in Figure 2-11 [181]. The Flash Lamp and Q-Switch were both triggered externally through the Programmable Timing Unit (PTU X). The PTU generates trigger pulses for the laser and the camera through controlling DaVis. The DaVis software was used to specify the timings of the camera exposure, intensifier gate and delay, and record the flame images during the experiment. Before the start of any PLIF experiment, the intensifier gate and delay timings were adjusted using the Pyroelectric energy sensor connected to the PicoScope oscilloscope in order to use an accurate narrow camera gate. The narrower camera gate is preferable for avoiding any noise and scattering from entering the camera. Unlike the timings of LII shown in Figure 2-8, the intensifier gate should be overlapping with the laser output pulse for PLIF measurements or have a 0 ns delay between the end of laser pulse and the camera gate. Different timings and laser settings were used for each of the OH-PLIF, NO-PLIF, and CH_2O-PLIF as seen in Table 2-7. The intensifier gain setting used for each measurement was slightly high to strengthen the fluorescence signal and the high intensifier gain settings increased the noise level in the images. However, the noise was eliminated through the background images correction. Quartz cuvettes containing deionised water were used to test the quality of the laser sheets at every peak wavelength transition, and to correct the NO and CH_2O results by dividing their fluorescence signal to the laser signal of the cuvette.

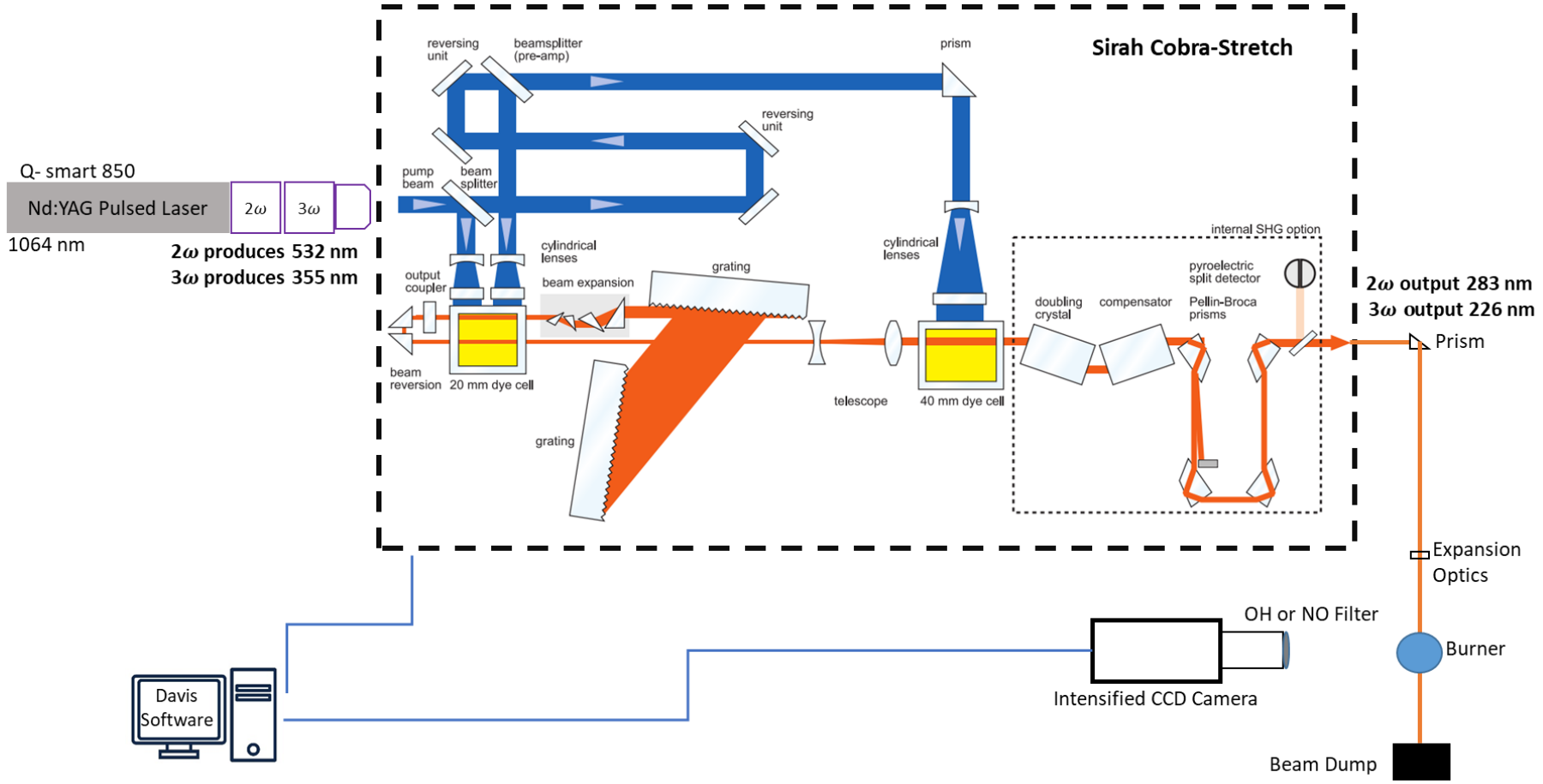

Figure 2-10 Schematic of the PLIF diagnostic setup. The optical layout of Sirah Cobra-stretch (squared with dash line) obtained from [182].

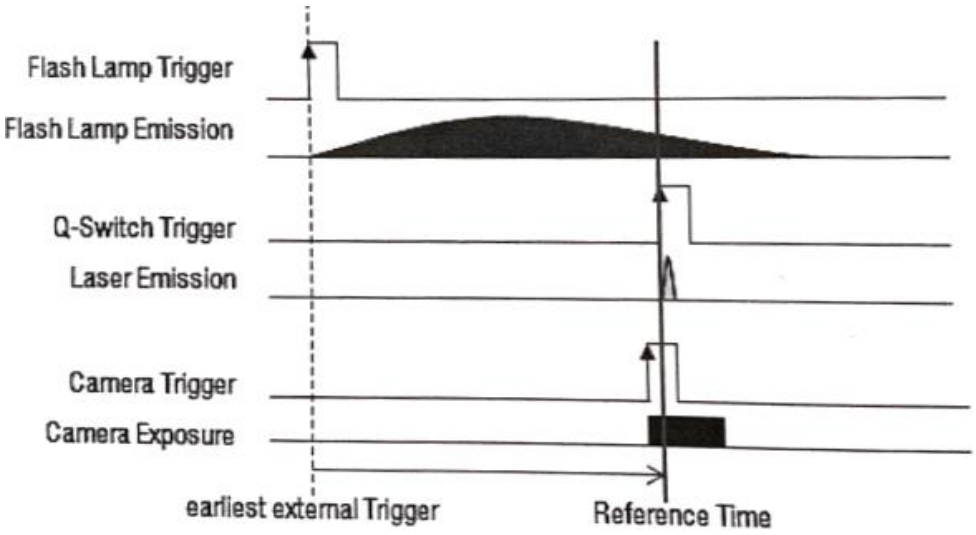

Figure 2-11 A schematic (example) of the triggering pulses with the Reference Time [181].

Table 2-7 Timings and laser settings used for the OH-PLIF, NO-PLIF, and CH_2O-PLIF measurements.

Parameter	OH-PLIF	NO-PLIF	CH_2O-PLIF
Wavelength (nm)	Q1(6) (282.9274) B(Q) (282.8000)	Q1(12) (226.0326) B(Q) (226.3100)	355
Laser power (%)	25	65	28
Intensifier delay (ns)	3635*	3575*	3610*
Intensifier gate (ns)	20	40	200
Intensifier gain (%)	70	80	60
Camera exposure (μs)	20000	20000	20000

* These values correspond to 0 ns relatively to off zero laser beam.

2.3.4 Data Processing & Analysis

2.3.4.1 Inverse Abel Transform (IAT)

In this thesis, the local distribution of heat release in flames was studied using the chemiluminescence imaging method in both laminar diffusion flames and swirl spray flames. As mentioned earlier in section 2.3.3.1, narrow bandpass filters of specific radicals were used as optical filters to enable the passing of the light wavelength produced by those radicals to the camera. Nonetheless, the resulting image by the detection system contains the entire volume's concentration. This is because every pixel records the total light from the total volume passing

by its line-of-sight. Therefore, a mathematical technique known as Inverse Abel Transform (IAT) was employed to reconstruct line-of-sight chemiluminescence measurements and to get 2D chemiluminescence results, assuming that the chemiluminescence signals were axisymmetric. For laminar diffusion flames, IAT can be applied for instantaneous and mean images, whereas for turbulent swirl spray flames IAT can only be applied on the mean images. This is because of the high turbulence in the flame which makes it difficult to use the assumption of axisymmetry for the instantaneous images. However, in some cases, the mean projected image of the turbulent swirl spray flame is also not axisymmetric. In such situation, only one half of the average projected image was selected for the IAT to reconstruct an axisymmetric image. There are multiple methods for applying the IAT including BASEX, onion-peeling, and FLiPPID. In this thesis, the onion-peeling technique was selected to apply the IAT because it is the most commonly employed technique and the easiest among all others [183]. The relationship between the measured chemiluminescence signal, $S(x)$, and the local chemiluminescence emission, $E(r)$, for a specific radial plane by the IAT, is as follows [183], [184]:

$$S(x) = 2\int_0^\infty E(r)dy = 2\int_x^\infty E(r)\frac{r}{\sqrt{r^2 - x^2}}dr \qquad 2.10$$

Both variables x and y are Cartesian coordinates, whereas r is the radius of the local emission. The local chemiluminescence emission, $E(r)$, can be obtained from the 1-D projected chemiluminescence emission signal (S). The distinct IAT is provided by [183], [184]:

$$E(r_j) = -\frac{1}{\pi}\sum_{k=j}^{\infty}\int_{0\ if\ k=j;\ -\frac{\Delta x}{2}\ if\ k>j}^{\frac{\Delta x}{2}} \frac{S'(r_k + \delta)}{\sqrt{(r_k + \delta)^2 - r_j^2}}d\delta \qquad 2.11$$

The lower limit depends on whether the pixel indices (k and j) in the radial direction are equal or not. The grid size in equation 2.11 is represented by Δx. S' is solved by the use of difference approximations. More details about the IAT equations can be found in Dasch [183].

IAT was also used to reconstruct the images that represent soot emissions in laminar diffusion flames. Regarding two-colour soot pyrometry results, the error comes mainly from the line-of-the-sight nature of the technique, which creates artificial errors using the inverse Abel transform to obtain the 2D information. The image processing aimed to correct the line-of-sight nature of the two-colour pyrometry measurements, however, suffers the drawback of

an artifact in the centreline due to the IAT algorithm. Nevertheless, the measurements could provide an indication of the soot occurrence and provide relative information on the soot concentration and temperatures among the cases of interest.

2.3.4.2 Soot Primary Particle Diameter and Soot Volume Fraction

The mass and heat transfer process of the flame's soot particles heated by the laser was described broadly in previous related studies, and found that the heat conduction (conductive cooling) is the dominant effect for the LII signal decays [98], [185]. Therefore, the formula for the energy balance can be defined as,

$$\frac{dU_{\text{internal}}}{dt} = -\dot{Q}_{\text{conduction}} \tag{2.12}$$

The shielding effect among the surrounding ambient gas and soot particle aggregates during the heat conduction process [101] is not taken into account in this thesis. This is due to the unavailability of transmission electron microscope (TEM) images which is needed to analyse the size distribution of the aggregated soot particles [186]. Instead, the effective primary particle diameter $d_{\text{p,eff}}$, defined as the diameter of an equivalence conduction effect, which is a function of the number of particles per aggregate and the primary particle diameter [187], is obtained in the time-resolved LII measurement. The effective primary particle diameter is estimated based on the heat conduction model of [188] and the temperature decay rate τ_T, as follows:

$$d_{\text{p,eff}} = \frac{12K_a\alpha_T\tau_T}{GL_{\text{MFP}}C_s\rho_s} \tag{2.13}$$

Where C_s and ρ_s are the soot's specific heat and density, K_a is the thermal conductivity of the surrounding gases, and α_T is the coefficient of thermal accommodation. According to previous related studies [98], [189], the value of ρ_s is approximated to be in the range between 1.85 and 2.26 (g/cm^3), whereas the value of C_s is temperature dependent. The factor of heat transfer G is given by,

$$G = \frac{8f}{\alpha_T(\gamma+1)} \tag{2.14}$$

Where γ is the gas's specific heat ratio. The Eucken correction of the thermal conductivity f is given by $\frac{9\gamma-5}{4}$. L_{MFP} is the mean free path length of this was described by [98] as,

$$L_{\mathrm{MFP}} = \frac{k_p T_o}{\sqrt{2}\sigma_m p_o} \qquad 2.15$$

Where T_o is the temperature of the ambient gases, k_p is the Boltzmann constant (1.381×10^{-23} J/K), σ_m is the average molecular cross section for air (about 3.0×10^{-15} cm^2), and p_o is the pressure of ambient gas (1 bar).

The internal energy term $\left(\frac{dU_{\mathrm{internal}}}{dt}\right)$ is a function of the laser-heated temperature T and time t. By assuming that the soot particles are mono-dispersed, an exponential expression behaviour is obtained from the steadily decayed temperature difference $(T - T_o)$. Therefore, by solving the energy balance equation when heat conduction is dominated, the temperature can be written as

$$(T - T_o) = \left(T_{\mathrm{peak}} - T_o\right) exp\ \left(-\frac{t}{\tau_T}\right) \qquad 2.16$$

Where T_{peak} is the peak temperature of the soot particle in the cooling regime. The temperature decay rate is calculated using the slop equation of $\ln(\frac{T-T_o}{(T_{\mathrm{peak}}-T_o)})$ against the delay time t plot over equal time intervals during the heat conduction process. The other parameters including C_{s}, ρ_{s}, α_T, K_a and L_{MFP} are estimated using the Liu model [98]. For easy comparison with the existing literature, the k_a and L_{MFP} values correspond to the surrounding ambient gas temperature of 1800 K.

The soot temperatures (T_{s}) are determined by the two-colour pyrometry method, and calculated using the following equation derived based on Planck's law

$$T_{\mathrm{s}} = \frac{hc}{k_p}\left(\frac{1}{\lambda_1} - \frac{1}{\lambda_2}\right)/\left(\ln\frac{S_{\lambda 2,soot}}{S_{\lambda 1,soot}} + \ln\frac{R_{\lambda 1}}{R_{\lambda 2}} + 5\ln\frac{\lambda_2}{\lambda_1}\right) \qquad 2.17$$

Where h and c are the Planck constant and the speed of light, respectively, $\lambda_{1,2}$ are the measuring wavelengths of 550 nm and 650 nm, $S_{\lambda,soot}$ is the soot signal detected by the camera, and R is the instrument responsivity at the two wavelengths. The soot temperature is used to obtain the soot volume fractions from the absolute LII-signal intensities regardless of the laser fluences applied. Low laser fluences may be preferred to avoid the reduction in particle volume at high fluence. Assuming a mono-disperse particle size distribution, the soot volume fraction is given by [186]

$$f_v = \frac{V\lambda^6(e^{\frac{hc}{\lambda k_p T_s}} - 1)}{\eta w_b 12\pi hc^2 E(m)} \quad 2.18$$

In which V is the detection volume, λ is the detection wavelength, w_b is the equivalent width of the laser sheet, η is the detection system calibration constant, and $E(m)$ is the soot absorption function.

The processing of the soot emission images was conducted using MATLAB. A simple flow chart presenting the stages in the processing of the soot data is shown in Figure 2-12. The two images reflected into the camera (one from the 550 nm filter and other from the 650 nm filter) were firstly aligned and rotated to provide similar image. The background noise was subsequently reduced by background subtraction and the use of 2-D median filtering. The background image is a mean of 100 instantaneous images captured without using a laser in order to account for the intrinsic luminance of the flame. After that, the IAT was applied on the two images separately. Thereafter, the ratio of the two filtered radiation images was calculated. Next, the soot temperature and SVF were then calculated using equations shown above.

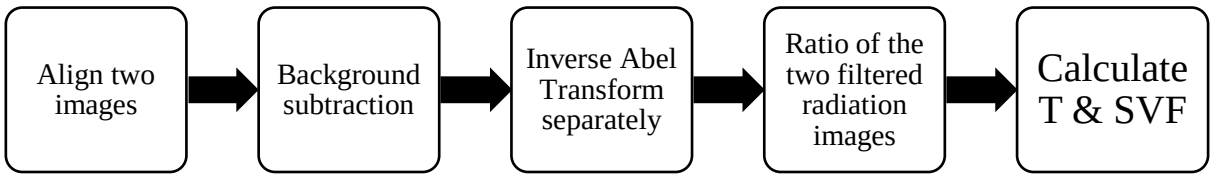

Figure 2-12 Flowchart presenting the stages in processing of the soot data.

2.3.4.3 PLIF Images

The background noise in all the images have been reduced by background subtraction and the use of 2-D median filtering. The off-resonance frequency signal images were used for the background noise correction as it contains signals from the fuel droplets. The median filtering is generally used in image processing (non-linear operation) to decrease the noise. This filtering method operates by going through all the pixels of the whole image and substituting every pixel value with the median value of adjacent pixels. Further details about the median filtering can be found in the Help Centre of MATLAB.

After finishing aligning the laser, the camera was focused using a target board aligned above the centre of the nozzle. This target board contained a pattern of intersecting squares (equal size) with numbers inside them to assist in the scaling and aligning the images. Before the starting of the recording data, an image of this target board was recorded without the use of any filter. The camera settings of the gate and gain used for collecting the target board image were 900000 ns and 45, respectively. For each case, 200 images were taken to obtain an ensemble mean image and the images were processed via MATLAB. The target board image was then used to rotate and align the PLIF images. After that, background subtraction was carried out for the PLIF images. Then, the noise in the images was further reduced by the use of 2-D median filtering. A threshold value was applied on all images, aiming to remove unnecessary pixels. The threshold value was selected based on the percentage of the signal level. Therefore, the threshold value is related to the background noise and signal (PLIF) levels. All the intensities were plotted and cut-off at the threshold value. Different threshold values were applied, and a value of 100 pixels was ultimately chosen as it could successfully exclude the majority of the noise without removing too much of the signal. Figure 2-13 shows a flowchart of the steps followed to process the PLIF images.

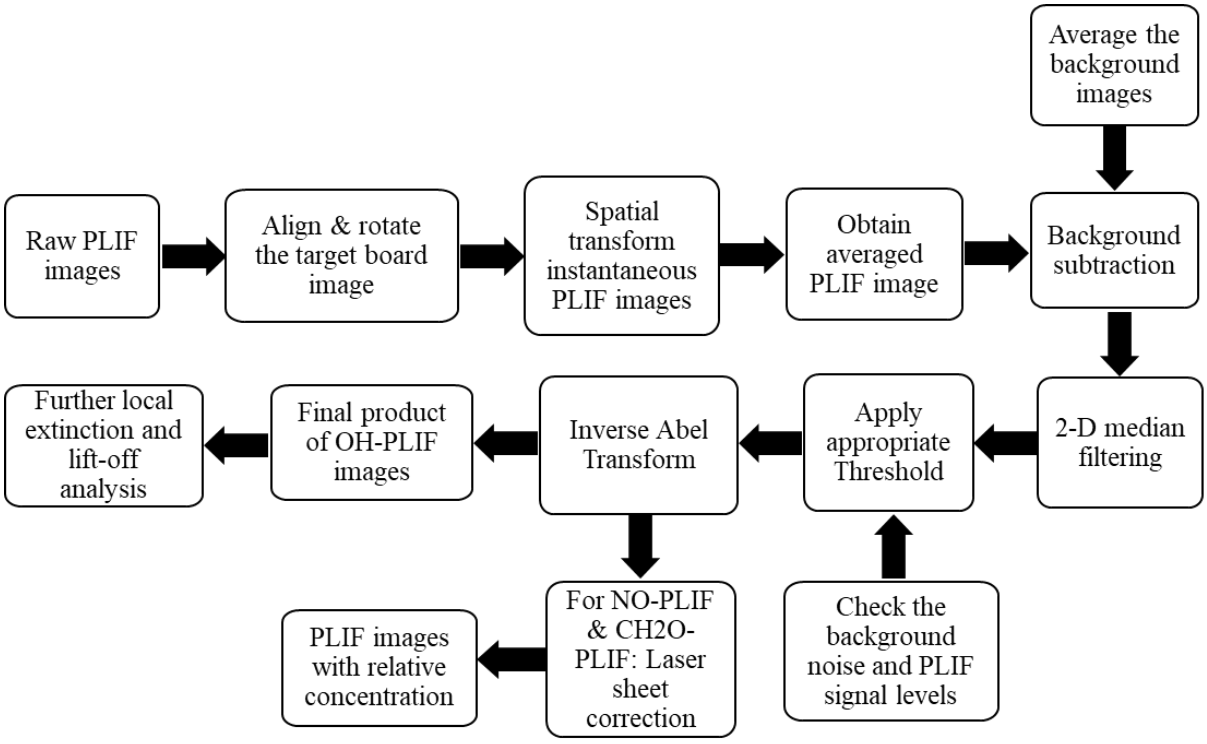

Figure 2-13 Flowchart presenting the stages in the processing of the PLIF images.

2.3.4.4 Local Extinction

Instantaneous images of OH-PLIF were used to measure the probability density function (PDF) of local extinction in flames. The PDF was calculated as the number of local extinctions in the flames. The OH-PLIF images used for analysing local extinction already passed through the processing steps shown in Figure 2-13. The local extinction was then calculated via Matlab by manually selecting the locations where the flame is cut off, for all the instantaneous images. The local extinction in both the inner and outer recirculation zones was taken into account. The number of local extinction events in each of the two zones was recorded in every instantaneous image. This was done by using the "ginput" function in MATLAB which enables one to make as many point selections as required. MATLAB then records the number of points selected in both recirculation zones. The results in this thesis show the PDF of the number of local extinction from 1 to 4 only. Figure 2-14 displays an example of the local extinction in instantaneous OH-PLIF images.

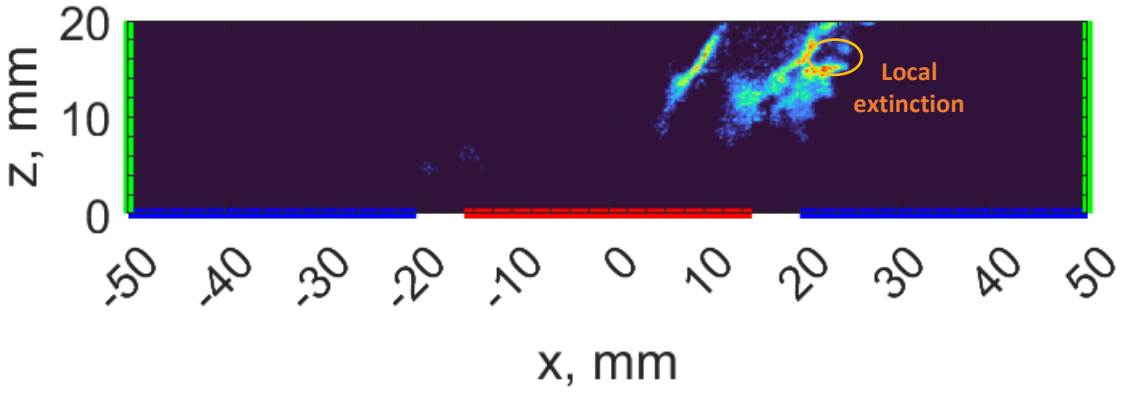

Figure 2-14 Example of the local extinction in instantaneous OH-PLIF images.

2.3.4.5 Lift-off Height

The lift-off height was analysed and measured using OH-PLIF instantaneous images. The lift-off height was calculated as the distance between the bluff-body and the nearest point of the flame sheet in the outer recirculation region to the bluff-body surface, and then the PDF of lift-off heights was plotted. The lift-off height calculation was processed in MATLAB (using the "ginput" function) by manually picking up the end point of the flame sheet on the left and right sides (outer recirculation zone) for each image. Flame stabilisation in terms of the lift-off height was investigated in both stable condition pairs (S1, NB, with varying air flow rates), far

from blow-off (S0) condition, and in the dilution air cases. Figure 2-15 displays an example of lift-off height in instantaneous OH-PLIF images.

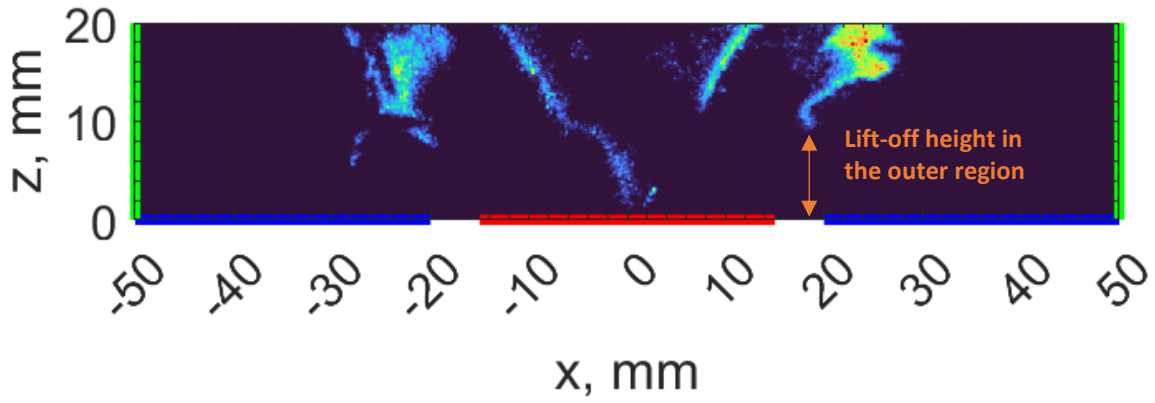

Figure 2-15 Example of the lift-off height in the instantaneous OH-PLIF images.

2.3.4.6 Chemiluminescence Images

The chemiluminescence images were captured at 10 Hz and 200 to 500 frames were collected for each flame condition. A target board image was used to rotate and align the chemiluminescence images, in a similar method to PLIF images alignment. The instantaneous images were then averaged. A background image was collected without having a flame on, but with the use of a chemiluminescence filter. In addition, background images were used to correct the background noise and 2-D median filtering was used to further reduce the noise. IAT was then applied on the chemiluminescence images, as described in Section 2.3.4.1.

2.4 Computational Fluid Dynamics (Soot Modelling)

Part of this thesis has been concentrated on the emissions and combustion characteristics of DME/ C_2H_4/ N_2 co-flow flame mixtures using the Computational Fluid Dynamics (CFD) approach. Ansys Fluent 21.1 was used to measure the flame temperature profile and species mole fraction under different conditions. Similar boundary conditions to those used in the experimental study were applied in this computational study to develop a new validated CFD model tailored to the DME which is currently missing and unknown. Moreover, this thesis investigates the impact of DME fuel on the soot model, and checks if the soot model can be used for DME (oxygenated fuel) flames.

A steady-state assumption can be implemented in this problem because no time dependency is involved. This laminar co-flow diffusion flame numerical problem can be solved using the governing equations in 2D cylindrical axisymmetric (r-x) coordinates. Hence, the conservation equations of mass (2.19), axial and radial momentums (2.20 and 2.21) in cylindrical coordinates can be written as follows [190]:

$$\frac{\partial(\rho v_x)}{\partial x} + \frac{1}{r}\frac{\partial(r\rho v_r)}{\partial r} = 0 \tag{2.19}$$

Axial Momentum Conservation:

$$\frac{\partial}{\partial x}(\rho v_x^2) + \frac{1}{r}\frac{\partial}{\partial r}(r\rho v_r v_x) = -\frac{\partial p}{\partial x} + \frac{1}{r}\frac{\partial}{\partial r}\left[r\mu_d\left(\frac{\partial v_x}{\partial r} + \frac{\partial v_r}{\partial x}\right)\right] + 2\frac{\partial}{\partial x}\left(\mu_d\frac{\partial v_x}{\partial x}\right) - \frac{2}{3}\frac{\partial}{\partial x}\left[\mu_d\left(\frac{\partial v_x}{\partial x} + \frac{\partial v_r}{\partial r} + \frac{v_r}{r}\right)\right] + F_x \tag{2.20}$$

Radial Momentum Conservation:

$$\frac{\partial}{\partial x}(\rho v_r v_x) + \frac{1}{r}\frac{\partial}{\partial r}(r\rho v_r^2) = -\frac{\partial p}{\partial r} + \frac{2}{r}\frac{\partial}{\partial r}\left(r\mu_d\frac{\partial v_r}{\partial r}\right) - 2\mu_d\frac{v_r}{r^2} + \frac{\partial}{\partial x}\left[\mu_d\left(\frac{\partial v_x}{\partial r} + \frac{\partial v_r}{\partial x}\right)\right] - \frac{2}{3}\frac{1}{r}\frac{\partial}{\partial r}\left[r\mu_d\left(\frac{\partial v_r}{\partial r} + \frac{v_r}{r} + \frac{\partial v_x}{\partial x}\right)\right] \tag{2.21}$$

Where v_x is axial velocity component, v_r is the radial velocity component, x is the axial coordinate, r is the radial coordinate, p is the pressure, F_x is the gravitational force in x direction, ρ is the density of the fluid, and μ_d is the dynamic viscosity of the fluid. For the species, the transport model was used to model the transport of the chemical species and mixing. The general form of the chemical species transport conservation equation is as follow:

$$\nabla.(\rho\vec{v}Y_i) = -\nabla.\vec{J_i} + R_i + S_i \tag{2.22}$$

Where $\vec{v}$ is the velocity, Y_i is the mass fraction of species i, R_i is the net rate production of species i, S_i is the rate of creation of species i, and $\vec{J_i}$ is the diffusion flux of species i. The energy equation is as follows [190]:

$$\nabla.[\vec{v}(\rho E_{\text{tot}} + p)] = \nabla.\left[k_{\text{eff}}\nabla\text{T} - \sum_{i=1}^{n} h_i J_i\right] + S_h \tag{2.23}$$

Where E_{tot} is the total energy, k_{eff} is the thermal conductivity, T is the temperature, h_i is the enthalpy for the i species, n is the number of species, and S_h is the volumetric heat source.

The governing equations mentioned above were solved using the finite rate method in Ansys Fluent 21.1. This package was used due to its capacity to combine fluid dynamics and chemical kinetics. In addition, it provides the ability to import kinetic chemical mechanisms and process chemical kinetic equations. The pressure-based solver was selected because it provides multiple physical features including soot model. In addition, to include both the terms of diffusion and convection at the inlets of the net transport of species. The absolute velocity formulation was used because it is preferred for not rotating flow in the domain. The viscous model was selected to be laminar because of the nature of the flame. Simulations were implemented with the Mech_56.54 mechanism and this comprises of 113 species and 710 reactions. The solution of the mass conservation is utilised to observe at every iteration the pressure field. This was done by selecting the Coupled scheme of pressure-velocity coupling. Second Order Upwind for the spatial discretization of the momentum, energy and all species is used because it provides results that are more accurate.

The geometry of the system used here had a similar concept to the Yale co-flow burner [170]. The simulation was implemented in a 2D axisymmetric space and a schematic of the co-flow diffusion flame geometry along with the setup of the walls is shown in Figure 2-16. The centreline of the geometry is a symmetry axis and hence only half of the geometry was built. The port where fuel is inserted (next to the axes of symmetry) was set as a fuel inlet with a velocity of 0.35 m/s (Normal to the Boundary) and ambient temperature. The remaining space next to the fuel inlet was set as an air co-flow inlet with a similar velocity and temperature to the fuel inlet. The wall was set to be stationary with no slip shear condition and flux. The exit of the geometry was set as a pressure outlet condition.

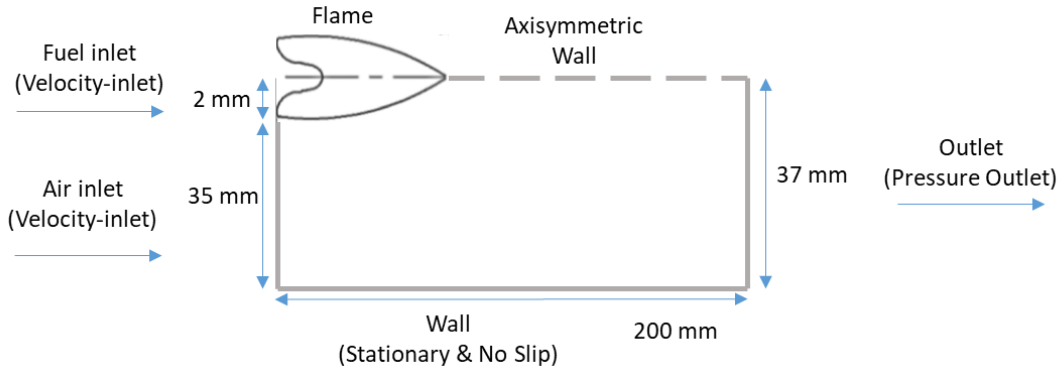

Figure 2-16 Schematic of the co-flow diffusion flame geometry along with the boundary conditions setup of walls.

Flame ignition for Steady-State Combustion Simulations in Ansys Fluent doesn't occur spontaneously when running the calculations. This is because the initial mixture temperature is not higher than the activation energy needed to start the ignition. Therefore, a non-reacting model (cold-flow) was initially ran until the convergence criteria was met in order to achieve an ignitable fuel/air mixture zone. After that, the volumetric reaction was turned on and an initial spark was introduced through patching a region (close to the inlets side) with high temperature to start the ignition.

The Moss-Brookes model which was created and validated for CH_4 flames was used for soot modelling in this study. The Moss-Brookes model solves transport equations including the normalised radical nuclei concentration (b^*_{nuc}) and soot mass fraction (Y_s) transport equations [190], as follows:

$$\frac{\partial}{\partial t}(\rho_s Y_{\mathrm{s}}) + \nabla.(\rho_s \vec{v} Y_{\mathrm{s}}) = \nabla.\left(\frac{\mu_t}{\sigma_{\mathrm{soot}}}\nabla Y_{\mathrm{s}}\right) + \frac{dM}{dt} \qquad 2.24$$

$$\frac{\partial}{\partial t}(\rho_s b^*_{\mathrm{nuc}}) + \nabla.(\rho_s \vec{v} b^*_{\mathrm{nuc}}) = \nabla.\left(\frac{\mu_t}{\sigma_{\mathrm{nuc}}}\nabla b^*_{\mathrm{nuc}}\right) + \frac{1}{N_{norm}}\frac{dN}{dt} \qquad 2.25$$

Where M is the soot mass concentration, N is the soot particle number density, and N_{norm} is equal to 10^{15} particles. The source terms in the above two equations refer to different nucleation soot source mechanisms. $\frac{dM}{dt}$ considers that the mechanisms of the soot source are nucleation, surface growth, and oxidation. Whereas $\frac{dN}{dt}$ only considers the gas phase (gaseous species) as the nucleation soot source and coagulation. The oxidation model which was reported by Fenimore and Jones [85] where OH is taken into account as a major contributor towards soot oxidation is included. More explanation and details about the Moss-Brookes model can be found in the Ansys Fluent theory guide [190]. The soot particle formation rate is given by:

$$\frac{dN}{dt} = \underbrace{C_\alpha N_{\mathrm{A}}\left(\frac{X_{\mathrm{prec}}P}{RT}\right)^{l} exp\left\{-\frac{T_\alpha}{T}\right\}}_{\text{Nucleation}} - \underbrace{C_\beta\left(\frac{24RT}{\rho_{\mathrm{s}}N_{\mathrm{A}}}\right)^{\frac{1}{2}} d_p^{\frac{1}{2}} N^2}_{\text{Coagulation}} \qquad 2.26$$

Where C_α and C_β are the model constant for soot inception and coagulation rate, respectively. N_{A} is the Avogadro number, X_{prec} is the soot precursor's mole fraction, T_α is the

activation temperature for soot inception, ρ_s is the soot mass density. The soot source for soot mass concentration is expressed as follows:

$$\underbrace{\frac{dM}{dt} = M_P C_\alpha \left(\frac{X_{\text{prec}} P}{RT}\right)^l exp\left\{-\frac{T_\alpha}{T}\right\}}_{\text{Nucleation}} + \underbrace{C_\gamma \left(\frac{X_{\text{sgs}} P}{RT}\right)^m exp\left\{-\frac{T_\gamma}{T}\right\}\left[(\pi N)^{\frac{1}{3}}\left(\frac{6M}{\rho_s}\right)^{\frac{2}{3}}\right]^n}_{\text{Surface Growth}} \underbrace{-C_{\text{oxid}} C_\omega \eta_{\text{coll}} \left(\frac{X_{\text{OH}} P}{RT}\right)\sqrt{T}(\pi N)^{1/3}\left(\frac{6M}{\rho_s}\right)^{\frac{2}{3}}}_{\text{Oxidation}} \quad 2.27$$

Where C_γ, C_{oxid}, and C_ω are the model constant for the soot surface growth, oxidation rate scaling parameter, and oxidation, respectively. M_P is the mass of an incipient soot particle, X_{sgs} is the mole fraction of surface growth species, T_γ is the activation temperature for surface growth, η_{coll} is the collision efficiency.

In this study, the formation of soot was solved and described through the two transport equations shown above. C_2H_2 and C_2H_4 were only considered as the soot precursors to investigate the soot formation in this study. As the Moss-Brookes soot model's default parameters were originally identified to predict soot production in CH_4 combustion [191], [192], they need to be adjusted to enhance the soot predictions of current fuels and to be able to replicate the current experimental findings [193], [194]. The activation energy (E_{activ}) is a parameter that is most commonly changed in most of the modelling works that include reactions. This is because the activation energy is simply defined as the smallest energy needed for a reaction to occur. Therefore, the activation energy is important to be calibrated. The E_{activ} can be expressed in terms of the activation temperature (T_a), as follows:

$$T_a = \frac{E_{\text{activ}}}{R} \quad 2.28$$

Where R is the ideal gas constant. The Moss-Brookes soot model in Ansys Fluent allows one to change the default parameters of the activation temperature for soot inception (T_α) and

for surface growth (T_γ). Therefore, these two quantities were chosen to be calibrated as they have a direct relationship to the activation energy. The default values for T_α and T_γ in the Moss-Brookes model are 21100 K and 12100 K, respectively. The value of 12100 K was initially determined by Vandsburger et al. [195]. According to the existing literature, wide range of values have been used for both T_α and T_γ. Nevertheless, all the literatures showed that T_α is always greater than T_γ. Pang et al. [194] carried out a parametric study of both activation temperatures as part of their modelling work on the production of soot from the combustion of diesel fuel. They found that the best results were when T_α and T_γ are equal to 16000 K and 7600 K, respectively. Leung and Lindstedt [196] proposed a reaction model for soot production in laminar diffusion flames. They found that the activation temperature of 21100 K is the best approximation for describing the first stage of the soot inception. Whereas for T_γ, they determined that the 12100 K value adequately characterises the temperature dependency of the surface growth phase. Pang et al. [197] investigated the soot production in a n-heptane spray flame using similar activation temperature values used by Leung and Lindstedt [196]. The Kong et al. [198] computational study on diesel combustion used a value of 6300 K for T_α, and this is lower than that used in the Moss-Brookes model. Only few shock tube researchers on hydrocarbon blends have suggested $T_\alpha$values between 15000 K to 25000 K [196]. In this work, a parametric study of the T_α and T_γ values was carried to study their impact on the soot production of the tested fuels as well as to select the most appropriate values for this study. The parametric study was conducted based on the approach proposed by Pang et al. [194], in which a test matrix was built for calibrating the activation temperatures. The test matrix is shown in Figure 2-17 and the values included in the test matrix are based on the values suggested in previous studies. For T_α, the lowest value was set to 6300 K and the highest to 21100 K, as proposed by the model in Ansys Fluent. Whereas for T_γ, the lowest value was set to 3100 K and the highest to 12100 K, as recommended by the model in Ansys Fluent. The test matrix used for calibrating the activation temperatures is shown in Figure 2-17.

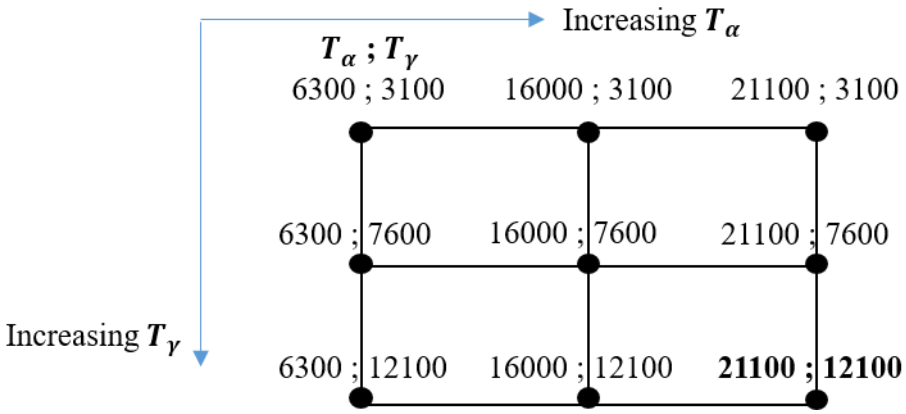

Figure 2-17 Test matrix for calibrating the activation temperatures [194].

Another two important default parameters in the Moss-Brookes soot model, and need to be calibrated because of their crucial roles in the soot generation, are the rates of soot inception (C_α) and soot surface growth (C_γ) [193], [196], [199], [200]. The default values for C_α and C_γ suggested in the Moss-Brookes model are 54 and 11700, respectively. According to the existing literature, many studies have used a value of 10000 for C_α [199]–[201]. Whereas more variation in the $C_\gamma$value has been observed in previous studies [199]–[202], ranging between 6000 to 72000. Therefore, another parametric study of the C_α and C_γ values was conducted based on the approach proposed by Choo et al. [193], in which a test matrix was built for calibrating the rates of soot inception and surface growth. Their approach was based on the values proposed in previous studies. The test matrix used for calibrating the rates for soot inception and surface growth is shown in Figure 2-18. For C_α, the lowest value was set to be 54 (as proposed by the model in Ansys Fluent) and the highest to 10000. Whereas for C_γ, the lowest value was set to 6000 and the highest to 72000. The intermediate value of 11700 for C_γ was also used as recommended by the model in Ansys Fluent.

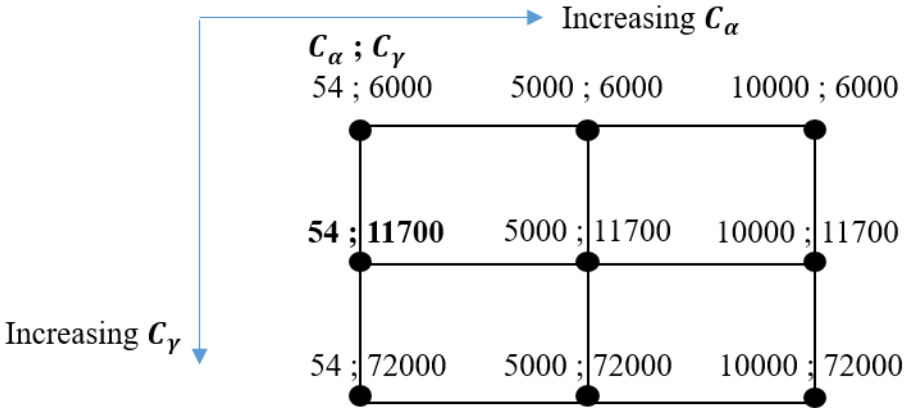

Figure 2-18 Test matrix for calibrating the rates of soot inception and surface growth [193].

A high-quality structured mesh was constructed for the domain shown in Figure 2-19 to calculate solutions of SVF, temperature, and OH*. The type of 2D cell shape used was Quadrilateral (4 sided cell) due its suitability for the current computation domain (structured grid). A total number of 36,000 quadrilateral cells were generated to provide high quality results. A fine mesh was generated near the fuel inlet and the axisymmetric wall, and it gets coarser on moving towards the wall and outlet due to the small gradients in the laminar diffusion flame at these areas. A mesh independence study was carried out by comparing the temperature profile along the centreline between the chosen mesh (36,000 cells) and four different meshes containing 9,000, 81,000, 110250, and 144,000 cells (Further details can be found in Chapter 4). The temperature profiles of 32% C_2H_4 and 68% N_2 flame mixture were compared with the experimental and computational outputs of McEnally et al. [203] at different heights above the burner base to evaluate the precision of the present new computational laminar diffusion flame model. In addition, a qualitative comparison between the OH* signal obtained from the experimental work and the OH* from the model for F13 case was carried out.

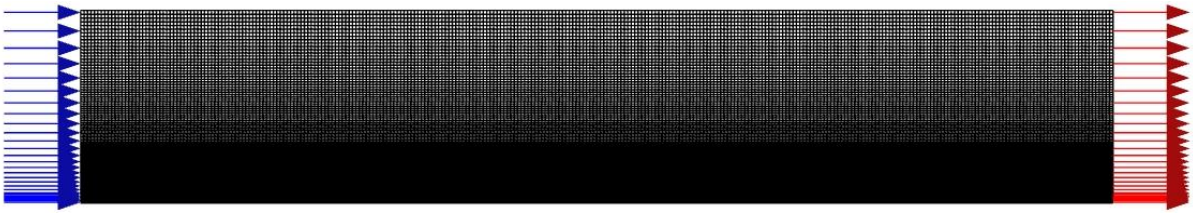

Figure 2-19 Mesh of computation domain.

2.5 Conclusion

This chapter described the experimental and numerical methodologies utilised in this thesis. The 1D simulations of non-premixed laminar flames using the counter flow COSILAB package have been described. In this thesis, two different burners are used, including a standard co-flow burner and a bluff-body swirl spray burner, described in this chapter. Multiple diagnostic methods have been implemented in this thesis to collect different data, as described in this chapter. The methodologies used for processing and analyzing the data collected by different diagnostic techniques were also described in this chapter. Finally, the setup and methods utilized for soot modelling in CFD were also discussed.

Chapter 3: Study of Flame Heat Release and Soot Emissions Characteristics in 1D Chemical Kinetic Simulations

3.1 Introduction

The novelty of this chapter is to provide a new understanding of the characteristics of soot emission, flame chemiluminescence, and HRR through 1D chemical kinetic simulations in the non-premixed DME/CH_4 and DME/C_2H_4 flames. The flame structures and species profiles, including OH*, OH, CH*, CH, HRR, CH_3, C_3H_3, C_2H_2, and flame temperature, were calculated numerically through 1D simulations implemented with a detailed chemical kinetic mechanism (Mech_56.54). Additionally, the impact of adding N_2 as a diluent into DME mixtures with hydrocarbon biofuels was studied numerically.

Another objective of this chapter is to study the role of CH_3 produced from ethanol in forming soot precursors and comparing the soot precursor's pathway to the DME flame and its mixtures. Thus, investigations were carried out on different mixture ratios of ethanol in CH_4, C_2H_4, and n-heptane flames. In addition to CH_3, multiple species have been calculated including, C_3H_3, C_2H_2, OH, OH*, and CH*. 1D simulation employed with the San Diego

mechanism [167] was applied using the counter flow configuration in the COSILAB package [165] to study the impact of Ethanol addition on the emissions formation.

The results of these species will enable a better understanding of the reaction pathways of soot and NO_x emissions and investigate the relationship between the OH*/CH* ratios and equivalence ratio (in Chapter 4). This chapter is essential as it provides a fundamental understanding of the combustion and emissions characteristics of DME and ethanol blended C1/C2 hydrocarbon.

Another objective of this study is to understand the formation routes of C_2H_2 and other soot precursors in a pure iso-pentanol flame. The isopentanol mechanism developed by Tsujimura et al. [122] was implemented to study the iso-pentanol flame in 1D simulations.

3.2 Flame Cases

In this chapter, the DME mixture ratio β (ratio of DME in the fuel mixture) is introduced in terms of the ratio of DME volumetric flow rate to the total fuel volumetric flow rates, i.e., $\beta = Q_{DME}/\sum Q_{fuel}$. Whereas the fuel mixture ratio α (ratio of the fuel in the mixture) is defined as the ratio of the total fuel volumetric flow rate to the total volumetric flow rate of the central jet, including N_2, i.e., $\alpha = \sum Q_{fuel}/\sum Q_{jet}$. The mixing ratios of the DME flames and its mixtures with $CH_4/C_2H_4/N_2$ are shown in Table 3-1.

Table 3-1 Boundary conditions of the DME flame and its mixture.

Jet component	Case	β	α
DME/CH_4	F1	0	1
	F2	0.25	1
	F3	0.50	1
	F4	0.75	1
	F5	1	1
DME/N_2	F6	1	0.75
	F7	1	0.50
	F8	1	0.25
CH_4/N_2	F9	0	0.75
	F10	0	0.50
	F11	0	0.25
$DME/C_2H_4/N_2$	F12	0	0.60
	F13	0.50	0.60
$DME/CH_4/N_2$	F14	0.25	0.85
	F15	0.50	0.75
	F16	0.75	0.70
	F17	1	0.60

For ethanol mixtures, 1D simulations were conducted across a wide range of ethanol mixing ratios along with C_2H_4/ CH_4/ C_7H_{16} (individually) fuels, mixing conditions shown in Table 3-2. The C_2H_2 and C_3H_3 mole fraction profiles were used to evaluate the soot formation characteristics because PAH species and benzene are not contained within the San Diego mechanism. Whereas NO species was used to indicate the formation of NO_x emissions.

Pure iso-pentanol flame was also investigated in 1D simulations in COSILAB. The isopentanol mechanism developed by Tsujimura et al. [122] was used to investigate the pure iso-pentanol flame. No mixed cases were investigated with iso-pentanol.

A Fixed strain rate value of 100 s^{-1} was initially used throughout all cases (3.3.2, 3.3.3 & 3.3.4 subsections) and then was varied to investigate the quenching point for some of those flame cases (3.3.5 subsection). The simulated flame cases' fuel inlet temperature and pressure were set to 298 K and 1 bar, respectively.

Table 3-2 Boundary conditions of the ethanol flame and its mixture.

Jet component	Case	Ethanol Mixing Ratio	Fuel Mixing Ratio
C_2H_5OH/CH_4	C1	0	1
	C2	0.25	0.75
	C3	0.50	0.50
	C4	0.75	0.25
	C5	1	0
C_2H_5OH/C_2H_4	C6	0	1
	C7	0.25	0.75
	C8	0.50	0.50
	C9	0.75	0.25
C_2H_5OH/C_7H_{16}	C10	0	1
	C11	0.25	0.75
	C12	0.50	0.50
	C13	0.75	0.25

3.3 Results and Discussions

The main species profiles and peak values of OH*, OH, CH*, CH, HRR, CH_3, C_3H_3, C_2H_2 and flame temperature obtained from the numerical simulations are presented and discussed in each subsection. The pathway analysis was used to identify the main pathways that contribute to the formation of the soot precursors, C_2H_2 and C_3H_3 in the work.

The following subsections start with the discussion on the model validation of the Mech_56.54 mechanism (Section 3.3.1). After that, the impact of the DME addition to the methane is discussed in Section 3.3.2.1, followed by the comparison with results of the N_2 addition to methane or DME (Section 3.3.2.2), and of the DME addition to ethylene cases (Section 3.3.2.3) on the HRR and soot emissions. The effect of ethanol addition on the flames temperature, soot, and key species mole fractions including NO, OH, C_3H_3 and C_2H_2 is addressed in Sections 3.3.3. The 1D simulation results of pure iso-pentanol are discussed in Section 3.3.4. Finally, strain rates required to quench the flames are then presented and discussed (Section 3.3.5).

3.3.1 Modelling Validation

The Mech_56.54 mechanism has been already validated for DME, CH_4, and their mixtures by Burke et al. [166] using a range of their data and previous literature data. In this section, the Mech_56.54 mechanism was validated in a 1D counter flow diffusion C_2H_4 flames with the available results of C_2H_4 in the Yoon et al. [104] study. Fig. 3-1A shows the comparison between the current simulation and Yoon et al. [104] results of C_2H_2 and C_3H_3 mole fractions of pure C_2H_4 fuel. As seen in Fig. 3-1A, the C_3H_3 mole fraction of both results increased monotonically with the increasing temperature. Whereas the comparison of the C_2H_2 mole fraction shows that both profiles peaked at about 1500 K. Overall, the current simulations showed good agreements with the Yoon et al. [104] outputs. Figure 3-1B shows a comparison between the peak values of the OH* mole fraction calculated by the current simulation and peak values of OH* intensity (normalized) measured from the counter flow experiment for the CH_4/N_2 flame mixture. The comparison here is between OH* mole fraction values and chemiluminescence intensities, so they are not expected to be identical. However, they should have similar trend, as shown in Fig. 3-1B. Therefore, the current simulation is in good agreement with the counter flow experimental results in terms of the trend in the peak values profile.

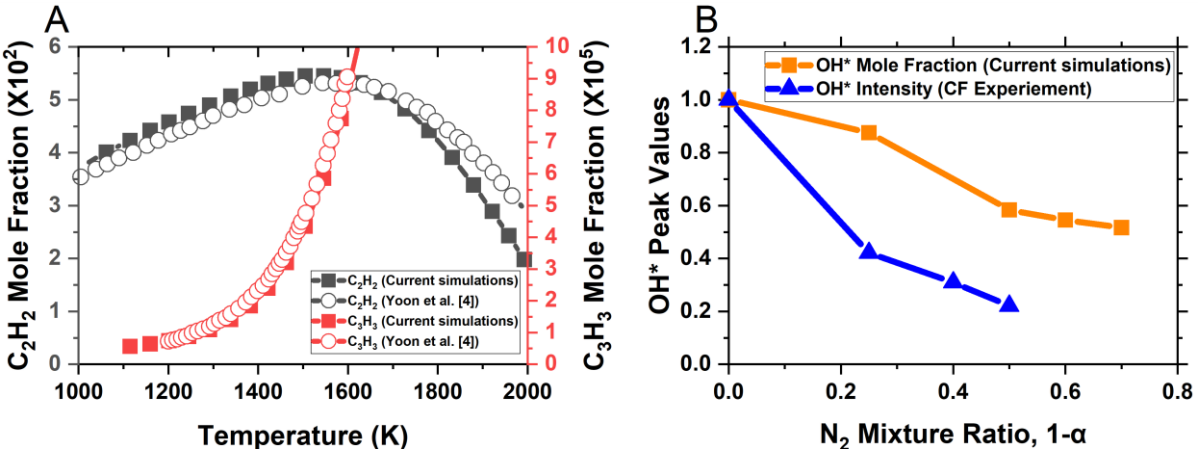

Figure 3-1 A) 1D counter flow flame COSILAB current simulation and Yoon et al. [104] results of C_2H_2 and C_3H_3 mole fractions against the temperature of pure C_2H_4 fuel. B) Comparison between the peak values of OH* mole fraction calculated by current simulation and peak values of OH* intensity measured from the counter flow experiment for the CH_4/N_2 flame mixture.

3.3.2 DME Blend with Methane (CH_4) and Ethylene (C_2H_4)

3.3.2.1 DME/ Methane (CH_4) Mixtures

The DME/CH_4 flames (F1-F5) results are plotted against the mixture fractions in Figure 3-2 A-C. The stoichiometric mixture fraction (ξ_{st}) values are 0.054, 0.069, 0.081, 0.090, and 0.098 for F1 (pure methane), F2, F3, F4, and F5 (pure DME), respectively. Figure 3-2A compares the normalized peak values of flame temperature, HRR, CH_3, C_3H_3, CH*, OH*, OH, CH, and C_2H_2 mole fractions produced from the different conditions of DME/CH_4 mixtures. The normalizations were achieved by referencing to the peak values of the baseline case (pure methane - F1 for the cases with methane, pure DME - F5 for the DME/N_2 cases, and F12 for the DME/C_2H_4 cases). The species mole fraction peak values for the baseline cases are summarised in Table 3-3. It is observed that with increasing DME mixture ratio, β, the peak values of the flame temperature (T) and OH increase gradually, whereas HRR, CH*, OH*, and CH mole fractions decrease. The peak temperature of DME is higher than that of methane by about 47 K. It also showed that DME addition to methane reduces the formation CH_3 and soot precursors in the mixture, as indicated by the drop of the C_3H_3 and C_2H_2 mole fractions shown in Fig. 3-2A.

OH and OH* are both considered hydroxyl radical, but OH* denotes the molecule in an excited state, whereas OH represents the molecule in the ground state. OH* represents HRR more accurately than OH because it is created at high temperature and produces a narrow spectrum of light directly proportional to the amount of HRR. The area under the curve of a specie's

mole fraction can be used for quantifying the total number of moles of the species in the flame. Despite the decrease in the peak value of OH* mole fraction and HRR as DME was added to methane, the area under the curve of the OH* mole fraction and HRR increased with the addition of DME. It was observed that the percentage contribution of oxygen (O) in forming OH* increases when adding more DME. The percentages contributions of oxygen (O) in forming OH* from the reaction of $H + O + M \leftrightarrow OH^* + M$ are 16.4%, 22.2%, 27.2%, and 34.2% for F1, F2, F3, and F5, respectively. Where H is hydrogen and M is a third body molecule (non-reacting molecule).

CH*, OH* and HRR peak values reach the lowest in the pure DME case (Figs. 3-2 A, B). Both OH* and CH* mole fraction profiles start increasing in the rich side of the stoichiometric line in all cases shown in Figure 3-2B, and as the DME mixing ratio increases, both mole fraction profiles start increasing further away from the stoichiometric line. A clear overlap of CH* and OH* profiles with the rich side of the HRR profile is observed, confirming the validity of utilising OH* and CH* chemiluminescence as markers for HRR regions on the rich side.

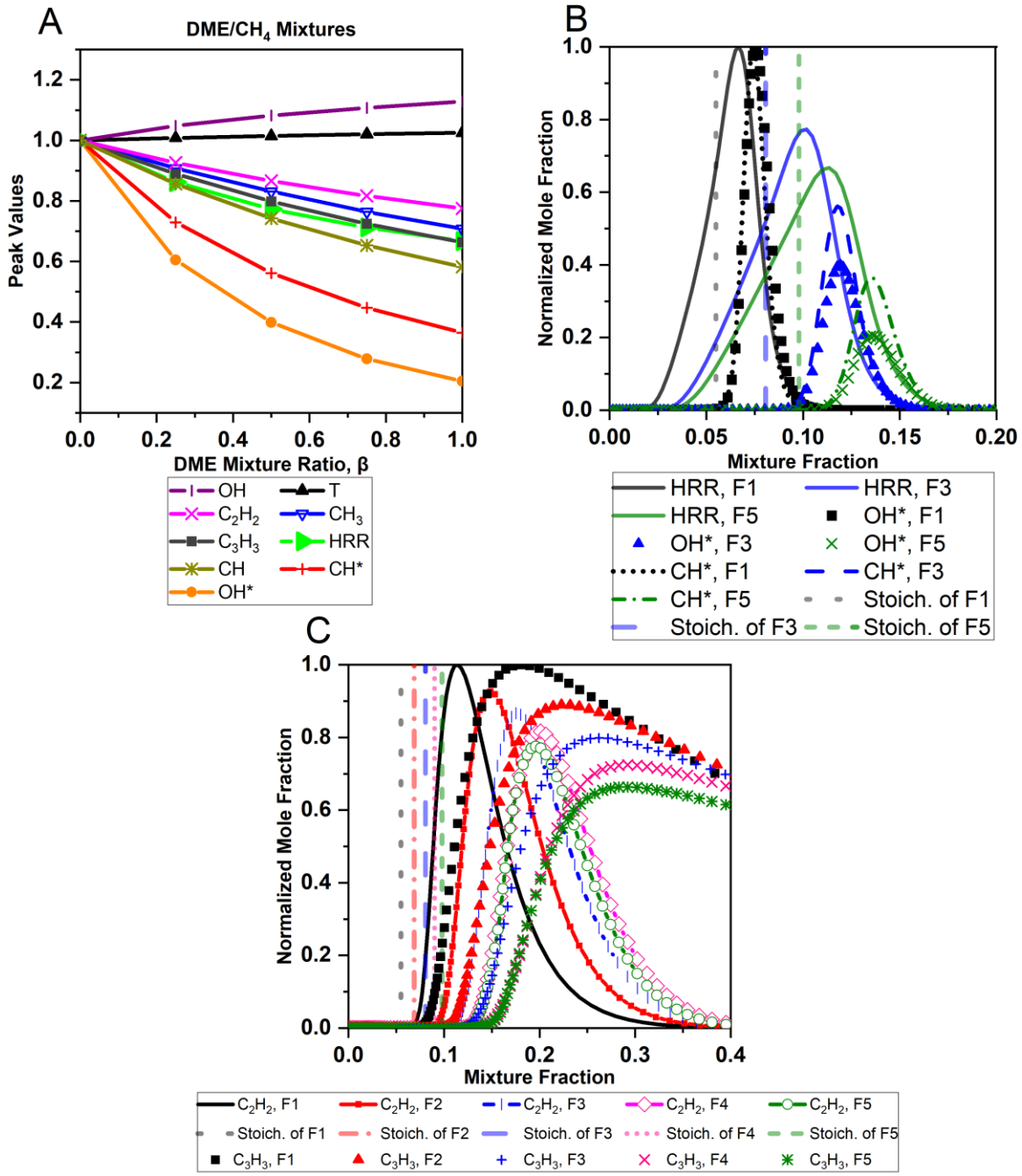

Figure 3-2 1D counter flow flame COSILAB simulation results from the various DME/CH_4 mixtures (F1-F5): (A) normalized peak values of key species, T and HRR, (B) profiles of HRR, CH* & OH* in mixture fraction zone, referenced with the stoichiometric values, and (C) comparison of C_2H_2, C_3H_3 & CH_3 profiles for the five cases.

Table 3-3 Species mole fraction peak values for the baseline F1, F5 and F12 cases.

Case	T (K)	OH*	CH*	HRR	CH_3	C_3H_3	C_2H_2	OH	CH
F1	1857.85	2.8E-09	2.75E-11	3.59E8	5.3E-04	6.88E-04	7.6E-03	9E-03	3E-6
F5	1904.68	5.7E-10	1E-11	2.39E8	3.7E-04	4.56E-04	5.9E-03	9E-03	6.8E-6
F12	1986.74	3.0E-09	4.99E-11	2.75E8	2.91E-04	1.32E-03	3.4E-02	6E-03	5.0E-06

Regarding the soot precursors' behaviours, the results are shown in Figs. 3-2A and 3-2C. Contrary to the findings for the DME addition to ethylene in the literature [4], no increase in the peak values with little addition of DME (25%) to methane was observed in the numerical results (Fig. 3-2A) for the C_3H_3 and C_2H_2. Nevertheless, the integrated C_2H_2 profile (Fig. 3-2C) increase could indicate higher soot concentration. C_2H_2 was shown to be only present in the fuel-rich side for all the cases shown in Fig. 3-2C, in which it starts increasing at about $\xi = 0.1$ and reaching its highest value at $\xi = 0.11$ for the pure methane case and at $\xi = 0.19$ for the pure DME case, and afterward it starts decreasing again to zero. In Figure 3-2C, the C_2H_2 and C_3H_3 mole fraction profiles are found to start increasing further away from the stoichiometric line (at a larger mixture fraction value) as the DME mixing ratio increases, which likely indicates less soot precursors reaching the flame sheet.

From the pathway analysis shown in Fig. 3-3, the soot reduction when adding DME to the methane flame is related to the decrease of the net concentration of CH_3, which further leads to the reduction of the net production of C_2H_2 and C_3H_3. In the pure methane case (Fig. 3-3, F1), formation pathways show that C_2H_2 was primarily formed from C_2H_3, and the latter is formed mainly from C_2H_4. C_2H_4 was mainly formed from C_2H_5. Multiple species, including CH_3, C_2H_6, C_3H_8, and IC_3H_7, contribute to forming C_2H_5 in the pure methane case. Whereas in the mixed case (Fig. 3-3, F2), although the species contributing to forming C_2H_5 are similar to the pure methane case, the percentages of their contributions towards C_2H_5 are reduced, thus causing a decrease in the C_2H_2 and C_3H_3 mole fractions.

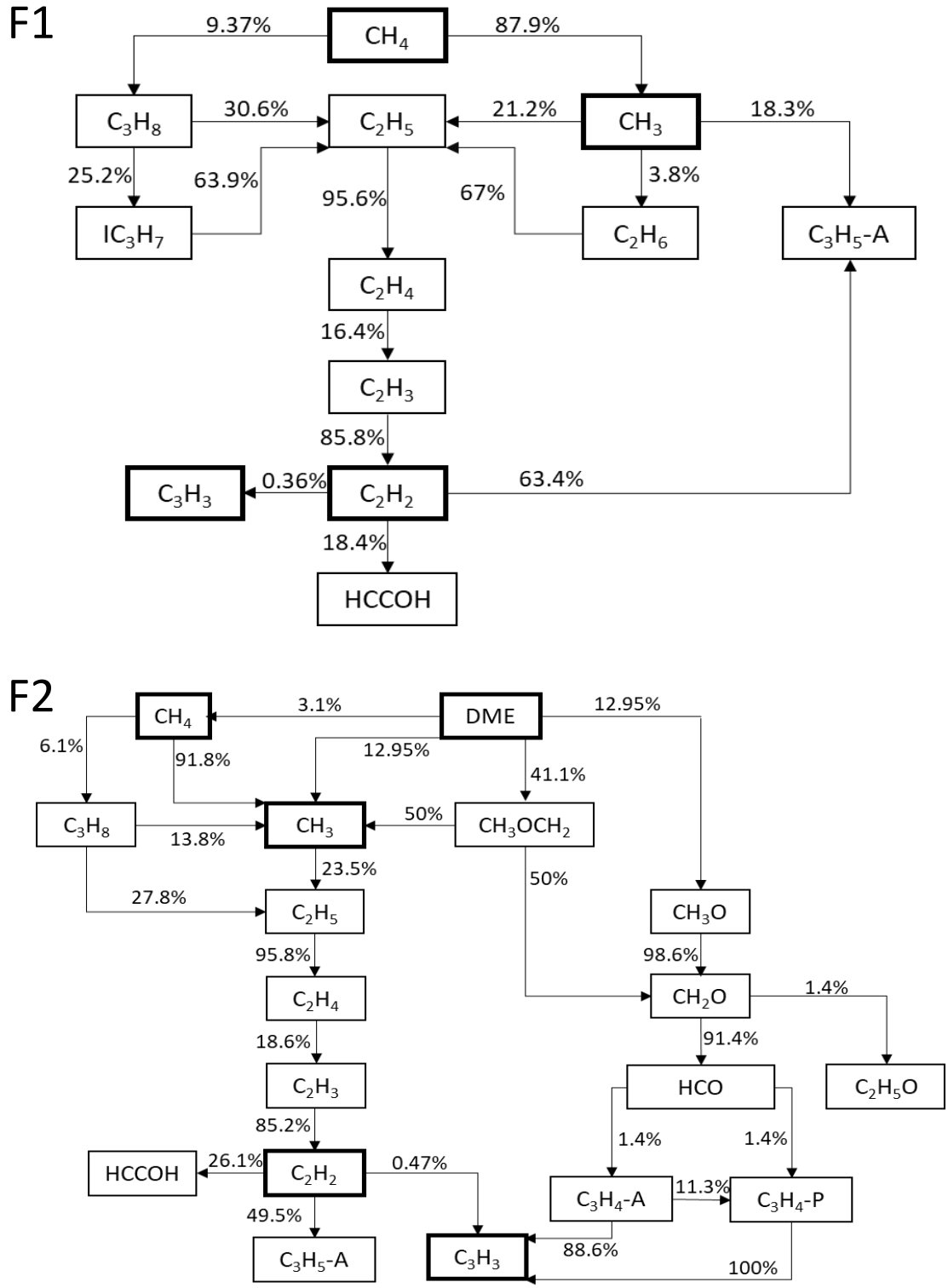

Figure 3-3 Dominant decomposition pathways of F1 (top) & F2 (bottom) cases. Values alongside arrows specify percentage of its contribution.

3.3.2.2 DME/N_2 Mixture and CH_4/N_2 Mixture

To maintain the power output at various DME mixing ratios, N_2 was introduced to the fuel mixture in equal power output cases. In this section, the effect of N_2 addition alone to the methane or DME flames was investigated, and the results are presented. This will assist in clarifying the soot emissions behavior in the equal power output section discussed later in Chapter 4.

The flame temperature, OH, CH, OH*, CH*, HRR, CH_3, C_3H_3, and C_2H_2 peak value profiles for CH_4/N_2 mixtures normalised by the peak values of F1 case (Table 3-3) are displayed in Fig. 3-4A. Fig. 3-4A shows that the addition of N_2 into CH_4 flames reduces the HRR, T, OH, CH, OH*, and CH* peak values. The OH* intensity was also investigated experimentally in counter flow (CF) CH_4/N_2 flames to validate the 1D numerical results. The results of CF flames confirmed that adding N_2 to CH_4 reduces the OH* values (Figure 3-4A). Furthermore, CH_3, C_3H_3, and C_2H_2 mole fractions were decreasing with the increase in N_2 mixture ratio, indicating less production of PAH and hence soot. In general, adding N_2 lowers the flame temperature, which can result in reducing the C_3H_3 and C_2H_2 mole fractions. The N_2 addition to CH_4 fuel (75% of N_2 & 25% of CH_4, F11 case) resulted in shifting the OH and HRR Profiles more into the lean region and caused C_2H_2 to start forming in the lean side at a mixture fraction of 0.21 ($\xi_{st} = 0.26$) as shown in Figure 3-4B. This could be caused by the mixture's local thermophysical characteristics (such as flame temperature) being influenced by the N_2 heat capacity, and hence alterations in the chemical kinetics occurred [204].

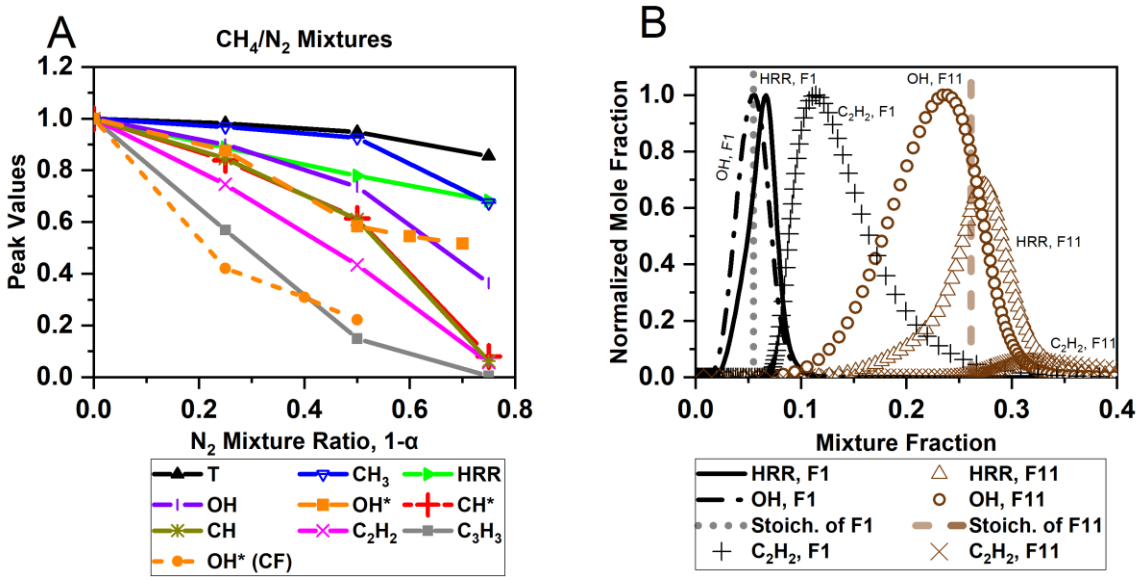

Figure 3-4 1D counter flow flame COSILAB simulation results from A) CH_4/N_2 mixtures peak values, B) F1 and F11 HRR, OH and C_2H_2 profiles: profiles of main species.

The behaviour of species profiles in DME/N_2 mixtures is quite similar to those in CH_4/N_2 mixtures, as shown in Fig. 3-5. Figure 3-5 shows that the addition of N_2 into a DME flame resulted in a significant decrease in the peak value for most species (i.e., C_2H_2, C_3H_3, OH, CH and OH*) and a graduate decrease in CH_3, HRR, CH* and T. The result of OH* for the 0.75 N_2 mixture ratio case is not shown in Figure 3-5 because the simulation model was not predicting well the OH*. The counter flow diffusion flames of DME/N_2 – air were not available to conduct in the current work to compare with the simulated results. The unexpected OH* behaviour for the 0.75 N_2 mixture ratio case suggests more investigation into the mechanism to be carried out in the future. Figure 3-5 shows that C_2H_2 decreases in the mixture as the mixture ratio of the N_2 increases, agreeing with the soot appearance in the experimental C_2* and CH* chemiluminescence results (shown later in Chapter 4). Furthermore, N_2 addition also shifted species profiles and the ξ_{st} lines towards a higher mixture faction value, with the ξ_{st} values at 0.098, 0.115, 0.149, and 0.235 for F5, F6, F7, and F8, respectively.

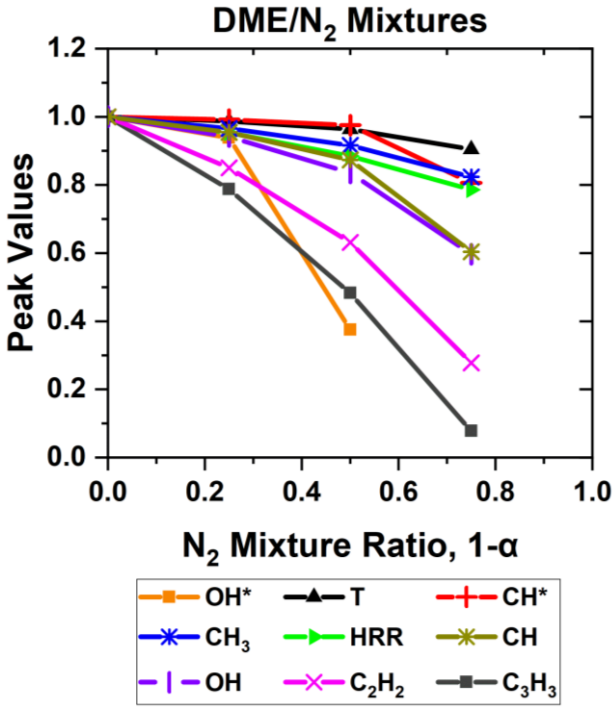

Figure 3-5 1D counter flow flame COSILAB simulation results from DME/N_2 mixtures peak values. α indicates the fuel (DME) percentage in the fuel stream (DME, N_2 mixture).

3.3.2.3 DME/C_2H_4/N_2 Mixtures

This subsection discusses the results for the DME/C_2H_4/N_2 flames. Numerical results of the DME/C_2H_4/N_2 mixtures are shown in Figs. 3-6A-D, at various DME mixture ratios (β = 0, 0.25, 0.5, 0.75, and 1), with constant fuel mixture ratio (α = 0.6). It is noticed in Fig. 3-6A that

most of the species peak values are decreasing as more DME is introduced, except for C_3H_3, which increased with 25% DME addition and then subsequently reduced as β increased. The peak mole fractions of OH* in Fig. 3-6A are positively correlated with the flame HRR similar to the F12 case results shown in Fig. 3-6B. Figures 3-6A-D illustrate the flame temperature, OH, CH, OH*, CH*, HRR, CH_3, C_3H_3, and C_2H_2 mole fraction profiles of DME/C_2H_4 with N_2 mixtures. As an increased percentage of DME is introduced to the ethylene fuel stream, the areas under the C_2H_2 and C_3H_3 profiles are decreased. Additionally, the CH_3 peak mole fraction increases as the DME mixture ratio increases. The role of CH_3 in the formation of C_2H_2 and C_3H_3 is discussed in the pathway analysis (Fig. 3-7).

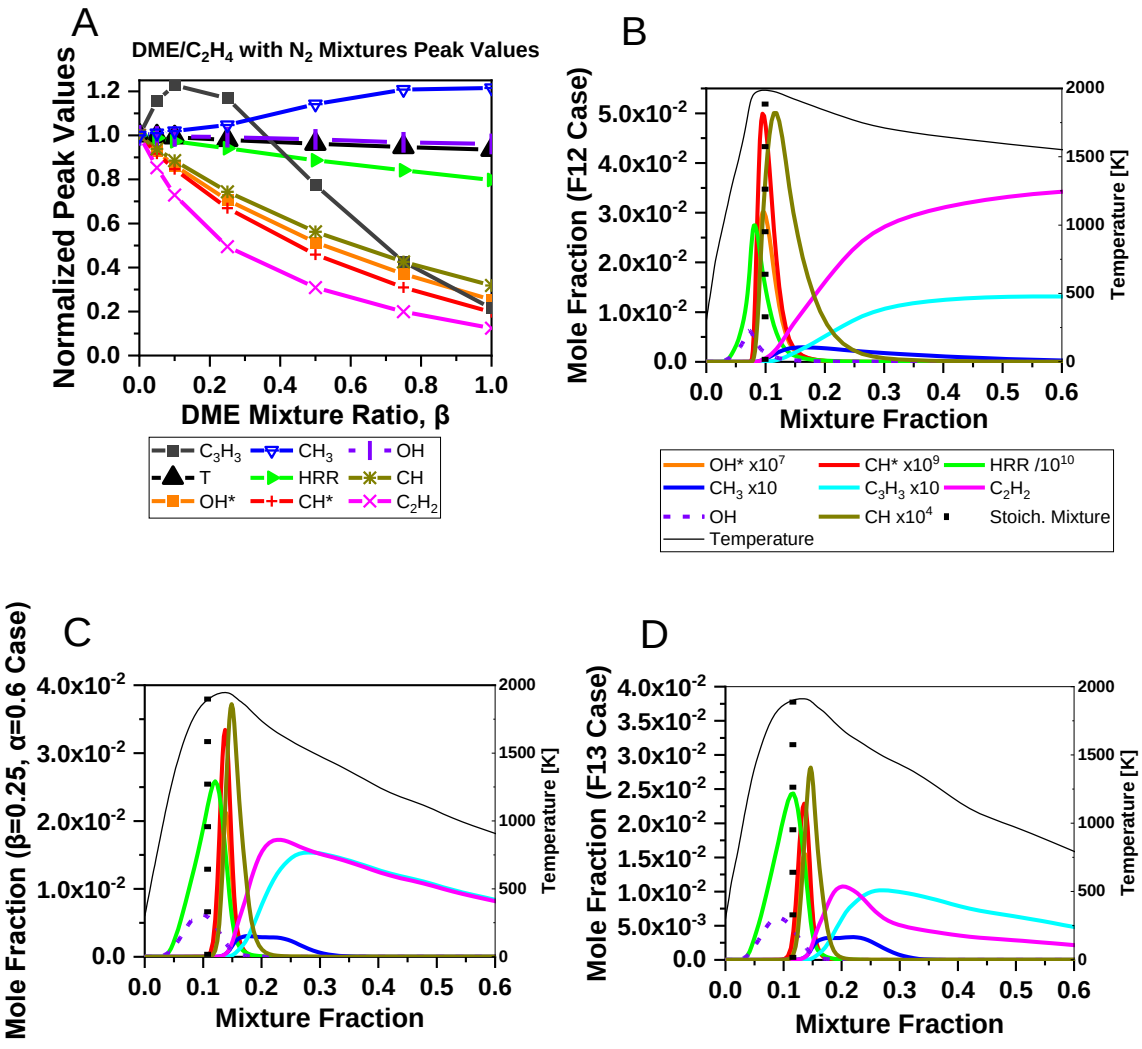

Figure 3-6 1D counter flow simulation results: A) normalised peak values of the major species, T and HRR, species profiles from B) β = 0 (F12), C) β = 0.25, and D) β = 0.50 (F13).

F12

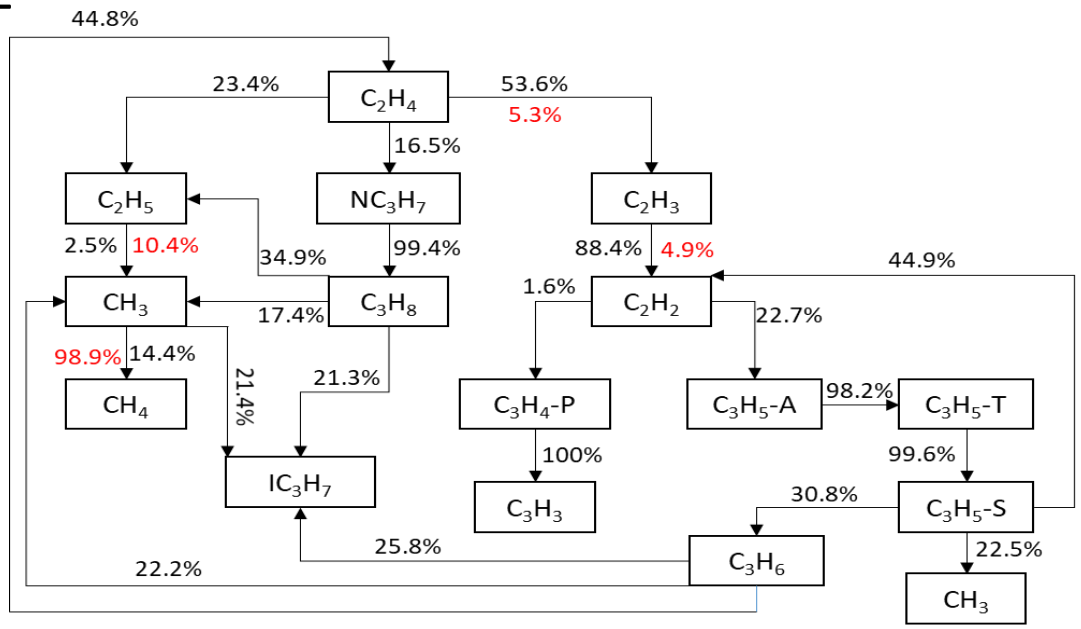

F13

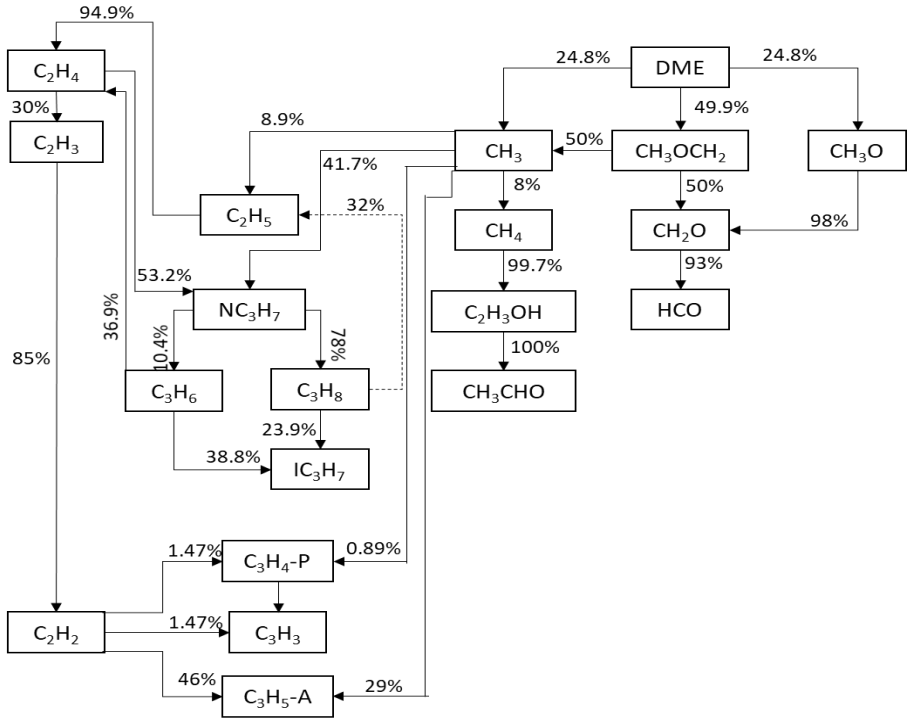

Figure 3-7 Dominant decomposition pathways of F12 & F13 cases. Values alongside arrows specify percentage of its contribution. Red value colored and dashed arrow indicate reverse contribution.

The pathways analysis shown in Fig. 3-7 illustrates that the combustion of C_2H_4 initially generates mostly C_2 species, for example, C_2H_3, C_2H_5, and C_2H_2. Therefore, it is likely that the CH_3 intensity is low in a pure C_2H_4 flame. Whereas the dissociation of DME produces CH_3 in the Mech_56.54 mechanism via the $CH_3OCH_2 \leftrightarrow CH_3 + CH_2O$ reaction. Consequently, the

concentration of CH_3 rises with adding DME, as indicated in Figs. 3-6 and 3-7, and hence the net formation of C_3H_3 increases initially through reactions the $C_2H_2 + CH_3 \leftrightarrow C_3H_4 - P + H$ and $C_3H_4 - P \leftrightarrow C_3H_3 + H$ and reduces at high DME mixture ratios due to limited C_2H_2. A reduced C_2H_2 net concentration is obtained due to the reduced amount of C_2H_4 and the additional reaction with CH_3 to form C_3H_3.

3.3.3 Ethanol Mixtures with Methane (CH_4), Ethylene (C_2H_4) and N-heptane (C_7H_{16})

To study the impact of Ethanol addition on the emissions generation, a 1D simulation was carried out using the San Diego mechanism [167] in counter flow configuration in the COSILAB software [165]. The San Diego mechanism was developed in the early 1990s, and since then, it has undergone several revisions and improvements, the latest updated version, which was released in 2016, was used in this study. Several experimental data sets, including species profiles, laminar flame speeds, ignition delays, and extinction limits, have validated the San Diego mechanism [167]. A comparison between the San Diego mechanism and the Mech_56.54 mechanism was carried out in this study, as presented in Fig. 3-8, for pure C_2H_4 flame to ensure the simulation models are consistent. The OH mole fraction results calculated by the San Diego mechanism are in good agreement with the results of the Mech_56.54 mechanism. For C_2H_2 mole fractions, the Diego mechanism is slightly lower than the Mech_56.54 mechanism results.

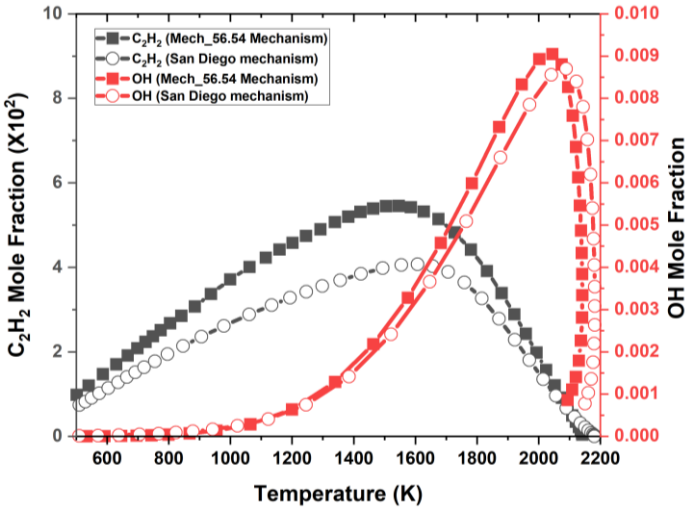

Figure 3-8 Comparison between the San Diego mechanism and the Mech_56.54 mechanism for C_2H_2 and OH mole fractions against temperature of pure C_2H_4 fuel.

3.3.3.1 Ethanol/Methane (CH_4) Mixtures

The results for Ethanol/CH_4 flames (C1-C5) are plotted against the mixture fractions in Figure 3-9 A-B. Figure 3-9A compares the normalized peak values of flame temperature, CH_3, C_3H_3, OH, CH and C_2H_2 mole fractions produced from the different conditions of Ethanol/CH_4 mixtures. The normalizations were achieved by referencing to the peak values of the baseline case (which is pure methane - C1 for the cases with methane, pure ethylene – C6 for the ethanol/C_2H_4 cases, and pure n-heptane – C10 for the ethanol/C_7H_{16} cases). It was observed that increasing the ethanol quantity (25%), increases the flame temperature and then decreases gradually as more ethanol is added. However, the pure ethanol case was found to have lower peak temperature than the mixed cases and a little higher than pure methane case. It was also observed that adding ethanol to CH_4 flame increased the OH mole fraction by about 0.0002405 (75% ethanol & 25% CH_4 flame blend), and so as reducing the CH mole fraction.

The peak values of NO mole fraction species profiles for Ethanol mixtures with CH_4 are also plotted against the ethanol mixture ratio in Fig. 3-9A. It was found that increasing the quantity of the ethanol in the mixture increases the NO mole fraction peak value. The increase in NO peak values with the increase in ethanol mixing ratio in CH_4 flames could be because NO forms via the oxidation of atmospheric nitrogen (N_2) with the oxygen (O_2) in the air through the thermal mechanism (as was mentioned in the literature review). Furthermore, as more ethanol (oxygenated fuel) is added to the mixture, the amount of oxygen increases, and hence NO increases. In addition, it was shown earlier that the OH mole fraction increases with increasing the ethanol quantity in CH_4 flame, which could also increase the NO through the $HNO + OH \leftrightarrow NO + H_2O$ & $N + OH \leftrightarrow NO + H$ reactions. The two explanations mentioned above are valid for the mixture of ethanol and CH_4.

In the ethanol mixtures study, soot formation behaviour was also investigated through C_2H_2 and C_3H_3 mole fractions because the San Diego mechanism does not include benzene PAH species. C_3H_3 mole fraction peak values decreased with increased ethanol quantity in CH_4 (as shown in Figure 3-9B). This was probably due to the slight increase in the formation of OH mole fractions in ethanol/CH_4 mixtures (as shown in Figure 3-9A) attacking the soot precursors and soot particles, reducing the soot formation. Nevertheless, the C_2H_2 mole fraction increased when ethanol was added to the CH_4. It was found that Ethanol (C_2H_5OH) directly contributes in forming C_2H_4 through the $C_2H_5OH(+M) \leftrightarrow C_2H_4 + H_2O(+M)$ reaction, as shown in Figure 3-10 (case C2). C_2H_4 is known to be one of the main contributors to forming C_2H_2 and soot.

Hence, this also explains why the C_2H_2 mole fraction increases as ethanol is added to CH_4. C_2H_4 contributes in forming C_2H_2 indirectly through C_2H_3, where 74% of C_2H_4 consumes in forming C_2H_3, and the latter contributes by 38% to form C_2H_2. In addition, CH_4 is one of the main contributors to forming C_2H_2. It was noticed in the pathway analysis of case C2 that the addition of C_2H_5OH contributes to forming more CH_4, and hence the quantity of C_2H_2 increases. In the pure methane case (F1 shown in Figure 3-3), the pathway from CH_4 to C_2H_2 is $CH_4 \rightarrow CH_3 \rightarrow C_2H_6 \rightarrow C_2H_5 \rightarrow C_2H_4 \rightarrow C_2H_3 \rightarrow C_2H_2$.

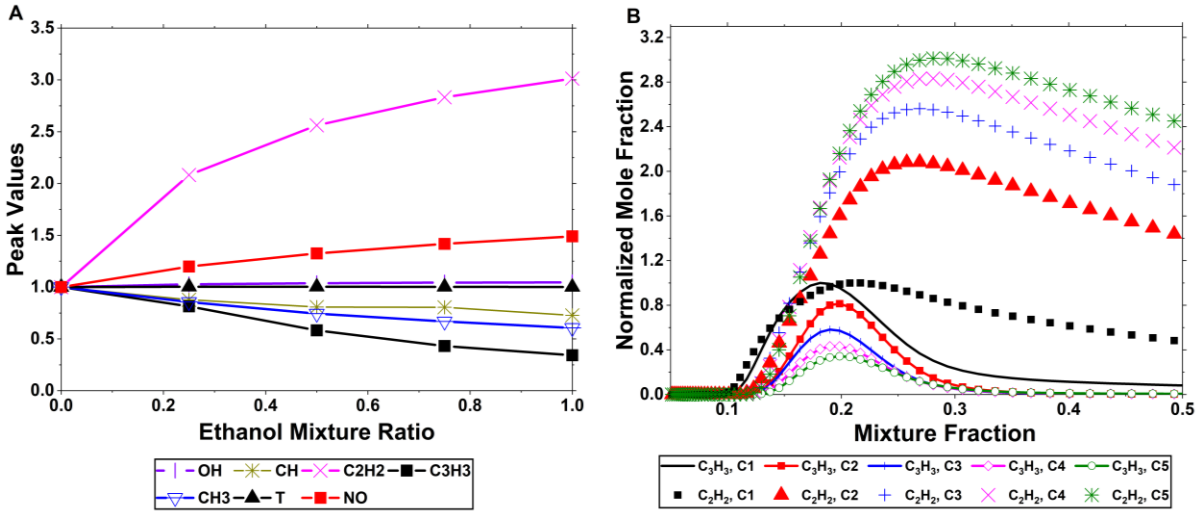

Figure 3-9 1D counter flow flame COSILAB simulation results from the various Ethanol/CH_4 mixtures (C1-C5): (A) normalized peak values of key species, and (B) comparison of C_2H_2 & C_3H_3 profiles for the five cases.

Figure 3-10 also shows that as ethanol is added to the CH_4 flame (C2), C_4H_6 starts contributing less in forming C_3H_3. This may explain why the C_3H_3 mole fraction reduces as more ethanol is added to the methane. However, as more ethanol is added, it was also noticed that C_4H_6 starts contributing more in forming both C_2H_3 and C_2H_2 through the following reaction $C_4H_6 + CH_3 \leftrightarrow CH_4 + C_2H_2 + C_2H_3$. Therefore, the C_4H_6 radical also plays a role in increasing the C_2H_2 mole fraction.

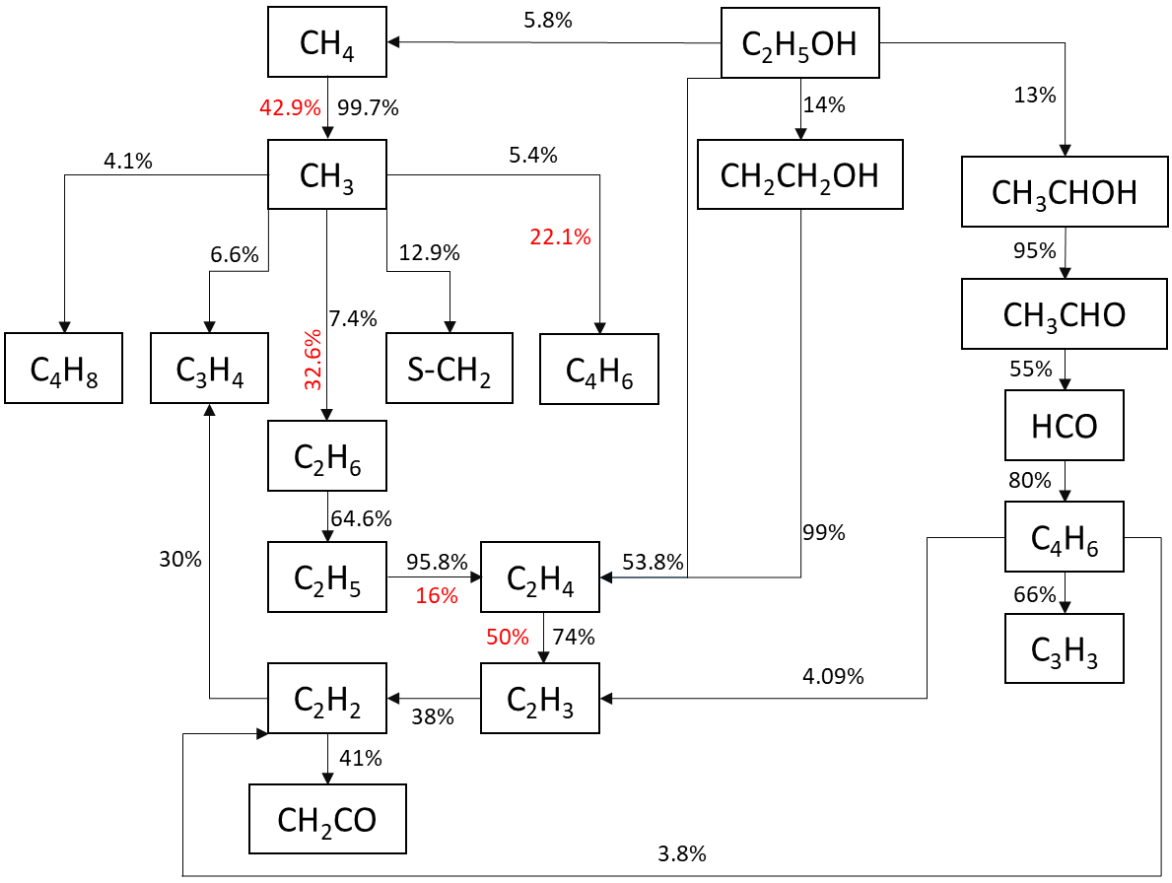

Figure 3-10 Pathway analysis of C2 case. Red value colored indicate reverse contribution.

3.3.3.2 Ethanol/Ethylene (C_2H_4) Mixtures

The results for Ethanol/C_2H_4 flames (C5-C9) are plotted against the mixture fractions in Figure 3-11A-B. Figure 3-11A compares the normalized peak values of flame temperature, CH_3, C_3H_3, OH, CH and C_2H_2 mole fractions produced from the different conditions of Ethanol/C_2H_4 mixtures. All the species and flame temperatures presented in Fig. 3-11A decreased their peak values as the ethanol mixture ratio increased in the C_2H_4 flame. The peak values of soot precursors were also decreased as the ethanol mixture ratio increased in the C_2H_4 flame, although the peak values of OH radicals in ethanol/C_2H_4 mixtures (that would attack the soot precursors and soot particles) were also decreased.

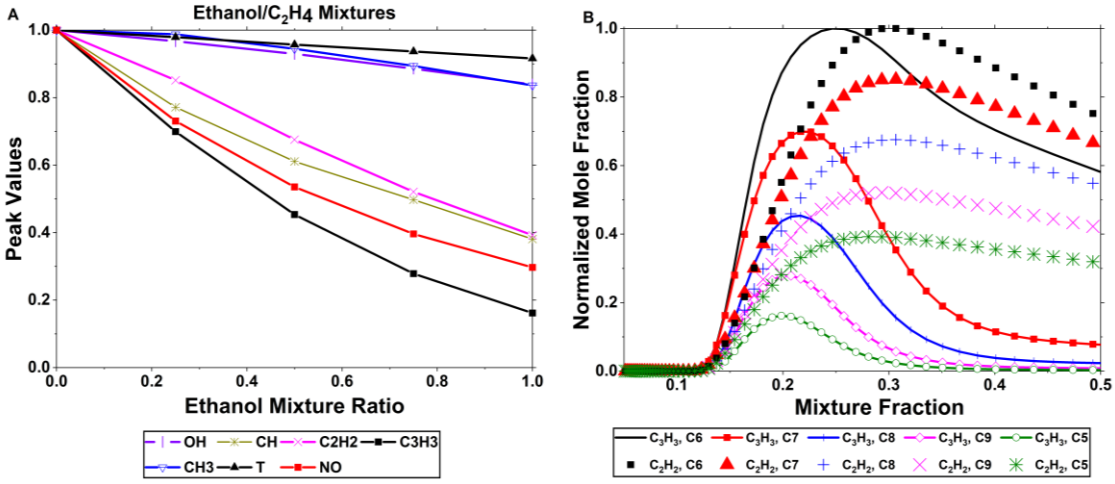

Figure 3-11 1D counter flow flame COSILAB simulation results from the various Ethanol/C_2H_4 mixtures (C5-C9): (A) normalized peak values of key species, and (B) comparison of C_2H_2 & C_3H_3 profiles for the five cases.

The results of the C_2H_2 mole fraction for the ethanol/ ethylene mixture shown in Figure 3-11A don't agree with McEnally and Pfefferle [114] and Bennett et al. [96]. Both of these studies [96], [114] concluded that adding ethanol to ethylene resulted in increasing soot and benzene (C_6H_6) formation. In the present study, soot precursors decreased with adding ethanol to ethylene. The current result is as expected, as ethanol is known to generate a low quantity of soot compared to ethylene. Figure 3-12 shows the pathway analysis of cases C6 and C7 generated from the current simulation. The pathway analysis displays that the amount of C_2H_4 decreases as more ethanol is added, and hence this is likely to be the main reason behind the decrease in C_2H_2 mole fraction. In the C7 case, ethanol is observed to generate CH_3 directly through $C_2H_5OH(+M) \leftrightarrow CH_3 + CH_2OH(+M)$ reaction, and C_2H_4 via $C_2H_5OH(+M) \leftrightarrow C_2H_4 + H_2O(+M)$ reaction. The direct and indirect generation of C_2H_2 mole fractions from CH_3 in the C7 case is very low (<1.6%). The pathway route through C_2H_4 and C_2H_3 is the only one that contribute significantly to forming C_2H_2.

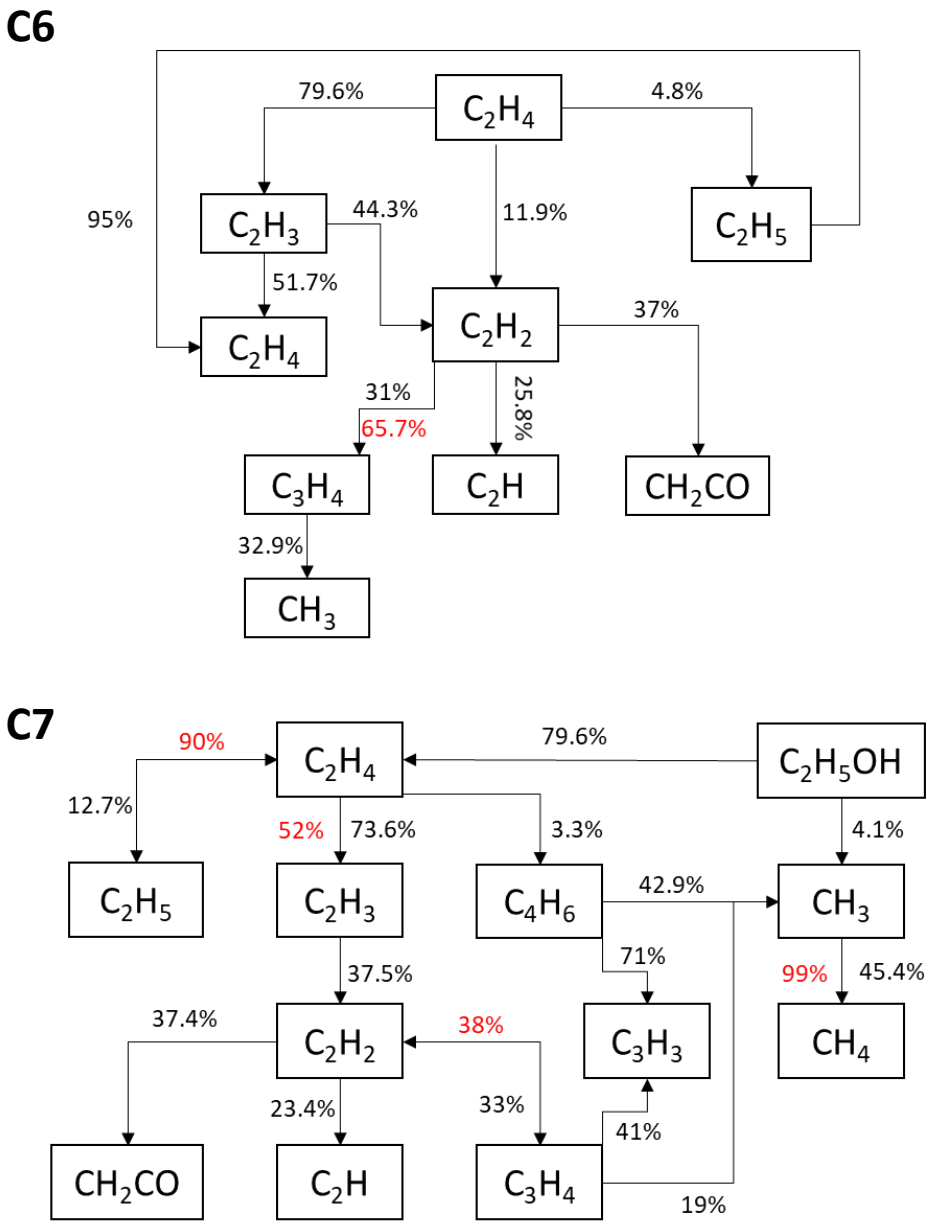

Figure 3-12 Pathway analysis of cases C6 (top) and C7 (bottom). Red value colored indicate reverse contribution.

Previously, there has been a disagreement about the formation route of C_6H_6 in an ethanol/ethylene mixture. The previous studies suggested that C_6H_6 can be either formed from the self-reaction of C_3H_3 or through the reaction of C_2H_2 with C_4H_5. The current mechanism does not include C_4H_5; hence, this study cannot make comments about the route of C_4H_5. However, the behaviour of the C_3H_3 mole fraction should still give a valid indication of the C_6H_6 behaviour. As shown in Fig. 3-11A-B, both C_2H_2 and C_3H_3 mole fractions were reduced when ethanol was added to ethylene. Regarding the formation pathway of C_3H_3, it has been found that CH_3 (produced from ethanol) generates C_4H_6 through the $C_3H_3 + CH_3 \leftrightarrow C_4H_6$

reaction (two ways reaction). Moreover, the C_4H_6 (produced from ethylene) generated through the $C_4H_6 + H \leftrightarrow C_2H_3 + C_2H_4$ reaction produces CH_3 with a contribution percentage of about 42.9%. Whereas, CH_3 (produced from ethanol) generated through the $C_2H_5OH(+M) \leftrightarrow CH_3 + CH_2OH(+M)$ reaction produces C_4H_6 with a contribution percentage of about 15.7%. Nevertheless, the current analysis shows that the dependence of C_3H_3 on C_4H_6 is more than CH_3. Thus, C_4H_6 reduces as the amount of C_2H_4 reduces, and hence the C_3H_3 mole fraction decreases.

3.3.3.3 Ethanol/ N-heptane (C_7H_{16}) Mixtures

The results for Ethanol/C_7H_{16} flames (C5, C10-C13 cases) are plotted against the mixture fractions in Figure 3-13A-B. Figure 3-13A compares the normalized peak values of flame temperature, CH_3, C_3H_3, OH, CH and C_2H_2 mole fractions produced from the different conditions of Ethanol/C_7H_{16} mixtures. Most of the species and flame temperature presented in Fig. 3-13A decreased their peak values as the ethanol mixture ratio increased in the C_7H_{16} flame. An unexpected significant decrease in the OH mole fraction was detected in case C12 (50% Ethanol & 50% Heptane), which suggests further investigation on the mechanism used to understand the reason behind this decrease. However, C10 (pure Heptane) and C5 (pure Ethanol) have almost equal OH mole fraction peak values of 0.0059 and 0.0057 for pure Heptane and Ethanol, respectively.

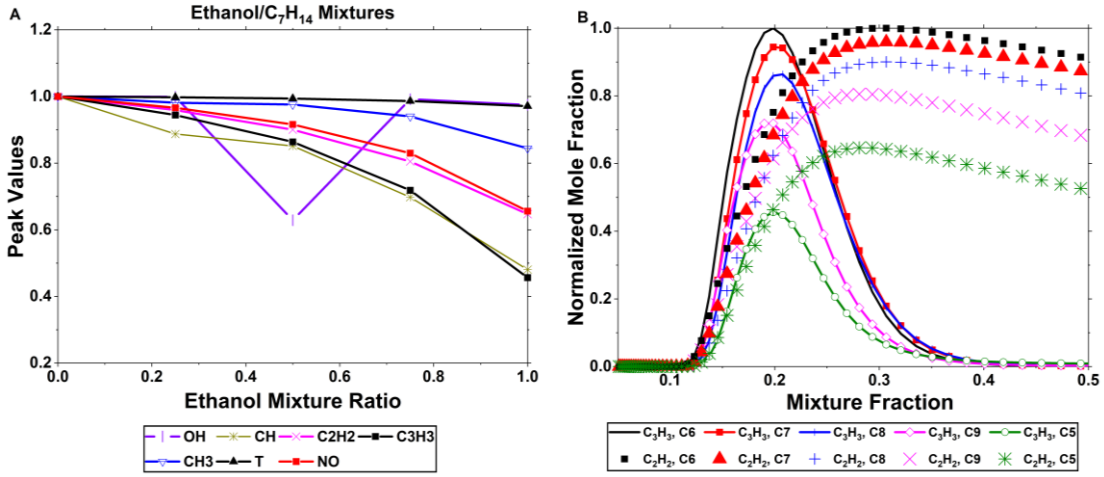

Figure 3-13 1D counter flow flame COSILAB simulation results from the various Ethanol/C_7H_{16} mixtures (C5, C10-C13): (A) normalized peak values of key species, and (B) comparison of C_2H_2 & C_3H_3 profiles for the all cases.

In all cases, it was observed that with increasing the ethanol quantity in C_7H_{16} flames, the C_3H_3 mole fraction decreases, as shown in Figure 3-13B. C_2H_2 mole fraction was also reduced as more ethanol was added to C_7H_{16}, as shown in Figure 3-13A-B.

The peak values of NO mole fraction species profiles for Ethanol mixtures with C_7H_{16} flames are plotted against the mixture fractions in Figure 3-13A. It was observed that the NO mole fraction decreases with increasing the ethanol quantity. The increase in the amount of oxygen (caused by ethanol) does not appear to play a role in ethanol-C_2H_4-C_7H_{16} mixtures because no NO mole fraction was detected. Therefore, it can be concluded that the dependence of the NO mole fraction on OH radicals is more than those of O_2. Figure 3-14 displays how OH contributes to forming NO in the pure heptane case (C10). In the San Diego mechanism, the OH radical reacts with NH_2 to form water and NH, and then NH reacts with oxygen forming NO. Moreover, OH reacts directly with nitrogen and forms NO. Therefore, OH plays a critical role in the NO behaviour.

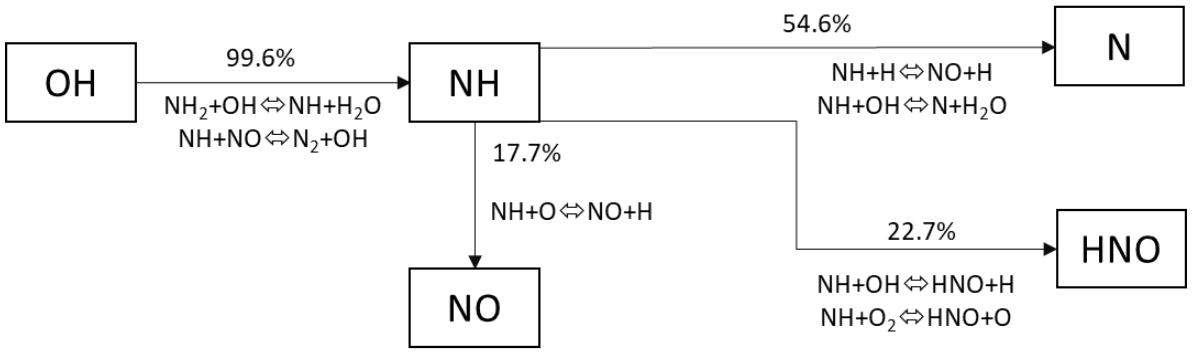

Figure 3-14 The pathway analysis from OH to NO in pure heptane case (C10).

Figure 3-15 shows the pathway analysis of the pure n-heptane case (C10) and the mixed case of 75% n-heptane and 25% ethanol (C11). The percentage contribution of C_7H_{16} to CH_3, C_2H_4, and C_2H_5 is almost the same in both cases presented in Fig. 3-15. However, the fuel concentration of C_7H_{16} is less in the C11 case, which resulted in producing lower amounts of C_2H_2. In case C11, ethanol also contributes to forming C_2H_4 by 38%; however, C_2H_4 only contributes by 3% in forming C_2H_2.

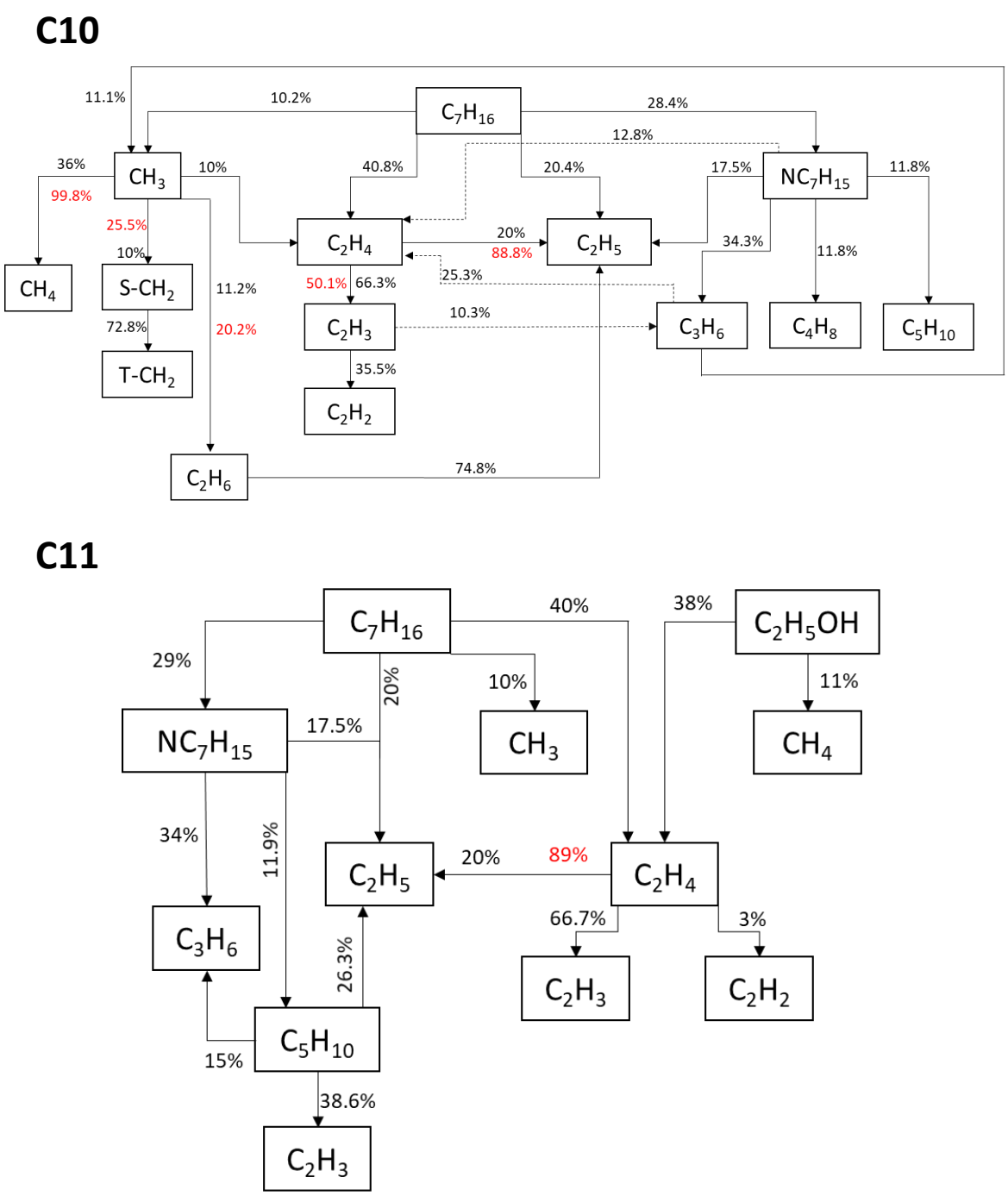

Figure 3-15 Pathway analysis of cases C10 (top) and C11 (bottom). Red value colored and dashed arrow indicate reverse contribution.

3.3.4 1D Simulation of the Iso-pentanol Flame

1D counter flow flame simulation of pure iso-pentanol was also investigated in COSILAB using an isopentanol mechanism developed by Tsujimura et al. [122]. Figures 3-16 show the flame temperature, OH, CH_3, C_3H_3, and C_2H_2 mole fraction profiles of the pure iso-pentanol flame. The stoichiometric mixture fraction (ξ_{st}) value of iso-pentanol is 0.23748. The peak

flame temperature of pure iso-pentanol is 1938.5 K, whereas the peak flame temperature of pure n-heptane is 2017.56 K (n-heptane results obtained from the San Diego mechanism). The mole fraction of C_2H_2 was the highest amongst the other soot precursors, i.e., CH_3 and C_3H_3, in pure iso-pentanol flame, as shown in Figure 3-16. Figures 3-17 illustrate the pathway analysis in the pure iso-pentanol flame. The direct contribution of iso-pentanol in forming CH_3 is only 1.86%. The pure iso-pentanol ($IC_5H_{11}OH$) is mostly decomposed to different isomers of the $C_5H_{10}OH$, as seen in Fig. 3-17. The CH_3 is mostly formed indirectly through isobutyl (IC_4H_9). The formation of C_2H_2 is shown to be formed mainly through two routes; one through $CH_3 \rightarrow C_2H_6 \rightarrow C_2H_5 \rightarrow C_2H_4 \rightarrow C_2H_3 \rightarrow C_2H_2$, and the second through $C_3H_6 \rightarrow C_2H_3 \rightarrow C_2H_2$. The propene ($C_3H_6$) route originated from the decomposition of iso-pentanol to $LC_5H_{10}OH$ (known as α-hydroxypentyl radicals [122]). The contribution in producing C_2H_4 in the pure n-heptane flame (Fig. 3-15, C10) is more than in the pure iso-pentanol flame (Fig. 3-17). This is possibly because pure n-heptane is actually a larger hydrocarbon than the pure iso-pentanol, and so more likely for the pure n-heptane to go through many chemical processes needed to decompose into C_2H_4. Therefore, the production rate of C_2H_2 is more likely to be higher in the pure n-heptane flame.

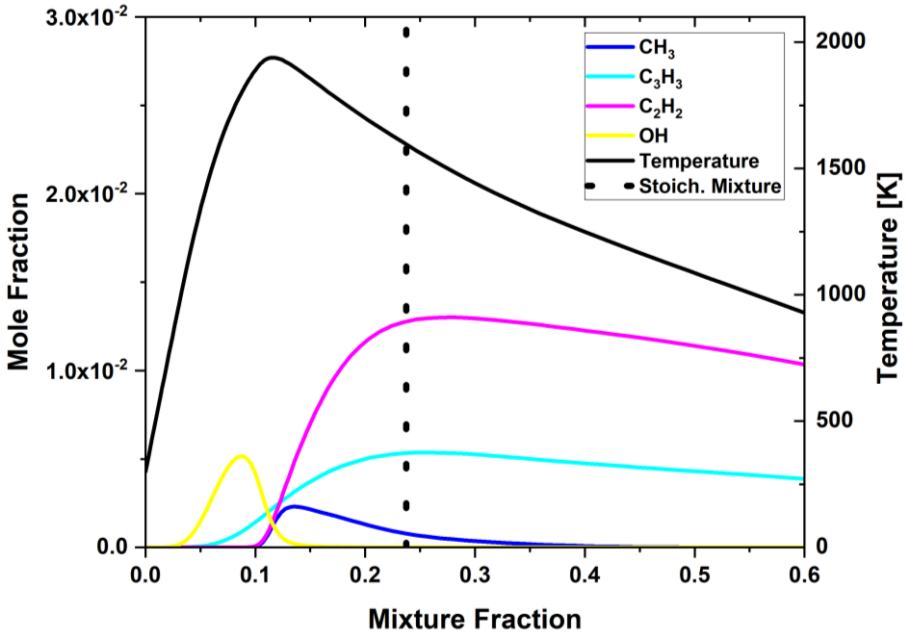

Figure 3-16 Flame temperature, OH, CH_3, C_3H_3 and C_2H_2 mole fraction profiles of pure iso-pentanol flame.

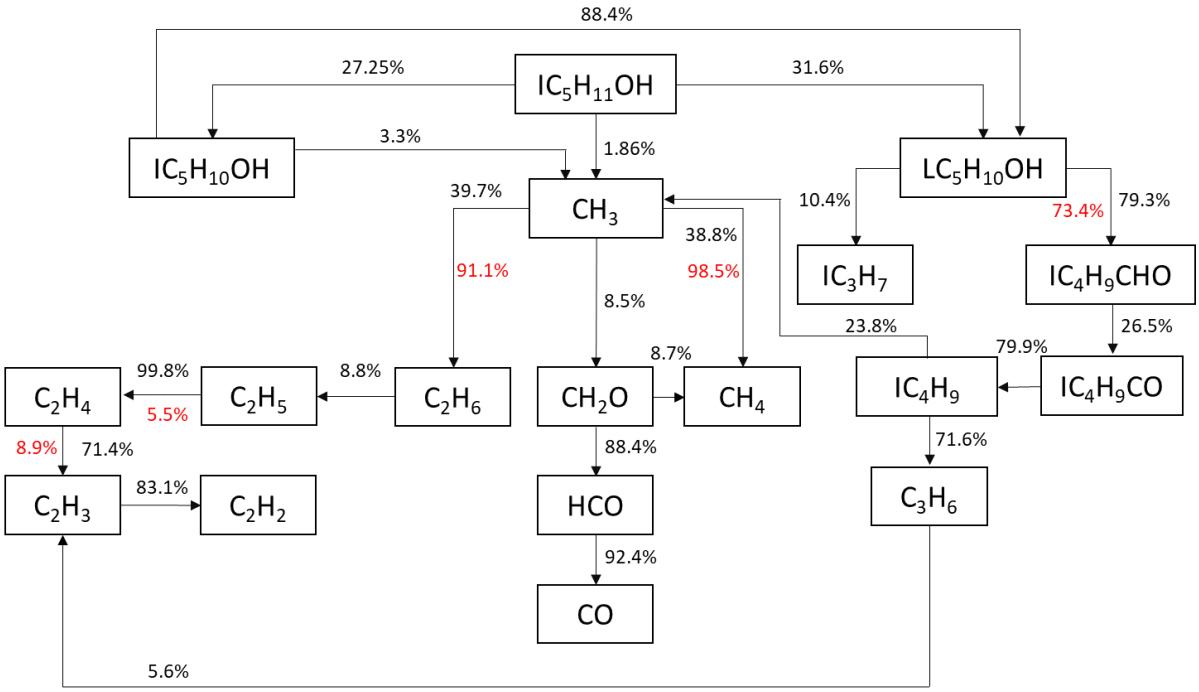

Figure 3-17 Pathway analysis of pure iso-pentanol case. Red value colored indicate reverse contribution.

3.3.5 Increasing the Strain Rate

The quenching point of some flame cases discussed above has been investigated numerically in COSILAB. The arclength-continuation procedure was used in which the strain rate was increased gradually until the quenching point Q was encountered. Increasing the strain rate in the counter flow configuration reduces the adiabatic flame temperature, and after a certain strain rate value, the flame gets extinguished [42]. This is because as the strain rate increases, the residence time reduces. Hence, less fuel/ air mixture is transferred to products (the diffusive time scale becomes shorter), and eventually, the flame is extinguished.

As seen in Table 3-4, pure DME and C_2H_4 flame's quenching points occur at the highest strain rate (>1300 s^{-1}) among the single-fuel flames. The combination of DME and C_2H_4 with a mixing ratio of 50:50 was quenched at a higher strain rate than that of pure DME. Pure CH_4 and C_7H_{16} flames were quenched at strain rates of 450 s^{-1} and 800 s^{-1}, respectively. The addition of DME to CH_4 and C_7H_{16} has increased the strain rate value required for quenching, as shown in Table 3-4.

Table 3-4 Quenching point of multiple flames

Flame & Mixing Ratios	Strain Rate at Quenching Point (s^{-1})
Pure DME	1400
Pure C_2H_4	1500
Pure CH_4	450
Pure C_7H_{16}	800
DME+ CH_4 50:50	1000
DME+ C_2H_4 50:50	1500
DME+ C_7H_{16} 50:50	1000
DME+ C_7H_{16} 10:90	850
DME+ CH_4 25:75	750
DME+ CH_4 75:25	1200

3.4 Conclusion

The work conducted in this chapter focused on investigating various flame mixtures in 1D simulations using the COSILAB software. This chapter provided a new understanding of the characteristics of soot emission, species profiles, flame chemiluminescence, and HRR in the non-premixed DME/CH_4 and DME/C_2H_4 flames. In addition, a numerical analysis was done to determine the effects of adding N_2 as a diluent to DME blends with hydrocarbon biofuels. Investigations were also carried out on different mixing ratios of ethanol in CH_4, C_2H_4, and n-heptane flames. The role of CH_3 produced from ethanol in forming soot precursors was studied, and the soot precursor's pathway was compared to the DME flame and its mixtures. The formation routes of C_2H_2 and other soot precursors in pure iso-pentanol flame were also investigated in this chapter. The key conclusions from this chapter are as follows:

1- The results showed a decrease in soot precursors (C_2H_2 and C_3H_3) concentration as the DME mixture ratio increased in the methane flame. Whereas the small addition of DME (25%) into an ethylene flame contributed to an increase in the concentration of C_3H_3, it is considered a vital species besides C_2H_2 that contributes to the forming C_6H_6 and soot. However, as the DME mixture ratio increased further into the ethylene flame, the C_3H_3 species concentration decreased.

2- Pathway analysis showed that in DME/CH_4 flame mixtures, CH_3 significantly affected the formation of soot precursors such as C_2H_2, C_3H_3, from which potentially further forms C_6H_6. While in the DME/C_2H_4 flame mixture, CH_3 had a positive influence on the C_3H_3 net production under small DME mixing ratios (25%). C_3H_3 and C_2H_2 soot precursors were found to decreases as the DME mixture ratio increases in the CH_4

flame. Nevertheless, the integrated C_3H_3 and C_2H_2 profiles increased with a 25% DME mixture ratio.

3- F12 and F13 cases displayed a reduction in HRR and C_2H_2 peak values as more DME and N_2 were added simultaneously to the ethylene flames. In addition, the integrated area of the C_2H_2 and C_3H_3 species profiles were decreased.

4- Flame temperature peak values decreased as the ethanol mixing ratio was increased in the CH_4, C_2H_4, and C_7H_{16} flames. In the ethanol/CH_4 mixture, C_2H_2 peak values increased with adding ethanol to CH_4, while CH_3 and C_3H_3 mole fractions were decreased with increasing ethanol mixing ratio in the fuel stream.

5- In the ethanol/ CH_4 mixture, it was found that ethanol addition contributes to forming more CH_4 to the quantity already exists in the fuel stream. Hence, CH_4 increases the quantity of C_2H_2 through the pathway of $CH_4 \rightarrow CH_3 \rightarrow C_2H_6 \rightarrow C_2H_5 \rightarrow C_2H_4 \rightarrow C_2H_3 \rightarrow C_2H_2$. Whereas in the ethanol/ C_2H_4 mixture, ethanol addition was observed to generate CH_3 directly; however, the amount of C_2H_2 and C_3H_3 was reduced.

6- The peak values of NO mole fractions were found to increase when ethanol was added to CH_4, but it was decreased when ethanol is added to C_2H_4 and C_7H_{16} fuels. The dependence of the NO mole fraction on OH radicals was observed to be more than those of O_2.

7- In the pure iso-pentanol flame, the formation of C_2H_2 was found to be formed mainly through two routes; one through $CH_3 \rightarrow C_2H_6 \rightarrow C_2H_5 \rightarrow C_2H_4 \rightarrow C_2H_3 \rightarrow C_2H_2$, and the second through $C_3H_6 \rightarrow C_2H_3 \rightarrow C_2H_2$. The contribution in producing C_2H_4 in the pure n-heptane flame was more than in the pure iso-pentanol flame.

8- Adding DME to CH_4 and C_7H_{16} has increased the strain rate value required for quenching.

Chapter 4: Co-flow non-premixed DME/C1-C2 hydrocarbon flames Experimental and Modelling studies

4.1 Introduction

This chapter aims to experimentally study the impact of adding DME to methane and ethylene fuels, across a full range of DME mixing ratios, on flame heat release and reaction zone using CH*, OH*, and C_2* chemiluminescence. In addition, a detailed mechanism and species transport model are used in a computation fluid dynamics (CFD) study to predict the temperature distribution in 2D. The CH*, OH*, and C_2* chemiluminescence results were used to locate flame heat release regions and investigate the soot signal's effect on their measurements. The ratios of the chemiluminescence pairs (OH*/CH*, OH*/C_2*) were studied on the feasibility of mapping local equivalence ratios.

Another aim of this chapter is to validate the CFD model using current experimental results of OH* and temperature profiles from the literature and study the impact of DME addition on flame temperature. This thesis's modelling study primarily concentrated on the soot emissions and combustion characteristics of DME/C_2H_4/N_2 co-flow flame mixtures using the CFD approach. Soot modelling validation and results for the different mixing conditions of DME/C_2H_4/N_2 co-flow flames will be presented and discussed in Chapter 6 (along with the

experimental soot emission results). Similar boundary conditions to those of the experimental study were applied in this computational study to develop a new validated CFD model tailored to DME, which is currently missing and unknown.

4.2 Flame Cases

The flame cases investigated in this chapter are similar to those in Table 2-1 (Chapter 2). The description of the experimental setup was mentioned in Section 2.3.2.1. The co-flow burner used in this work for collecting chemiluminescence measurements had a similar structure to the Yale co-flow burner [170].

Different conditions of DME/C_2H_4/N_2 co-flow flame mixtures were tested in this study. The numerical simulation conditions are displayed in Table 4-1. In this work, the DME mixture ratio is introduced by the ratio of the DME in the fuel mixture. In contrast, the fuel mixture ratio without including nitrogen (N_2) is introduced by α (ratio of the fuel in the mixture). The oxidizer mixture (21% O_2 and 79% N_2) was kept constant throughout all cases.

Table 4-1 The numerical simulation conditions.

Case	DME Mixing Ratio	C_2H_4 Mixing Ratio	N_2 Mixing Ratio
Case1 (same as F12)	0	0.6	0.4
Case2	0.15	0.45	0.4
Case3	0.25	0.35	0.4
Case4 (same as F13)	0.3	0.3	0.4

4.3 Results and Discussion

The direct and Inverse Abel Transform (IAT) images of OH*, CH*, and C_2* chemiluminescence results of all mixtures are presented and discussed. Direct images were used to discuss the appearance of flames in terms of shape and colour as an indication of soot formation, whereas HRR and soot concentrations were approximated through IAT chemiluminescence images.

The following subsections start with the experimental results discussing the impact of DME addition to the methane and ethylene (Section 4.3.1), followed by the correlation between the OH* and CH* chemiluminescence ratios and the equivalence ratio (ϕ) (Section 4.3.2). After that, CFD model validation and results are presented and discussed (Section 4.3.3).

4.3.1 DME Mixtures with Methane (CH_4) and Ethylene (C_2H_4)

4.3.1.1 DME/Methane (CH_4) Mixtures

Results for DME/CH_4-air flames (F1-F5) are shown in Fig.4-1. The direct images demonstrate an axisymmetric and stable flame for all conditions. The soot radiation intensity in the direct images signifies the relative soot concentration in flames. It is clearly visible from direct images in Fig. 4-1 that as the amount of DME is increasing in the mixture (F5 is purely DME), the intensity of soot radiation appearance in the flame becomes weaker, indicating reduced soot concentration, assuming the changes in flame temperatures are small. Nevertheless, the soot radiation appearance in F2 (β = 0.25) is stronger (more soot) than F1 (β = 0) and then starts to decrease as the DME mixture ratio increases beyond β = 0.25 in the fuel stream.

Figure 4-1 shows that the flame height (measured in this study as the axial distance from the fuel exit to the visible tip of the soot emissions from the direct image) increases when DME is introduced to the fuel stream. The flame becomes longer so that enough oxygen can reach the central axis of the flame and burn all of the fuel since DME takes more oxygen to burn stoichiometrically than methane does [205]. OH* and CH* IAT images are mostly showing intensities at a thin layer located in between the central jet and the co-flow air stream (reaction zone), confirming the validity of using OH* and CH* chemiluminescence as an HRR marker in non-premixed flames. The OH* emission intensity, shown in Fig. 4-1, shows a gradual decrease in intensity, thereby decrease in HRR for $\beta < 0.50$ and a rapid decrease for $\beta > 0.50$. CH* chemiluminescence images representing HRR, however, are prone to contamination by soot radiation in the laminar diffusion DME/CH_4-air flames investigated. Considering that HRR can be denoted by both CH* and OH* chemiluminescence images, then the blue-coloured signal shown at the tip of the flame in CH* images (marked by the yellow square in Fig. 4-1) is mostly indicating soot. This can be verified by comparing CH* and C_2* images since C_2* is primarily a result of soot radiative emission and does not represent the heat release rate for the DME/CH_4-air flames studied. C_2* chemiluminescence images show an increase in soot signal when adding a small quantity of DME of 25% (F2) to pure methane, and subsequently, the soot decreased as more DME was added. Note that the soot signal is a combined effect of soot concentration and soot temperature, according to Planck's law. The increased soot signal observed at 25% DME addition indicated by C_2* does conflict with the findings in Yoon's work [104], where a reduced soot concentration was found with DME addition compared with

pure methane flame. The measurement of soot concentrations by the two-colour pyrometry of the F1 to F4 flame will be discussed further in Chapter 6.

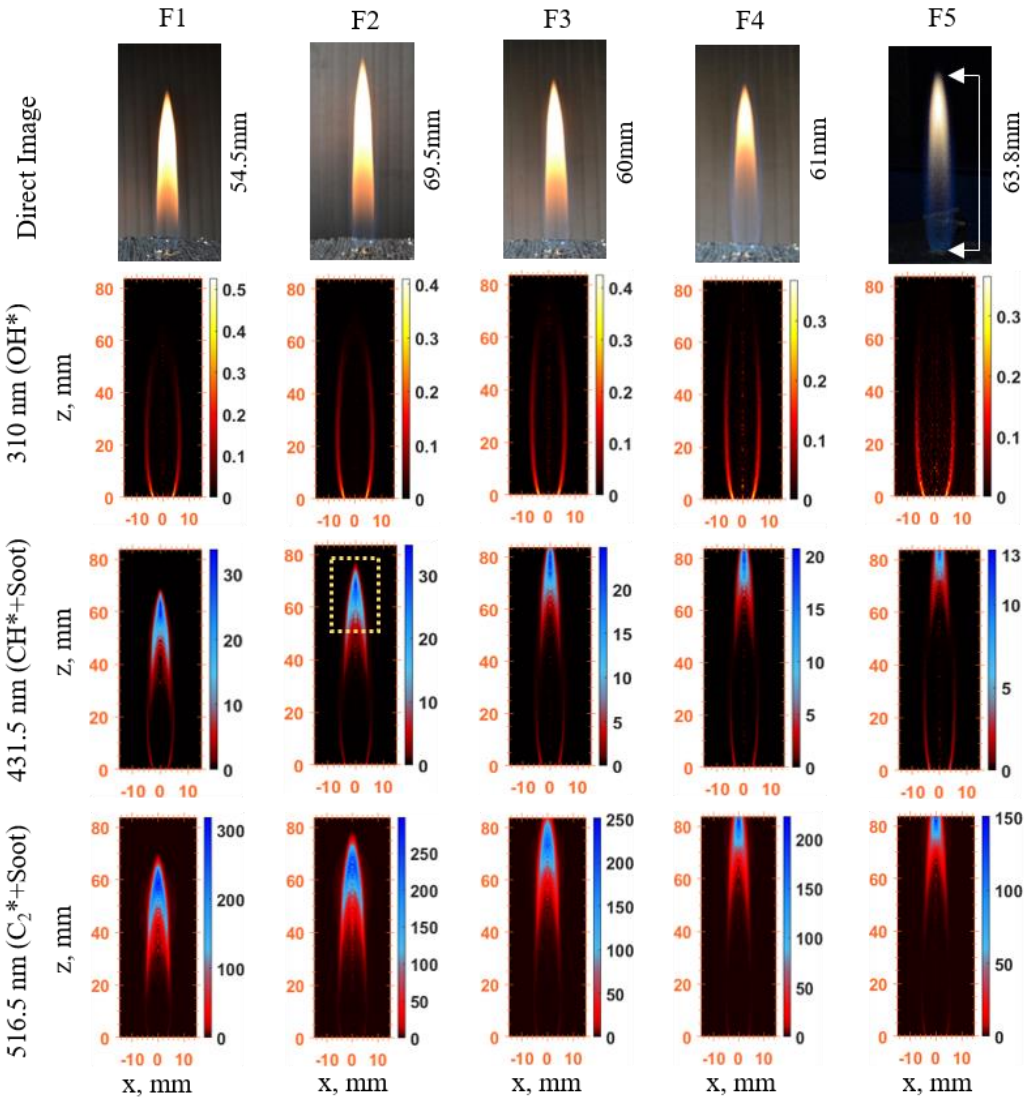

Figure 4-1 CH*, OH* and C2* chemiluminescence, and direct images results of DME/CH4 mixtures: flame structure and prediction of soot and HRR. (F1) β = 0, (F2) β = 0.25, (F3) β = 0.50, (F4) β = 0.75, (F5) β = 1.

The soot signal in some CH* chemiluminescence images potentially still exists with DME added flames. However, it is still important to study the characteristics of CH* as it provides an alternative endoscopic in-cylinder measurement potentially for HRR and soot when UV based OH* measurements are not feasible due to the optical transmission limitation. In addition, when both OH* and CH* measurements are conducted, the measurements could provide equivalence ratio information (to be discussed in Section 4.3.2). Thus, the CH* measurement is useful to interpret flame structures and for CFD comparisons.

4.3.1.2 DME/N_2 Mixture and CH_4/N_2 Mixture

Direct and IAT images of OH*, CH*, and C_2* chemiluminescence for DME/N_2 mixtures (F5 to F8) are shown in Fig. 4-2. The direct images, as well as in C_2* and CH*, indicate a clear drop in the intensity of soot radiation as the percentage of the dilution (N_2) increases in the fuel stream. With 75% N_2 addition (F8), there is no soot visible in the direct image, and the OH*, CH* and C_2* images overlap well with each other at this condition. The total intensities of OH* chemiluminescence images are shown to be decreased as more N_2 is added to the mixture (F6, F7, F8). This agrees with the power outputs indicated in Table 2-1 in Chapter 2.

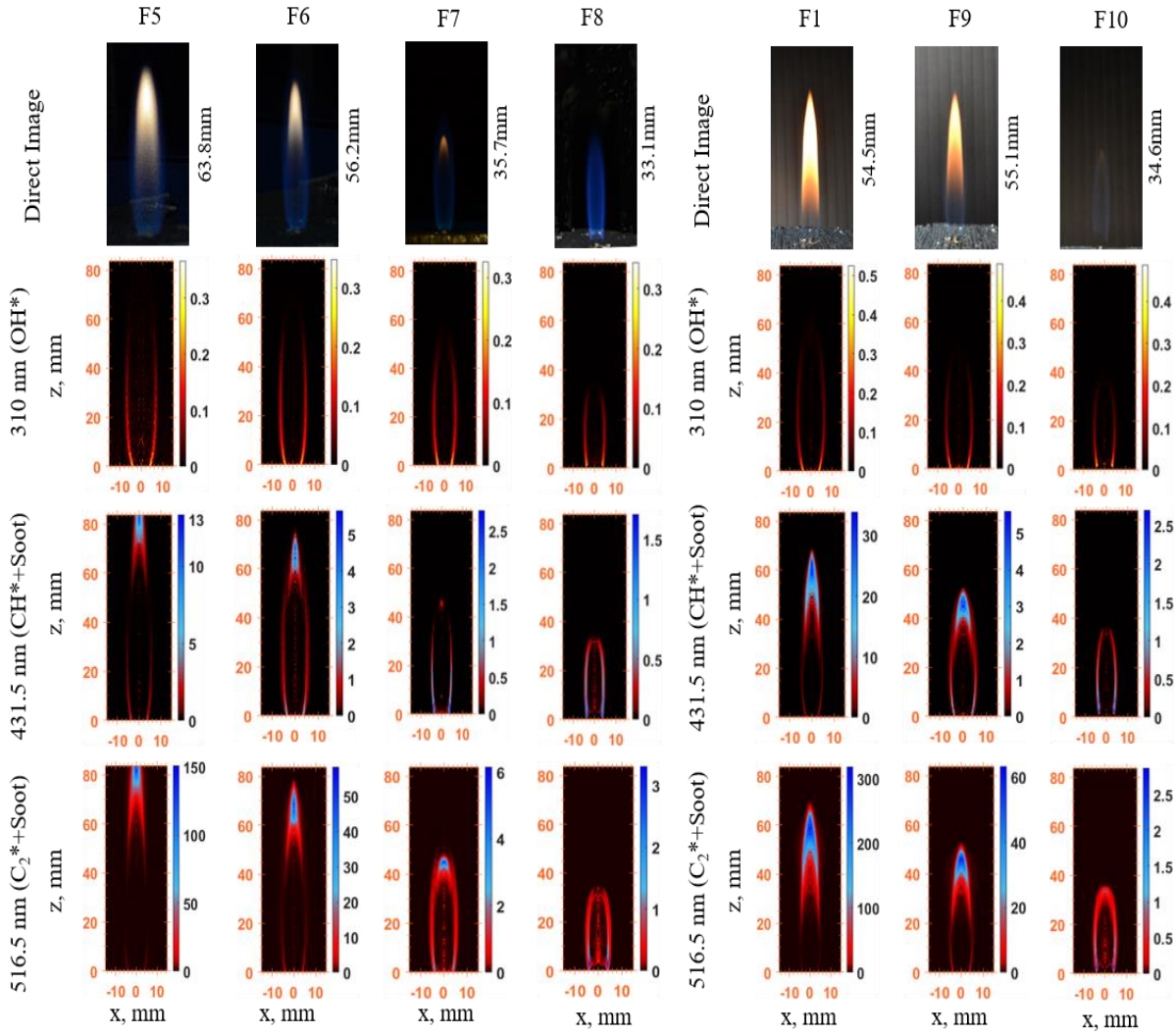

Figure 4-2 CH*, OH* and C2* chemiluminescence, and direct images results of DME/ N_2 mixtures (F5-F8) and CH4/N2 Mixture (F9-F10): flame structure and observation of soot and HRR. From left: (F5) α = 1, (F6) α = 0.75, (F7) α = 0.50, (F8) α = 0.25, (F1) α = 1, (F9) α = 0.75, (F7) α = 0.50, (F8) α = 0.25, (F1) α = 1, (F9) α = 0.75, (F10) α = 0.50. Symbol G refers to the gain setting: G1 = 10ms, G2 = 50ms and G3 = 200ms.

Similar to the DME/N_2 mixtures, the flame height is found to reduce as more N_2 is added to CH_4, as shown in the direct images in Fig. 4-2 (F1, F9, F10). The addition of N_2 as a diluent

decreases the power output of the mixture significantly, as shown in Table 2-1. In CH_4/N_2 mixtures (F9 to F10), the OH* chemiluminescence indicates that HRR is not affected substantially by the addition of N_2. Whereas the soot emission was drastically decreased when adding N_2 to 50%, as shown in C_2* chemiluminescence images (F10) in Fig. 4-2. As seen and mentioned in Chapter 3, adding N_2 lowers the flame temperature. Hence it hence reduces the concentration of reactants in the flame because it does not contribute to the combustion reaction, which reduces the HRR. As mentioned in the literature review in Chapter 1, soot tends to produce more at high temperatures, in which the pyrolysis reactions occur much faster due to high flame temperature. Therefore, the decrease in flame temperature reduces the pyrolysis reactions and soot production.

4.3.1.3 Constant Power Output

DME/methane mixture tests were repeated with a constant power output of 0.195 kW (identical to the pure methane case, F1) and a fixed volumetric flow rate of 356.6 SCCM for flames F14 to F17 (as shown in Table 2-1), by adding nitrogen N_2 as a diluent. Fig. 4-3A shows the direct and IAT images of OH*, CH* and C_2* chemiluminescence results. Similar to the previous cases discussed, OH* chemiluminescence is mainly located at the edges of the flame potential core region (near the nozzle exit) and then gradually started stretching towards the edge of the flame centre region as DME and N_2 mixture ratios increased. The CH* and C_2* chemiluminescence images clearly show a reduction in soot signal as the DME and N_2 mixture ratios increase.

Numerically (following a similar methodology to Chapter 3), the trend of the normalised peak values (by F1, Table 3-3 in Chapter 3) for the equal power output cases (Fig. 4-3B) are similar to the DME/CH_4 flames (F1-F5, in Fig. 3-2A in Chapter 3). A reduction is seen in the species' peak concentrations apart from OH and temperature, which remained unchanged. The OH* and CH* are positively correlated with the HRR. Apart from the peak values, species' profiles and integral areas of which are similar to each other. Figure 4-3C shows an example of the relative position of the investigated species (F14). As more DME and N_2 are introduced, more species profiles are shifted towards the lean side of the stoichiometric line (ξ_{st} is 0.054, 0.082, 0.103, 0.120, and 0.133 for F1, F14 to F17, respectively). This is mostly caused by the addition of N_2, which reduces the concentration of reactants (fuel) and hence reduces the species concentration on the fuel-rich side.

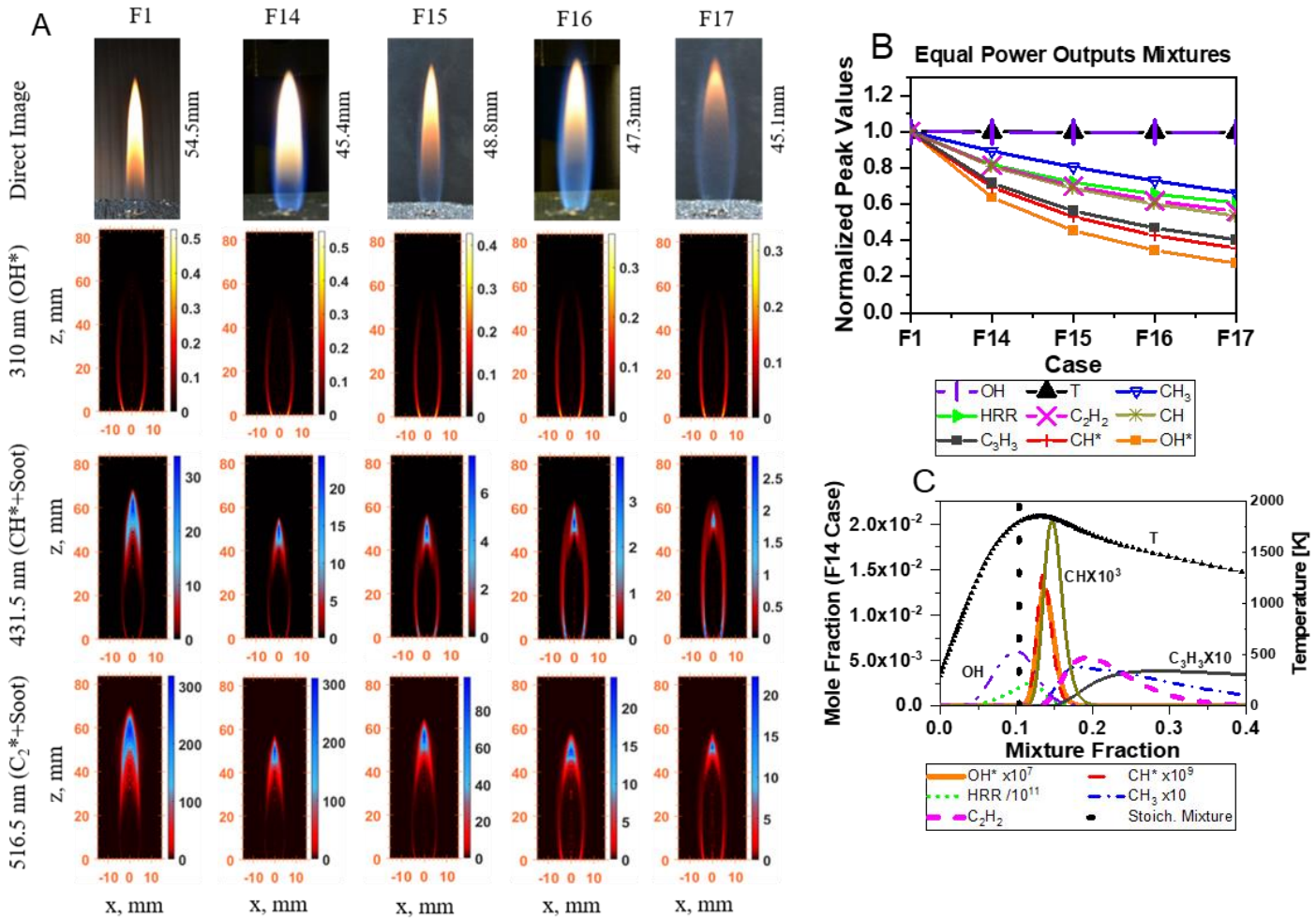

Figure 4-3 Flame structure, and prediction of soot and HRR of the equal power output of DME/CH_4/N_2 mixture. (A) direct image, CH*, OH* and C2* chemiluminescence, (F1) α = 1, (F14) α = 0.85, (F15) α = 0.75, (F16) α = 0.70, (F17) α = 0.60, (B) Simulation results – normalised peak values, and C) profiles of main species, case F14.

4.3.1.4 DME/C_2H_4/N_2 Mixtures

This subsection discusses the results for the two equal power cases (F12, F13, flow conditions refer to Table 2-1) of DME/C_2H_4/N_2. The direct images show a slight increase in the flame height when DME is added to the C_2H_4/N_2 mixture (F12) due to an increase in the mixture's molar mass (Figure. 4-4). Similar to DME/CH_4 mixtures, the OH* chemiluminescence indicated a decrease in HRR when DME was added (F13) to the C_2H_4/N_2 mixture. Furthermore, CH* and C_2* chemiluminescence images show a lower soot signal in F13 than in F12. This means that DME addition (at 50%) to ethylene reduces the soot concentration, in agreement with Yoon et al. [104], Liu et al. [23], Sirignano et al. [112], and Choi et al. [117]. The amount of N_2 remains unchanged in the F13 case. Therefore it is more likely that the addition of DME caused the decrease in the heat release rate. The addition of DME to C_2H_4 counter flow flame resulted in reducing the peak values of OH (see Figure 3-6 in Chapter 3). The OH is known to be an essential component in the process of producing larger hydrocarbons. Hence, the reduction in OH concentration leads to a reduction in the formation of hydrocarbons, thus lowering the HRR.

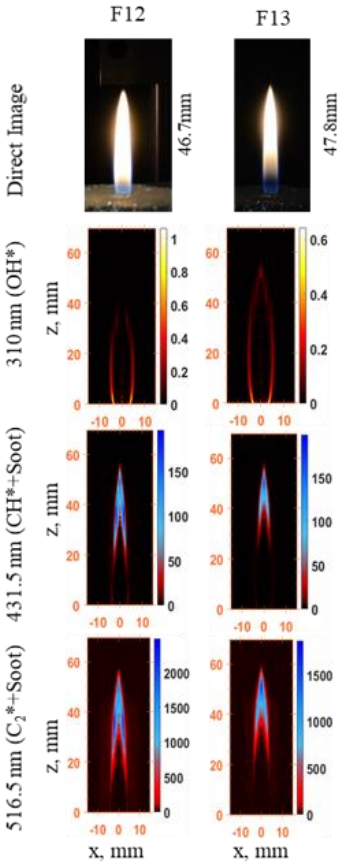

Figure 4-4 DME/C_2H_4/N_2 mixture direct images and chemiluminescence images of F12 and F13.

4.3.2 Chemiluminescence ratios and equivalence ratios

This section investigated the correlation among the OH* and CH* chemiluminescence ratios and the equivalence ratio (ϕ) in the non-premixed flames of methane and ethylene with DME addition. The results were compared to the chemiluminescence measurement to investigate the suitability as an equivalence ratios marker via the OH* and CH* chemiluminescence ratios measurements in non-premixed flames. It has been found from simulations that the OH*/ CH* ratio peaks only once against ϕ in the cases with DME absent in the mixture. Whereas in most cases studied in this work with DME present, a second peak forms at around an equivalence ratio of about 6 to 12, as shown in Fig. 4-5A. This makes it challenging to use the OH*/CH* ratio to correlate ϕ for the DME cases because it is not performing an ideal monotonic function of ϕ. It is still unknown whether strain rates affect the OH*/CH* ratios in non-premixed flames. Using other chemiluminescence spectral band ratios such as CH*/C_2* to correlate ϕ would be interesting to investigate numerically. However, it will be difficult to conduct experimentally due to the high soot radiation in non-premixed flames, which could affect the measurement of CH*/C_2* ratios.

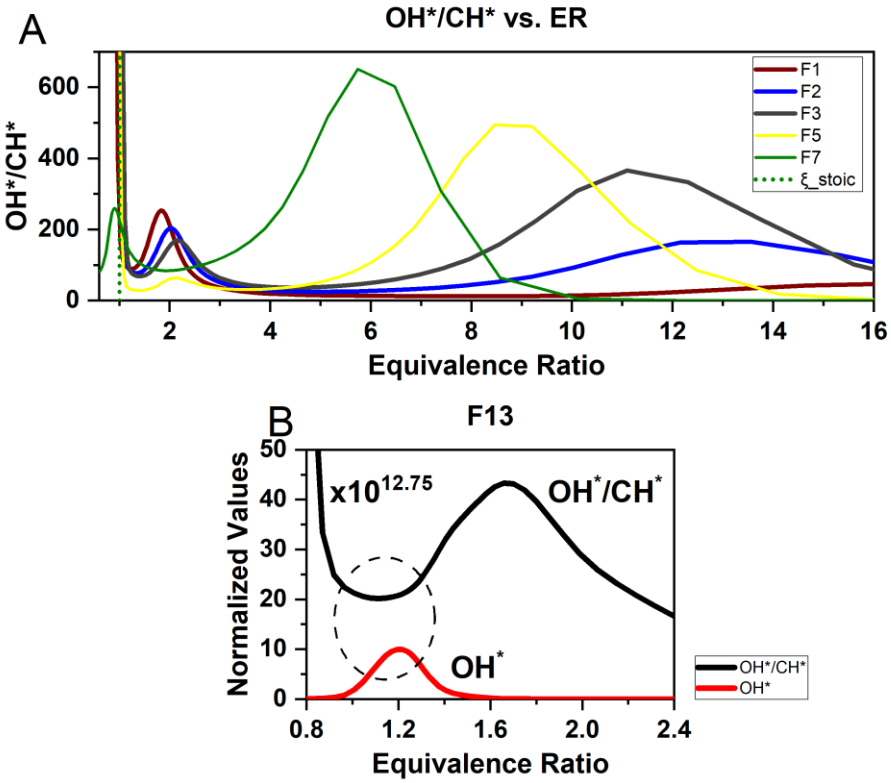

Figure 4-5 1D simulations of A) OH*/CH* chemiluminescence ratios vs. equivalence ratio and B) normalized values of OH* and OH*/CH* for F13 case.

Although the OH*/CH* alone is not feasible to correlate ϕ in non-premixed flames with DME, a combined approach utilising OH* behaviours together with the ratios can be useful. In all simulation results, only a single peak in the OH* profile has been shown for each case aligning closely to the stoichiometric line. This suggests that mapping numerical to experimental results for OH*/CH* ratios conditional to the OH* profiles could provide useful information on the ϕ values. Take the DME/C_2H_4/N_2 case F13 as an example; Fig. 4-5B shows that OH* and OH*/CH* ratio profiles have an opposite trend (circled) near ϕ = 1.2, where the OH* single peak is located (F13). This means that if the chemiluminescence experimental results for OH* and OH*/CH* follow a similar trend to the simulation results, then a limited range of ϕ can be mapped from the numerical results.

Figures 4-6 and 4-7 show the experimentally obtained OH*/CH* and OH*/C_2* ratios images (in log values) of F12 (Fig. 4-6) and F13 (Fig. 4-7) and the line profiles of the ratios and the OH* (a.u.) at several locations above the burner exit. A single peak for OH* at low height (8 mm) is overall obtained in both cases, agreeing with the numerical results; however, at higher heights (i.e. 40 mm for F13), an additional second peak for OH* is observed. The formation of a second peak could be attributed to the existence of a second reaction zone at higher heights in the flame. At a low height (8 mm in F13), OH* and OH*/CH* ratio profiles have an opposite trend (i.e., at about a radius of 4 -5 mm, where it shows an increase in OH*, and a decrease in the OH*/CH* ratio as approaching to the centerline), in agreement with the numerical results. This suggests that at a radial position of about 4 mm in F13, ϕ is equal to 1.2 in accordance with Fig. 4-7. In Fig. 3-6B, Chapter 3 (F12 case), the peak of OH* is aligned with the stoichiometric line, and when DME is added to the mixture in Fig. 3-6D, Chapter 3 (F13 case), the position of OH* was shifted towards the rich side of the stoichiometric line and the OH* signal almost cut-off at the stoichiometric line (corresponding to a radial position of 5 mm in F13, Fig. 4-7). This provides a limited mapping for the ϕ measurements in the lower heights of the non-premixed DME flames from the combined OH* and OH*/CH* ratio images.

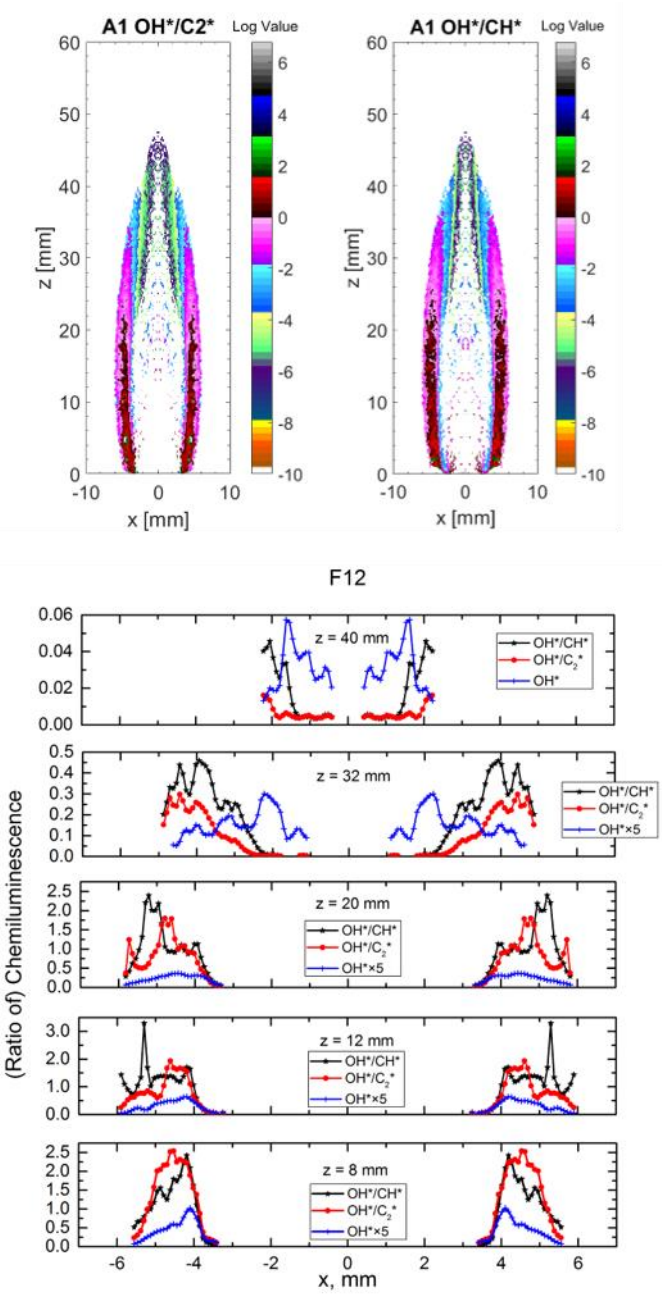

Figure 4-6 OH*,OH*/CH* and OH*/C_2* ratios of experimental results in the F12 at axial locations of 8, 12, 20, 32 and 40 mm above the burner.

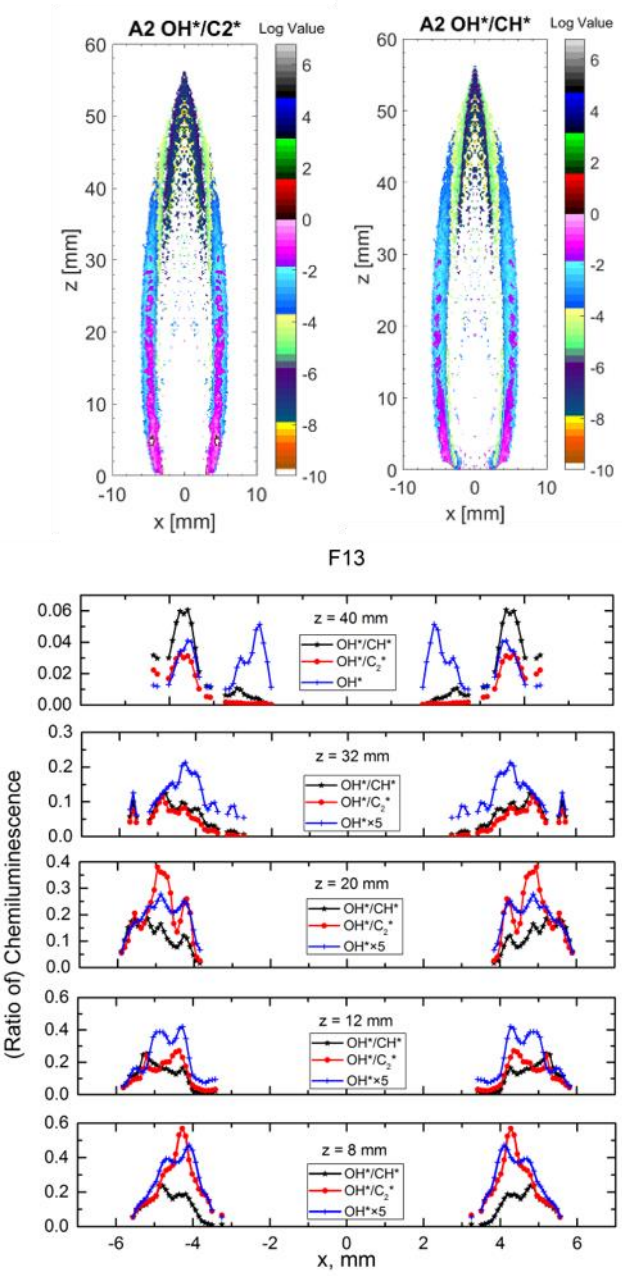

Figure 4-7 OH*, OH*/CH* and OH*/C_2* ratios of experimental results in the F13 at axial locations of 8, 12, 20, 32 and 40 mm above the burner.

4.3.3 Computational Fluid Dynamics Results & Discussions

4.3.3.1 Mesh Independence

A sensitivity analysis was performed on a case with similar boundary conditions as the other cases shown in Table 4-1 but with a fuel mixture inlet of 32% C_2H_4 and 68% N_2 to confirm the grid's independence. This flame mixture was computed for validation purposes. In the beginning, the model contained 9,000 elements. This number was increased by increasing the number of divisions at each surface (including inlet, outlet, axes, and wall surfaces) and then re-meshing the body surface. Five different meshes containing 9,000, 36,000, 81,000, 110250, and 144,000 elements were created for the sensitivity test. The temperature profiles along the axis (centreline) of the flame for all the meshes are shown in Figure 4-8. All the temperature profiles were found to follow the same trend and peak location but with very small variations. The differences between the temperature profiles are very small which makes it hard to assess the convergence. Therefore, the maximum temperatures of all profiles shown in Figure 4-8 are plotted against the element size (see Figure 4-9) to assess the convergence criteria. In addition, the percentage difference in the centreline peak temperatures was calculated for each mesh to find when the grid independence was accomplished, as shown in Table 4-2.

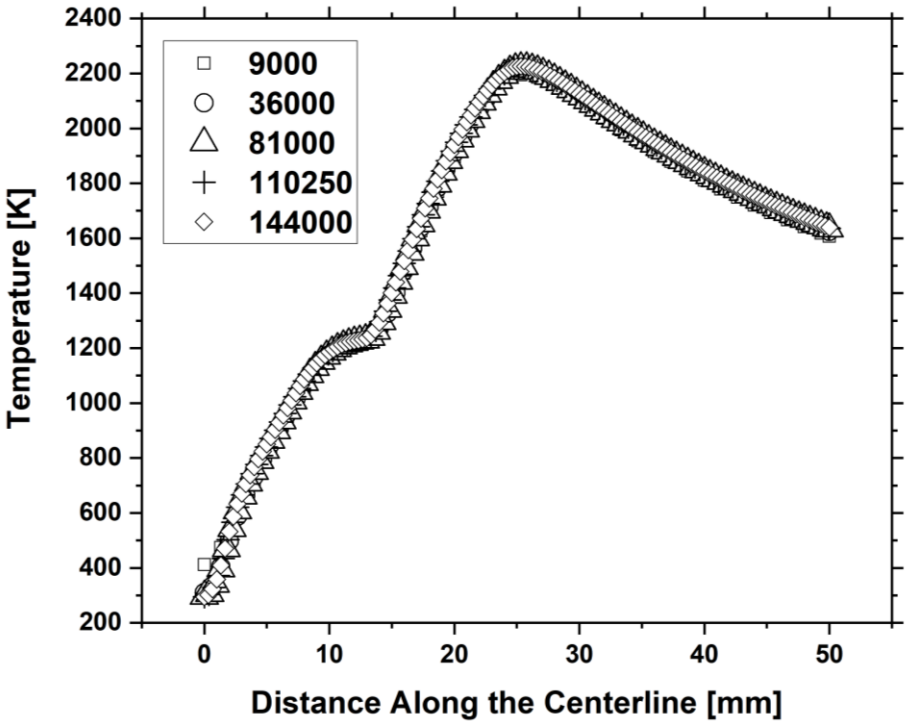

Figure 4-8 Temperature profiles along the centreline for five different meshes containing 9,000, 36,000, 81,000, 110250, and 144,000 number of elements.

Each percentage in Table 4-2 represents the difference between two meshes. For example, the percentage difference between the peak temperature values along the centreline computed from mesh 1 and mesh 2 is 0.85%, and between mesh 2 and mesh 3 is 0.31%. The results in Table 4-2 reveal that the percentage difference decreases as the number of elements increases. This is also reflected in Figure 4-9, where the convergence between the peak temperature values becomes very clear after the 36,000 (mesh 2) number of elements. The percentage difference between mesh 2 and mesh 5 (finest among the five meshes) in peak temperature value is about 0.5%. Due to the slight percentage difference between the use of the meshes 2 and 5, the convergence criteria are considered to have been met using 36,000 elements. In addition, using mesh 2 (36,000 elements) costs less computational expense than using mesh 5. Hence, mesh 2 was used for all simulations in this study to obtain high-accuracy results with less expensive computational time.

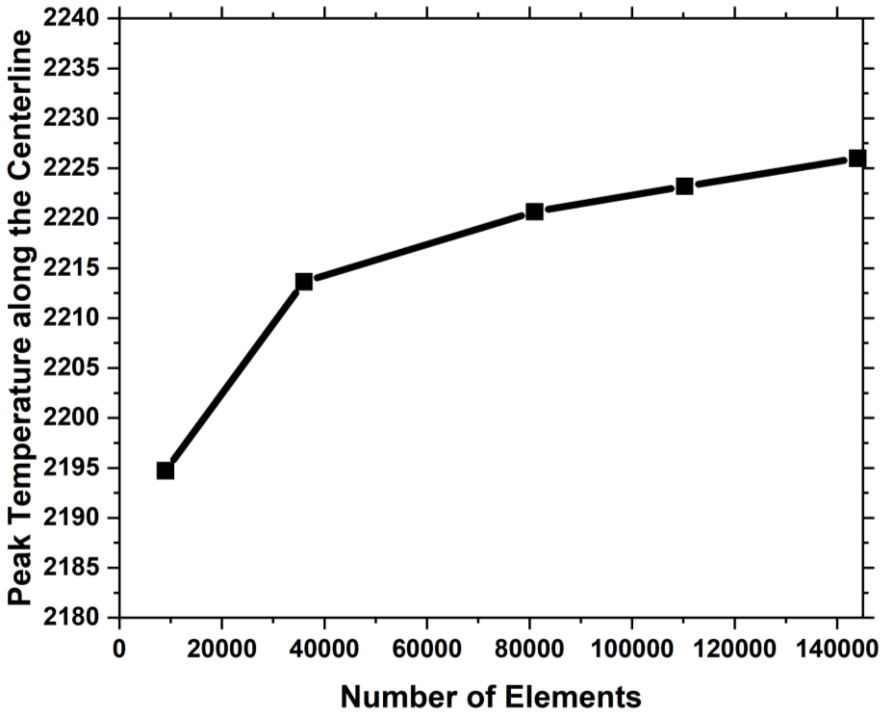

Figure 4-9 Peak temperatures along the centreline against the element size.

Table 4-2 Percentage difference in the centerline peak temperatures between the five different meshes.

	Number of Elements	Percentage Difference (%)
Mesh 1	9,000	-
Mesh 2	36,000	0.85
Mesh 3	81,000	0.31
Mesh 4	110,250	0.11
Mesh 5	144,000	0.12

4.3.3.2 Model Validation

To assess the accuracy of the current computational laminar diffusion flame model, a comparison between the temperature profiles produced from this study and the experimental and computational results of McEnally et al. [203] was carried out at different heights above the nozzle (axial height), as depicted in Figure 4-10. The comparison presented in Figure 4-10 is on the flame mixture of 32% C_2H_4 and 68% N_2. The experimental and model configuration of McEnally et al. [203] is similar to the one used in the study (Yale co-flow burner [170]). The comparison was carried out at axial heights of 5 mm and 25 mm. The temperature computations of the current model and thermocouple measurements [203] demonstrate a very good agreement at both flame heights. At 5 mm axial height, the peak temperature of the current model is higher by about 2.7% than the thermocouple peak temperature of McEnally et al. [203]. This is lower than the percentage difference between McEnally et al. [203] thermocouple and computational peak temperatures, in which their computed peak temperature is higher by about 3.3% than their thermocouple peak temperature. At 25 mm axial height, the temperature profile of the current model is a little higher than the profile obtained by the thermocouple [203], where the percentage difference between peak temperatures is about 5%. However, the current model temperature profile follows a similar trend to the thermocouple at 25 mm axial height.

A qualitative comparison of the OH* signal obtained from the experimental work and the OH* from the model for the F13 case is shown in Figure 4-11. The OH* model results are in good agreement with the experimental results. Both offer similar signal distribution at the reaction zone. The signal shown along the centreline of the flame in the experimental image is a noise resulting from the IAT processing. The computational result also agrees with the experimental result regarding height, in which both images showed a height of about 50 mm for the OH* signal.

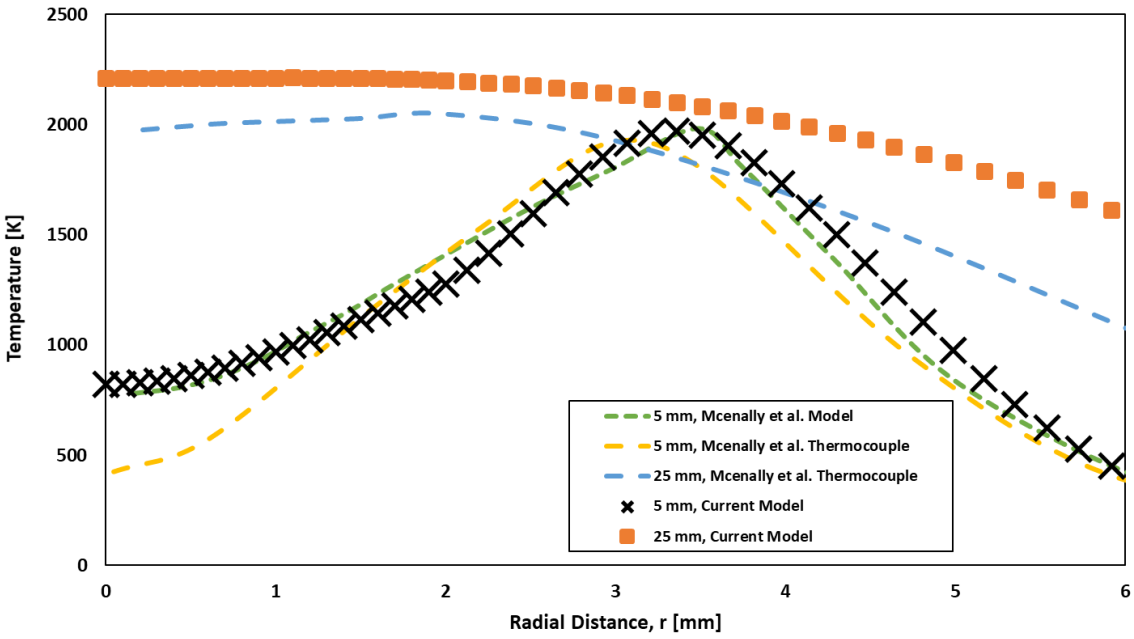

Figure 4-10 Comparison between the current model results and Mcenally et al. [203] results of temperature profiles at various axial heights.

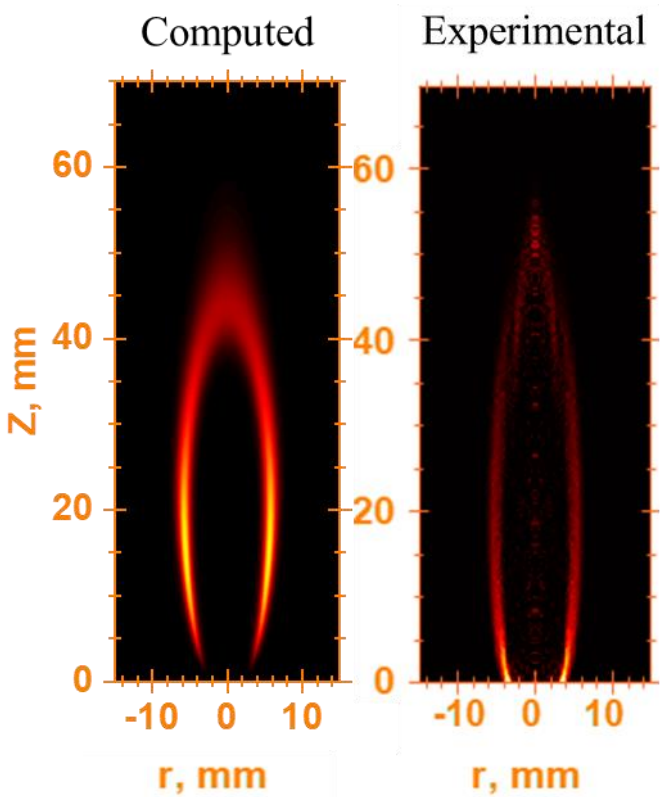

Figure 4-11 A qualitative comparison between the experimental and computational results on the OH* signal.

4.3.3.3 Temperature Distribution

The computed temperature distribution across the DME/C_2H_4/N_2 flames is shown in Figure 4-12. In the pure ethylene case with N_2 diluent (60% C_2H_4, Case 1), the peak temperature is 2326 K and this occurs in the low middle (annular) region parallel to the edge of the fuel nozzle and air co-flow of the flame at about Z=10 mm and r=4 mm. After that, as the flame travels further in the axial direction (Z), the temperature decreases. As DME fuel is introduced to the mixture (Case 2, Case 3, and Case 4), the peak temperature drops to 2268 K in Case 4. The location where the peak temperature takes place has moved further to the lower region of the flame as more DME was added to the mixture. The decrease in flame temperature when DME was added is expected because it has been reported previously that the adiabatic flame temperature of DME is less than C_2H_4. The findings of temperature distribution are in good agreement with the results of Liu et al. [23].

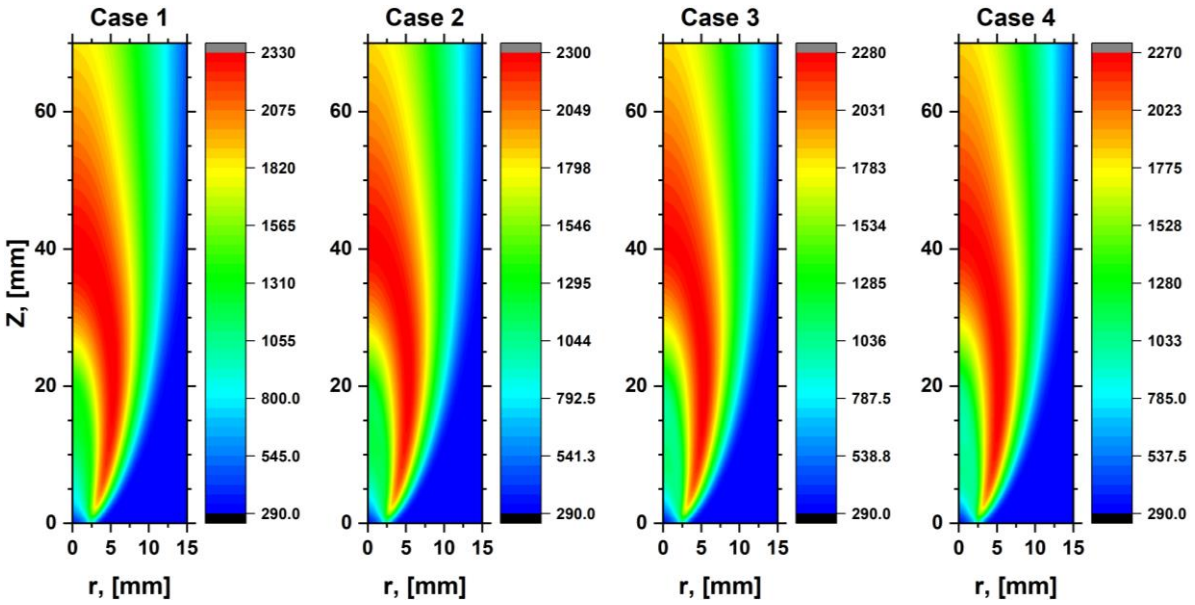

Figure 4-12 The computed temperature distribution across the DME/C_2H_4/N_2 flames.

4.4 Conclusion

The work carried out in this chapter mainly focused on studying the impact of DME addition to methane and ethylene fuels experimentally, across a full range of DME mixing ratios, on flame heat release and reaction zone using CH*, OH*, and C_2* chemiluminescence. Moreover, the ratios of the chemiluminescence pairs (OH*/CH*, OH*/C_2*) were studied on the feasibility of mapping local equivalence ratios. In addition, a CFD analysis was done to measure fluid behaviour, such as the temperature of fluids when mixed. The key conclusions from this chapter are as follows:

1- The soot radiation appearance in C_2* chemiluminescence for methane flames became initially stronger with a small addition of DME (25%). However, when the DME mixture ratio was increased by more than 25%, the soot radiation appearance became weaker, indicating either less soot concentration or reduced soot temperature.
2- The flame height was found to reduce as more N_2 is added to CH_4 or DME flames. In addition, a clear drop in the intensity of soot radiation was shown as the percentage of the dilution (N_2) increased in the fuel stream.
3- Equal power output cases displayed a reduction in OH* signal (HRR) and soot as more DME and N_2 are added simultaneously to the methane and ethylene flames, agreeing with the numerical results presented in Figure 4-3.
4- In the DME cases, the OH*/CH* ratio does not perform an ideal monotonic function of equivalence ratio.
5- Mapping numerical to experimental results for OH*/CH* ratios conditional to the OH* profiles could provide useful information on the equivalence ratio values.
6- The CFD results showed that adding DME to the C_2H_4/N_2 flame decreases the peak temperature of the flame.

Chapter 5: Reaction zone characteristics of turbulent swirl spray flames of iso-pentanol and ethanol blends with n-heptane using PLIF and OH* chemiluminescence

5.1 Introduction

This Chapter discusses the reaction zone and stability characteristics of swirl spray flames of iso-pentanol and blends. As mentioned earlier, iso-pentanol is an oxygenated alcoholic fuel, which could potentially reduce emissions, especially NO_x and soot. Iso-pentanol/kerosene blends have been found to increase thermal efficiency and decrease CO and unburned hydrocarbon emissions at high loads in an aircraft compression ignition (CI) engine [206]. Therefore, iso-pentanol (if bio-derived) can be used as a carbon-neutral fuel to decarbonize the transport sector, such as aviation or marine.

Flame lift-off and local extinction are important features to investigate and study as they help understand the flame stabilization and dynamics of liquid fuel combustion. Few studies have investigated the lift-off and local extinction characteristics of liquid fuels in swirl spray

burners, as discussed in Chapter 1. Also there needs to be more studies on the flame lift-off and local extinction of iso-pentanol fuel in a bluff-body swirl spray flame. Therefore, this chapter concentrates on how iso-pentanol (the low-carbon alternative) would affect the flame structure, including lift-off and local extinction.

The OH planar laser induced fluorescence (PLIF) measurements were used to study the lift-off and local extinction features. Fuels used in this study were n-heptane, iso-pentanol, ethanol and blends of n-heptane/iso-pentanol and n-heptane/ethanol. Different operating conditions were tested and categorized into three flame types, including stable, near blow-off, and far away from blow-off. Far away from blow-off conditions are also stable conditions but with lower fuel and air flow rates than the others.

NO-PLIF measurements were also used to study the relative NO concentrations in the turbulent swirl spray flames. In addition, the impact of swirl number on NO emissions of iso-pentanol swirl spray flames has been investigated.

The main objectives of this chapter are to deliver new information on how the addition of iso-pentanol to n-heptane swirl spray flame would affect the heat release, flame structure, and flame stabilization, including lift-off and local extinction at different operating conditions. In addition, to compare and show the variations between the swirl spray flames of iso-pentanol/n-heptane blends and ethanol/ n-heptane blends. Additionally, to study the relative NO concentration in the swirl spray flames.

5.2 Flow Conditions

Liquid fuels including pure iso-pentanol, n-heptane, ethanol, a 50:50 volume ratio mixture of iso-pentanol/ n-heptane, and a 50:50 volume ratio mixture of ethanol/n-heptane were used in this study. Fuel mass flow rates were in the range of 0.50 - 0.54 g/s. The investigations were mostly carried out on those conditions with a fuel mass flow rate of 0.52 g/s for stable and near blow-off events. Moving from stable to near blow-off condition was achieved by increasing the air flow rate. A lower fuel mass flow rate of 0.506 g/s was applied to study the soot signal in iso-pentanol, n-heptane, and blended flames. The air flow was supplied by an air compressor (SXC 4), which was controlled using an Alicat mass flow controller (calibrated). The air flow

went through a swirl (6-vanes) before it entered the combustion chamber. Air volumetric flow rates were in the range of 350 - 950 SLPM, which corresponded to an air velocity between 10.6 and 28.4 m/s.

The flow conditions and fuel properties are shown in Table 2-2 in Chapter 2. The non-dimensional parameters shown in Table 2-2 were calculated using different equations, all shown in Table 2-3 in Chapter 2 [150]. S denotes the stable conditions, NB as conditions nearer to blow-off. Table 2-2 showed a number of key parameters that are essential for describing the atomization process to account for the variation in the atomization process caused by changing the liquid fuel and the flow rate. The surface tension and viscosity of the mixture are calculated using the linear function and Grunberg-Nissan [207], [208] mixing rule separately. The physical properties shown in Table 2-2 are useful when analysing the combustion characteristics. For example, in the atomization process, surface tension, viscosity, and density are crucial factors in understanding the behavior of fuel spray [209], [210]. The physical properties of the air and liquid fuels shown in Table 2-2 were calculated at a temperature of 20℃. The non-dimensional value of the Weber number changes from one place to another. Therefore, it is worth noting that all values presented in Table 2-2 were evaluated at the exit of the fuel nozzle. The Weber number is beneficial when analyzing the flow fields and the droplet break-ups.

NO-PLIF measurements in this study are only for HS1, HNB, HPS1, HPNB, PS1, and PNB cases. The impact of swirl number on NO emissions is only studied on pure iso-pentanol flame (PS1 case).

5.3 Results and Discussion

This section displays results on the heat release, flame structure, and flame stabilization including, lift-off and local extinction at different conditions: stable, near blow-off, and far away from blow-off. Initially, the limit of stability for pure n-heptane, pure iso-pentanol, and 50:50 iso-pentanol/ n-heptane mixture is revealed in Section 5.3.1. After that, the bluff swirl spray flame appearance is shown for selected fuel mixtures in Section 5.3.2. The OH* chemiluminescence is then presented in Section 5.3.3. The fuel-PLIF and OH-PLIF are discussed in section 5.3.4. Lift-off and local extinction are analysed in Section 5.3.5. Finally,

NO-PLIF measurements in n-heptane, iso-pentanol/ n-heptane, and pure iso-pentanol swirl spray flames and the impact of swirl number on the NO emissions of iso-pentanol swirl spray flames are presented in Section 5.3.6.

5.3.1 Flame Quenching

Figure 5-1 shows the air flow velocities at global quenching against fuel mass flow rates for pure n-heptane, pure iso-pentanol, and 50:50 iso-pentanol/ n-heptane flame mixture. The flames should be stable at any air flow velocities under the lines shown in Figure 5-1. Pure n-heptane was found to quench at higher air flow velocities across various fuel mass flow rates than pure iso-pentanol and the mixed flame. At high fuel mass flow rates (>0.55 g/s), the difference between the quenching limits of pure n-heptane and pure iso-pentanol is smaller than at low fuel mass flow rates.

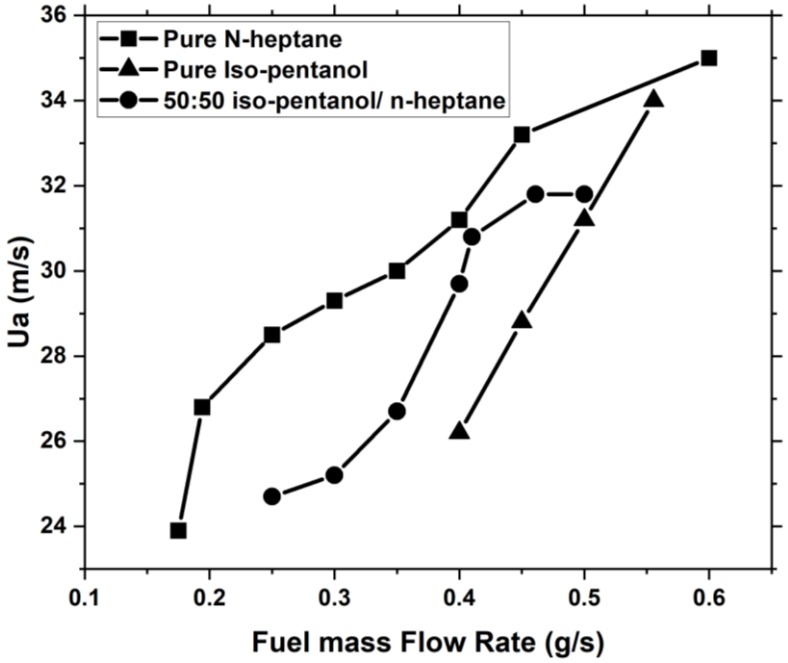

Figure 5-1 Air flow velocities at global quenching against fuel mass flow rates for pure n-heptane, pure iso-pentanol, and 50:50 iso-pentanol/ n-heptane flame mixture.

5.3.2 Flame appearance

Figure 5-2 shows direct images of swirl spray flames from left to right of iso-pentanol, ethanol, and n-heptane/ethanol blend. These flames had identical flow conditions in terms of air and

fuel mass flow rates. Most of the flames showed an open-up spray in a cone-like “V” shape. In addition, most of flames presented a clear double flame branched structure, formed along the outer shear layer above the edge of the bluff-body (outer region) and inside the V shape spray cone (inner region). The ethanol flame is blue-purple, whereas n-heptane/ ethanol mixture and iso-pentanol are yellow-blue flames. The yellow color is mostly located in the inner region of the flames and little in between the inner and outer regions of the flames. This yellow color in the flames could indicate soot. Nevertheless, more results and discussions on soot will be discussed later in Chapter 6. It can be observed in Fig. 5-2 that the iso-pentanol flame did not present a clear inner region of the flame structure. This is because the fuel is not as well atomized as the others.

The lift-off feature could be observed in the outer and inner regions of all flames, such as shown in n-heptane/ ethanol blend (Fig. 5-2). The lift-off height in the outer region from the bluff-body surface is different for each fuel. In the inner region, ethanol and its mixture with n-heptane showed a clear lift-off from the fuel nozzle. Hence, lift-off of all flames was analyzed and quantified using OH-PLIF measurements, which will be shown later in this chapter.

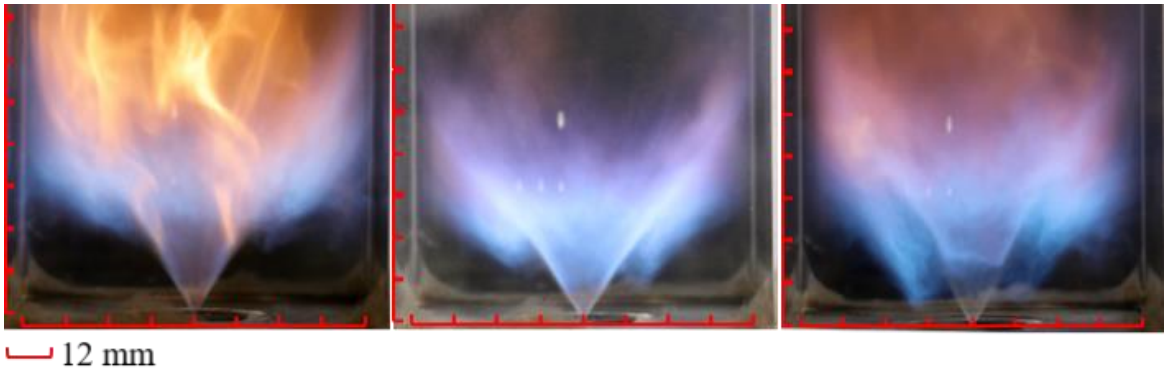

Figure 5-2 Flame images of solid-cone swirl spray flames of (left to right) iso-pentanol, ethanol, and n-heptane/ethanol blend.

Figure 5-3 displays direct images taken for the n-heptane and iso-pentanol/ n-heptane swirl spray flames at stable and near blow-off conditions. All images show that the n-heptane and iso-pentanol/ n-heptane fuels spray were atomized with a full-cone spray output profile of a 60° cone angle. The two distinct flame branches are seen on each of the flame cases. The outer flame branch is formed over the bluff-body edge, showing intermittent flame lift-off. The inner branch also starts at a distance from the fuel exit plane, especially for the heptane cases, where the spray cone is visible upstream of the inner flame branch. The images also present how the

heights of flames reduced as moving into near blow-off conditions. The ORZ became more attached in the near blow-off condition.

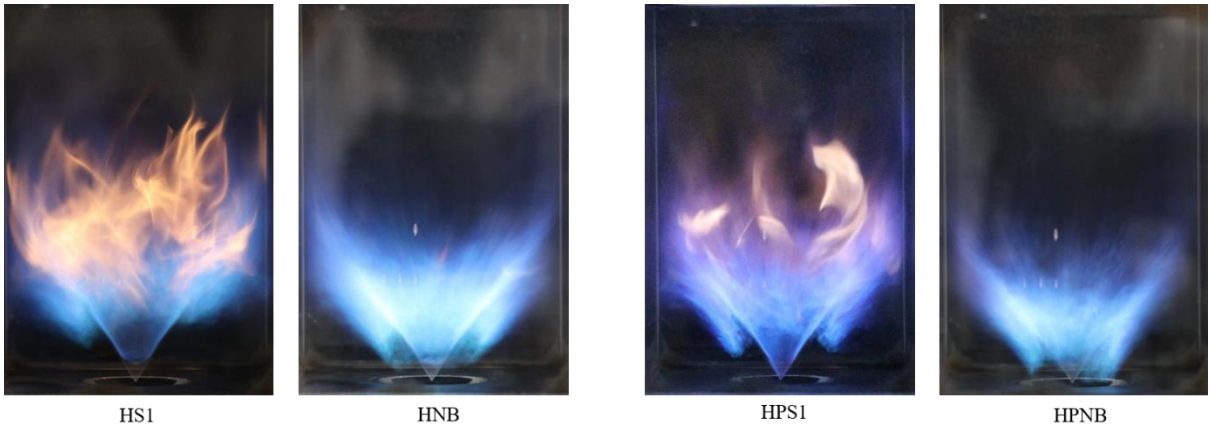

Figure 5-3 Flame images of solid-cone swirl spray flames of (left to right) HS1, HNB, HPS1, and HPNB flames. The flow conditions are shown Table 2-2 (Chapter 2).

5.3.3 OH* Chemiluminescence

OH* visualization is a good representative of heat release in flames, as mentioned in Chapter 1. This Chapter only presents the OH* results of n-heptane and iso-pentanol stable flames. Mean OH* chemiluminescence images of HS1, HPS1, and PS1 flames are shown in Figure 5-4. In almost all cases, the distribution of the OH* signal takes place at similar locations. Figure 5-4 shows that most of the OH* (heat release) is happening inside the inner recirculation zone (within the "V" like shape) and along the fuel trajectory at the "V" shape. The OH* signal was increased by adding iso-pentanol to n-heptane flame (HPS1), indicating a higher heat release rate than pure n-heptane flame (HS1). However, pure iso-pentanol (PS1) flame was found to have a lower OH* signal than HS1 and HPS1 flames. The peak OH* signal of HS1 flame is higher by about 37.7% than the pure iso-pentanol flame (PS1).

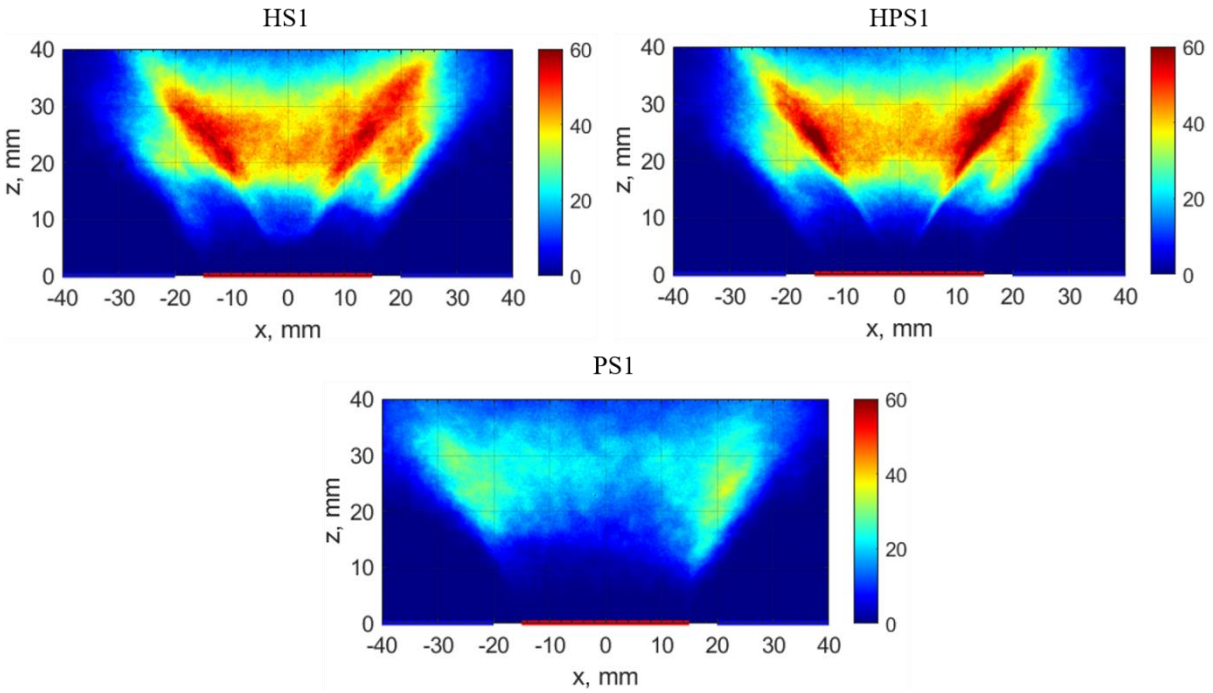

Figure 5-4 Mean OH* chemiluminescence images of HS1, HPS1, and PS1 flames.

5.3.4 PLIF signal at Q1(6) and its background B(Q)

In this sub-section, the instantaneous fuel-PLIF results are discussed firstly for all the fuels at stable conditions. The fuel-PLIF results reveal the trajectory and fuel spray droplets distribution. Then, the instantaneous and mean OH-PLIF results for all fuels at stable and near blow-off conditions are discussed. The OH-PLIF results are mainly used to evaluate each fuel's lift-off and local extinction.

5.3.4.1 Fuel-PLIF

The background signal of Q1(6), B(Q), provided the opportunity to measure the fuel-PLIF of all the cases. The measurement of the fuels fluorescence signal is important as it gives indications of the fuel spray distribution and trajectory. During the experiment, 200 images of Q1(6) and B(Q) were recorded for each of the cases. Figure 5-5 shows examples of instantaneous images of fuel-PLIF of the stable conditions of HS1, PS1, HPS1, ES1, and HES1. The red line shown along the x-axis is an indication of the bluff-body surface, and the region between the red and blue lines is where the annular air enters the chamber. The pure n-heptane (HS1) and ethanol (ES1) cases showed a clear V-shape (opened-up) atomization, where no

apparent fuel (liquid or vapor) was observed in the inner recirculation zone (IRZ), similar to fuel distributions observed in the hollow-cone spray flames [151]. Whereas the trajectory of pure iso-pentanol spray fuel has a narrower angle, distributing in a jet-like shape, where abundant fuel was seen in the downstream region of the spray cone inside the IRZ. This caused complexity in analyzing the OH signal in the inner region of pure iso-pentanol flames (PS1, PNB). The high viscosity of a liquid fuel can cause poor atomization and hence may rises carbon deposition [211]. Therefore, the lower efficiency of iso-pentanol fuel's breakup than n-heptane fuel can be attributed to the fact that iso-pentanol has a higher viscosity than n-heptane [212], as shown in Table 2-2 (Chapter 2). The addition of iso-pentanol to n-heptane (50:50) reduced the fuel mixture viscosity. Nevertheless, the mixture of iso-pentanol and n-heptane provided similar distribution of fuel trajectory to pure n-heptane case, although still has a higher viscosity than pure n-heptane. The density, surface tension and boiling point of the iso-pentanol are all higher than n-heptane of which can cause poor atomization [213]. In terms of the soot emissions released from the iso-pentanol combustion, this will be investigated in the following Chapter 6.

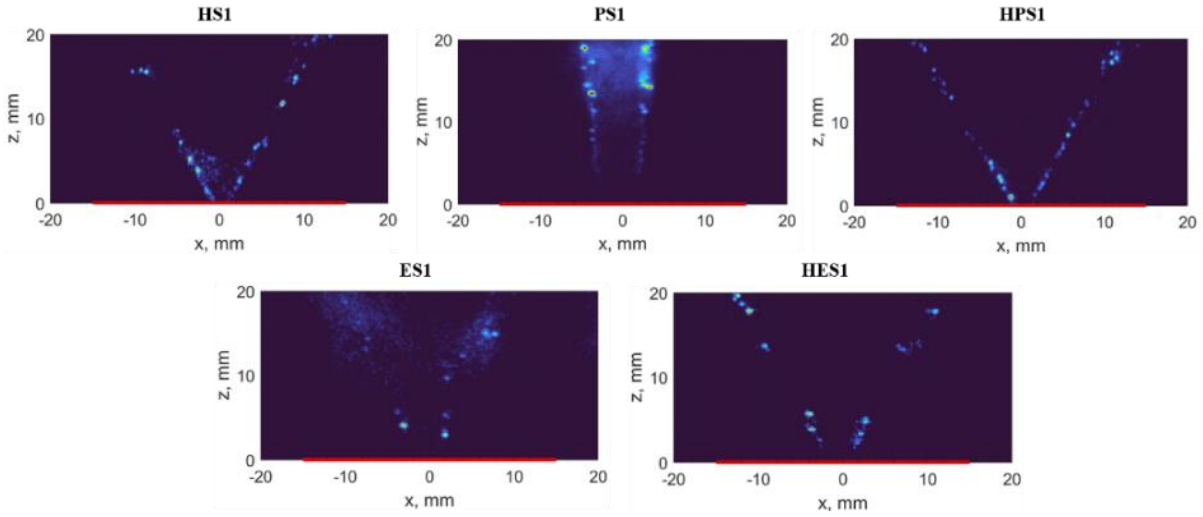

Figure 5-5 Instantaneous images of fuel-PLIF signal for HS1, PS1, HPS1, ES1, and HES1. Red line indicates the bluff-body.

5.3.4.2 OH-PLIF

Figure 5-6 displays the OH-PLIF images of the stable and near blow-off cases of n-heptane, iso-pentanol, and n-heptane/iso-pentanol mixture. The circles shown on the instantaneous images were drawn to indicate the local extinctions. The OH-PLIF images shown provide visualization of the flame sheet and its location in different flames. The double structures of

the flame sheets are shown in the OH-PLIF mean images in all the cases, in which the fuel spray is located in between them. The outer flame sheet of all conditions is observed to be wider near the blow-off event. Although the inner flame sheet of the iso-pentanol is absent in the cases studied due to the poor atomization compared with other fuels, but the outer region is similar in terms of size and location, as the other cases. The instantaneous OH-PLIF images of pure n-heptane (e.g. HS1 in Figure 5-6) and pure ethanol (e.g. ES1 in Figure 5-7) have almost no OH signal/ intensity near the fuel nozzle and bluff-body. This indicates that those flames exhibit a flame lift-off. In addition, OH-PLIF mean images of n-heptane and ethanol flames show that the inner flame sheet between the "V" shape is lifted in both stable and near blow-off conditions. However, the start of flame sheets in the outer region are closer to bluff-body at near blow-off conditions of all flames, as observed by the mean images in Fig. 5-6. The mean OH-PLIF images of the other cases (e.g. PS1, PNB, HPS1 and HPNB) have a very small OH signal/ intensity near the fuel nozzle and bluff-body, signifying intermittent lift-off occurring here.

The instantaneous images show that OH sheets of iso-pentanol flames (e.g. PS1 and PNB) in the outer region are thin and relatively continuous in comparison to n-heptane flames (e.g. HS1 and HNB). In addition, the OH sheets in the outer region of iso-pentanol flame (e.g. PS1) is more attached to the trajectory of the spray (cone angle shape), and less spreading into the recirculation zone (not curvy). The low volatility of iso-pentanol fuel most likely causing this behavior, which prevents the vapour of the fuel from penetrating to the recirculation zone [150]. OH-PLIF instantaneous images are used to study lift-off and local extinction features of all flames. It has been noticed that local extinction occurs more at near blow-off events in all cases because the OH containing regions are significantly fragmented and split apart. Whereas generally more of continues OH containing regions exist in most of the stable flame cases. Nevertheless, in between the snapshots recorded for each fuel, a very diverse range of behaviour is seen. For example, the playback of the snapshots displays that the breaks in the OH sheets can close and other new local extinctions can take place because of the turbulence level.

Figure 5-7 shows the instantaneous and mean OH-PLIF images of ethanol and ethanol/heptane cases: ES1, ENB, HES1, and HENB. The observations for ethanol here are very similar to the n-heptane ones shown in Fig. 5-6 in terms of flame sheet locations and

lift-off. The addition of ethanol to the n-heptane (e.g. HES1 & HENB cases) flame resulted in a narrower fuel spray angle as can be seen in the mean images in Fig 5-7. Whereas the addition of iso-pentanol to the n-heptane (e.g. HPS1 & HPNB cases in Figure 5-6) flame showed a slightly wider angle of fuel spray. Although the viscosity, density and surface tension of iso-pentanol/ n-heptane mixtures are bigger than those for ethanol/ n-heptane mixtures.

Overall, all flames have almost identical flame structure. Although utilizing a solid-cone spray atomizer, no apparent signal from the fuel spray were observed in the inner recirculation zone in most of the cases, except for iso-pentanol flames (PS1 and PNB in Figure 5-6), for which under the same flow conditions, abundant fuel was observed in the inner recirculation zone. The reaction zone locations and appearance are similar to the ones utilizing a hollow-cone nozzle in the previous study [150], except for the pure iso-pentanol flames, where the inner flame branches were absent at the lower distance (0-20 mm) to the nozzle, dominated by fluorescence signals from the fuel.

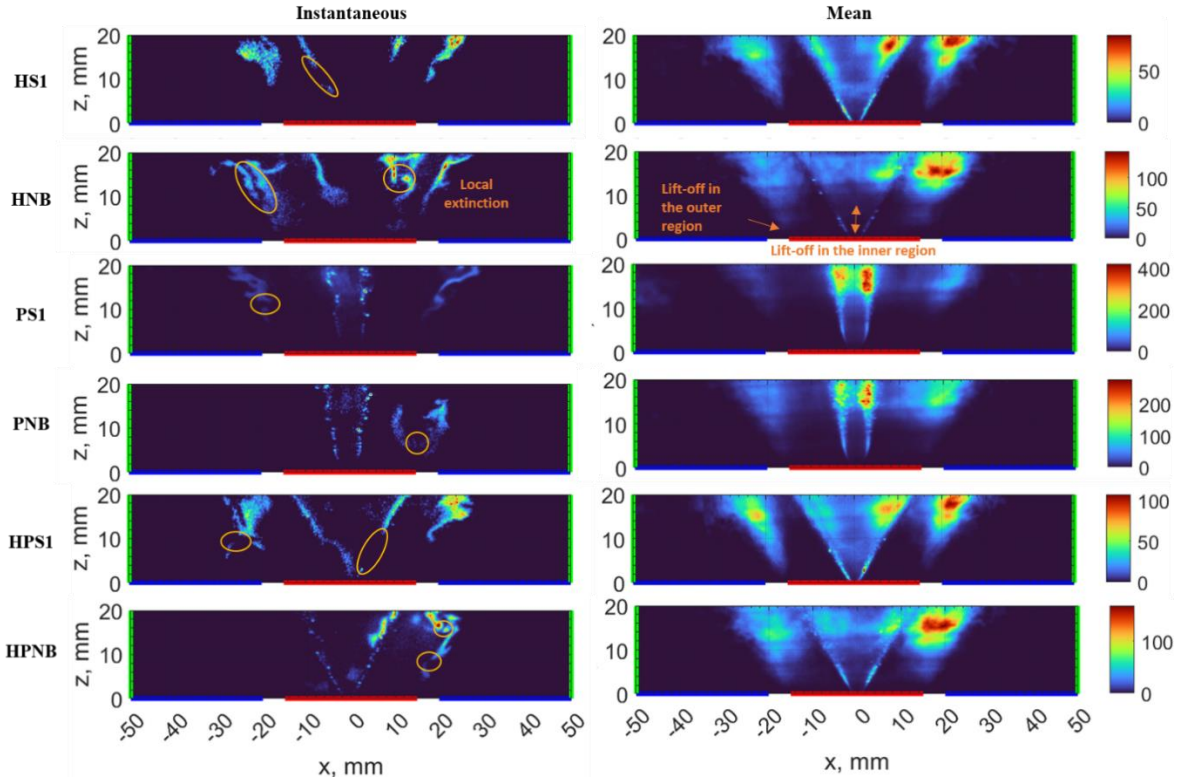

Figure 5-6 Instantaneous and mean images of OH-PLIF for HS1, HNB, PS1, PNB, HPS1, and HPNB cases. Red line indicates the bluff-body surface, blue line indicates the bottom surface of the combustion chamber, and green line indicate the location of the laser beam.

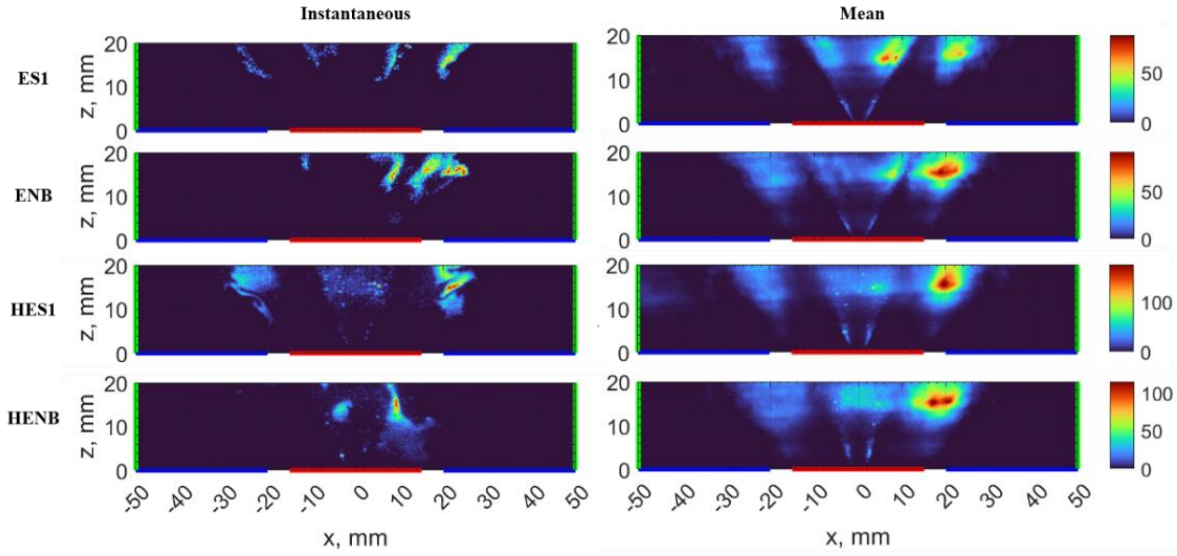

Figure 5-7 Instantaneous and mean images of OH-PLIF for ES1, ENB, HES1, and HENB cases. Red line indicates the bluff-body surface, blue line indicates the bottom surface of the combustion chamber, and green line indicate the location of the laser beam.

5.3.5 Lift-off and Local Extinction

Flame stabilisation in terms of the local extinction and lift-off was investigated in both stable condition pairs (S1, NB, with varying air flow rates) and the far from blow-off (S0) condition (a richer flame with lower fuel and air flow rates).

5.3.5.1 Stable Condition

In this sub-section, the lift-off and local extinction features of all stable flames are discussed. Figure 5-8 presents the probability density function (PDF) of all the cases of stable flames. The peak of HS1, HPS1, PS1, ES1, and HES1 occurred at lift-off heights of 12 mm, 6 mm, 12 mm, 9 mm, and 9 mm, respectively. The addition of iso-pentanol to the n-heptane flame caused the flame to become more attached to the bluff-body. Also Ethanol had the same impact on the n-heptane flame, but less than iso-pentanol. In regard to the local extinction in stable flames, pure iso-pentanol had the highest occurrence (more than 55% showing local extinctions) compared to other flames, and lowest in the n-heptane/ethanol mixture. The addition of iso-pentanol to n-heptane increased the number of local extinction events. Whereas the addition of ethanol to n-heptane showed less occurrences of local extinction.

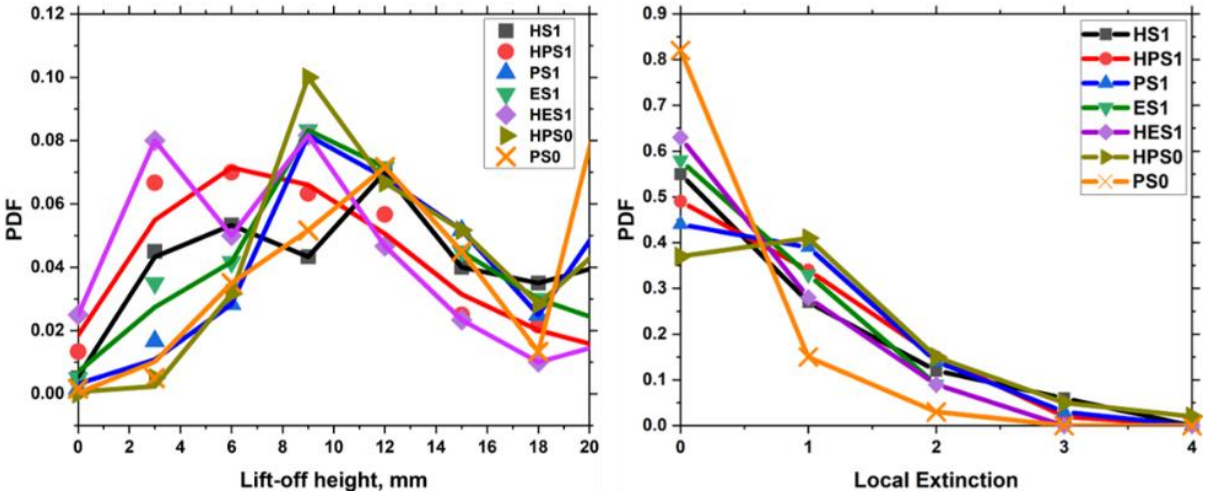

Figure 5-8 PDF of lift-off and local extinction of stable condition and far away from blow-off conditions. Lines shown for lift-off height figure are Loess fit.

5.3.5.2 Near Blow-off Condition

In general, it was found that as the air flow rate increases and approaches blow-off, lift-off height decreases. Figure 5-9 shows the mean lift-off heights normalized by the bluff-body diameter for the stable and near blow-off conditions. Pure iso-pentanol showed the highest average lift-off amongst the stable and near blow-off cases. However, the iso-pentanol /n-heptane blend (HPNB) showed the lowest mean lift-off height of 4.8 mm amongst all near blow-off cases. The stable condition of n-heptane/ ethanol mixture had almost same mean lift-off height as near blow-off condition of pure iso-pentanol. The near blow-off case of pure ethanol had an average lift-off height of 5.6 mm, lower than iso-pentanol (PNB, 8 mm). Nevertheless, the impact on lift-off height caused by ethanol when was added to n-heptane is less than iso-pentanol.

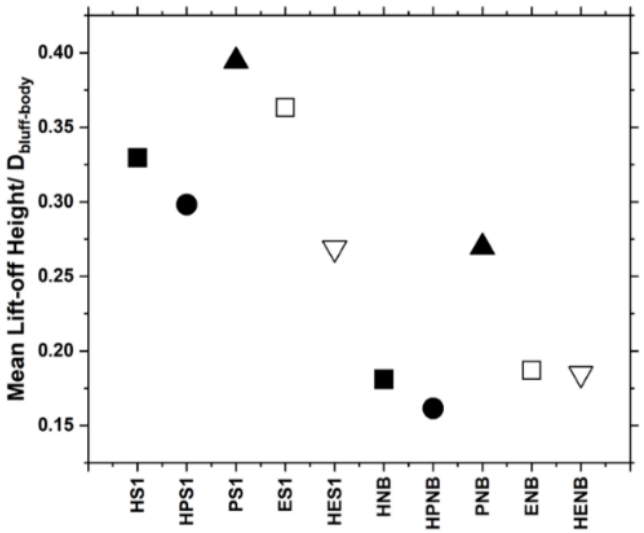

Figure 5-9 The mean lift-off heights normalized by the diameter of bluff-body (30 mm) for the stable and near blow-off cases.

Figure 5-10 displays the PDF of local extinction for near blow-off cases. Overall, the number of local extinctions occurrence were found to happen more near the blow-off event than the stable case. Iso-pentanol (PNB) was found to have the highest number of local extinction events, and ethanol the lowest. The addition of iso-pentanol to n-heptane resulted in increasing the local extinctions.

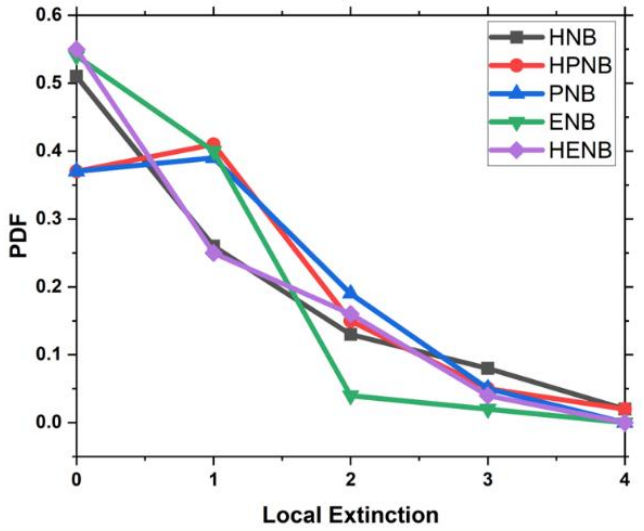

Figure 5-10 PDF of local extinction for all near blow-off cases including HNB, HPNB, PNB, ENB, and HENB.

5.3.5.3 Far away from the Blow-off Condition

Far away from the blow-off cases of iso-pentanol and its mixture with n-heptane were investigated to study the soot emission concentrations. This sub-section discusses their lift-off heights and local extinctions before presenting their soot volume fraction in Chapter 6. Figure 5-8 shows the PDF of lift-off for HPS0 and PS0. Both profiles have similar trends, but the HPS0 have overall lower lift-off heights than the PS0 case. Regarding local extinctions, pure iso-pentanol was found to have fewer local extinctions than n-heptane/iso-pentanol.

The laminar flame speed of iso-pentanol *vs* heptane were reported at almost similar levels (i.e. similar chemical time scales) [123], [214]; however, the atomisation of iso-pentanol (of a lower *We* and *Re* number, and a narrower cone angle) is not as efficient *vs* heptane under the same flow conditions studied. The effect from the insufficient atomisation may have led to the increased local extinction occurrence in the outer flame branch of the iso-pentanol cases.

5.3.6 NO-PLIF Measurements

Mean images of NO-PLIF for HS1, HNB, HPS1, HPNB, PS1, and PNB cases are shown in Figure 5-11. The contour plot of the averaged OH-PLIF data shown in Figure 5-6 are superimposed on each flame condition and this is shown in Figure 5-11. Those contour plots provide insight into the spray trajectory and the recirculation. A six-vane swirler with a cone angle of 60° and SN of 1.25 has been used for the cases shown in Figure 5-11. In all cases, the relative NO concentration peaks between heights of 10 mm to 20 mm (Z-axis), where the recirculation zones occurs according to the OH contour plots. Lower relative NO concentration was detected in the IRZ and ORZ as more iso-pentanol was added to the n-heptane flame, as shown in Figure 5-11. The peak relative NO concentrations are 46.79, 31.41, and 26.81 (a.u.) for H1, HPS1, and PS1, respectively. According to previous studies [215], [216], the latent heat of evaporation for iso-pentanol is higher than n-heptane, which could assist in reducing the temperature inside the combustion chamber and hence the NO_x emissions [73]. At near blow-off conditions, pure n-heptane and iso-pentanol/ n-heptane fuel mixture showed lower NO emission intensity than at stable conditions. The NO-PLIF images of iso-pentanol fuel near blow-off (PNB) show a high intensity along the spray v-shape trajectory (Fig.5-12, dot circle) compared to the other cases. The pure iso-pentanol does not atomize as effectively as the other fuel mixture, as explained in Section 5.3.4.1. The inefficient atomization of iso-pentanol caused

an apparent fuel-LIF signal from the fuel droplets, such as the signals seen along the spray v-shape trajectory in the NO-PLIF result, giving a high intensity in the NO-PLIF images. The fuel-LIF signal is obvious in the instantaneous images of the PNB case; an example is shown in Figure 5-12.

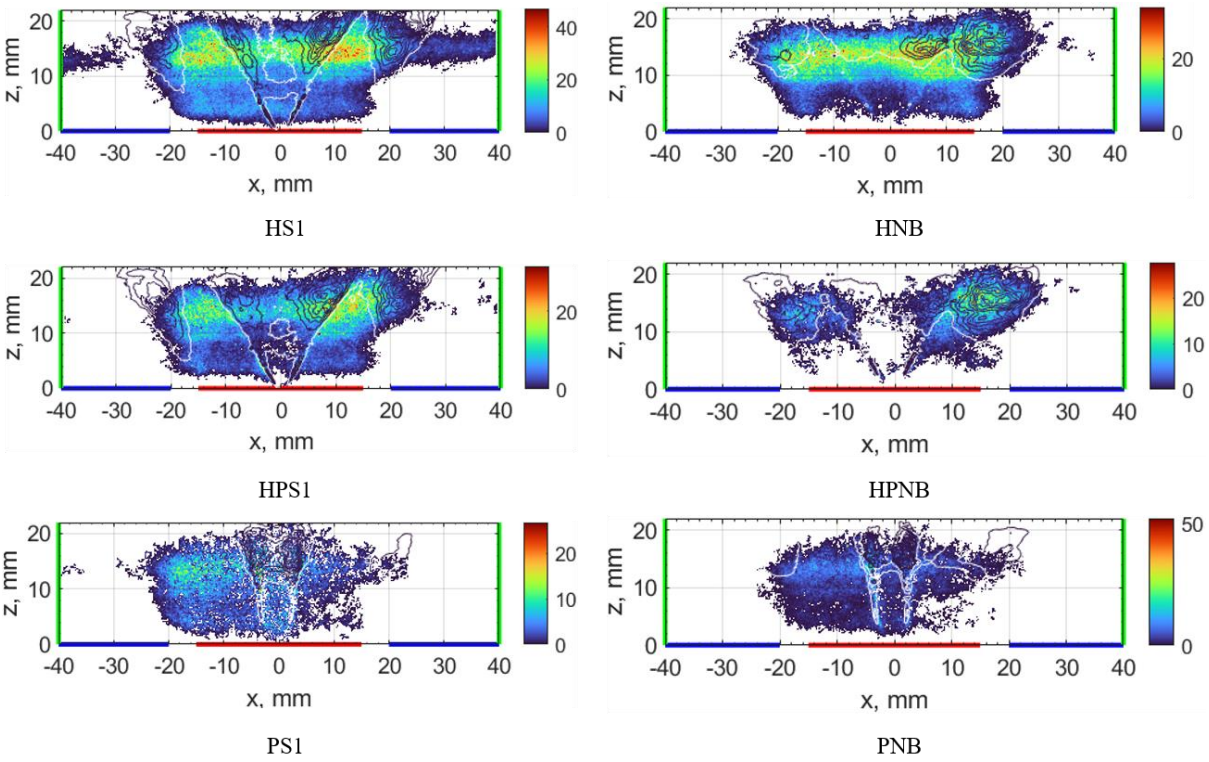

Figure 5-11 Mean images of NO-PLIF for HS1, HNB, HPS1, HPNB, PS1 and PNB cases. A contour plot of averaged OH-PLIF data shown in Figure 5-6 are superimposed on each flame condition. The surface of the bluff body is shown in red along the x-axis, the base of the combustion chamber is shown in blue, and the space between the red and blue is where co-flow air enters. The laser beam's location is shown in green.

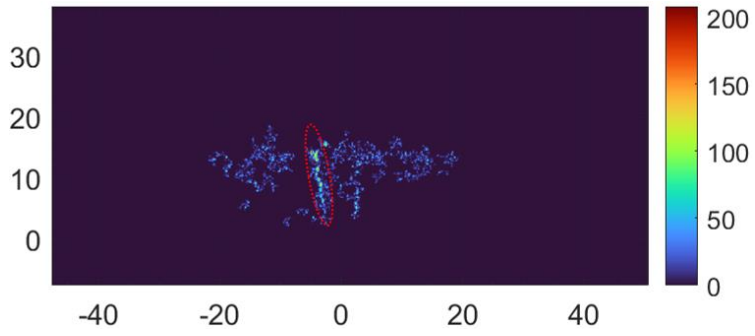

Figure 5-12 Instantaneous image of the PNB case.

5.3.6.1 Impact of Swirl Number on the NO Formation

Mean images of the NO-PLIF for the PS1 flame at three swirls having different swirl numbers (SN) of 0.36, 0.63, and 1.25 are shown in Figure 5-13. The swirl cone angles are 30°, 45°, and 60° for SN of 0.36, 0.63, and 1.25, respectively. The fuel-LIF signal from the fuel droplets are shown clearly along the spray trajectory and in the inner zone. Lower relative NO concentration is observed as the swirler number increases. At SN of 0.36, the NO signal is mostly confined above the surface of the bluff body. The increase in the swirl number extended the distribution of the NO signal to a broader region in the combustion chamber. The high swirl number generates more turbulent flow, thus providing better mixing between fuel, air, and combustion products in a liquid fuel burner. Numerous previous works [60], [67] have shown that the swirl motion causes an increase in the air and fuel mixing rate, which lowers the flame temperature and the NO_x emissions. Thus, increasing the swirl number cause a decrease in the residence time of NO_x production.

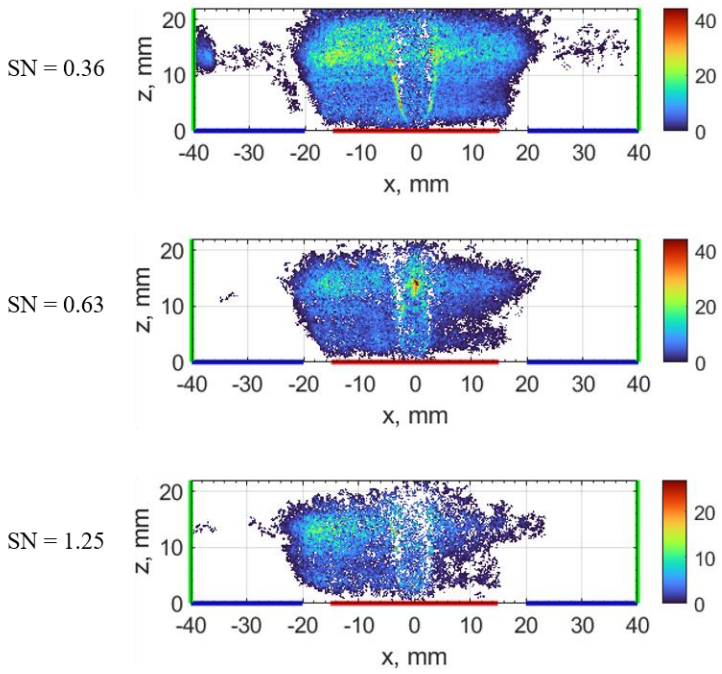

Figure 5-13 Mean images of NO-PLIF of pure iso-pentanol (PS1) case using at three different swirl numbers (SN).

5.4 Conclusion

This chapter mainly focused on the swirl spray flame reaction zone characteristics of iso-pentanol and blended flames, including flame stabilization and heat release. Iso-pentanol fuel and its mixture with n-heptane were also compared at the same operating conditions as ethanol flames. The OH-PLIF measurements were used to investigate the flame sheet characteristics, whereas OH* chemiluminescence was utilized to represent the heat release distribution.

The results showed that all the flames presented a clear double flame sheet structure, described as inner and outer regions in this thesis. In addition, most of the flames showed, with the exception of pure iso-pentanol, an open-up spray in a cone-like “V” shape. The outer flame sheet for all the conditions is observed to be wider (of a broader region) near the blow-off event. Also, the start of flame sheets in the outer region are more attached to the bluff-body surface at near blow-off conditions.

Lift-off and local extinction features of all stable flames were investigated and discussed. In stable flame conditions, the addition of iso-pentanol to n-heptane flame caused the flame to become more attached to the bluff-body. The largest number of local extinction events occurred in the pure iso-pentanol flame, and the lowest in the n-heptane/ethanol mixture. In addition, the addition of iso-pentanol to n-heptane increased the number of local extinctions. Whereas the addition of ethanol to n-heptane decreased the occurrence of local extinction. In near blow-off flame conditions, iso-pentanol showed the highest average lift-off height amongst all near blow-off cases. The addition of iso-pentanol to n-heptane decreased the lift-off height to the lowest amongst all near blow-off cases. Additionally, the impact on the lift-off height that is caused by ethanol when added to n-heptane was less than that of iso-pentanol.

In far away from blow-off conditions, the n-heptane/ iso-pentanol flame had an overall lower lift-off height than the iso-pentanol flame case. Less local extinction in pure iso-pentanol was found compared to the n-heptane/iso-pentanol mixture. Regarding heat release, adding iso-pentanol to the n-heptane flame (HPS1) made the OH* signal stronger, suggesting a higher rate of heat release compared with the pure n-heptane flame. However, the pure iso-pentanol (PS1) flame was found to have a lower OH* signal than the HS1 and HPS1 flames.

The findings of the NO-PLIF measurements indicated that as iso-pentanol is added to the n-heptane flame, the relative NO content was decreased in the IRZ and ORZ. The NO content was decreased by roughly 32.87% when iso-pentanol was added to n-heptane fuel in a volume ratio of 50% at steady conditions. Pure n-heptane and iso-pentanol/n-heptane fuel mixtures demonstrated lower NO emission intensity at near blow-off conditions than at stable conditions. Also it was found that the relative NO concentration dropped as SN increased. Additionally, when the swirl number increased, the distribution of the NO signal spread to a larger portion of the combustion chamber.

Chapter 6: Soot emissions characteristics of DME laminar diffusion flames and iso-pentanol swirl spray flames

6.1 Introduction

This chapter discusses the soot emissions of the laminar diffusion flames of DME and blends and swirl spray flames of iso-pentanol and blends. It was shown in Chapter 3 how the DME contributes to reducing the main soot precursors through the pathway analysis produced from 1D numerical simulations. Information and understanding of soot particles volume fraction and size are essential to investigate the soot emission processes in hydrocarbon/ biofuels flames. Experimental measurements on the formation characteristics of soot in flames containing DME are limited in the literature, as mentioned in Chapter 1. Most of those studies used a point-wise approach rather than an imaging method. The latter could provide snapshots of 2-dimensional quantifications of soot emissions, thus they are beneficial in turbulent conditions. Multiple experimental and modelling studies have investigated the ignition behaviour of iso-pentanol, as mentioned in Chapter 1. However, there needs to be more studies on soot emissions of

iso-pentanol flames. In addition, there needs to be more reported data on iso-pentanol combustion from swirl spray flames.

The effects from the detection parameters of the LII signal (i.e., acquisition delay time, duration) and the laser fluence level on the derived soot concentration or particle diameters have not been fully addressed in the literature, which could affect the quantitative measurement of DME/hydrocarbon flames. Thus, it has been investigated further. Another objective of this chapter is to obtain soot particle measurements from self-calibrated planar time-resolved two-colour Laser-induced incandescence (2C-LII) in a range of co-flow laminar diffusion flames of methane and ethylene blended with DME, and in turbulent swirl spray flames of iso-pentanol/ n-heptane blends. The DME soot data from this work was utilised to compare with the CFD soot modelling data.

Another aim of this chapter is to show the soot modelling results obtained for the DME/C_2H_4/N_2 flames and assess the validity of using the existing developed soot model in Ansys Fluent (Moss-Brooks model, discussed in Ch.2). Parametric studies have been carried out on some key parameters in the soot model to find optimum values that can be used for the current flames.

6.2 Flame Conditions

A standard co-flow burner was used for the methane and ethylene-air diffusion flames with DME blends. Whereas a bluff-body swirl spray burner with a solid-cone spray configuration was used for turbulent flame measurements. The schematics of the co-flow burner and swirl spray burner experiments are shown in Figures 2-3 and 2-4 (Chapter 2), respectively.

The fuel and air flow rates of the laminar diffusion flames investigated in this chapter are similar to those investigated in Chapter 4. The experimentally investigated laminar diffusion flame cases include the F1, F2, F3, F4, F12, and F13 cases. The flow conditions are shown in Table 2-1 (Chapter 2). For the methane/DME mixture cases (F1-F4), the volumetric flow rate of the fuel flow remained constant at 356 ± 1 SCCM, while the volumetric flow rate of ethylene/DME mixture cases (F12, F13) maintained at 263 ± 1 SCCM. Measurements were

calculated and expressed at 25 °C and 1 bar standard conditions. The Soot Modelling flow conditions are presented in Table 4-1 (Chapter 4).

Pure n-heptane (HS0), pure iso-pentanol (PS0), and a 50:50 volume ratio blend of n-heptane/iso-pentanol (HPS0) were used as liquid fuels for the bluff-body swirl flames to measure the soot emission. The flow conditions of the turbulent swirl flames are shown in Table 2-2. The rig had a similar setup as described in Section 2.3.2.2 (Chapter 2). A lower fuel mass flow rate of 0.506 g/s than the mass flow rates used in Chapter 5 was applied for studying the soot signal in iso-pentanol, n-heptane, and blended flames. The swirl spray burner was also used to study the characteristics of soot emissions for turbulent flames at different camera gate widths (TTL) and delay times.

The DME/C_2H_4/N_2 flame boundary conditions investigated computationally are presented in Table 4-1 (Chapter 4). Case 1 (F12 flame) and Case 4 (F13 flame) were only investigated computationally.

6.3 Results and Discussions

This section discusses the effects of soot emission measurements by the laser energy and acquisition parameters. In addition, this section shows the results of the soot particle emissions in methane, DME/methane, and DME/ethylene diffusion flames and in heptane/iso-pentanol swirl spray flames. Initially, the impact of laser energy and acquisition parameters on laminar diffusion flames soot emission measurements is discussed (Sections 6.3.1.1 to 6.3.1.4). After that, the planar two-colour soot pyrometry measurements of the laminar diffusion flames are presented to compare with the quantitative LII measurements and to obtain the flame temperature. Soot emissions measurements of swirl spray flame are discussed in Section 6.3.2. Soot modelling results of the laminar diffusion flames are presented in Section 6.3.3.

6.3.1 Laminar Diffusion Flames

6.3.1.1 Laser Energy Effect on the Soot Concentration Quantifications

The impact of the laser energy on the peak soot temperature and soot volume fraction measurements at two different acquisition delay times of 0 ns and 20 ns (with respect to the

end of the laser pulse) in a methane–air diffusion (F1) flame have been investigated, as displayed in Fig. 6-1. These measurements were conducted at a constant TTL width (20 ns) and intensifier gain (at 75% of the full range).

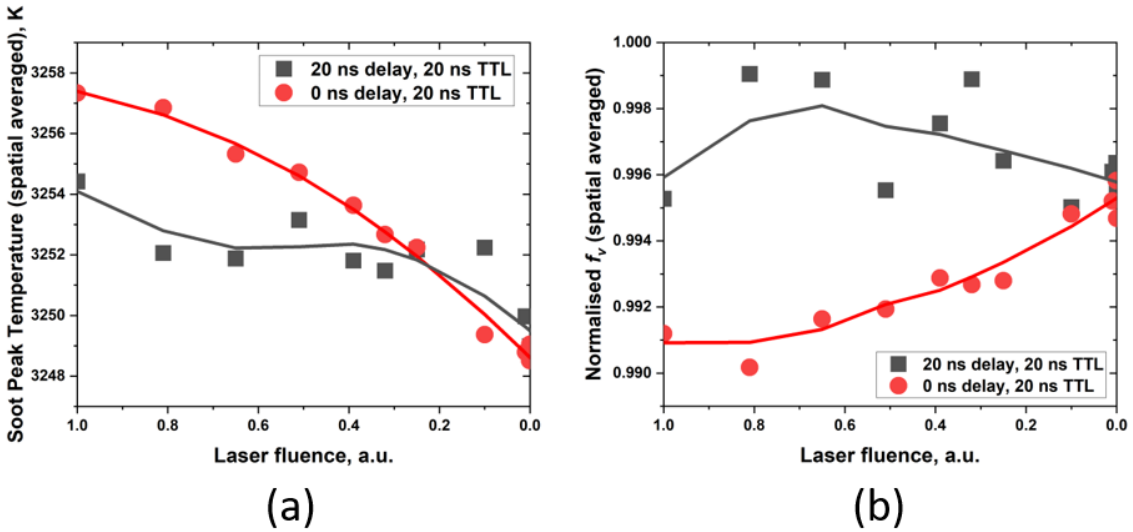

Figure 6-1 Dependence of laser fluence: soot temperature and soot volume fraction measurements from 2C-LII in a methane – air diffusion flame (F1). Acquisition duration of 20 ns and delay time of 0 ns (red) and 20 ns (black). Lines shown are Loess fit.

A difference within 10 K was observed between the peak soot temperatures at laser energy from 1 (arbitrary unit, a.u., corresponding to the full power) to 10% a.u. For the cases with high laser energies (>25% of the full range), the measured peak soot temperature is higher with an acquisition delay of 0 ns compared to the one measured with a 20 ns delay, possibly because the impact of the laser heating process is more significant at 0 ns delay compared to at 20 ns delay. As expected, the measured peak soot temperature reduces at both time delays as the laser energy decreases. At mid-low laser energy (< 50% of the full range), the peak soot temperatures at the two different delay times were very similar, indicating the delay time of 20 ns after the laser pulse is considered to be small in the timescales of the cooling process of the soot particles at the medium or low laser energy conditions.

Figure 6-1b shows the impact of laser energy on the soot volume fraction. At laser energy > 10%, there is a small inverse relationship between incident laser energy and measured soot concentration, with a difference in soot volume fractions of less than 1%. At less than 10% laser energy, the effect on the SVFs is negligible. In this study, the impact of the sublimation process on soot concentration measurements was not taken into account because not enough laser power was used to reach the sublimation regime (also known as plateau regime), as shown

in Fig. 6-1a, where the peak soot temperatures at high laser energies are below the sublimation temperature range (4000-4500 K [217]–[220]). Therefore, the decrease in the measured SVFs with 0 ns delay time at high laser energies shown in Figure 6-1b is not evidence of mass loss in this study, but an inverse effect from the measured peak soot temperature, as shown in Equation 2.18 (Chapter 2).

6.3.1.2 Time-Resolved Acquisition: The Effect from the Delay Time, and With DME Addition

Figure 6-2a shows the measured soot temperature (spatial averaged) cooldown of methane–air diffusion flame (F1) with full laser energy at a series of acquisition delay times (0-2000 ns) with the ICCD camera (with a constant 20 ns TTL). Also, it shows a variation in the measured SVFs (spatial averaged) obtained at different delay times. An increase in the measured soot concentration during the first 150 ns of the end of the laser pulse is shown, agreeing with the results in [186]. The changes in the measured SVFs level out at longer delay times. The cause of the variation in measured SVFs may be related to the uncertainty associated with Equation 2.18 (Chapter 2), which is out of the focus in this thesis. Nevertheless, the effect of the acquisition delay time on the measured SVFs is small (within 1.2% compared to the value measured at 0 ns delay). Thus, in the following 2D measurement of the SVFs, a constant 0 ns delay time was used to compare the soot emissions of different DME/methane flames.

In addition, the soot temperature cool down curves of methane–air diffusion flame (F1) at different laser energy were compared (Fig. 6-2b), and the derived ePPDs (for the cases shown in Fig. 6-2b) were identical at ~ 33.7 nm. Therefore, the current study's laser energy levels have a negligible effect on the ePPDs. Full laser power was used in the following ePPDs measurements in DME/methane flames.

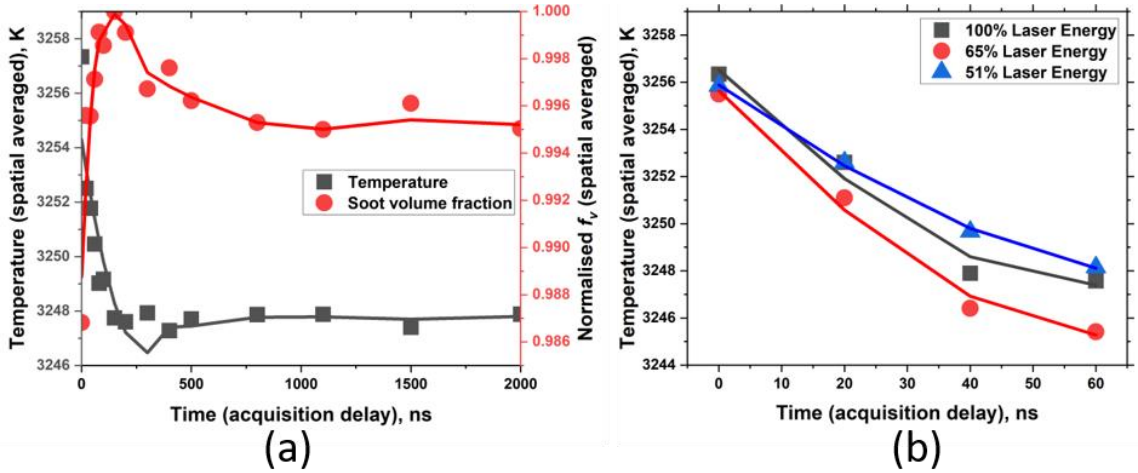

Figure 6-2 (a) effect from the acquisition delay time on the soot temperature and concentration measurements from the 2C-LII, at an acquisition duration (TTL) of 20 ns, at a fixed laser energy (full power of 1 a.u.). (b) effect from the laser energy on the soot temperature. Lines shown are Loess fit.

Planar soot volume fraction measurements of methane / DME - air laminar diffusion flames across a wide range of mixing ratios are shown in Figure 6-3. The measurements were conducted at full laser power, with 40 ns TTL and 0 ns delay. It was observed that the SVF decreases as the mixing ratio of DME increases in the flame, possibly due to the increased oxygen content from the increased amount of DME fuel in the mixture, which assists in the soot oxidation process. Adding DME to the methane flame with full laser energy (cases shown in Figure 6-4) increased the ePPDs. The ePPDs are 33.7 nm, 33.7 nm, 48.1 nm, and 112 nm for DME mixing ratios (molar ratio of the DME/methane mixture) of 0, 0.25, 0.50, and 0.75, respectively.

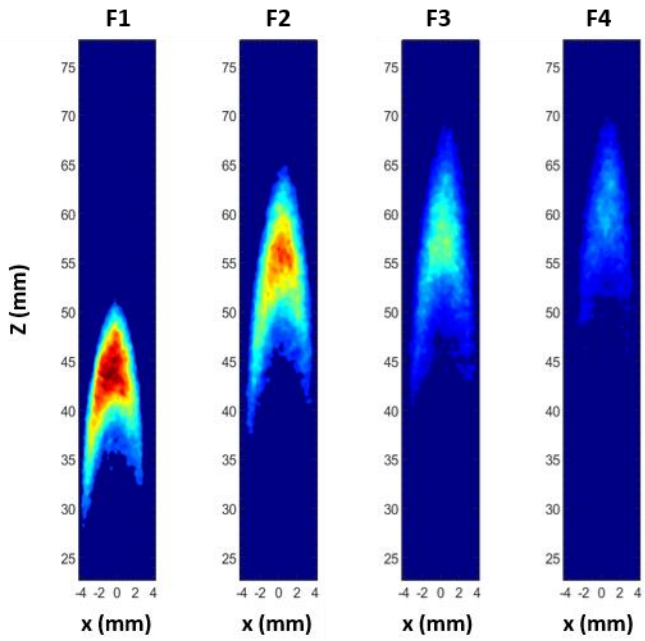

Figure 6-3 Planar soot volume fraction measurements in methane/DME - air flames at molar concentration of F1 (pure CH_4), F2 (0.75 CH_4 and 0.25 DME), F3 (0.5 CH_4 and 0.5 DME), and F4 (0.25 CH_4 and 0.75 DME) cases. All cases have the same colour map.

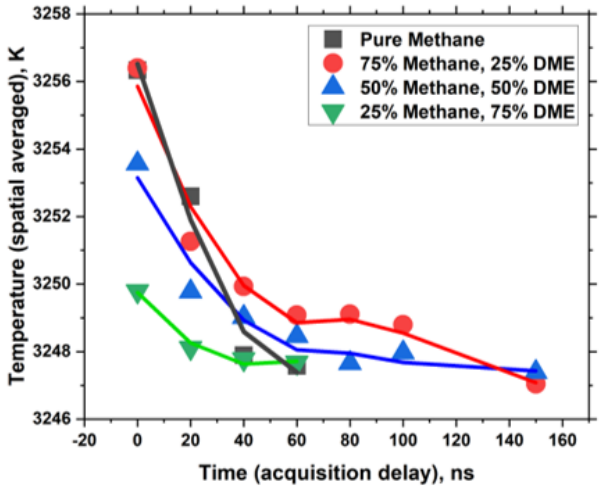

Figure 6-4 Soot temperatures in methane / DME flames at molar concentration of pure methane, 0.75 CH_4 and 0.25 DME, 0.5 CH_4 and 0.5 DME, and 0.25 CH_4 and 0.75 DME. Lines shown are Loess fit.

6.3.1.3 Effect from acquisition duration

The impact of the acquisition duration (ICCD camera gate width, expressed as TTL in this thesis) on measured soot temperature and concentration has been investigated and displayed in Figure 6-5. In principle, applying a larger TTL corresponds to a collection of more soot signals

(thus a high signal-to-noise ratio but a less temporal resolution) during the experiment. Nevertheless, it is not necessarily that the acquisition duration has a direct relationship with the measured soot temperature or concentration. Therefore, this section provides more insight into their connection and how the camera gate width can affect the soot emission measurements. The ICCD camera gate width was set to different acquisition durations (TTLs) of 10 ns, 20 ns, and 40 ns. Results (spatial averaged) shown in Figure 6-5 illustrate that the SVF increases as a larger acquisition duration is applied. The soot temperature at 0 ns delay time (i.e., the peak soot temperature at the beginning of the cool down) was highest with the acquisition duration of 40 ns TTL and lowest with the 10 ns TTL. Nonetheless, the decrease of soot temperature during the cooling process was found to occur faster with higher acquisition duration, reaching a lower temperature after about a 100 ns delay.

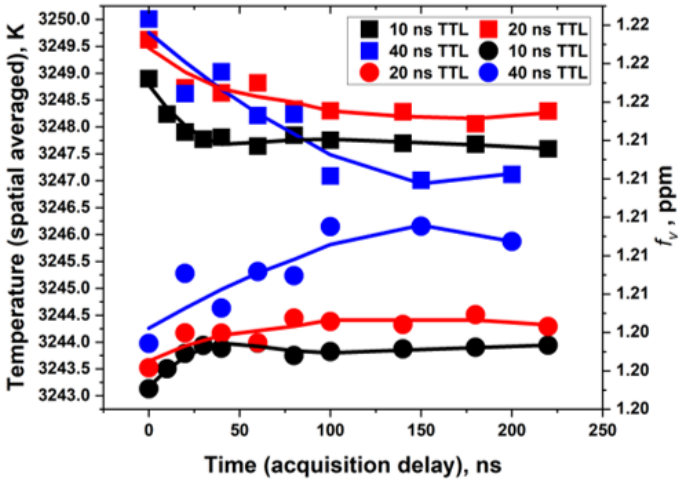

Figure 6-5 Soot temperature and concentration measurements of methane – air diffusion flame (F1): results at different acquisition delay times (10 ns, 20 ns and 40 ns) across several acquisition delays (from 0 ns to 220 ns), square - temperature, round - soot volume fraction. Lines shown are Loess fit.

The temperature during the cooling process of 10 ns and 20 ns TTL cases decreases slower than the temperature of the 40 ns TTL case, resulting in a larger value of τ_T and ePPDs. $\tau_T$was calculated using the Slop equation over equal time intervals of 0 ns to 50 ns during the heat conduction process. The resulting ePPDs measured with 10 ns and 20 ns TTL were similar at ~112 nm. On the other hand, a smaller value (~ 67.4 nm) of the ePPD has been obtained from the 40 ns TTL cases. As a TTL of 10 ns or 20 ns has shown little effect on the measured ePPDs, 20 ns TTL was used to measure ePPDs of ethylene / DME – air diffusion flames in the next section.

6.3.1.4 Measurement of soot concentrations in ethylene / DME – air diffusion flames

The influence of DME low-carbon fuel addition into ethylene diffusion flame on soot emissions has been investigated with the full incident laser energy and a constant 20 ns TTL. The soot temperature and SVFs measured at a range of time delays (0 ns to 500 ns) of the two flames (F12 – pure ethylene, F13– 50:50 volume ratios of ethylene and DME) are shown in Figure 6-6. Although the same laser energy was applied, a higher soot peak temperature was reached at the pure ethylene case (F12) compared to the one with DME addition (F13), with a difference at about 30 K. The temperature difference at 0 ns delay could be due to the difference in soot properties, possibly with extra energy consumed to vaporise the volatile content of the soot particles formed in DME added flames, ending a lower soot temperature at the end of the laser heating process. The soot particles from DME/ethylene flames (F13) have shown (Figure 6-6, in black) a slower cool-down process compared to those from pure ethylene flames (F12). After a delay time of 150 ns, the temperature measured in the F13 case reached a plateau higher than the one from F12, which continued to cool down till 500 ns. The derived SVFs were lower at F13 with DME addition compared to the pure ethylene flame (F12) when evaluating at the plateau region of the SVFs profiles or a delay > 20 ns. However, an opposite conclusion can be obtained if compared at 0 ns delay, where a smaller SVF was found in F12 compared to F13. It is outside the direct knowledge of the current thesis to justify which delay would be the correct one without further investigation using additional measurement approaches, such as sensor-based soot mass concentration measurement. However, it is still essential to notice the different trends in the obtained SVFs evaluated at different delay times highlighted in this study.

Regarding the ePPDs, the spatial averaged ePPD of the F12 flame (~ 11.2 nm) was smaller than in the F13 flame (~ 33.7 nm). The F13 flame effective diameter is within the range of the results obtained by Ahmed et al. [105].

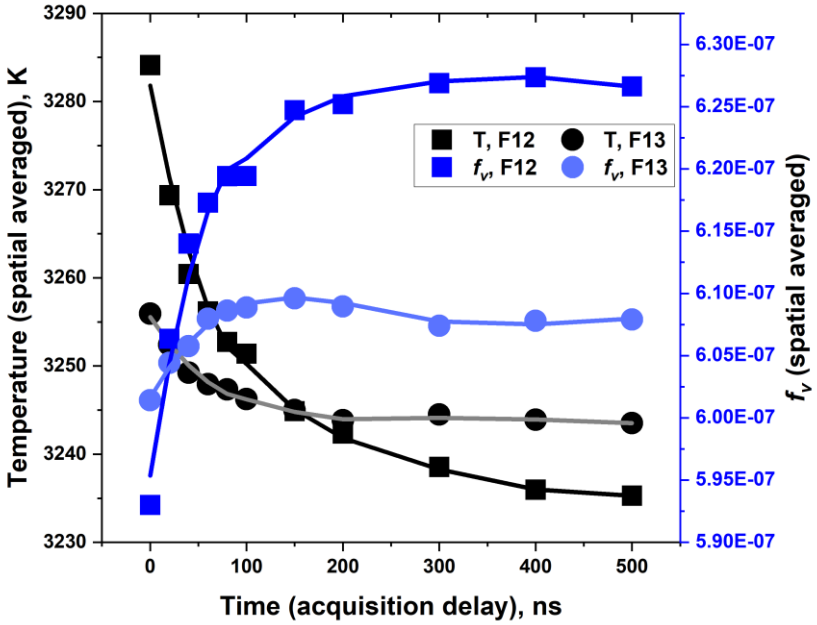

Figure 6-6 Time resolved measurements on soot temperature and concentration by the 2C-LII method at an acquisition duration of 20 ns, in a (1) F12: ethylene – air diffusion flame, and (2) F13: ethylene/DME – air diffusion flame. Lines shown are Loess fit.

6.3.1.5 The planar two-colour soot pyrometry measurement

The planar two-colour soot pyrometry (similar to LII but without using a laser) technique has been implemented to study and compare the quantitative LII soot measurements and obtain the flame temperature. Figure 6-7 clearly shows that the intensity of soot is lower in F13 (β = 0.5) than in F12 (β = 0), indicating the addition of DME to an ethylene flame reduces the net soot formation. The mean soot volume fraction in F12 and F13 is 0.22 ppm and 0.09 ppm, respectively. The corresponding OH* images for F12 and F13 cases are shown in Figure 4-4 (page 104).

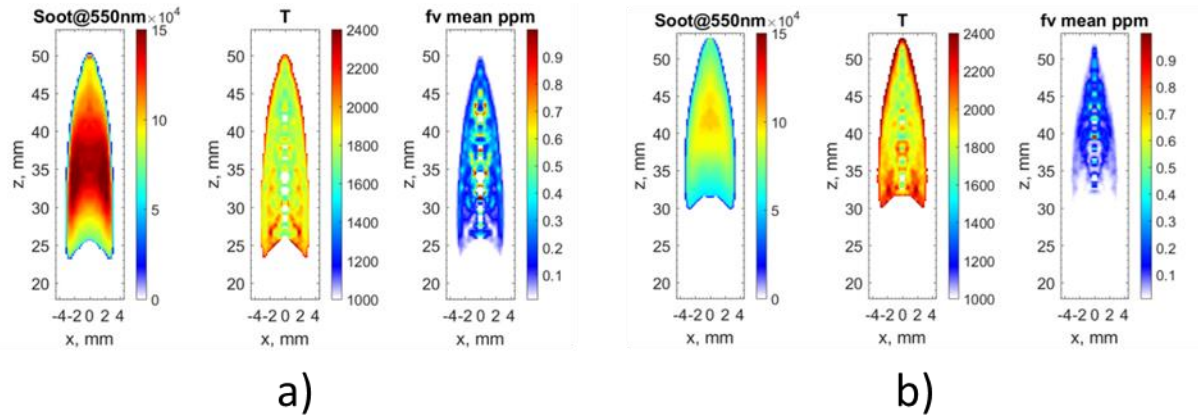

Figure 6-7 The planar two-colour soot pyrometry results of a) F12 and b) F13.

The two-colour soot pyrometry SVF measurements values (shown in Figure 6-7) is very close to the LII SVF measurement values shown in Figure 6-6, as they both have a similar order of magnitude of SVF values. Therefore, both two-colour soot pyrometry and LII can be used to measure SVF. However, LII can not provide the flame temperature because of the laser heating. The advantage of using LII is that it can offer better species resolution and soot temperature, which can be used to calculate the cool-down effect and predict the effective primary particle diameter.

Figure 6-7 illustrates that the mean soot temperature is slightly increased for F13, where the temperature in F12 and F13 are 1867 K and 1969 K, respectively. At the flame front, where the temperature peak roughly is located, there should not be much soot, and it should be oxidized when passing the flame front. There is no signal displayed outside the flame front in both cases in Figure 6-7. Thus, the flame temperature in these regions was not investigated. The peak temperature values obtained by the two-colour soot pyrometry technique are lower than the peak of the temperature profiles obtained by the 1D simulations in Chapter 3. This is expected due to the locations of the soot formations and the radiation heat loss in the experiments.

The drawback of the two-colour soot pyrometry measurement is mainly from the line-of-the-sight nature of the technique, which creates artificial errors using the IAT to obtain the 2D information. However, this technique provides a low-cost measurement of soot temperature and concentration, which will allow an integrated approach to study the flame structure along with the chemiluminescence measurements of OH*, CH*, and C_2* (presented in Chapter 4).

Table 6-1 displays the planar two-colour results of relative spatial soot volume fraction against DME volume fraction for the F1 to F4 cases. The planar two-colour results of DME/CH_4 mixtures (F1-F4) indicate a decrease in soot volume fraction when the DME in fuel mixture volume increases, agreeing with both chemiluminescence and 1D simulation results shown earlier in Section 3.3.2.1 and Section 4.3.1.1.

Table 6-1 Results obtained by the two-colour technique for F1-F4 cases showing the relative spatial-averaged soot volume fraction vs. DME volume fraction.

Case	DME mixture fraction β	Relative spatial-averaged soot volume fraction
F1	0	1
F2	0.25	0.8
F3	0.5	0.78
F4	0.75	0.35

The agreements found between the soot concentration measurements by the two-colour pyrometry and the mole fraction trends of the soot precursors predicted by the numerical simulation (shown in Chapter 3) confirm the validity of the Mech_56.54 mechanism in the C_2H_2 and C_3H_3 as markers and precursors for soot models.

6.3.2 Bluff-body Swirl Spray Flames

This section discusses the measured soot emission characteristics, including soot temperature, soot volume fraction, and effective primary particle diameter in n-heptane and n-heptane/iso-pentanol swirl spray flames. The impact of the acquisition duration and delay times on soot emission behaviour in swirl spray flames are also discussed in this section. The data presented in this section corresponds to the soot emissions of the flame's inner recalculation zone. Figure 6-8 displays a photograph of an n-heptane swirl flame, where the blue dashed circle indicates the recorded region in the inner recalculation zone. The incident laser beam is located at a height of 3-5 cm above the bluff-body. It can be observed from the direct photograph that the location of soot appears both at the spray trajectory and the inner recirculation zone.

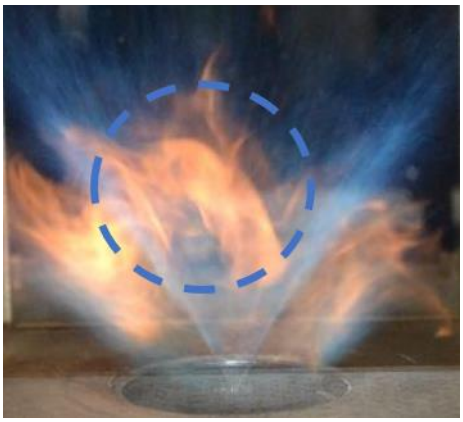

Figure 6-8 Direct image of a steady heptane swirl flame studied with a solid-cone spray atomizer.

The measured soot temperature (spatial averaged) of n-heptane and n-heptane/ iso-pentanol swirl spray flames (HS0, HPS0) at different delay times (0 ns, 20 ns, 40 ns, and 60 ns) and acquisition duration (TTL of 20 ns, 40 ns, and 100 ns) are shown in Figure 6-9. The soot temperature in both flames reduced further as a larger delay time was applied, similar to the soot temperature in laminar diffusion flames discussed earlier in Section 6.3.1.2. In addition, both flames displayed the highest soot temperatures with an acquisition duration of 100 ns and the lowest with a 20 ns acquisition duration. In comparison to the laminar diffusion flames, the soot temperature between 0 ns and 60 ns decreased at a much faster rate than those of laminar diffusion flames, possibly due to the higher convection cooling effect from the turbulence in the swirl flames compared to in the laminar flames.

The addition of iso-pentanol to n-heptane fuel was found to have a higher peak soot temperature at the end of the laser heating process, as shown in Figure 6-9. It was also noticed that the soot temperature difference between different acquisition duration (TTL) is smaller in the mixed (n-heptane/ iso-pentanol) flame than in the pure n-heptane flame. Data with longer delay times (>60) were not obtained (not enough samples) because of the low soot signal. Whereas in laminar diffusion flames, data were collected with longer delay times of up to 500 ns, as shown in Figure 6-6. The soot temperature cool down was fast in comparison to the laminar diffusion flames.

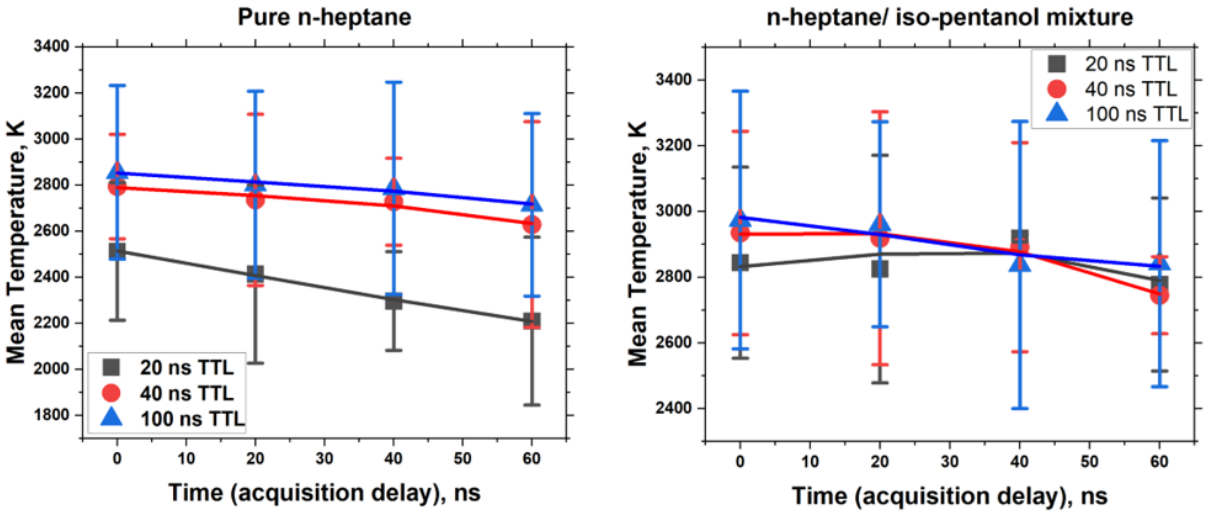

Figure 6-9 Effect from the acquisition delay time on the soot temperature measurements from the 2C-LII, at acquisition durations (TTL) of 20 ns, 40 ns, and 100 ns and a fixed laser energy (50% laser power) in swirl spray flames of (left) n-heptane, HS0, and (right) 50:50 volume blend of n-heptane/iso-pentanol, HPS0.

The 2D measurement of soot volume fractions in the turbulent swirl flames of HS0 and HPS0 at 0 ns delay time and acquisition durations of 20 ns, 40 ns, and 100 ns are shown in Figure 6-10 (instantaneous images) and Figure 6-11 (averaged images), where all colour maps are presented in parts per million (ppm) unit. The red line displayed along the x-axis denotes the surface of the bluff-body. Whereas the area between -15 and -20 mm on the x-axis indicates the region where the air stream enters the confined chamber. The dashed blue circles shown in Figures 6-10 and 6-11 correspond to the area of the flame region marked with a blue circle in Figure 6-8. The SVF results shown in Figure 6-11 were calculated from 50-200 instantaneous images which contain soot signals of an area larger than 50 pixels. Images which contain almost no soot signals were not included in the calculation for the mean images. The SVF increased in both flames as a larger acquisition duration was applied. In general, the SVF of the n-heptane/ iso-pentanol mixture flame was found to be lower than in pure n-heptane flame.

The effective primary particle diameters for pure n-heptane flame at acquisition durations of 20 ns, 40 ns, and 100 ns are 1.08 nm, 3.84 nm, and 11.4 nm, respectively. On the other hand, the particle diameters for the n-heptane/ iso-pentanol flame at acquisition durations of 20 ns, 40 ns, and 100 ns are 4.86 nm, 4.86 nm, and 5.66 nm, respectively. The parameters used to calculate the effective primary particle diameters are similar to all cases (as discussed in the methodology section), except for the temperature decay rate τ_T. τ_T is very dependent on the temperature calculation and its cooling curve along different delay times. Due to the turbulence or stochastic nature of the flow/soot, the spatial average soot temperature varies slightly at different instantaneous images. For example, the uncertainty of the temperature for n-heptane/ iso-pentanol mixture measured at 20 ns TTL and 0 ns delay time is about 109.925 K (corresponding to a relative error of about 3.4%). Whereas the uncertainty of the temperature for n-heptane measured at 40 ns TTL and 0 ns delay time is about 80.1 K (corresponding to a relative error of about 2.8%). The majority of the other cases have almost similar temperature uncertainty of about $\pm$100 K. Therefore, the determination of τ_T contributes to the main uncertainty of the measured ePPDs. Additionally, with the assumption of the dominant heat conduction effect adopted in the current work (as described in the methodology section and Eqs. 2.12 and 2.13), the cooling effects from other mechanism, such as convection and radiation, were not taken into account in the calculations of ePPDs reported in this work. This could be another source of uncertainties in the measured ePPDs in the turbulent swirl flames studied, which is to be investigated in future work.

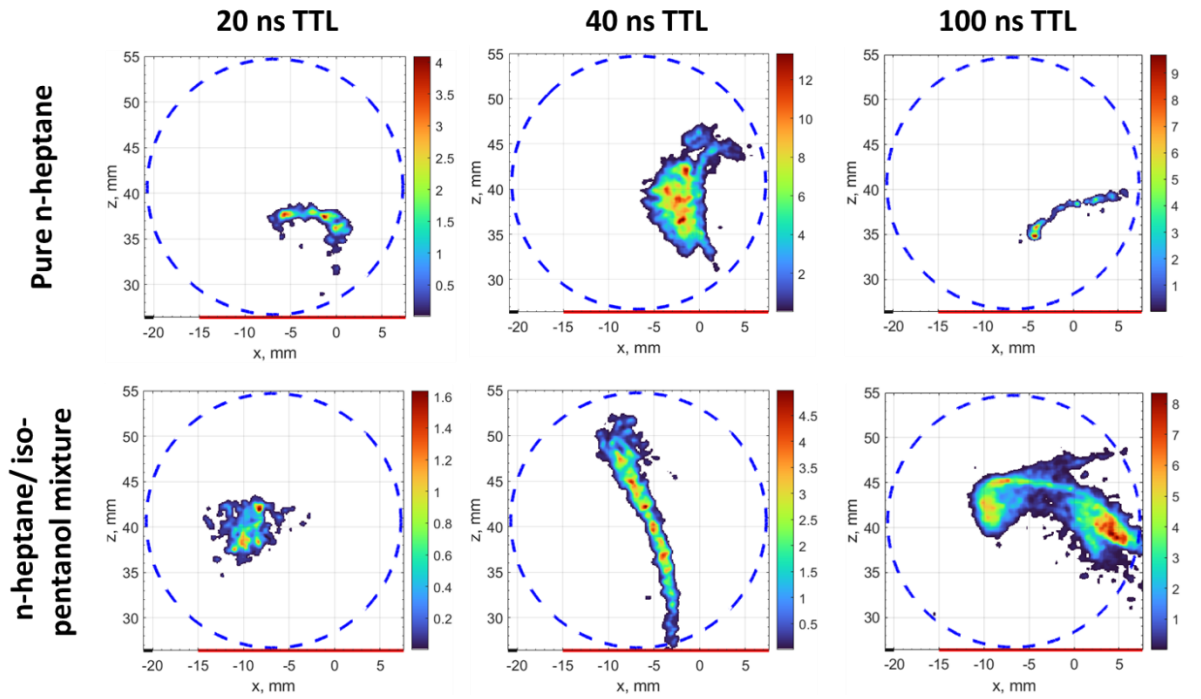

Figure 6-10 Effect from the iso-pentanol addition to n-heptane flame on the SVF measurements from the 2C-LII instantaneous images, at fixed delay time (0 ns) and different acquisition durations (TTL) of 20 ns, 40 ns, and 100 ns. Colour maps are presented in parts per million (ppm). Top row: from flame HS0, and bottom row: from flame HPS0. The dashed circle line marks the field of view region, the red line indicates the bluff body surface and the black line shows the burner plate surface.

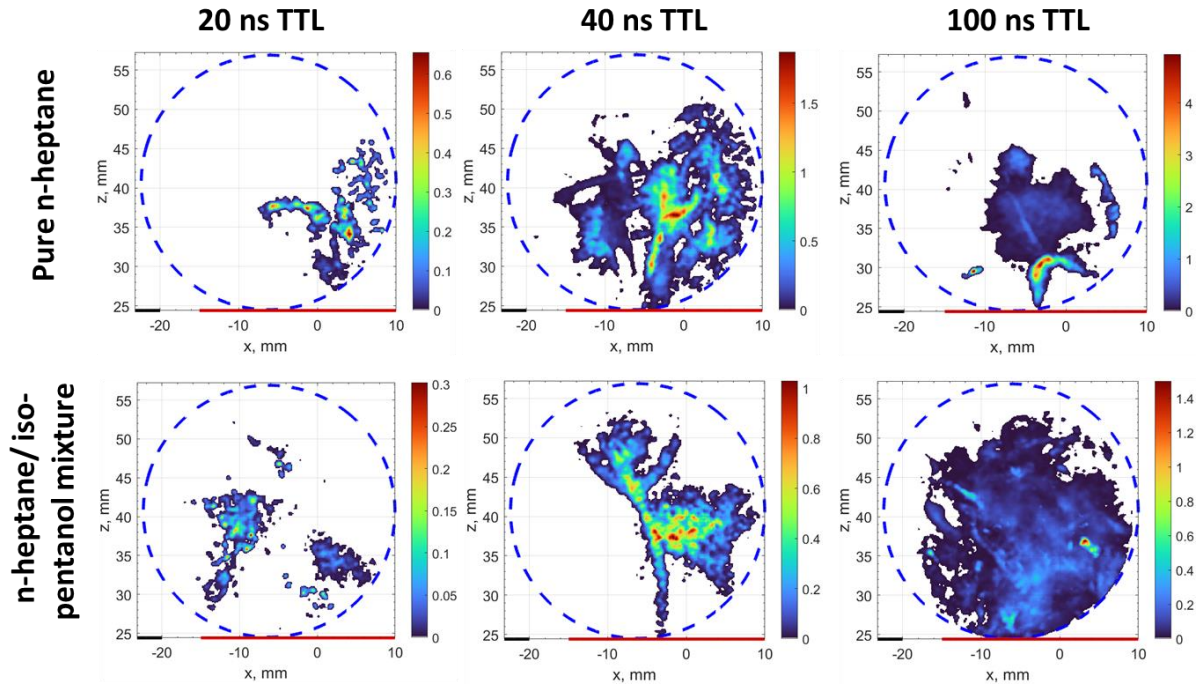

Figure 6-11 Effect from the iso-pentanol addition to n-heptane flame on the SVF measurements from the 2C-LII averaged images, at fixed delay time (0 ns) and different acquisition durations (TTL) of 20 ns, 40 ns, and 100 ns. Colour maps are presented in parts per million (ppm). Top row: from flame HS0, and bottom row: from flame HPS0. The dashed circle line marks the field of view region, the red line indicates the bluff body surface and the black line shows the burner plate surface.

100 ns TTL was used to measure and compare the SVF and soot temperatures for the n-heptane, n-heptane/iso-pentanol blend, and iso-pentanol flames because 100 ns TTL has shown a good SVF signal in Figures 6-10 and 6-11. Figure 6-12 shows the 2D soot volume fraction measurements from instantaneous images of n-heptane, n-heptane/iso-pentanol, and iso-pentanol flames at 0 ns delay time and acquisition durations of 100 ns. The color maps in Figure 6-12 indicate that adding iso-pentanol to n-heptane flame reduces the soot volume fraction. Pure iso-pentanol was found to have the lowest soot volume fraction amongst the other cases shown in Figure 6-12. Therefore, this gives a positive sign in achieving carbon neutral combustion (if bio-derived) and soot emissions reductions with iso-pentanol addition.

The averaged soot volume fraction results are shown in Figure 6-13, along with the contour plot of the mean OH-PLIF data of each case. The trend in soot levels in averaged results is similar to the one from the instantaneous images and a reduced soot level was found with the addition of iso-pentanol to n-heptane.

The same laser fluence was used for the measurement in the three flames. The mean (spatial) soot temperature of instantaneous cases in Figure 6-12 was 2495.5 K, 3188.4 K and 3793.9 K for HS0, HPS0, and PS0, respectively, indicating possible differences in the soot compositions (such as any coating with volatile organic compounds) generated in these flames.

Soot temperature is needed to calculate the soot volume fraction, as shown in Eq. 2.18. Therefore, the soot temperature considers the main contributor to the uncertainty of soot volume fraction due to the slight temperature variation among instantaneous images. In this study, the spatial averaged soot temperature was used in the calculation enabling to obtain a relative soot volume fraction distribution. The uncertainty calculated using the relative spatial-averaged soot volume fraction of different instantaneous images for n-heptane/ iso-pentanol flame mixture measured at 20 ns TTL and 0 ns delay time is about 26.9%. Whereas the uncertainty of the relative spatial-averaged soot volume fraction for n-heptane flame measured at 40 ns TTL and 0 ns delay time is about 17.4%. Yuan et al. [221] conducted a similar 2C-LII diagnostic methodology and found that the uncertainty in emissivity (which is calculated using soot temperature) is up to 34%. Therefore, the level of uncertainty in SVF obtained from this study is within the expected range due to the soot temperature as well as other assumptions explained above.

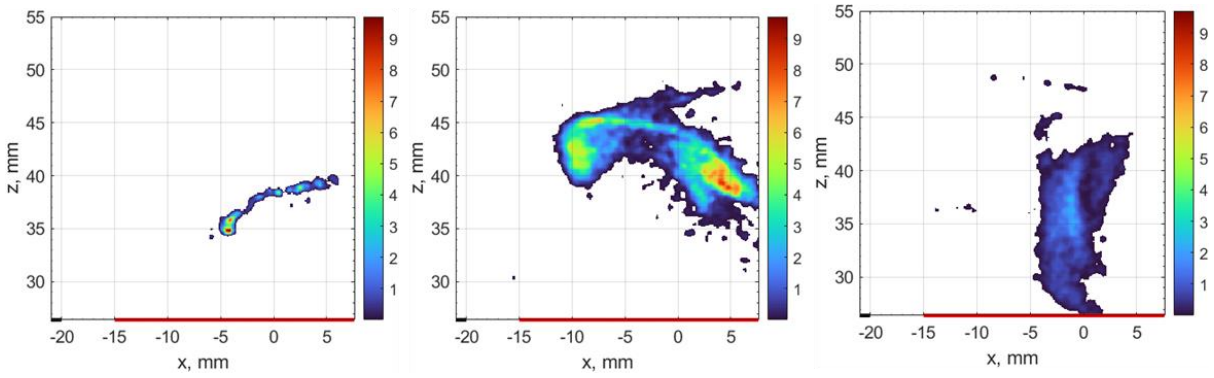

Figure 6-12 Soot volume fraction measurements from instantaneous images of (from left) n-heptane (HS0), n-heptane/iso-pentanol (HPS0), and pure iso-pentanol (PS0) flames from 2C-LII. Colour maps are shown in parts per million (ppm).

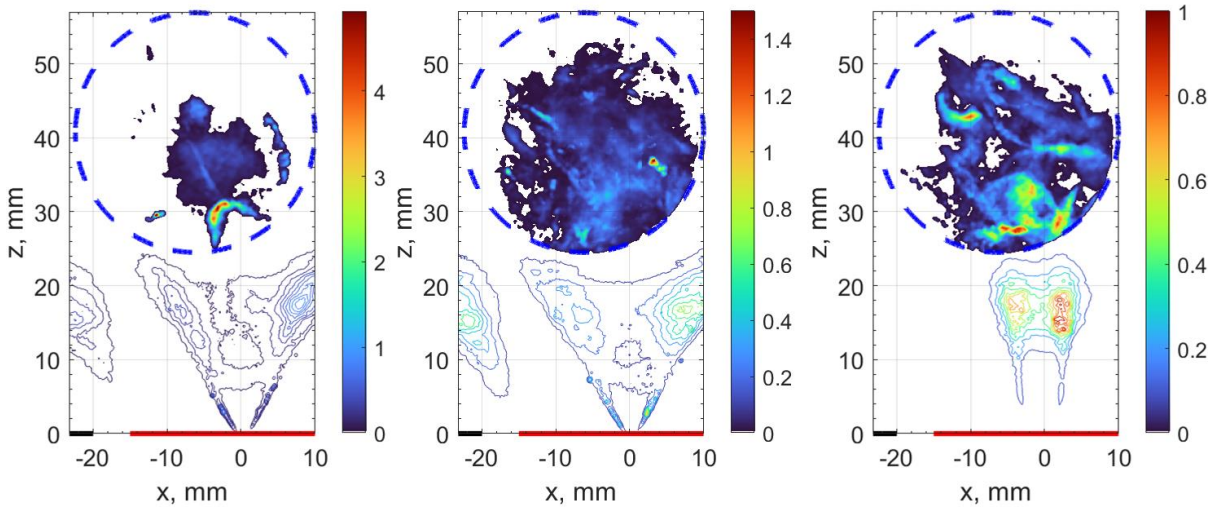

Figure 6-13 Mean soot volume fraction measurements of (from left) n-heptane (HS0), n-heptane/iso-pentanol (HPS0), and pure iso-pentanol (PS0) flames from 2C-LII. Colour maps are shown in parts per million (ppm). Blue dashed circle indicates the field of view of the 2C-LII measurements. Superimposed on each case the contour plot of mean OH-PLIF data, showing the main reaction zone, the spray trajectories, and inner recirculation zone for information.

6.3.3 Laminar Diffusion Flames Soot Modelling

Besides the experimental work on laminar diffusion flames, computational investigation on the formation of soot was also done using the Brookes and Moss model, as mentioned in Chapter 2. C_2H_2 was only considered the soot precursor and surface growth to investigate the soot formation in this study. As described in Chapter 2, adjusting the default model parameters to replicate the experimental findings is important because the default model parameters are primarily created to model CH_4 combustion [191]. Some of those model parameters include the rate of soot inception (C_α), rate of soot surface growth (C_γ), activation temperature for soot

inception (T_α), and the activation temperature for surface growth (T_γ) are chosen to be calibrated because of their important involvement in the creation of the soot [193], [194], [196], [199], [200], as mentioned in Chapter 2.

Following the mesh independence study and model validation through flame temperature and OH* species presented in Chapter 4, a parametric study was carried out to find the typical values of C_α and C_γ for the C_2H_4/N_2 (F12 case) flame soot modelling. The default values recommended by Ansys Fluent are 54 and 11700 for C_α and C_γ, respectively. However, wide ranges of these values were recommended in the literature, as discussed in Chapter 2. Therefore, based on the values given by different studies [193], [199]–[202], a test matrix was built for carrying out the parametric study of the soot inception and soot surface growth rates; test matrix used is shown in Figure 2-18 Chapter 2. The activation temperatures of soot inception and surface growth rate remained unchanged (T_α=16000 K; T_γ=12100 K) initially to study the impact of C_α and C_γ values on SVF. It was observed (from Figure 6-14) that increasing any or both values (C_α and C_γ) increases the peak soot volume fraction. However, the soot surface growth rate increase has a bigger impact on peak SVF than the soot inception rate. The highest SVF of the C_2H_4/ N_2 flame mixture was obtained with values of 10000 and 72000 for C_α and C_γ, respectively. This agrees with Choo et al. [193] study in which their highest SVF for n-dodecane flame obtained the same values for C_α and C_γ. The LII experimental results showed that the peak SVF of F12 and F13 flames along the centreline is around 0.6 ppm (across different acquisition delay times up to 500 ns). 10000 and 72000 values for C_α and C_γ, respectively, provided the closest peak SVF to the experimental results. Therefore, it was decided to use 10000 and 72000 values of C_α and C_γ, respectively, to carry out a further parametric study on T_α and T_γ to find the typical values. The default values for C_α and C_γ suggested by Fluent significantly underestimate the peak SVF, as shown in Figure 6-14.

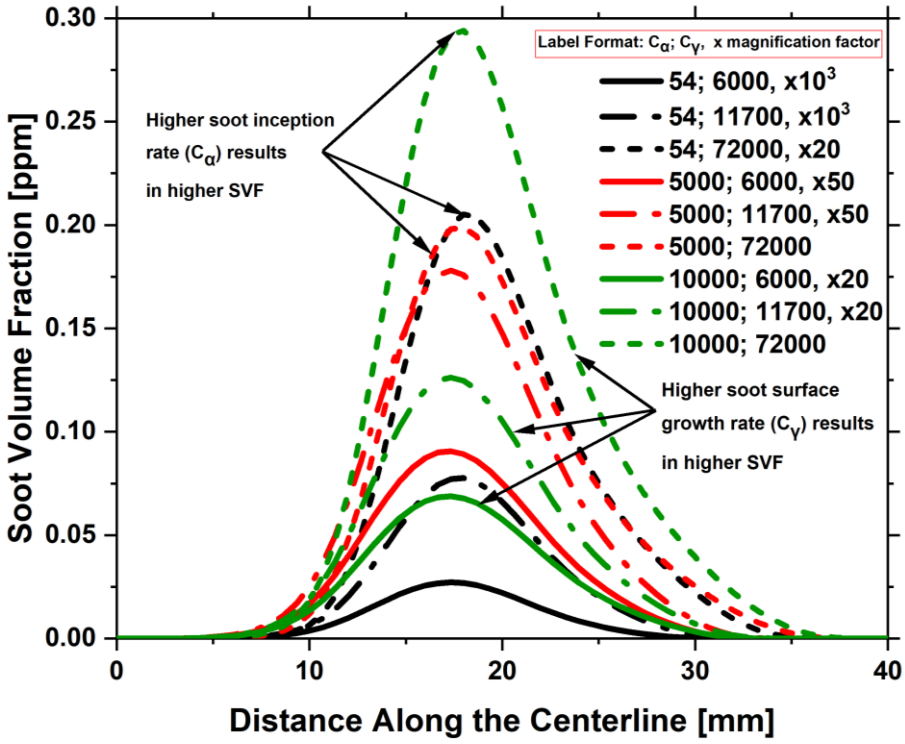

Figure 6-14 Impact of C_α and C_γ values on SVF of the C_2H_4/ N_2 (F12 case) flame. The format of the legend label is "C_α; C_γ, × magnification factor".

The impact of T_α and $T_\gamma$values on SVF of the C_2H_4/N_2 (F12 case) flame was then investigated with the use of a fixed C_α and C_γ of 10000 and 72000. The results of the parametric study on different T_α and T_γ values are presented in Figure 6-15. The increase of any or both values (T_α and T_γ) was found to decrease the SVF. The impact of T_γ is higher than the impact of T_α on SVF. Cases with low T_γ values (3100 K and 7600 K) and low T_α values (6300 K) produced a very high and unexpected SVF. Therefore, these cases did not reasonably predict the SVF of the C_2H_4/ N_2 (F12 case) flame. Cases with T_α and T_γ values of 16000; 12100 (T_α; T_γ) and 21100; 12100 (T_α; T_γ) produced a better estimate of SVF than the other cases. The case with T_α and T_γ values of 16000 and 12100, respectively, is the same case shown in Figure 6-14 with C_α and C_γ values of 10000 and 72000, respectively. This case produced the closest estimate to the peak SVF experimental results of the F12 flame shown in Figure 6-6. Therefore, parameters of $C_\alpha = 10000$, $C_\gamma = 72000$, $T_\alpha = 21100$, and $T_\gamma = 12100$ were used for the F12 flame in this study.

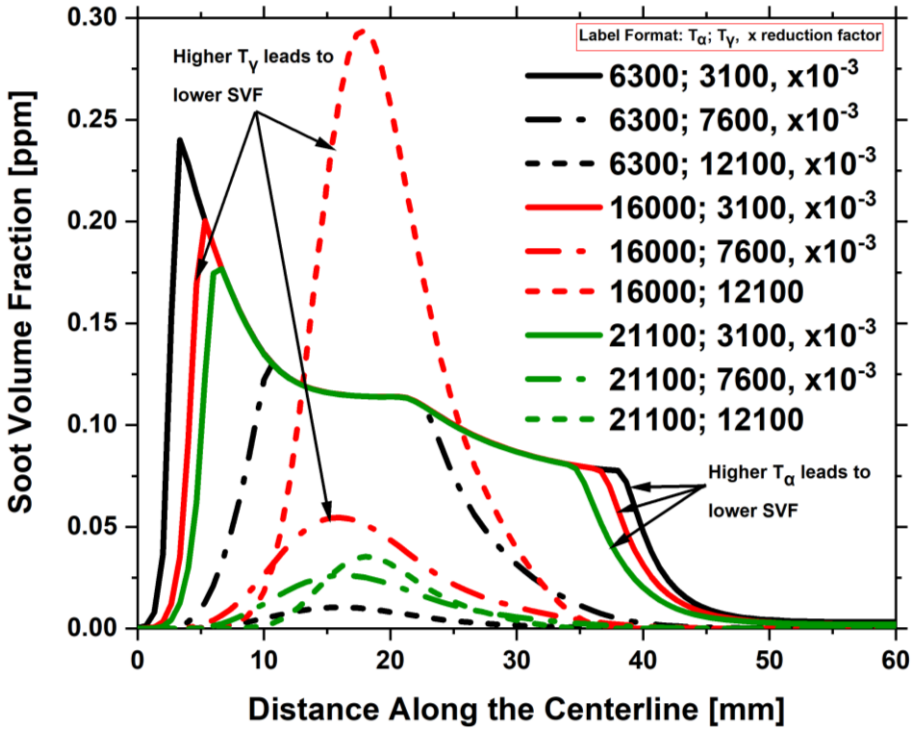

Figure 6-15 Impact of T_α and T_γ values on SVF of the C_2H_4/ N_2 (F12 case) flame. The format of the legend label is "T_α; T_γ, × reduction factor".

The two parametric studies were repeated for the F13 flame condition (30% DME, 30% C_2H_4, and 40%N_2). For C_α and C_γ values, the values of 10000 and 72000 were used respectively, as they provided a peak SVF within the same order of magnitude as SVF values shown in Figure 6-6. The results of the parametric study on different T_α and T_γ values for the F13 flame are shown in Figure 6-16. The impact of increasing or decreasing the T_α and T_γ on the SVF of the F13 flame is similar to the observations noticed on the SVF of the F12 flame, as shown in Figure 6-16. However, for F13 flame, T_α and T_γ values of 6300 K and 12100 K, respectively, produce the closest peak SVF to the experimental results. The calculated peak SVF of F12 and F13 are 0.293 ppm and 0.258 ppm, respectively. Whereas the experimental peak SVF of F12 and F13 are 0.625 ppm and 0.609 ppm, respectively. Experimentally, the peak SVF of the F12 flame is higher than the F13 flame by 2.56%. Whereas computationally, the peak SVF of the F12 flame is higher than the F13 flame by about 11%. In the current computational study, only C_2H_2 was utilised as a main precursor of soot, which could be a probable reason for the less-than-anticipated prediction of the SVF.

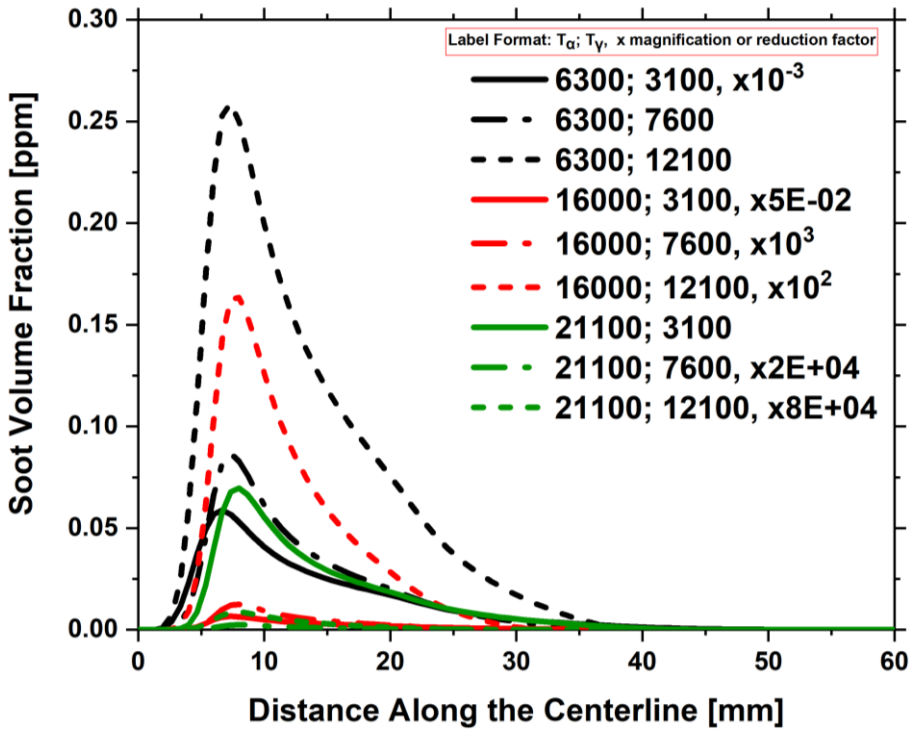

Figure 6-16 Impact of T_α and T_γ values on SVF of the DME/C_2H_4/N_2 (F13 case) flame. The format of the legend label is "T_α; T_γ, × magnification or reduction factor".

Figure 6-17 shows computational and experimental results of the SVF distribution of both flames (F12 and F13). The computationally computed peak SVF is shown to occur along the central flame axis (inner annular area of the flame). However, the experimental height SVF results are spread more at the flame's edge (outer annular area of the flame). This disagreement between the results is likely to be due to the broad range of variability that may have occurred in the dynamic of the soot structure. In addition, soot precursors play a crucial effect on the shape of SVF, as discussed and shown by Reddy et al. [222]. Reddy et al. [222] found that including C_6H_6 as a soot precursor in the Moss-Brooks model significantly synergizes the SVF values and shape. Therefore, it is essential to include C_6H_6 in the chemical mechanism when carrying out soot modelling using the Moss-Brooks model to accurately replicate the experimental study, which can be considered in future work. However, this study has found the typical values of the T_α, T_γ C_α, and C_γ parameters for both the F12 and F13 flames, which can be used in the future along with the inclusion of C_6H_6 as a soot precursor.

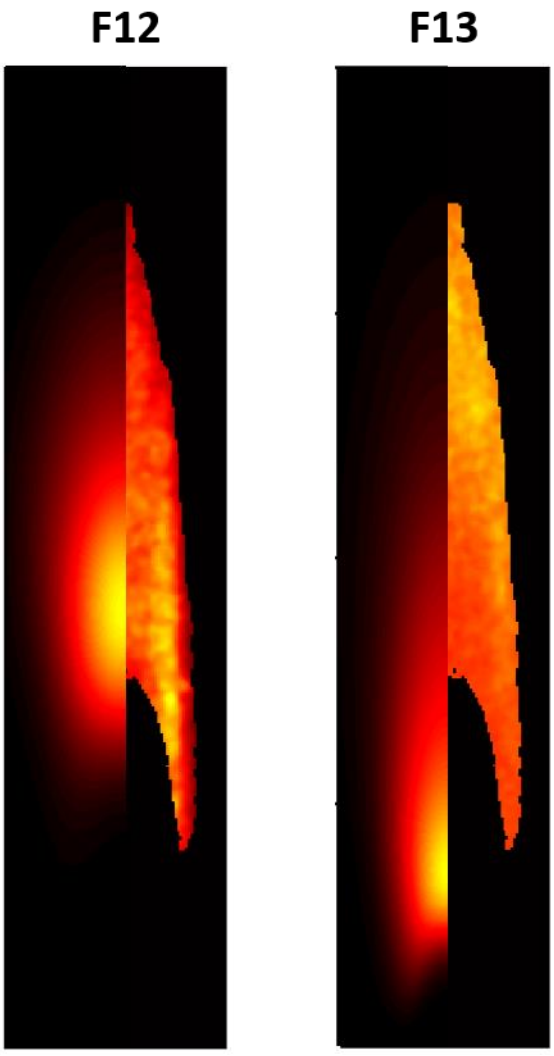

Figure 6-17 Comparison among computational and experimental results of SVF distribution. The leftmost side of each sub-figure represent the computational result, and the rightmost side of each figure represent the experimental result.

6.4 Conclusion

This chapter discussed the impact of the laser energy and acquisition parameters on soot temperatures, soot concentration quantification, and effective primary particle diameter of different fuels in laminar diffusion flames and turbulent swirl spray flames. In methane laminar diffusion flames, the results suggested that the soot temperature and soot volume fraction obtained from the measurement depend on the laser fluence, acquisition delay time, and acquisition duration. Although the soot volume fraction is almost constant (variations less than 1 %) across different applied laser energy, the soot temperature reduced as the laser energy decreased with a difference of about 10 K. The soot temperature at 0 ns delay time was highest with the acquisition duration of 40 ns TTL and lowest with the 10 ns TTL. In all laminar flames, the soot temperature was found to have an inverse relationship to the acquisition delay.

The planar soot volume fraction measurements in methane/ DME - air flames at various fuel blending ratios displayed a reduction in soot volume fraction as DME was added to methane flame. The effect of acquisition delay time on temperature and soot volume fraction in ethylene/ DME air diffusion flames was also discussed. The results showed that the soot volume fraction in DME/ ethylene flame is less than in the pure ethylene flame. Whereas the addition of DME fuel into ethylene diffusion flame evidenced a reduced soot temperature at the end of the laser heating up to a time delay of 150 ns.

In turbulent swirl spray flames, the soot temperature reduced as a larger delay time was applied. On the other hand, the measured soot temperatures and concentrations showed a positive correlation relationship to the acquisition duration (TTL). The addition of iso-pentanol to n-heptane fuel was found to have a higher soot peak temperature at the end of the laser pulse and a decrease in the overall soot volume fraction.

The acquisition duration (TTL) was found to have an impact on the effective primary particle diameter measurement of all the flames, including laminar and turbulent. In laminar flames, it was found that the effective primary particle diameter at 10 ns and 20 ns TTL were equal to each other, whereas at 40 ns TTL diameter was lower. On the other hand, the effective primary particle diameter measurements in turbulent flames showed a direct relationship to the acquisition duration. The addition of DME to ethylene was found to increase the effective

primary particle diameter. Whereas the addition of iso-pentanol to n-heptane decreased the effective primary particle diameter.

Soot modelling of the F12 and F13 laminar diffusion flames was also carried out using the Moss-Brooks model to evaluate the potentiality of predicting soot in DME / C_2H_4 using the existing developed soot model in Ansys Fluent. The computational SVF results of F12 and F13, laminar diffusion flames, found a less-than-anticipated prediction because of not including all needed soot precursors in the chemical mechanism. Nevertheless, this study suggested the typical values of the T_α, T_γ C_α, and C_γ parameters for both the F12 and F13 flames, which can be used in the future for further investigations.

Chapter 7: The Impact of Dilution Air Strategy on the N-heptane Turbulent Swirl Spray Flames

7.1 Introduction

The injection of dilution air/ secondary air strategy downstream of the combustion chamber, also known as the Rich-Burn, Quick-Mix, Lean-Burn (RQL) combustor, of gas turbine engines was introduced in 1980 to reduce the NO_x emissions [62]. Using dilution air leads to a lean combustion, which decreases NO_x emissions. The global blow-off event may occur due to lean combustion, which is often linked with a higher probability of extinction. Therefore, this Chapter investigates the impact of dilution air strategy on the stability, HRR, and flame structure of n-heptane bluff-body swirl spray flames. The data measured using OH-PLIF, CH_2O-PLIF, and OH* chemiluminescence are presented in this chapter.

Besides the experimental work, 1D non-premixed laminar counter flow flame simulations were conducted to understand the flame structure behaviour and temperature when adding more air with hot products. 1D n-heptane non-premixed laminar diffusion flame simulations were performed using the counter flow COSILAB package [165] employed with the San Diego mechanism [167].

7.2 Flow Conditions

Pure n-heptane liquid fuel was tested in a bluff-body swirl spray burner with and without dilution air in this Chapter. The burner used for this chapter is the same for the cases of Chapters 5 and 6, but air tubes were inserted into the combustion chamber to introduce the air dilution. More details about the experimental rig setup can be found in Section 2.3.2.3 (Chapter 2). The flame conditions are shown in Table 2-4 (Chapter 2).

The mixing conditions for the 1D simulations are shown in Table 7-1. Two pure n-heptane flame conditions were numerically studied; one case (#1) with an oxidiser of air and hot combustion products, which can be considered as a close representation of the interaction in the shear layer (reaction zone area) of the swirl spray flame (without dilution air). The second case (#2) is with an oxidiser of 10% more air and hot combustion products representing the impact of dilution air. The mixing ratios of the hot combustion products (shown in Table 7-1) were decided based on laminar premixed flame calculations suggested by Sidey and Mastorakos [223]. The strain rate was varied to understand better the flame structure at conditions away and close to extinction. The simulated flame cases were set to a fixed fuel inlet temperature of 298 K, whereas the oxidiser inlet temperature was fixed at 1838 K for all cases. As mentioned in the introduction (Chapter 1), swirling flows generate an inner recirculation zone (IRZ) within the flame, creating an ideal condition for the hot, recirculated products to keep the newly injected reactants into the combustor constantly ignited. Therefore, the high inlet temperature set for the oxidiser and the introduction of hot products in the oxidiser stream provide a closer representation of the hot products generated in the swirl spray flames.

Table 7-1 Molar concentrations of the oxidiser stream for the 1D simulations of pure n-heptane counter flow flames.

Case	**Strain Rates (s^{-1})**	T_{ox} **(K)**	X_{O_2}	X_{N_2}	X_{H_2O}	X_{OH}	X_{CO_2}	X_{NO}
#1	1000, & 2000	1838	0.06	0.729258	0.14	7.3×10^{-4}	0.07	1.2×10^{-5}
#2	1000, & 2000	1838	0.075	0.7353322	0.126	6.6×10^{-4}	0.063	1.1×10^{-5}

7.3 Results and Discussion

This section shows the results of 1D counter flow simulations, OH-PLIF, CH_2O-PLIF, and OH* chemiluminescence for the n-heptane swirl spray flame with and without the addition of dilution air. The following subsections start with the 1D numerical results of counter flow flame (Section 7.3.1), followed by presenting the direct images to discuss the impact of dilution air on the flame appearance (Section 7.3.2). After that, stability limit testing is presented and discussed (Section 7.3.3). The fuel-PLIF, OH-PLIF, and CH_2O-PLIF results are then discussed (Section 7.3.4), followed by local extinction and lift-off results (Section 7.3.5). Finally, the OH* chemiluminescence are then presented in section 7.3.6.

7.3.1 Simulations of Laminar Counter flow Flames

The laminar counter flow flame simulation results of temperature, OH mole fraction, and heat release rate for pure n-heptane flame (#1 and #2 flame conditions) at strain rates of 1000 s^{-1} and 2000 $s^{-1}$are shown in Figures 7-1 and 7-2. The addition of 10% more air (#2 flame condition) on the oxidiser side increased the peak values of the temperature and HRR. The increased air in the oxidiser side makes the fuel burn more completely because more quantities of O_2 become available in the mixture. Consequently, the flame combustion generates more heat, increasing the flame's temperature, as shown in Figures 7-1 and 7-2. Adding 10% more air also increased the OH mole fraction. Increasing the OH mole fraction promotes more combustion reactions and increases the flame's temperature. Therefore, the flame stability can be enhanced by the increase in the concentration of OH. As expected, the increase in the strain rate from 1000 s^{-1} to 2000 s^{-1} decreased the peak values of temperature, OH mole fraction, and heat release rate. However, the increase in strain rate decreased the flame temperature by about 1.6% for #1 and 1.5% for #2. Therefore, it is expected that the case with an oxidiser of 10% more air to sustain longer.

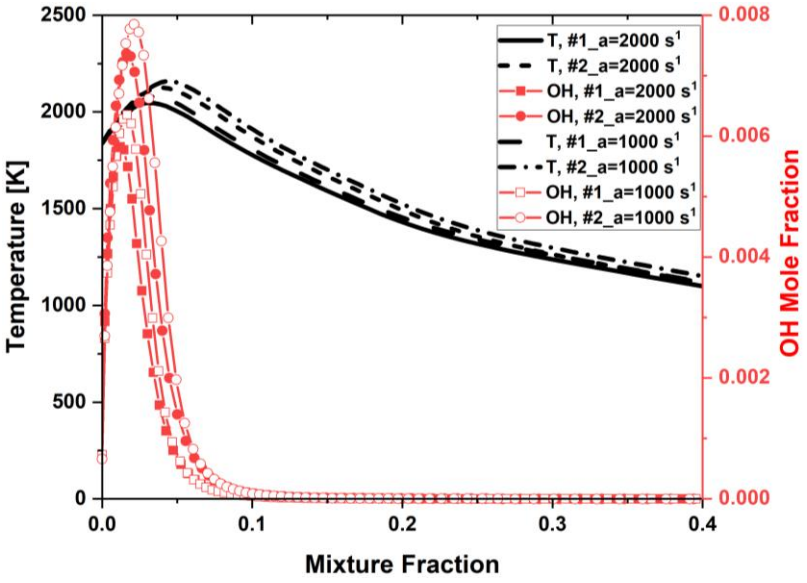

Figure 7-1 1D counter flow flame COSILAB simulation results of temperature and OH mole fraction for pure n-heptane (#1 and #2 flame conditions) at strain rates of 1000 s^{-1} and 2000 s^{-1}.

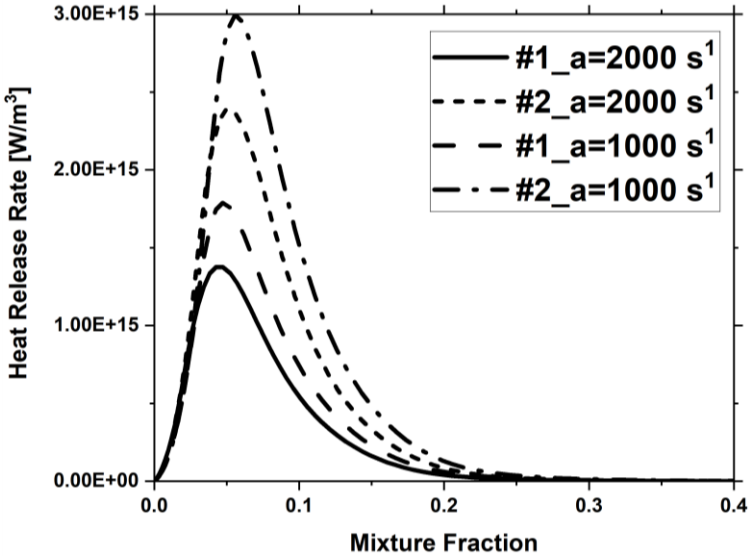

Figure 7-2 1D counter flow flame COSILAB simulation results of heat release rate for pure n-heptane (#1 and #2 flame conditions) at strain rates of 1000 s^{-1} and 2000 s^{-1}.

7.3.2 Flame Appearance

Figure 7-3 displays direct images of the n-heptane swirl spray flame with (QD_L) and without the (QN_L) dilution air effect. Prior to the introduction of air dilution, yellow was the dominant color appearance in the flame, indicating the presence of soot. Two clear flame branches at the inner recirculation zone (inner flame branch, IFB) and near the outer shear layer (outer flame branch, OFB) were shown in the flame. The IFB of the QN_L flame exhibited less reaction

(less luminous flame area) than the IFB of the QD_L flame. This possibly occurs because the hot product entering the IRZ is more with the effect of dilution air, making this flame branch look bigger. Introducing dilution air to the flame removed almost all the yellow luminosities. In addition, the flame was contained above the edge of the bluff-body within the outer shear layer and the height of the flame remained almost unchanged. The lift-off from the bluff-body is unclear from the direct images shown in Figure 7-3. More analysis on flame stabilization is to be discussed in the OH-PLIF subsection.

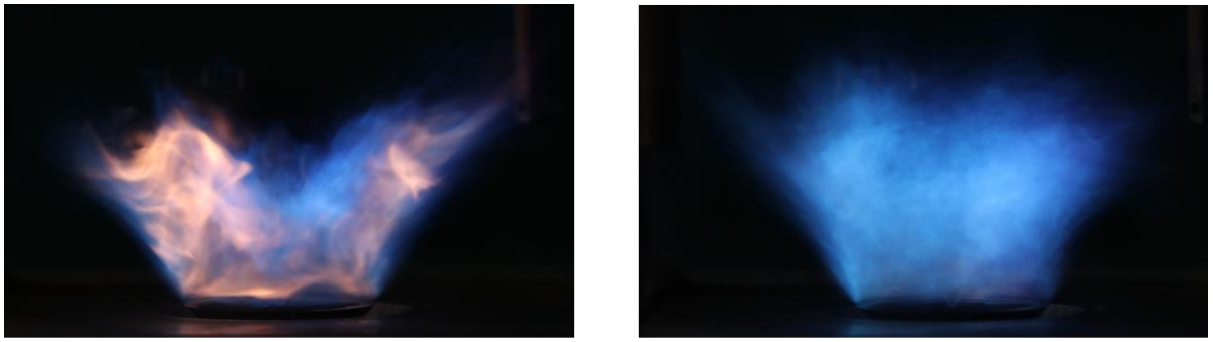

QN_L QD_L

Figure 7-3 N-heptane swirl spray flame with (QN_L) and without (QD_L) dilution air effect.

7.3.3 Stability Limit Testing

Stability limit testing was done at two fuel mass flow rates of 630 g/h and 700 g/h. The blow-off condition at each of these mass fuel rates was identified first, and then the dilution air was introduced. The mass flow rates of dilution air were added to each case by 2% and 5% of the co-flow air mass flow rate at blow-off condition. For example, 2% dilution air means the co-flow air kept at blow-off condition (i.e., 790 SLPM for the condition at 630 g/h) and 15.8 SLPM (2% of the 790 SLPM) added through the air dilution holes. Generally, the introduction of dilution air was found to increase the stability limit, as shown in Figure 7-4. The no dilution case quenched at 790 SLPM (Blow-off condition). The introduction of 2% dilution air made the flame last longer (unstable flame died after 5 minutes). Whereas the introduction of 5% dilution air turned the flame to be in a completely stable condition.

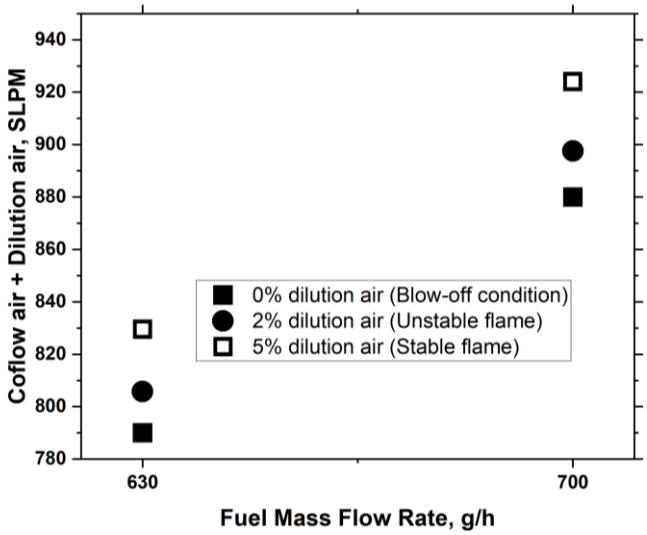

Figure 7-4 Fuel mass flow rate against the sum of co-flow air and dilution air.

7.3.4 PLIF

7.3.4.1 Fuel-PLIF

The background B(Q) signal near the Q1(6) transition was used to correct the background noise and to study the impact of dilution air on the fuel fluorescence signal, including the fuel trajectory and spray droplets. Figure 7-5 presents the mean images of the fuel-PLIF signal for the SN_H, SD1_H, SD2_H, and SD3_H (see Table 2-4, all are reacting cases, and the notation 1, 2, 3 refers to 2%, 5%, and 10% dilution). For the flame case names, S denotes the stable condition, N denotes the cases with no air dilution, and D is the conditions with air dilution. The overall spray trajectory and structure of all the cases have a cone-like shape, as shown in Figure 7-5. However, the droplet dispersion differs significantly. The effect of adding dilution air was found to break up the droplets into smaller droplets and spread them more broadly towards the IRZ region. This is caused by the force exerted (such as the aerodynamic drag force) from the diluted air combined with the recirculation air hitting the droplets. This enhances the direct removal of small droplets from the liquid jets surface (shear breakup). The surface area covered by the droplets increases with the increase of the amount of very small droplets, and hence the heat and mass exchange rates increase too. Therefore, the radial injection of air dilution produces fast mixing and a more stable flame.

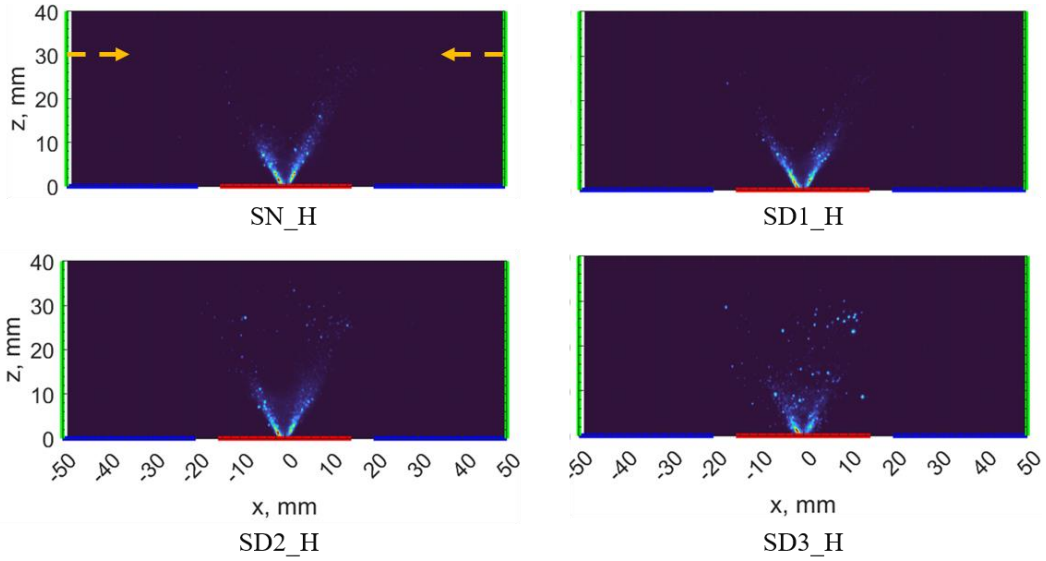

Figure 7-5 Mean images of fuel-PLIF signal for SN_H, SD1_H, SD2_H, and SD3_H. The arrows shown in the SN_H case indicate the height (30 mm above the nozzle) and location of dilution air injection (this applies to all cases).

7.3.4.2 OH-PLIF

In this study, the OH-PLIF images are used to give information and insight on the flame sheet characteristics affected by the introduction of dilution air. Figure 7-6 shows the instantaneous and averaged images of OH-PLIF for QN_L, QD_L, NN_L, ND_L, SN_L, and SD_L (Table 2-4). The instantaneous images suggest that cases without the dilution air (i.e., QN_L, NN_L, and SN_L) mostly have continuous OH flame sheets, in which the flame sheet in the OFB is extended from one edge of the bluff-body to the other edge. The flame sheet in the cases with dilution air (i.e., QD_L, ND_L, and SD_L) presents more local extinction due to the high turbulence level. The relatively small mass fuel flow rates used in this study (630 g/h and 700 g/h) resulted in a less effective liquid atomization, in which droplets were not efficiently broken to the finest size. This resulted in fuel-LIF signals from the fuel droplets contained in the OH-PLIF results, such as the signals found along the spray v-shape trajectory, adding difficulty in analyzing the characteristics of IRZ. The instantaneous images in Figure 7-6 clearly show the fuel-LIF signal. With background correction, the averaged images in Figure 7-6 mostly show no signal where the spray v-shape trajectory occurs. Nevertheless, few fuel-PLIF signals remain in the averaged OH-PLIF, as seen clearly in the QN_L case in Figure 7-6. Therefore, for a better comparison, relative OH intensity data across the height of 10 mm (Z-axis) were extracted and plotted against the radial position (see Figure 7-8) to avoid interference with the fuel-PLIF signal.

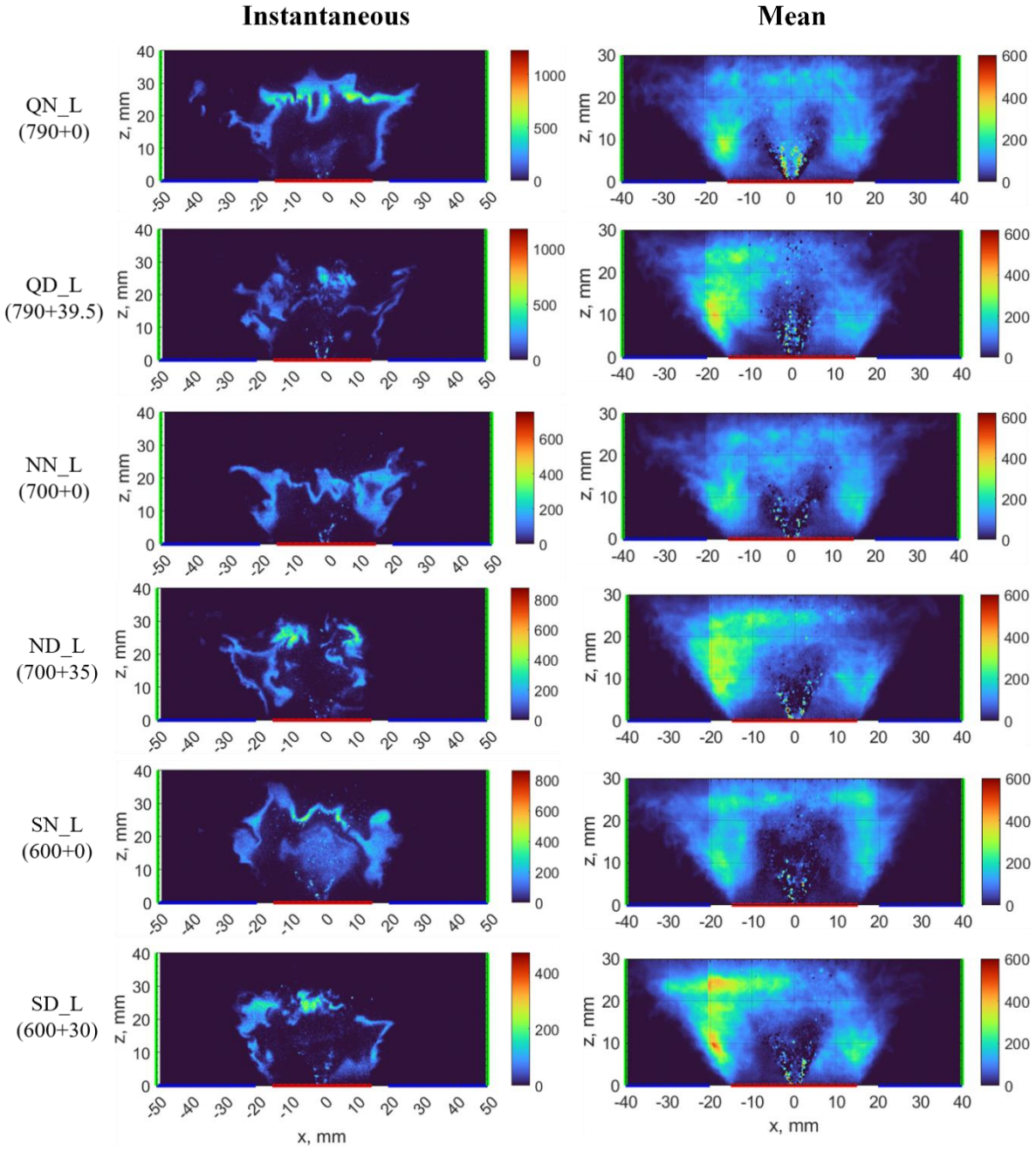

Figure 7-6 Instantaneous and averaged images of OH-PLIF for QN_L, QD_L, NN_L, ND_L, SN_L, and SD_L. Bracketed numbers underneath the case names denote the annular air flow rate (SLPM) + dilution air flow rate (SLPM). The laser beam's location is shown in green, the combustion chamber's bottom surface is shown in blue, and the surface of the bluff body is shown in red.

Figure 7-7 displays the instantaneous and averaged images of OH-PLIF for QN_H, QD_H, SN_H, SD1_H, SD2_H, and SD3_H. The observations presented here are almost similar to those delivered by Figure 7-6 regarding the direct relationship between the local extinction and dilution air. Nevertheless, it is shown in Figure 7-7 that the addition of dilution by 2% (SD1_H) of the co-flow air did not have a big impact on the flame sheet continuity, but it only shrank

towards the center of the flame and bluff-body. The corrected averaged OH-PLIF images suggest that adding dilution air increases the relative OH intensity in the OFB. This can be noticed by the increase in the red and yellow colour in the mean images (Figure 7-7) on adding more dilution air.

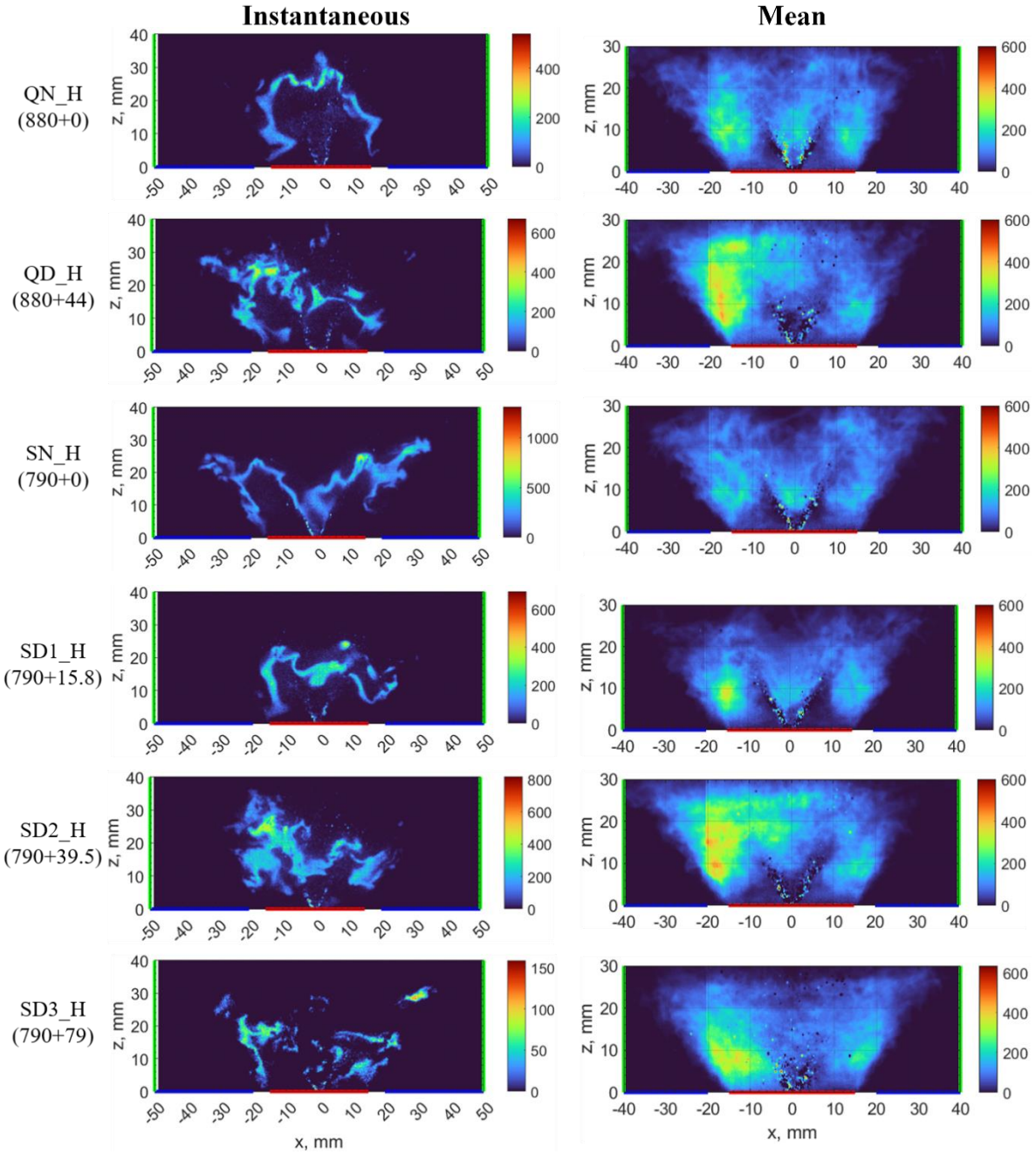

Figure 7-7 Instantaneous and averaged images of OH-PLIF for QN_H, QD_H, SN_H, SD1_H, SD2_H, and SD3_H. Bracketed numbers underneath the case names denote the annular air flow rate (SLPM) + dilution air flow rate (SLPM). The laser beam's location is shown in green, the combustion chamber's bottom surface is shown in blue, and the surface of the bluff body is shown in red.

The relative OH intensity across the height of 10 mm in the Z-axis was plotted against the radial position for all cases in Figure 7-8. In cases where air dilution was added, the relative intensity of OH was higher and the location where the OH peak values occur is almost consistent in all cases. The OFB is where the OH intensity peaks above the region where the annular air enters the chamber. The IRZ is found to have lower OH intensities generally than OFB. Without dilution air addition, the blow-off condition had higher OH intensity than the stable condition. However, adding dilution air to both conditions (stable and blow-off) increased the OH intensity to higher levels for the stable conditions compared to the blow-off case. Measurements shown in Figure 7-8 are plotted at 10 mm above the nozzle, so the peak values shown do not necessarily mean the peak values of the overall OH (only valid at 10 mm height) because the flame may become more compact when approaching the bluff-body in the blow-off condition. The cases with dilution air (dashed lines in Figure 7-8) have higher OH signal than those without dilution air (solid lines in Figure 7-8) at the same conditions. This means that the flame heights are similar at the same conditions, and therefore the OFB has a higher OH signal in cases with dilution air.

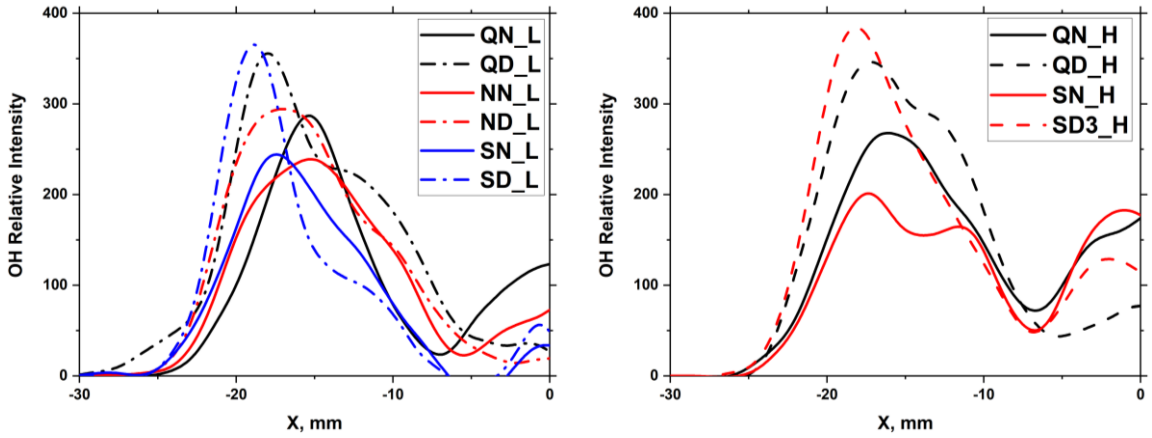

Figure 7-8 Relative OH intensity across the height of 10 mm in the Z-axis against the radial position for (left) cases with fuel mass flow rate of 630 g/h, and (right) cases with fuel mass flow rate of 700 g/h. Solid lines represent cases with no dilution air, and the discontinues lines represent cases with dilution air.

7.3.4.3 CH_2O-PLIF

The CH_2O-PLIF images are used to mark the low-temperature HRR regions in the flame. Figure 7-9 shows the instantaneous and averaged images of CH_2O-PLIF for NN_L, ND_L, SN_L, SD_L, and SD_L. Unlike the OH-PLIF signal, CH_2O-PLIF instantaneous images show

less CH_2O signal in the OFB in the cases with dilution air (i.e., ND_L and SD_L), indicating low HRR in the region above the bluff-body in between the OFB and IFB. In the cases with dilution air, most of the CH_2O signal is confined in the IRZ. The concentration of CH_2O signal in the IRZ is higher in SD_L (5% added air dilution) case than in SN_L (no air dilution). This is mainly because the radial introduction of air dilution interferes with the motion of the swirling air and makes the flow of air and fuel to recirculate more in the IRZ. The intense degrees of mixing and turbulence within the IRZ may enable the fuel to remain in the flame for more time. This will give it more opportunity to react with the oxygen and promote the production of CH_2O. The mean images in Figure 7-9 suggest less CH_2O signal in the cases with dilution air than those with no addition of dilution air.

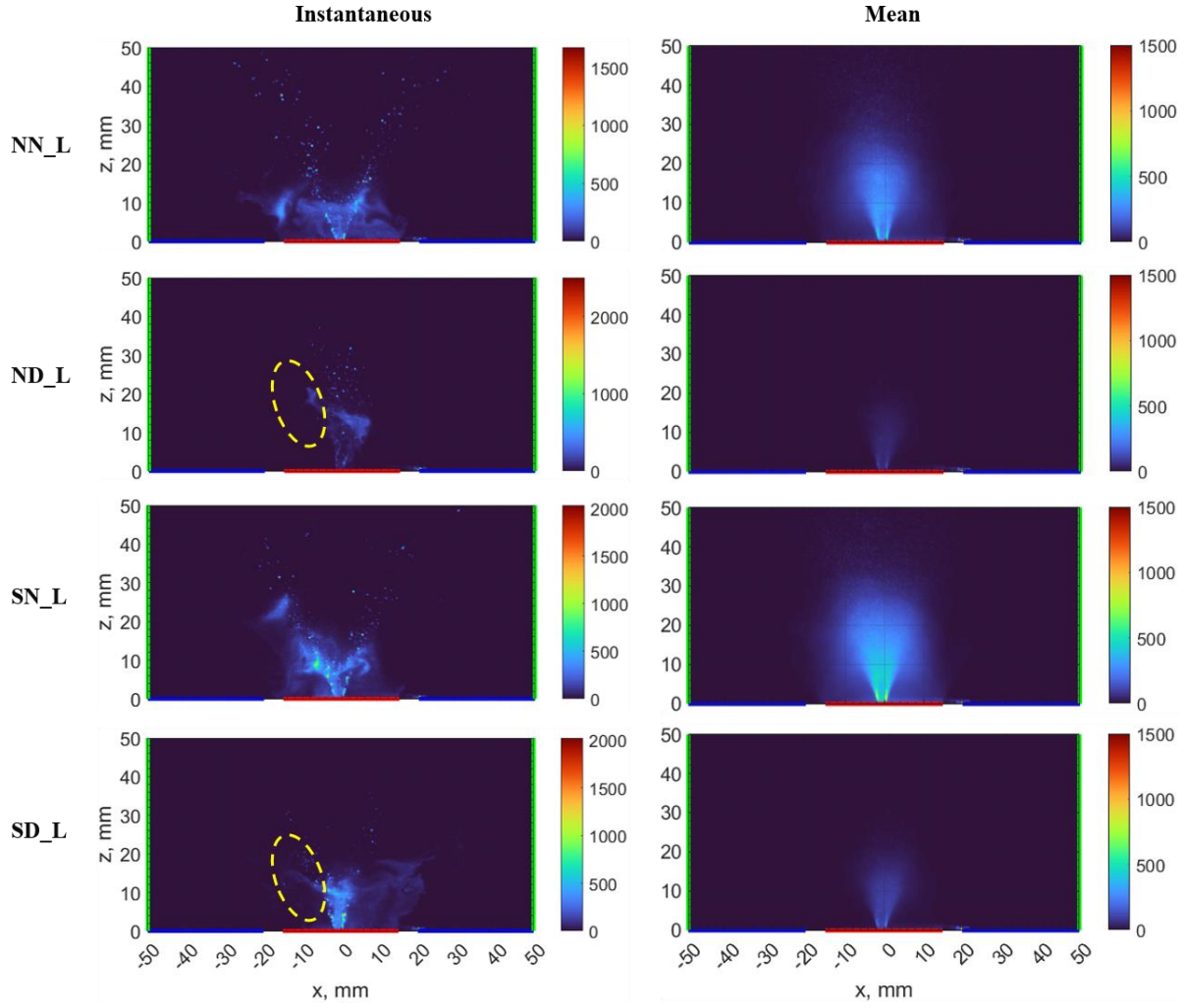

Figure 7-9 Instantaneous and mean images of CH_2O-PLIF for NN_L, ND_L, SN_L, ND_L, SD_L, and SD_L. The combustion chamber's bottom surface is shown in blue, and the surface of the bluff body is shown in red.

7.3.5 Local Extinction & Lift-off

Local extinction and lift-off characteristics of the flame sheets were investigated through the OH-PLIF results. Figure 7-10 illustrates the probability density function (PDF) against the number of local extinction events for all cases. Generally, all cases with dilution air added exhibited higher PDF of local extinction events than those without dilution air. The addition of dilution air (5% of air co-flow) to the cases with a lower fuel mass flow rate of 630 g/h resulted in increasing the occurrence of local extinction by 6-7.5%, regardless of the flame condition (i.e., at quenching, near blow-off, or stable condition). Whereas adding dilution air (5% of air co-flow) to the cases with a higher fuel mass flow rate of 700 g/h increased the occurrence of local extinction by 3.9%. The addition of dilution air by 2% of the air co-flow (i.e. SD1_H case) had negligible impact on the amount of local extinction occurrence. These percentages are calculated based on the difference of the areas under the curves.

The increase in the degree of local extinction with the addition of dilution air is due to the high turbulence flow. Local extinction occurrences were likely caused by the enormous air strain that the extremely high turbulence levels put on the flame front. The rate of diffusive mixing is accelerated by turbulence, which raises the flame surface area and scalar gradients [224]. Rapid mixing makes higher heat release rates (HRR) possible. Nevertheless, the rise in mixing rates could result in quenching the flame. The current cases studied in this work showed more stability when more dilution air was added to the flame despite the fact that local extinction events also increased. This could mean that the rates of heat diffusion did not outpace the rate of combustion's heat release in the current cases.

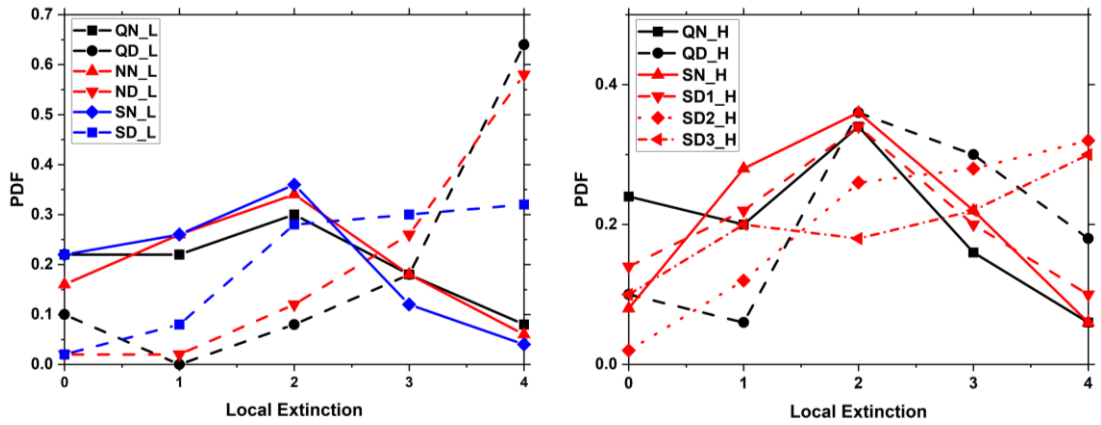

Figure 7-10 PDF of local extinction of (left) cases with fuel mass flow rate of 630 g/h, and (right) cases with fuel mass flow rate of 700 g/h.

Figure 7-11 shows the PDF of the lift-off height for all cases. The lift-off height decreased on moving from the stable condition towards the blow-off condition. Overall, the mean lift-off height reduces only slightly with the addition of dilution air. The addition of dilution air (5% of air co-flow) decreased the mean lift-off heights by about 0.007-0.01%. The lift-off heights were reduced by roughly 0.0145% when dilution air (10% of the air co-flow) was added. Therefore, there is almost no impact of the dilution air on the lift-off heights at the flow conditions tested. This is possibly due to the current location of the dilution air ports (30 mm above the burner surface) and the direction of dilution air injection (towards the burner central axis). The flame sheets were found to be confined further toward the burner's centre by the high air strain caused by the air dilution, as shown in SD1_H in Figure 7-7.

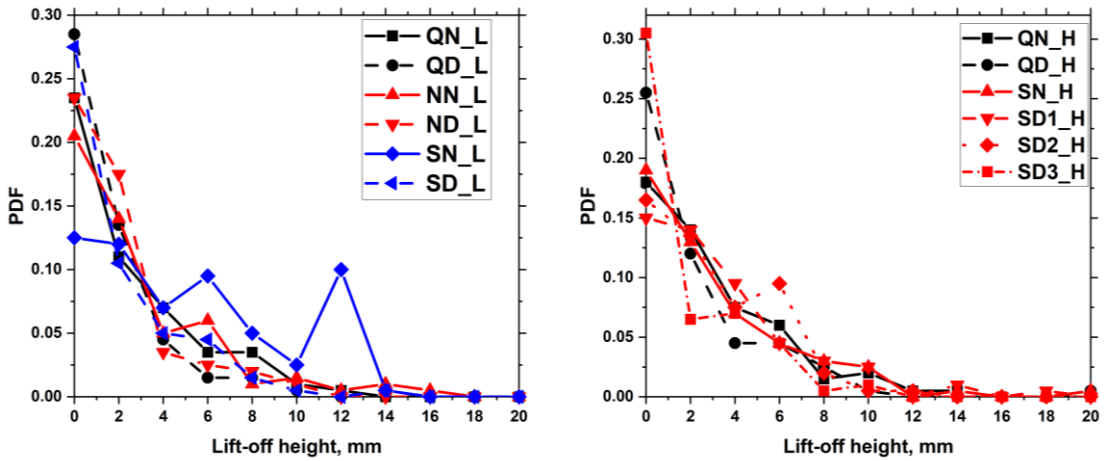

Figure 7-11 PDF of lift-off height of (left) cases with fuel mass flow rate of 630 g/h, and (right) cases with fuel mass flow rate of 700 g/h.

7.3.6 Chemiluminescence

OH* Chemiluminescence is well known as a heat release indicator. Figure 7-12 displays averaged inverse Abel transformed OH* Chemiluminescence images for QN_L, QD_L, NN_L, ND_L, SN_L, and SD_L cases. The two flame branches (IFB & OFB) are shown clearly in Figure 7-12 in the flame cases with no air dilution (QN_L, NN_L, and SN_L). Similar to what was observed earlier in the OH-PLIF results, OH* Chemiluminescence also confirms that the addition of dilution air confines the OFB further toward the center of the flame due to the high air strain caused by the air dilution. At all three flow conditions, the addition of dilution air increased the OH* signal (i.e., heat release rate) by 148%, 128%, and 47% for blow-off, near blow-off, and stable conditions, respectively, compared with the counterparts without

dilution. This increase is because of the rapid mixing between air and fuel, hence more recirculation of hot combustion products inside the IRZ. The results presented in Figure 7-12 show that the inner recirculation zone is where the OH* signals are at their greatest. More details on the flow field motion can be observed from a PIV study in the future. The addition of dilution air by 2% of the air co-flow (i.e., SD1_H) did not cause any increase in the HRR, as shown in Figure 7-12. Whereas adding dilution air by 5% and 10% (i.e., SD2_H & SD3_H) of the air co-flow increased the heat release rate by about 132% and 247%, respectively.

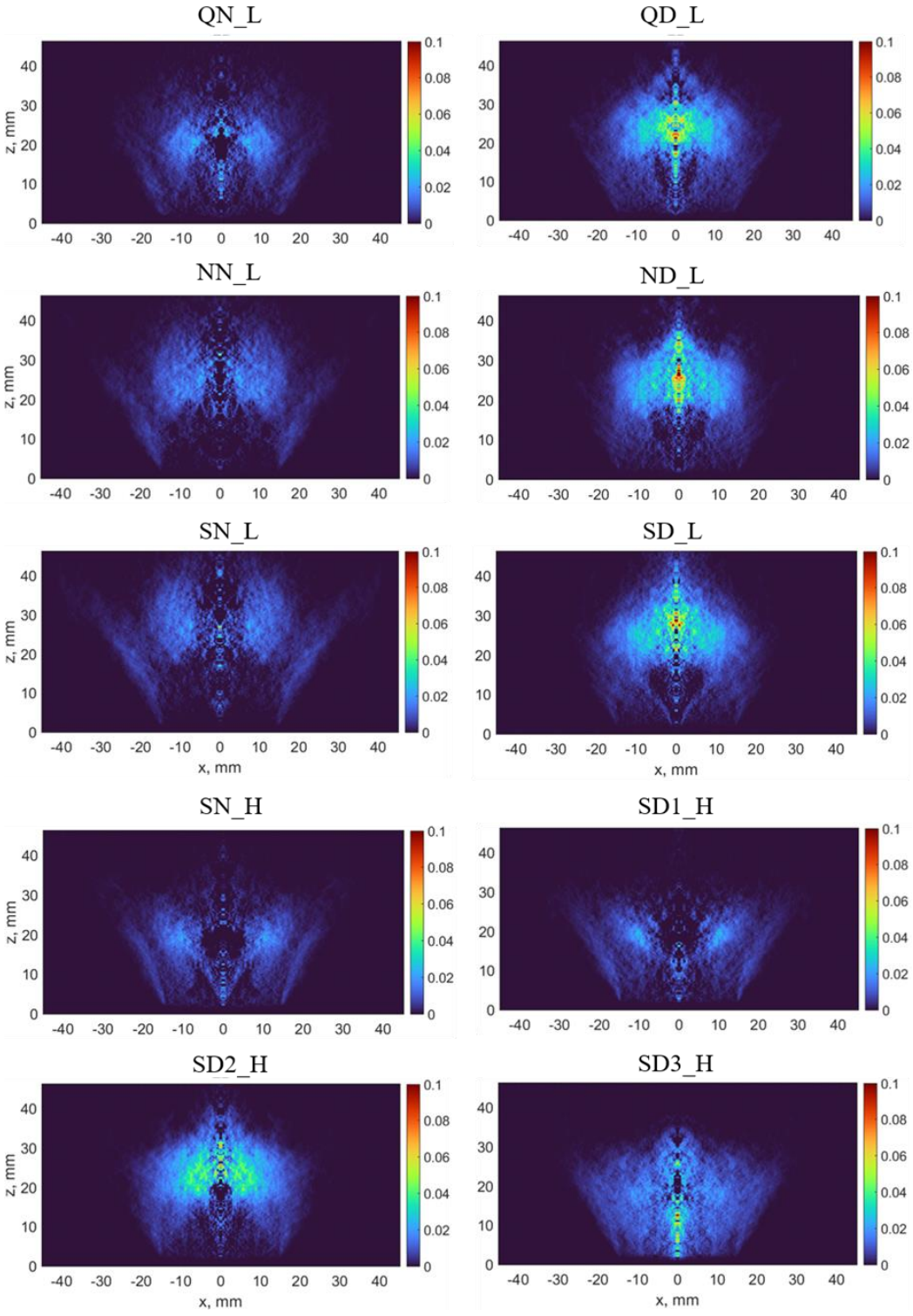

Figure 7-12 Averaged inverse Abel transformed images of OH* Chemiluminescence for QN_L, QD_L, NN_L, ND_L, SN_L, SD_L SN_H, SD1_H, SD2_H, and SD3_H cases.

7.4 Conclusion

This chapter has focused mainly on the impact of dilution air strategy on the stability, HRR and flame structure of n-heptane bluff-body swirl spray flames. N-heptane bluff-body swirl spray flame was studied in this chapter under different flow conditions including at quenching (global blow-off), near to blow-off, and stable conditions. In addition, simulations of 1D n-heptane non-premixed laminar counter flow flames were performed to gain a preliminary understanding of the behaviour and flame structure when adding air to heated products.

The results of a 1D simulation demonstrated that the addition of 10% more air to the oxidiser side increased the maximum temperature, OH mole fraction, and heat release rate. Direct images of n-heptane bluff-body swirl spray flames showed that adding dilution air removed almost all the dominant yellow color appearance (luminosity from the soot particles) in the flame. In addition, the flame branch in the IRZ appeared to cover a larger area in the case with added dilution air. The flame's stability limit increased when adding dilution air, and a 2% addition made the flame persist longer. The flame became completely steady with the addition of 5% dilution air at the blow-off co-flow conditions of the non-diluted flames. The addition of dilution air evidenced more efficient spray breakups closer to the nozzle, and visible droplets spread more widely into the IRZ. Cases without dilution air exhibited continuous OH flame sheets, overall thin, with the flame sheet extending from one edge of the bluff-body to the other. Whereas OH appears more cloud-shaped, wrinkled, and disturbed in the dilution cases. More local extinction occurred in the flame sheet in the dilute air cases due to the increased turbulence. OH-PLIF results showed that the addition of dilution air increases the relative OH intensity in the OFB at the same horizontal plane downstream. The concentration of the CH_2O signal in the IRZ became higher with the addition of air dilution. The impact of dilution air addition is very small on the lift-off height of the flame. A similar OH* (HRR) signal level was observed after adding dilution air at a rate of 2% of the air co-flow. While OH* intensity was raised by about 132% and 247% when dilution air was added to the air co-flow at 5% and 10%, respectively. The increase shown in OH (reaction zone), CH_2O, and OH* (HRR) agree with the observation of extended stability (blow-off limit) when adding dilution air studied in this chapter.

Chapter 8: Conclusions and Recommendations for Future Work

8.1 Conclusions from this Thesis

This thesis presents an experimental and numerical investigation of the combustion and emission characteristics of two key biofuels (DME & iso-pentanol) and their mixtures in different flame configurations and conditions. The primary aims of this thesis were to assess the effects of DME fuel addition on soot formation, heat release rate, and flame structure in co-flow laminar diffusion flames of hydrocarbon fuels, including methane and ethylene. In addition, to investigate the influence of iso-pentanol fuel addition on flame stability, soot formation, NO_x emission, heat release rate, and flame structure in n-heptane turbulent bluff-body swirl spray flames under different conditions, such as when the flame is far from blow-off and when it is close to blow-off.

1D laminar non-premixed flame calculations of DME/ methane/ ethylene flame mixtures, n-heptane flame, and iso-pentanol flame were conducted to obtain preliminary information on the mixtures flame structures and species profiles including OH*, OH, CH*, CH, HRR, CH_3, C_3H_3, C_2H_2, and flame temperature. The formation pathways of soot precursors were also

investigated from these simulations. The impact of adding DME to hydrocarbon fuels on combustion heat release and reaction zone was determined and investigated using CH*, OH*, and C_2* Chemiluminescence imaging systems over a wide range of DME mixing ratios. The OH-PLIF diagnostic method was used to determine how adding iso-pentanol fuel to n-heptane bluff-body swirl spray flames affect the structure of the flames, namely the lift-off heights and the amount of local extinction, at three different operating conditions including, stable, near blow-off, and far away from blow-off. Far away from blow-off conditions are also stable conditions, but with lower fuel and air flow rates than the others to examine the soot behaviours. Quantitative soot volume fraction and soot temperatures, measured using the 2C-LII technique, were also presented for DME flames and its mixtures as well as for iso-pentanol/ n-heptane flames. Additionally, the soot effective primary particle diameter was measured in n-heptane and n-heptane/ iso-pentanol swirl spray flames. Qualitative measurements of NO emissions were conducted using NO-PLIF for the iso-pentanol/ n-heptane flames. The results are summarised in the following subsections.

This thesis also included further investigations on the diagnostic methods and flame stability, which are helpful for current and future works. The feasibility of utilising OH*, CH*, or C_2* chemiluminescence as an HRR and equivalence ratio marker in non-premixed flames has been investigated on the DME/ hydrocarbon flames. For the 2C-LII diagnostic method, the impact of the laser fluence level, acquisition delay, and duration times on the calculated soot concentration was investigated, and its effect on the measurements was evaluated. A dilution air strategy was implemented in the n-heptane bluff-body swirl spray flame to investigate its effect on flame stability, HRR, and flame structure.

The subsequent sections of this chapter conclude the main outcomes of this thesis on the combustion and emission characteristics of DME & iso-pentanol and their mixtures. The last section (8.2) of this Chapter provides a few suggestions for future work.

8.1.1 Dimethyl Ether (DME) Fuel

Counter flow flame type along with a detailed chemical kinetic mechanism were used for the laminar flame calculations to study the characteristics of the flame structure, soot emission, and HRR of the DME/CH_4 and DME/C_2H_4 flames. Soot precursors (C_2H_2 and C_3H_3) were found to have a decreasing concentration in the CH_4 flame as the DME mixture ratio increased.

While 25% DME addition to a C_2H_4/N_2 flame raised C_3H_3 concentration, this effect was decreased when more DME was introduced into the flame. At 50% DME addition, the C_3H_3 concentration is lower than the C_2H_4/N_2 flame case. The reduction in net CH_3 concentration is directly connected to the decrease in net C_2H_2 and C_3H_3 production in DME/CH_4 flame mixes, but in DME/C_2H_4/N_2 flame mixtures, CH_3 had a positive impact on C_3H_3 net production at low DME mixing ratios (25%). Peak values of flame temperature (T) and OH were found to steadily increase with increasing DME mixture ratio in a CH_4 flame, while HRR, CH*, OH*, and CH mole fractions are found to decrease with increasing DME mixture ratio in CH_4 and C_2H_4 flames. As more DME and N_2 were introduced concurrently to methane and ethylene flames in equal power output conditions, the HRR and soot concentration peak values decreased. Adding DME to CH_4 and C_7H_{16} increased the required strain rate for quenching.

Experimentally, with a 25% addition of DME to CH_4 co-flow laminar diffusion flame, soot radiation appearance became more noticeable in C_2* chemiluminescence. On the contrary, increasing the DME mixture ratio by more than 25% weakened the soot radiation appearance, indicating either a lower soot concentration or a lower soot temperature. In conditions of equal power output, adding DME and N_2 concurrently caused a decrease in the OH* signal (HRR) and soot, in agreement with numerical observations. 2C-LII measurements showed that adding DME to CH_4 flame, at various fuel blending ratios reduces the planar soot volume fraction in the flame. However, the addition of DME to CH_4 flame increases the ePPDs, in which the ePPDs are equal to 33.7 nm, 33.7 nm, 48.1 nm, and 112 nm for DME mixing ratios (molar ratio of the DME/methane mixture) of 0, 0.25, 0.50, and 0.75, respectively.

The acquisition delay time affected the SVFs measurement from the 2C-LII technique. In methane–air diffusion flame, the observed SVF increased for the first 150 ns after the laser pulse ended, and subsequently, the variations in SVFs reached a plateau regime at longer delay durations (>500 ns). In addition, a small inverse relationship was observed at laser energy greater than 10% between incident laser fluence and measured soot concentration, with soot volume fractions differing by less than 1%. At less than 10% laser energy, however, the impact on SVFs is negligible. For DME/C_2H_4/N_2 flame mixture, when comparing the calculated SVFs at a delay time of > 20 ns to the pure ethylene/N_2 flame, the DME addition decreased SVFs. Nevertheless, an opposite conclusion was obtained when compared at delay times < 20 ns. In both DME/C_2H_4/N_2 and ethylene/N_2 flame mixtures, the observed SVF increased during the

first 100 ns after the laser pulse ended and reached a plateau regime after 150 ns. The addition of DME to C_2H_4/N_2 flame was also found to increase the ePPDs.

8.1.2 Iso-pentanol Fuel

The 1D laminar non-premixed flame calculations showed that pure iso-pentanol flame has a lower flame temperature than the pure n-heptane flame. The production of C_2H_2 occurs primarily via two routes: one via $CH_3 \rightarrow C_2H_6 \rightarrow C_2H_5 \rightarrow C_2H_4 \rightarrow C_2H_3 \rightarrow C_2H_2$ and the other via $C_3H_6 \rightarrow C_2H_3 \rightarrow C_2H_2$. The contribution of n-heptane to the production of C_2H_4 was greater than that of iso-pentanol.

Investigations on reaction zone characteristics and soot emission of the pure iso-pentanol, pure n-heptane fuels, and their 50:50 volume ratio mixtures were also carried out experimentally using a bluff-body swirl spray burner. This study also tested the pure ethanol flame and a 50:50 volume ratio mixture of ethanol/n-heptane to compare their reaction zone characteristics to iso-pentanol and n-heptane flames. All bluff-body swirl spray flames investigated in this study showed clear double flame sheet structures (inner and outer). It was observed that the atomisation of iso-pentanol is less efficient than heptane under the same flow conditions studied.

Far away from blow-off (sooting) and stable conditions, the n-heptane/iso-pentanol flame exhibited a lower overall lift-off height than the pure iso-pentanol flame. Pure iso-pentanol at near blow-off conditions showed the highest average lift-off amongst the pure iso-pentanol at stable and near blow-off cases. Iso-pentanol /n-heptane blend at near blow-off condition showed the lowest mean lift-off height amongst all near blow-off cases, including pure iso-pentanol, n-heptane, ethanol flames, and 50:50 volume ratio mixture of ethanol/n-heptane flame.

Regarding local extinction, pure iso-pentanol far away from the blow-off condition was found to have fewer local extinctions than n-heptane/iso-pentanol. In stable flame conditions, the highest occurrence of local extinctions was found in pure iso-pentanol compared to other flames and the lowest in the n-heptane/ethanol mixture. In near blow-off conditions, the number of local extinction events was highest in pure iso-pentanol and lowest in pure ethanol. In addition, the local extinctions increased when iso-pentanol was added to n-heptane.

In terms of heat release, adding iso-pentanol to the n-heptane flame increased the OH* chemiluminescence signal, which likely indicates the greater rate of heat release than pure n-heptane flame. 2C-LII measurements showed that adding iso-pentanol to n-heptane fuel resulted in a lower soot volume fraction overall and a greater soot peak temperature under the same laser fluence input. Furthermore, adding iso-pentanol to n-heptane reduces the ePPD.

The addition of dilution air downstream the chamber in n-heptane bluff-body swirl spray flame increased the flame's stability limit. Spray breakups were more effective near the nozzle area once dilution air was added, and visible droplets were observed to disperse more widely into the IRZ. In the dilute air cases, more local extinction was observed in the flame sheet, whereas the impact of dilution air addition on the flame's lift-off height was almost negligible.

8.2 Recommendations for Future Work

In this thesis, DME gaseous fuel demonstrated good combustion characteristics and the ability to reduce soot emissions when mixed with hydrocarbon fuels. From the combustion and emission side, DME showed to be a great potential alternative clean fuel. However, there still needs to be DME spray combustion studies in fundamental rigs. DME is a gas at room temperature (25 ℃), and thus in a fuel system, it requires to be pressurized to remain in the liquid state [225]. It is very difficult to fulfil the requirement of having a system that can pressurise or cool the DME (also very expensive), which may explain there is no research on DME spray combustion in atmospheric rigs. However, despite the difficulties, studying DME in a spray flame configuration is necessary for collecting information about the atomization process. Such data is essential for multiple factors; this includes improving the burning efficiency as well as engine performance. In addition, thorough research on DME in a spray flame configuration can aid in producing and developing accurate models of DME fuel combustion.

A quantitative measurement of OH-PLIF and NO-PLIF can be achieved for the DME co-flow laminar diffusion flame. This can be done using the quantitative OH study methodology explained by Hughes et al. [226]. It is extremely hard to quantitative one LIF signal as it may cause lots of errors, but the question can be simplified with collecting two LIF

signals with the same detection equipment. Apart of DME, a referenced fuel such as CH_4, where the mechanism is relatively validated by the community, can be considered as a second LIF signal. And, if accurate flame temperature profiles are available for both fuels (i.e., DME and CH_4), one of the ways that can help in obtaining a quantitative concentration profile of OH from the DME flame is to use both temperature profiles and back-calculate an OH fraction for DME. Boltzmann fraction and quenching rate are another important factors in the quantitative study, which are both temperature dependent. Boltzmann fraction population can be obtained from the LIFBASE simulation, whereas quenching rate can be obtained from previous experimental or theoretical investigations. For turbulent flames, this method remains a challenge, and further research is needed to apply this methodology.

Iso-pentanol fuel combustion studies in this thesis showed that it could enhance flame stability and reduce soot and NO_x emissions when added to the n-heptane bluff-body swirl spray flame. However, there was difficulty in obtaining some of the quantitative measurements, such as flame temperature and OH mole fractions from OH-PLIF, because of the inherent complexity of turbulent bluff-body swirl spray flames. The turbulence nature made it very difficult to precisely record and process the fluorescence signals. Nevertheless, despite these challenges, conducting further combustion studies on iso-pentanol and obtaining some quantitative measurements is essential and suggested. This will provide more important data on the combustion characteristics of iso-pentanol, even if it is through point-wise and not laser diagnostic methods.

Soot particles are not actually considered or categorised as GHGs. However, soot particles contribute to global warming. Soot particles can absorb the radiation coming from the sun and convert it into heat, which can affect the surrounding atmosphere. This little climatic impact on the atmosphere can play a role in changing the temperature. Therefore, soot has global warming potential, so the decarbonisation reduction effect by adding iso-pentanol needs to be evaluated further. In addition, a life-cycle assessment, including fuel production pathways and supply chain analysis, may be necessary for the next step to quantify CO_2 equivalent emissions further.

In Chapter 6, it was shown that there is a variation in measured SVFs that may be related to the uncertainty associated with the soot volume fraction Equation 2.18 (Chapter 2), in which

the soot temperature was used to obtain the SVF. Therefore, further investigations are also required in the next step to understand the source of uncertainty.

References

[1] K. Kohse-Höinghaus, “Combustion in the future: The importance of chemistry,” *Proc. Combust. Inst.*, vol. 38, no. 1, pp. 1–56, 2021, doi: 10.1016/J.PROCI.2020.06.375.

[2] A. M. Liaquat, M. A. Kalam, H. H. Masjuki, and M. H. Jayed, “Potential emissions reduction in road transport sector using biofuel in developing countries,” *Atmos. Environ.*, vol. 44, no. 32, pp. 3869–3877, 2010, doi: 10.1016/j.atmosenv.2010.07.003.

[3] UK Government, “Health matters: air pollution - GOV.UK,” *UK Government*, 2018. https://www.gov.uk/government/publications/health-matters-air-pollution/health-matters-air-pollution?fbclid=IwAR3rxTWjV5pjcGd3JBWSSVG_D7e6mO81fgi67vm2v8bfw6fvzif8F4mkRAs (accessed Apr. 16, 2022).

[4] World Health Organization, “Ambient (outdoor) air pollution,” *World Health Organization*, 2022. https://www.who.int/news-room/fact-sheets/detail/ambient-(outdoor)-air-quality-and-health (accessed Apr. 18, 2023).

[5] D. Dajnak, D. Evangelopoulos, N. Kitwiroon, S. Beevers, and H. Walton, “London Health Burden of Current Air Pollution and Future Health Benefits of Mayoral Air Quality Policies,” *Imp. Coll. London Proj.*, 2021, [Online]. Available: http://erg.ic.ac.uk/research/home/projects/tfl-hia-maqp.html.

[6] Environmental Audit Committee, “Are biofuels sustainable?,” London, 2008. [Online]. Available: https://publications.parliament.uk/pa/cm200708/cmselect/cmenvaud/76/76ii.pdf.

[7] J. Norman MP and Department For Transport, “New regulations to double the use of sustainable renewable fuels by 2020,” *Gov.Uk*, 2018. https://www.gov.uk/government/news/new-regulations-to-double-the-use-of-sustainable-renewable-fuels-by-2020#:~:text=The key changes to the,rising to 2.8%25 in 2032 (accessed Feb. 01, 2020).

[8] C. Bae and J. Kim, “Alternative fuels for internal combustion engines,” *Proc. Combust. Inst.*, vol. 36, no. 3, pp. 3389–3413, 2017, doi: 10.1016/J.PROCI.2016.09.009.

[9] I. M. Yusri *et al.*, “Alcohol based automotive fuels from first four alcohol family in compression and spark ignition engine: A review on engine performance and exhaust emissions,” *Renew. Sustain. Energy Rev.*, vol. 77, pp. 169–181, 2017, doi: 10.1016/J.RSER.2017.03.080.

[10] E. Sadeghinezhad *et al.*, “A comprehensive literature review of bio-fuel performance in internal combustion engine and relevant costs involvement,” *Renew. Sustain. Energy Rev.*, vol. 30, pp. 29–44, 2014, doi: 10.1016/J.RSER.2013.09.022.

[11] V. S. Sikarwar, M. Zhao, P. S. Fennell, N. Shah, and E. J. Anthony, “Progress in biofuel production from gasification,” *Prog. Energy Combust. Sci.*, vol. 61, pp. 189–248, Jul. 2017, doi: 10.1016/J.PECS.2017.04.001.

[12] A. A. Saleh, K. J. Hughes, and R. Yuan, “Reaction zone characteristics of iso-pentanol swirl

spray flames using OH-PLIF and 2C-LII," *Proc. Combust. Inst.*, vol. 39, no. 2, pp. 2663–2672, 2023, doi: 10.1016/j.proci.2022.07.232.

[13] L. Xu, Y. Wang, and D. Liu, "Effects of oxygenated biofuel additives on soot formation: A comprehensive review of laboratory-scale studies," *Fuel*, vol. 313, p. 122635, Apr. 2022, doi: 10.1016/J.FUEL.2021.122635.

[14] K. A. Sorate and P. V. Bhale, "Biodiesel properties and automotive system compatibility issues," *Renewable and Sustainable Energy Reviews*, vol. 41. Elsevier Ltd, pp. 777–798, 2015, doi: 10.1016/j.rser.2014.08.079.

[15] R. Karmakar, K. Kundu, and A. Rajor, "Fuel properties and emission characteristics of biodiesel produced from unused algae grown in India," *Pet. Sci.*, vol. 15, no. 2, pp. 385–395, May 2018, doi: 10.1007/s12182-017-0209-7.

[16] C. Arcoumanis, C. Bae, R. Crookes, and E. Kinoshita, "The potential of di-methyl ether (DME) as an alternative fuel for compression-ignition engines: A review," *Fuel*, vol. 87, no. 7, pp. 1014–1030, Jun. 2008, doi: 10.1016/J.FUEL.2007.06.007.

[17] Pubchem, "Ethanol, CH3CH2OH, CID 702," *Pubchem*, 2019. https://pubchem.ncbi.nlm.nih.gov/compound/Ethanol (accessed Mar. 06, 2023).

[18] Engineering Toolbox, "Fluids - Latent Heat of Evaporation," *Engineering ToolBox*. https://www.engineeringtoolbox.com/fluids-evaporation-latent-heat-d_147.html (accessed Feb. 10, 2023).

[19] H. Jääskeläinen, "Ethanol-Diesel Blends," 2006. https://dieselnet.com/tech/fuel_ediesel.php (accessed Jan. 15, 2020).

[20] Y. Yang, J. Dec, N. Dronniou, and B. Simmons, "Characteristics of isopentanol as a fuel for HCCI engines," *SAE Tech. Pap.*, vol. 3, no. 2, pp. 725–741, 2010, doi: 10.4271/2010-01-2164.

[21] U. Pfahl, K. Fieweger, and G. Adomeit, "Self-ignition of diesel-relevant hydrocarbon-air mixtures under engine conditions," *Symp. Combust.*, vol. 26, no. 1, pp. 781–789, 1996, doi: 10.1016/S0082-0784(96)80287-6.

[22] Z. Chen, X. Qin, Y. Ju, Z. Zhao, M. Chaos, and F. L. Dryer, "High temperature ignition and combustion enhancement by dimethyl ether addition to methane-air mixtures," *Proc. Combust. Inst.*, vol. 31 I, no. 1, pp. 1215–1222, 2007, doi: 10.1016/j.proci.2006.07.177.

[23] F. Liu *et al.*, "An experimental and numerical study of the effects of dimethyl ether addition to fuel on polycyclic aromatic hydrocarbon and soot formation in laminar coflow ethylene/air diffusion flames," *Combust. Flame*, vol. 158, no. 3, pp. 547–563, Mar. 2011, doi: 10.1016/J.COMBUSTFLAME.2010.10.005.

[24] S. L. Fischer, F. L. Dryer, and H. J. Curran, "The Reaction Kinetics of Dimethyl Ether. I: High-Temperature Pyrolysis and Oxidation in Flow Reactors," *Int. J. Chem. Kinet.*, vol. 32, no. 12, pp. 713–740, 2000, doi: 10.1002/1097-4601(2000)32:12<713::AID-KIN1>3.0.CO;2-9.

[25] Z. Li, H. M. F. Amin, P. Liu, Y. Wang, S. H. Chung, and W. L. Roberts, "Effect of dimethyl ether (DME) addition on sooting limits in counterflow diffusion flames of ethylene at elevated pressures," *Combust. Flame*, vol. 197, pp. 463–470, 2018, doi: 10.1016/j.combustflame.2018.09.003.

[26] C. Jin *et al.*, “Effects of C3–C5 alcohols on solubility of alcohols/diesel blends,” *Fuel*, vol. 236, pp. 65–74, Jan. 2019, doi: 10.1016/j.fuel.2018.08.129.

[27] S. Mani Sarathy *et al.*, “A comprehensive experimental and modeling study of iso-pentanol combustion,” *Combust. Flame*, vol. 160, no. 12, pp. 2712–2728, 2013, doi: 10.1016/j.combustflame.2013.06.022.

[28] A. C. Hansen, Q. Zhang, and P. W. L. Lyne, “Ethanol-diesel fuel blends - A review,” *Bioresour. Technol.*, vol. 96, no. 3, pp. 277–285, 2005, doi: 10.1016/J.BIORTECH.2004.04.007.

[29] S. Arias, M. L. Botero, F. Molina, and J. R. Agudelo, “Pentanol/diesel fuel blends: Assessment of inhalation cancer risk and ozone formation potential from carbonyl emissions emitted by an automotive diesel engine,” *Fuel*, vol. 321, no. December 2021, p. 124054, 2022, doi: 10.1016/j.fuel.2022.124054.

[30] S. Y. No, “Utilization of Pentanol as Biofuels in Compression Ignition Engines,” *Front. Mech. Eng.*, vol. 6, p. 15, 2020, doi: 10.3389/FMECH.2020.00015/BIBTEX.

[31] Y. Hua, F. Liu, H. Wu, C.-F. Lee, and Y. Li, “Effects of alcohol addition to traditional fuels on soot formation: A review,” *Int. J Engine Res.*, vol. 22, no. 5, pp. 1395–1420, 2021, doi: 10.1177/1468087420910886.

[32] L. Li, J. Wang, Z. Wang, and J. Xiao, “Combustion and emission characteristics of diesel engine fueled with diesel/biodiesel/pentanol fuel blends,” *Fuel*, vol. 156, pp. 211–218, Sep. 2015, doi: 10.1016/J.FUEL.2015.04.048.

[33] J. Abboud *et al.*, “Impacts of oxygenated compounds concentration on sooting propensities and soot oxidative reactivity: Application to Diesel and Biodiesel surrogates,” *Fuel*, vol. 193, pp. 241–253, Apr. 2017, doi: 10.1016/J.FUEL.2016.12.034.

[34] L. Li, J. Wang, Z. Wang, and H. Liu, “Combustion and emissions of compression ignition in a direct injection diesel engine fueled with pentanol,” *Energy*, vol. 80, pp. 575–581, Feb. 2015, doi: 10.1016/J.ENERGY.2014.12.013.

[35] E. Koivisto, N. Ladommatos, and M. Gold, “Systematic study of the effect of the hydroxyl functional group in alcohol molecules on compression ignition and exhaust gas emissions,” *Fuel*, vol. 153, pp. 650–663, Aug. 2015, doi: 10.1016/J.FUEL.2015.03.042.

[36] B. Rajesh Kumar and S. Saravanan, “Use of higher alcohol biofuels in diesel engines: A review,” *Renew. Sustain. Energy Rev.*, vol. 60, pp. 84–115, Jul. 2016, doi: 10.1016/J.RSER.2016.01.085.

[37] T. Suchocki *et al.*, “A comparative study of pentanol (C5 alcohol) and kerosene blends in terms of gas turbine engine performance and exhaust gas emission,” *Fuel*, vol. 334, no. July 2022, 2023, doi: 10.1016/j.fuel.2022.126741.

[38] Joint Bioenergy Institute, “JBEI Performance Metric for FY16: Develop an improved metabolic engineering method for modifying microorganisms for biofuel production from cellulosic sugars.,” 2015. Accessed: May 23, 2022. [Online]. Available: https://www.jbei.org/wp-content/uploads/2015/12/Q1-report_Developing-new-biofuels-at-JBEI.pdf.

[39] W. Bartok and adel f. Sarofim, *FOSSIL FUEL COMBUSTION*. NEW JERSEY: John Wiley & Sons, Inc, 1991.

[40] H. Pitsch, “Laminar Diffusion Flames,” *CEFRC Combustion Summer School*, 2014. https://cefrc.princeton.edu/sites/g/files/toruqf1071/files/Files/2014 Lecture Notes/Pitsch/Lecture6_LamDiffFlames_2014.pdf (accessed Jun. 06, 2021).

[41] S. M. Ali and Varunkumar, “On extinction Strain rate of Counterflow diffusion flames.,” 2017, [Online]. Available: file:///C:/Users/mep18aya/Downloads/On_extinction_Strain_rate_of_Counterflow_diffusion.pdf.

[42] A. Jordà Juanós and W. A. Sirignano, “Extinction Analysis of a Methane-Oxygen Counterflow Flame at High Pressure,” *Combust. Sci. Technol.*, vol. 189, no. 12, pp. 2180–2194, Dec. 2017, doi: 10.1080/00102202.2017.1367293.

[43] M. D. Smooke, M. B. Long, B. C. Connelly, M. B. Colket, and R. J. Hall, “Soot formation in laminar diffusion flames,” *Combust. Flame*, vol. 143, no. 4, pp. 613–628, Dec. 2005, doi: 10.1016/J.COMBUSTFLAME.2005.08.028.

[44] C. Presser, A. K. Gupta, and H. G. Semerjian, “Aerodynamic characteristics of swirling spray flames: Pressure-jet atomizer,” *Combust. Flame*, vol. 92, no. 1–2, 1993, doi: 10.1016/0010-2180(93)90196-A.

[45] A. Williams, “Fundamentals of oil combustion,” *Prog. Energy Combust. Sci.*, vol. 2, no. 3, pp. 167–179, 1976, doi: 10.1016/0360-1285(76)90011-3.

[46] G. M. Faeth, “Evaporation and combustion of sprays,” *Prog. Energy Combust. Sci.*, vol. 9, no. 1–2, pp. 1–76, 1983, doi: 10.1016/0360-1285(83)90005-9.

[47] W. A. Sirignano, “Fuel droplet vaporization and spray combustion theory,” *Prog. Energy Combust. Sci.*, vol. 9, no. 4, pp. 291–322, Jan. 1983, doi: 10.1016/0360-1285(83)90011-4.

[48] C. Presser, A. K. Gupta, C. T. Avedisian, and H. G. Semerjian, “Fuel property effects on the structure of spray flames,” *Symp. Combust.*, vol. 23, no. 1, pp. 1361–1367, Jan. 1991, doi: 10.1016/S0082-0784(06)80401-7.

[49] S. Russo and A. Gomez, “Structure of laminar coflow spray flames at different pressures,” *Proc. Combust. Inst.*, vol. 29, no. 1, pp. 601–608, 2002, doi: 10.1016/s1540-7489(02)80077-3.

[50] C. Hollmann and E. Gutheil, “Flamelet-Modeling of Turbulent Spray Diffusion Flames Based on a Laminar Spray Flame Library,” *Combust. Sci. Technol.*, vol. 135, no. 1–6, pp. 175–192, 1998, doi: 10.1080/00102209808924156.

[51] E. Gutheil, “Structure and extinction of laminar ethanol-air spray flames,” *http://dx.doi.org/10.1088/1364-7830/5/2/301*, 2006, doi: 10.1088/1364-7830/5/2/301.

[52] E. Gutheil and W. A. Sirignano, “Counterflow spray combustion modeling with detailed transport and detailed chemistry,” *Combust. Flame*, vol. 113, no. 1–2, pp. 92–105, Apr. 1998, doi: 10.1016/S0010-2180(97)00192-2.

[53] B. Guo and A. Ghalambor, “Natural Gas Engineering Handbook: Second Edition,” *Nat. Gas Eng. Handb. Second Ed.*, pp. 1–472, May 2012, doi: 10.1016/C2013-0-15534-1.

[54] P. Weigand, W. Meier, X. R. Duan, W. Stricker, and M. Aigner, “Investigations of swirl flames in a gas turbine model combustor: I. Flow field, structures, temperature, and species

distributions," *Combust. Flame*, vol. 144, no. 1–2, pp. 205–224, Jan. 2006, doi: 10.1016/j.combustflame.2005.07.010.

[55] M. Juddoo and A. R. Masri, "High-speed OH-PLIF imaging of extinction and re-ignition in non-premixed flames with various levels of oxygenation," *Combust. Flame*, vol. 158, no. 5, pp. 902–914, May 2011, doi: 10.1016/j.combustflame.2011.02.003.

[56] V. N. Prasad, M. Juddoo, A. R. Masri, W. P. Jones, and K. H. Luo, "Investigation of extinction and re-ignition in piloted turbulent non-premixed methane–air flames using LES and high-speed OH-LIF," *Combust. Theory Model.*, vol. 17, no. 3, pp. 483–503, Jun. 2013, doi: 10.1080/13647830.2013.779389.

[57] B. V. Raushenbakh and S. A. Belyy, *Physical Principles Of the Working Process in Combustion Chambers of Jet Engines*. 1967.

[58] P. Flohr and P. Stuttaford, "Combustors in gas turbine systems," *Mod. Gas Turbine Syst. High Effic. Low Emiss. Fuel Flex. Power Gener.*, pp. 151-191e, Jan. 2013, doi: 10.1533/9780857096067.2.151.

[59] D. C. Dayton and T. D. Foust, "Optimized Biofuels for High-Efficiency, Low-Emission Engines," *Anal. Methods Biomass Charact. Convers.*, pp. 129–145, Jan. 2020, doi: 10.1016/B978-0-12-815605-6.00009-3.

[60] N. Syred and J. M. Beér, "Combustion in swirling flows: A review," *Combust. Flame*, vol. 23, no. 2, pp. 143–201, Oct. 1974, doi: 10.1016/0010-2180(74)90057-1.

[61] S. Candel, D. Durox, T. Schuller, J. F. Bourgouin, and J. P. Moeck, "Dynamics of swirling flames," *Annu. Rev. Fluid Mech.*, vol. 46, pp. 147–173, 2014, doi: 10.1146/annurev-fluid-010313-141300.

[62] R. M. Pierce, S. A. Mosier, C. E. Smith, and B. S. Hinton, "Advanced combustion systems for stationary gas turbine engines. Volume II. Bench scale evaluation. Final report September 1976-January 1978." Jan. 01, 1980.

[63] S. Samuelsen, *The Gas Turbine Handbook*, 3.2.1.3. Morgantown, WV: U.S. Department of Energy-National Energy Technology Laboratory (NETL), 2006.

[64] I. El Helou, J. M. Foale, R. S. Pathania, R. Ciardiello, and A. W. Skiba, "A comparison between fossil and synthetic kerosene flames from the perspective of soot emissions in a swirl spray RQL burner," *Fuel*, vol. 331, no. P1, p. 125608, 2023, doi: 10.1016/j.fuel.2022.125608.

[65] P. Basu, C. Kefa, and L. Jestin, *Boilers and burners: desing and theory*, vol. 1. Springer, 2000.

[66] D. E. Cavaliere, J. Kariuki, and E. Mastorakos, "A Comparison of the Blow-Off Behaviour of Swirl-Stabilized Premixed, Non-Premixed and Spray Flames," *Flow Turbul. Combust*, vol. 91, pp. 347–372, 2013, doi: 10.1007/s10494-013-9470-z.

[67] T. Boushaki, "Introductory Chapter: Swirling Flows and Flames," in *Swirling Flows and Flames*, IntechOpen, 2019.

[68] H. J. Sheen, W. J. Chen, S. Y. Jeng, and T. L. Huang, "Correlation of Swirl Number for a Radial-Type Swirl Generator," *Exp. Therm. Fluid Sci.*, vol. 12, no. 4, pp. 444–451, May 1996, doi: 10.1016/0894-1777(95)00135-2.

[69] İ. Yılmaz, “Effect of Swirl Number on Combustion Characteristics in a Natural Gas Diffusion Flame,” *J. Energy Resour. Technol.*, vol. 135, no. 4, Dec. 2013, doi: 10.1115/1.4024222.

[70] S.-H. Chuang, C.-S. Yang, and N.-J. Wu, “Predictions of swirling flow in sudden-expansion dump combustor with flameholder side-inlet using two-step combustion model,” *Int. J. Numer. Methods Heat Fluid Flow*, vol. 9, no. 7, pp. 764–787, 1999, doi: 10.1108/09615539910291154.

[71] F. K. Owen, L. J. Spadaccini, and C. T. Bowman, “Pollutant formation and energy release in confined turbulent diffusion flames,” *Symp. Combust.*, vol. 16, no. 1, pp. 105–117, Jan. 1977, doi: 10.1016/S0082-0784(77)80317-2.

[72] M. S. A. Ishak and M. N. M. Jaafar, “The effect of swirl number on reducing emissions from liquid fuel burner system,” *J. Mek.*, no. 19, pp. 48–56, 2005.

[73] X. Yang, X. Huang, W. Zhang, P. Wei, and S. Xu, “Comparisons of the Emissions of Ethanol/Diesel and n-Pentanol/Diesel Fuel Blends: Engine Test and Kinetic Modeling Study,” *IEEE Access*, vol. 7, pp. 106213–106224, 2019, doi: 10.1109/ACCESS.2019.2928315.

[74] J. P. Longwell, E. E. Frost, and M. A. Weiss, “Flame Stability in Bluff Body Recirculation Zones,” *Ind. Eng. Chem.*, vol. 45, no. 8, pp. 1629–1633, Aug. 1953, doi: 10.1021/ie50524a019.

[75] P. Kumar and D. P. Mishra, “Effects of bluff-body shape on LPG-H2 jet diffusion flame,” *Int. J. Hydrogen Energy*, vol. 33, no. 10, pp. 2578–2585, May 2008, doi: 10.1016/j.ijhydene.2008.02.075.

[76] S. Chaudhuri and B. M. Cetegen, “Blowoff characteristics of bluff-body stabilized conical premixed flames with upstream spatial mixture gradients and velocity oscillations,” *Combust. Flame*, vol. 153, no. 4, pp. 616–633, Jun. 2008, doi: 10.1016/j.combustflame.2007.12.008.

[77] L. Wang, M. Salewski, B. Sundén, A. Borg, and H. Abrahamsson, “Endwall convective heat transfer for bluff bodies,” *Int. Commun. Heat Mass Transf.*, vol. 39, no. 2, pp. 167–173, Feb. 2012, doi: 10.1016/j.icheatmasstransfer.2011.10.006.

[78] M. Namazian, J. Kelly, and R. W. Schefer, “Velocity Measurements in a Turbulent Nonpremixed Bluff-Body Stabilized Flame,” *Combust. Sci. Technol.*, vol. 56, no. 4–6, pp. 101–138, Dec. 1987, doi: 10.1080/00102208708947084.

[79] W. M. Roquemore, R. S. Tankin, H. H. Chiu, and S. A. Lottes, “A study of a bluff-body combustor using laser sheet lighting,” *Exp. Fluids*, vol. 4, no. 4, pp. 205–213, Jul. 1986, doi: 10.1007/BF00717816.

[80] F. El-Mahallawy and S. E.-D. Habik, “Fundamentals and Technology of Combustion,” 2002. doi: 10.1016/B978-008044106-1/50007-3.

[81] United States Environmental Protection Agency, “Particulate Matter (PM) Pollution EPA, US,” *EPA.gov*. https://www.epa.gov/pm-pollution (accessed Mar. 14, 2021).

[82] H. Guo, Z. Gub, K. A. Thomson, G. J. Smallwood, and F. F. Baksh, “Soot formation in a laminar ethylene/air diffusion flame at pressures from 1 to 8 atm,” *Proc. Combust. Inst.*, vol. 34, no. 1, pp. 1795–1802, Jan. 2013, doi: 10.1016/j.proci.2012.07.006.

[83] D. R. Tree and K. I. Svensson, “Soot processes in compression ignition engines,” *Progress in*

Energy and Combustion Science, vol. 33, no. 3. Pergamon, pp. 272–309, Jun. 2007, doi: 10.1016/j.pecs.2006.03.002.

[84] I. Glassman and R. A. Yetter, *Combustion*, vol. 136, no. 1. Academic Press, 2008.

[85] C. P. Fenimore, "Oxidation of soot by hydroxyl radicals," *J. Phys. Chem.*, vol. 71, no. 3, pp. 593–597, 1967, doi: 10.1021/j100862a021.

[86] K. G. Neoh, J. B. Howard, and A. F. Sarofim, "Effect of oxidation on the physical structure of soot," *Symp. Combust.*, vol. 20, no. 1, pp. 951–957, Jan. 1985, doi: 10.1016/S0082-0784(85)80584-1.

[87] A. Garo, G. Prado, and J. Lahaye, "Chemical aspects of soot particles oxidation in a laminar methane-air diffusion flame," *Combust. Flame*, vol. 79, no. 3–4, pp. 226–233, Mar. 1990, doi: 10.1016/0010-2180(90)90134-D.

[88] R. Puri, R. J. Santoro, and K. C. Smyth, "The oxidation of soot and carbon monoxide in hydrocarbon diffusion flames," *Combust. Flame*, vol. 97, no. 2, pp. 125–144, May 1994, doi: 10.1016/0010-2180(94)90001-9.

[89] O. I. Smith, "Fundamentals of soot formation in flames with application to diesel engine particulate emissions," *Prog. Energy Combust. Sci.*, vol. 7, no. 4, pp. 275–291, 1981, doi: 10.1016/0360-1285(81)90002-2.

[90] X. Wang *et al.*, "Soot formation during biomass pyrolysis: Effects of temperature, water-leaching, and gas-phase residence time," *J. Anal. Appl. Pyrolysis*, vol. 134, pp. 484–494, Sep. 2018, doi: 10.1016/j.jaap.2018.07.015.

[91] M. Frenklach, "Reaction mechanism of soot formation in flames," *Phys. Chem. Chem. Phys.*, vol. 4, no. 11, pp. 2028–2037, 2002, doi: 10.1039/b110045a.

[92] H. Böhm, H. Jander, and D. Tanke, "PAH growth and soot formation in the pyrolysis of acetylene and benzene at high temperatures and pressures: Modeling and experiment," in *Symposium (International) on Combustion*, 1998, vol. 27, no. 1, pp. 1605–1612, doi: 10.1016/S0082-0784(98)80570-5.

[93] H. Richter and J. B. Howard, "Formation and consumption of single-ring aromatic hydrocarbons and their precursors in premixed acetylene, ethylene and benzene flames," in *Physical Chemistry Chemical Physics*, 2002, vol. 4, no. 11, pp. 2038–2055, doi: 10.1039/b110089k.

[94] J. A. Miller and C. F. Melius, "Kinetic and thermodynamic issues in the formation of aromatic compounds in flames of aliphatic fuels," *Combust. Flame*, vol. 91, no. 1, pp. 21–39, 1992, doi: 10.1016/0010-2180(92)90124-8.

[95] C. H. Wu and R. D. Kern, "Shock-tube study of allene pyrolysis," *J. Phys. Chem.*, vol. 91, no. 24, pp. 6291–6296, Nov. 1987, doi: 10.1021/j100308a042.

[96] B. A. V. Bennett, C. S. McEnally, L. D. Pfefferle, M. D. Smooke, and M. B. Colket, "Computational and experimental study of the effects of adding dimethyl ether and ethanol to nonpremixed ethylene/air flames," *Combust. Flame*, vol. 156, no. 6, pp. 1289–1302, Jun. 2009, doi: 10.1016/J.COMBUSTFLAME.2009.01.020.

[97] M. Frenklach and H. Wang, “Detailed modeling of soot particle nucleation and growth,” *Symp. Combust.*, vol. 23, no. 1, pp. 1559–1566, 1991, doi: 10.1016/S0082-0784(06)80426-1.

[98] H. A. Michelsen *et al.*, “Modeling laser-induced incandescence of soot: A summary and comparison of LII models,” *Appl. Phys. B Lasers Opt.*, vol. 87, no. 3, pp. 503–521, May 2007, doi: 10.1007/s00340-007-2619-5.

[99] A. Miffre, C. Anselmo, S. Geffroy, E. Fréjafon, and P. Rairoux, “Lidar remote sensing of laser-induced incandescence on light absorbing particles in the atmosphere,” *Opt. Express*, vol. 23, no. 3, p. 2347, Feb. 2015, doi: 10.1364/oe.23.002347.

[100] Z. W. Sun, D. H. Gu, G. J. Nathan, Z. T. Alwahabi, and B. B. Dally, “Single-shot, Time-Resolved planar Laser-Induced Incandescence (TiRe-LII) for soot primary particle sizing in flames,” *Proc. Combust. Inst.*, vol. 35, no. 3, pp. 3673–3680, Jan. 2015, doi: 10.1016/j.proci.2014.07.066.

[101] D. R. Snelling, G. J. Smallwood, F. Liu, Ö. L. Gülder, and W. D. Bachalo, “A calibration-independent laser-induced incandescence technique for soot measurement by detecting absolute light intensity,” in *Applied Optics*, Nov. 2005, vol. 44, no. 31, pp. 6773–6785, doi: 10.1364/AO.44.006773.

[102] R Marsh *et al.*, “Studying, sampling and measurement of aircraft particulate emissions II (SAMPLE II) – Final Report,” Köln, Dec. 2009. Accessed: Nov. 30, 2021. [Online]. Available: https://www.easa.europa.eu/document-library/research-reports/easa2009op18.

[103] K. Hayashida, T. Mogi, K. Amagai, and M. Arai, “Growth characteristics of polycyclic aromatic hydrocarbons in dimethyl ether diffusion flame,” *Fuel*, vol. 90, no. 2, pp. 493–498, Feb. 2011, doi: 10.1016/j.fuel.2010.10.012.

[104] S. S. Yoon, D. H. Anh, and S. H. Chung, “Synergistic effect of mixing dimethyl ether with methane, ethane, propane, and ethylene fuels on polycyclic aromatic hydrocarbon and soot formation,” *Combust. Flame*, vol. 154, no. 3, pp. 368–377, Aug. 2008, doi: 10.1016/j.combustflame.2008.04.019.

[105] H. A. Ahmed, M. A. Ashraf, S. A. Steinmetz, M. J. Dunn, and A. R. Masri, “The role of DME addition on the evolution of soot and soot precursors in laminar ethylene jet flames,” *Proc. Combust. Inst.*, vol. 38, no. 4, pp. 5319–5329, Jan. 2021, doi: 10.1016/J.PROCI.2020.06.055.

[106] T. Li, T. Mitra, C. Chu, Y. Yuan, and M. J. Thomson, “Investigation of PAH and soot formation in a dimethyl ether (DME) laminar coflow diffusion flame,” *Combust. Flame*, vol. 223, pp. 437–449, Jan. 2021, doi: 10.1016/j.combustflame.2020.10.019.

[107] B. H. Timmerman, S. Patel, P. Dunkley, and P. J. Bryanston-Cross, “Optical investigation of heat release and NOx production in combustion,” *Opt. Diagnostics*, vol. 5880, no. August 2005, p. 58800Q, 2005, doi: 10.1117/12.619230.

[108] C. T. Bowman, “Kinetics of nitric oxide formation incombustion processes,” *Symp. Combust.*, vol. 14, no. 1, pp. 729–738, Jan. 1973, doi: 10.1016/S0082-0784(73)80068-2.

[109] S. R. Turns, *Introduction to Combustion: Concepts and Applications*, Second. New York: McGraw-Hill, 2000.

[110] C. P. Fenimore, “Formation of nitric oxide in premixed hydrocarbon flames,” *Symp. Combust.*, vol. 13, no. 1, pp. 373–380, 1971, doi: 10.1016/S0082-0784(71)80040-1.

[111] J. A. Miller and C. T. Bowman, “Mechanism and modeling of nitrogen chemistry in combustion,” *Progress in Energy and Combustion Science*, vol. 15, no. 4. Pergamon, pp. 287–338, Jan. 1989, doi: 10.1016/0360-1285(89)90017-8.

[112] M. Sirignano, M. Salamanca, and A. D’Anna, “The role of dimethyl ether as substituent to ethylene on particulate formation in premixed and counter-flow diffusion flames,” *Fuel*, vol. 126, pp. 256–262, Jun. 2014, doi: 10.1016/J.FUEL.2014.02.039.

[113] B. C. Choi, S. K. Choi, S. H. Chung, J. S. Kim, and J. H. Choi, “Experimental and numerical investigation of fuel mixing effects on soot structures in counterflow diffusion flames,” *Int. J. Automot. Technol. 2011 122*, vol. 12, no. 2, pp. 183–191, Mar. 2011, doi: 10.1007/S12239-011-0022-Z.

[114] C. S. McEnally and L. D. Pfefferle, “The effects of dimethyl ether and ethanol on benzene and soot formation in ethylene nonpremixed flames,” *Proc. Combust. Inst.*, vol. 31, no. 1, pp. 603–610, Jan. 2007, doi: 10.1016/J.PROCI.2006.07.005.

[115] J. Y. Hwang, W. Lee, H. G. Kang, and S. H. Chung, “Synergistic Effect of Ethylene–Propane Mixture on Soot Formation in Laminar Diffusion Flames,” *Combust. Flame*, vol. 114, no. 3–4, pp. 370–380, Aug. 1998, doi: 10.1016/S0010-2180(97)00295-2.

[116] M. R. J. Charest, Ö. L. Gülder, and C. P. T. Groth, “Numerical and experimental study of soot formation in laminar diffusion flames burning simulated biogas fuels at elevated pressures,” *Combust. Flame*, vol. 161, no. 10, pp. 2678–2691, Oct. 2014, doi: 10.1016/J.COMBUSTFLAME.2014.04.012.

[117] J. H. Choi *et al.*, “Effects of DME mixing on number density and size properties of soot particles in counterflow non-premixed ethylene flames,” *J. Mech. Sci. Technol.*, vol. 29, no. 5, pp. 2259–2267, 2015, doi: 10.1007/s12206-015-0447-9.

[118] M. Serwin and A. E. Karataş, “Effects of oxygen on soot formation in laminar co-flow flames of binary mixtures of ethane, DME, and oxygen,” *Combust. Flame*, vol. 229, p. 111413, Jul. 2021, doi: 10.1016/J.COMBUSTFLAME.2021.111413.

[119] W. Ying, Z. Longbao, and W. Hewu, “Diesel emission improvements by the use of oxygenated DME/diesel blend fuels,” *Atmos. Environ.*, vol. 40, no. 13, pp. 2313–2320, Apr. 2006, doi: 10.1016/J.ATMOSENV.2005.12.016.

[120] C. Tang, L. Wei, X. Man, J. Zhang, Z. Huang, and C. K. Law, “High temperature ignition delay times of C5 primary alcohols,” *Combust. Flame*, vol. 160, no. 3, pp. 520–529, Mar. 2013, doi: 10.1016/J.COMBUSTFLAME.2012.11.018.

[121] S. Mani Sarathy *et al.*, “A comprehensive experimental and modeling study of iso-pentanol combustion,” *Combust. Flame*, vol. 160, no. 12, pp. 2712–2728, Dec. 2013, doi: 10.1016/j.combustflame.2013.06.022.

[122] T. Tsujimura *et al.*, “Development of Isopentanol Reaction Mechanism Reproducing Autoignition Character at High and Low Temperatures,” *Energy and Fuels*, vol. 26, no. 8, pp. 4871–4886, Aug. 2012, doi: 10.1021/EF300879K.

[123] D. Nativel *et al.*, “Laminar flame speeds of pentanol isomers: An experimental and modeling study,” *Combust. Flame*, vol. 166, pp. 1–18, 2016, doi: 10.1016/j.combustflame.2015.11.012.

[124] T. Tsujimura, W. J. Pitz, Y. Yang, and J. E. Dec, “Detailed Kinetic Modeling of HCCI Combustion with Isopentanol,” *SAE Int. J. Fuels Lubr.*, vol. 4, no. 2, pp. 257–270, Dec. 2011, doi: 10.4271/2011-24-0023.

[125] G. Dayma, C. Togb, and P. Dagaut, “Experimental and Detailed Kinetic Modeling Study of Isoamyl Alcohol (Isopentanol) Oxidation in a Jet-Stirred Reactor at Elevated Pressure,” vol. 25, pp. 4986–4998, 2011, doi: 10.1021/ef2012112.

[126] Y. Ying, C. Xu, D. Liu, B. Jiang, P. Wang, and W. Wang, “Nanostructure and Oxidation Reactivity of Nascent Soot Particles in Ethylene/Pentanol Flames,” *Energies 2017, Vol. 10, Page 122*, vol. 10, no. 1, p. 122, Jan. 2017, doi: 10.3390/EN10010122.

[127] P. A. Carniglia, “Effects of Flow Field and Spray Characteristics on Soot in a Swirl-Stabilized Model Combustor,” University of Toronto, 2021.

[128] Y. Ma, S. Huang, R. Huang, Y. Zhang, and S. Xu, “Ignition and combustion characteristics of n-pentanol–diesel blends in a constant volume chamber,” *Appl. Energy*, vol. 185, pp. 519–530, Jan. 2017, doi: 10.1016/J.APENERGY.2016.11.002.

[129] L. Wei, C. S. Cheung, and Z. Huang, “Effect of n-pentanol addition on the combustion, performance and emission characteristics of a direct-injection diesel engine,” *Energy*, vol. 70, pp. 172–180, Jun. 2014, doi: 10.1016/J.ENERGY.2014.03.106.

[130] B. Rajesh Kumar and S. Saravanan, “Effect of exhaust gas recirculation (EGR) on performance and emissions of a constant speed DI diesel engine fueled with pentanol/diesel blends,” *Fuel*, vol. 160, pp. 217–226, Nov. 2015, doi: 10.1016/J.FUEL.2015.07.089.

[131] N. Yilmaz and A. Atmanli, “Experimental evaluation of a diesel engine running on the blends of diesel and pentanol as a next generation higher alcohol,” *Fuel*, vol. 210, pp. 75–82, Dec. 2017, doi: 10.1016/J.FUEL.2017.08.051.

[132] Z. Li, Q. Zhang, X. Hu, B. Liu, Z. Chen, and J. Liu, “Combustion and Emission Characteristics of Diesel Engines Using Diesel, DMF/Diesel, and N-Pentanol/Diesel Fuel Blends,” *Artic. J. Energy Eng.*, 2018, doi: 10.1061/(ASCE)EY.1943-7897.0000549.

[133] B. Rajesh Kumar and S. Saravanan, “Effects of iso-butanol/diesel and n-pentanol/diesel blends on performance and emissions of a DI diesel engine under premixed LTC (low temperature combustion) mode,” *Fuel*, vol. 170, pp. 49–59, Apr. 2016, doi: 10.1016/J.FUEL.2015.12.029.

[134] Y. Yoshimoto, E. Kinoshita, and T. Otaka, “Trade-off Improvements by Combining EGR and Supercharging Ignited by Next Generation Bio-alcohol Blended FAME Fuels in Diesel Dual Fuel Operation Using Natural Gas,” *Front. Mech. Eng.*, vol. 6, p. 67, Aug. 2020, doi: 10.3389/FMECH.2020.00067/BIBTEX.

[135] T. Tsujimura *et al.*, “Development of Isopentanol Reaction Mechanism Reproducing Autoignition Character at High and Low Temperatures,” 2012, doi: 10.1021/ef300879k.

[136] B. O. Ayoola, R. Balachandran, J. H. Frank, E. Mastorakos, and C. F. Kaminski, “Spatially resolved heat release rate measurements in turbulent premixed flames,” *Combust. Flame*, vol. 144, no. 1–2, pp. 1–16, Jan. 2006, doi: 10.1016/J.COMBUSTFLAME.2005.06.005.

[137] J. P. Hathout, M. Fleifil, A. M. Annaswamy, and A. F. Ghoniem, “Heat-release actuation for

control of mixture-inhomogeneity-driven combustion instability," *Proc. Combust. Inst.*, vol. 28, no. 1, pp. 721–730, 2000, doi: 10.1016/S0082-0784(00)80274-X.

[138] N. Swaminathan, G. Xu, A. P. Dowling, and R. Balachandran, "Heat release rate correlation and combustion noise in premixed flames," *J. Fluid Mech.*, vol. 681, pp. 80–115, Aug. 2011, doi: 10.1017/JFM.2011.232.

[139] I. A. Mulla *et al.*, "Heat release rate estimation in laminar premixed flames using laser-induced fluorescence of CH2O and H-atom," *Combust. Flame*, vol. 165, pp. 373–383, Mar. 2016, doi: 10.1016/J.COMBUSTFLAME.2015.12.023.

[140] R. Yuan, J. Kariuki, A. Dowlut, R. Balachandran, and E. Mastorakos, "Reaction zone visualisation in swirling spray n-heptane flames," *Proc. Combust. Inst.*, vol. 35, no. 2, pp. 1649–1656, 2015, doi: 10.1016/j.proci.2014.06.012.

[141] J. G. Lee and D. A. Santavicca, "Experimental Diagnostics for the Study of Combustion Instabilities in Lean Premixed Combustors," *https://doi.org/10.2514/2.6191*, vol. 19, no. 5, pp. 735–750, May 2012, doi: 10.2514/2.6191.

[142] Y. Hardalupas and M. Orain, "Local measurements of the time-dependent heat release rate and equivalence ratio using chemiluminescent emission from a flame," *Combust. Flame*, vol. 139, no. 3, pp. 188–207, Nov. 2004, doi: 10.1016/J.COMBUSTFLAME.2004.08.003.

[143] S. Sardeshmukh, M. Bedard, and W. Anderson, "The use of OH* and CH* as heat release markers in combustion dynamics," *Int. J. Spray Combust. Dyn.*, vol. 9, no. 4, pp. 409–423, 2017, doi: 10.1177/1756827717718483.

[144] M. E. Baumgardner and J. Harvey, "Analyzing OH*, CH*, and C2* chemiluminescence of bifurcating FREI propane-air flames in a micro flow reactor," *Combust. Flame*, vol. 221, pp. 349–351, 2020, doi: 10.1016/j.combustflame.2020.08.009.

[145] C. S. Panoutsos, Y. Hardalupas, and A. M. K. P. Taylor, "Numerical evaluation of equivalence ratio measurement using OH∗ and CH∗ chemiluminescence in premixed and non-premixed methane–air flames," *Combust. Flame*, vol. 156, no. 2, pp. 273–291, Feb. 2009, doi: 10.1016/J.COMBUSTFLAME.2008.11.008.

[146] H. N. Najm, P. H. Paul, C. J. Mueller, and P. S. Wyckoff, "On the Adequacy of Certain Experimental Observables as Measurements of Flame Burning Rate," *Combust. Flame*, vol. 113, no. 3, pp. 312–332, May 1998, doi: 10.1016/S0010-2180(97)00209-5.

[147] A. Stagni *et al.*, "The influence of low-temperature chemistry on partially-premixed counterflow n-heptane/air flames," *Combust. Flame*, vol. 188, pp. 440–452, 2018, doi: 10.1016/j.combustflame.2017.10.002.

[148] A. Verdier, J. Marrero Santiago, A. Vandel, G. Godard, G. Cabot, and B. Renou, "Local extinction mechanisms analysis of spray jet flame using high speed diagnostics," *Combust. Flame*, vol. 193, pp. 440–452, Jul. 2018, doi: 10.1016/J.COMBUSTFLAME.2018.03.032.

[149] A. M. Steinberg, I. Boxx, C. M. Arndt, J. H. Frank, and W. Meier, "Experimental study of flame-hole reignition mechanisms in a turbulent non-premixed jet flame using sustained multi-kHz PIV and crossed-plane OH PLIF," *Proc. Combust. Inst.*, vol. 33, no. 1, pp. 1663–1672, 2011, doi: 10.1016/J.PROCI.2010.06.134.

[150] R. Yuan, J. Kariuki, and E. Mastorakos, “Measurements in swirling spray flames at blow-off,” *Orig. Res. Artic.*, doi: 10.1177/1756827718763559.

[151] J. Benajes, J. M. García-Oliver, J. M. Pastor, I. Olmeda, A. Both, and D. Mira, “Analysis of local extinction of a n-heptane spray flame using large-eddy simulation with tabulated chemistry,” *Combust. Flame*, vol. 235, p. 111730, Jan. 2022, doi: 10.1016/J.COMBUSTFLAME.2021.111730.

[152] J. Gimeno, P. Martí-Aldaraví, M. Carreres, and S. Cardona, “Experimental investigation of the lift-off height and soot formation of a spray flame for different co-flow conditions and fuels,” *Combust. Flame*, vol. 233, p. 111589, Nov. 2021, doi: 10.1016/J.COMBUSTFLAME.2021.111589.

[153] Y. C. Chen, C. C. Chang, K. L. Pan, and J. T. Yang, “Flame lift-off and stabilization mechanisms of nonpremixed jet flames on a bluff-body burner,” *Combust. Flame*, vol. 115, no. 1–2, pp. 51–65, 1998, doi: 10.1016/S0010-2180(97)00336-2.

[154] T. Nishimura, K. Kunitsugu, and K. I. Morio, “The hysteresis phenomenon in flame lift-off on a bluff-body burner under airflow dominant conditions,” *Combust. Flame*, vol. 159, no. 4, pp. 1499–1502, Apr. 2012, doi: 10.1016/J.COMBUSTFLAME.2011.12.010.

[155] I. A. Mulla and B. Renou, “Simultaneous imaging of soot volume fraction, PAH, and OH in a turbulent n-heptane spray flame,” *Combust. Flame*, vol. 209, pp. 452–466, Nov. 2019, doi: 10.1016/J.COMBUSTFLAME.2019.08.012.

[156] A. Giusti and E. Mastorakos, “Turbulent Combustion Modelling and Experiments: Recent Trends and Developments,” *Flow, Turbul. Combust.*, vol. 103, no. 4, pp. 847–869, Nov. 2019, doi: 10.1007/S10494-019-00072-6/FIGURES/4.

[157] I. El Helou, A. W. Skiba, and E. Mastorakos, “Experimental Investigation of Soot Production and Oxidation in a Lab-Scale Rich–Quench–Lean (RQL) Burner,” *Flow, Turbul. Combust.*, vol. 106, no. 4, pp. 1019–1041, Apr. 2021, doi: 10.1007/S10494-020-00113-5/FIGURES/11.

[158] G. De Falco *et al.*, “Soot particle size distribution measurements in a turbulent ethylene swirl flame,” *Proc. Combust. Inst.*, vol. 38, no. 2, pp. 2691–2699, Jan. 2021, doi: 10.1016/J.PROCI.2020.06.212.

[159] K. P. Geigle, W. Meier, and R. Hadef, “Soot formation and flame characterization of an aero-engine model combustor burning ethylene at elevated pressure,” *Proc. ASME Turbo Expo*, vol. 1 B, pp. 1–8, 2013, doi: 10.1115/GT2013-95316.

[160] K. P. Geigle, W. O’Loughlin, R. Hadef, and W. Meier, “Visualization of soot inception in turbulent pressurized flames by simultaneous measurement of laser-induced fluorescence of polycyclic aromatic hydrocarbons and laser-induced incandescence, and correlation to OH distributions,” *Appl. Phys. B Lasers Opt.*, vol. 119, no. 4, pp. 717–730, Jun. 2015, doi: 10.1007/S00340-015-6075-3/FIGURES/11.

[161] M. Stöhr *et al.*, “Time-resolved study of transient soot formation in an aero-engine model combustor at elevated pressure,” *Proc. Combust. Inst.*, vol. 37, no. 4, pp. 5421–5428, Jan. 2019, doi: 10.1016/J.PROCI.2018.05.122.

[162] T. M. Farag, M. Arai, M. Shimizu, and H. Hiroyasu, “The Effect of Fuel Volatility on Spray

Flame Stabilization," *Bull. JSME*, vol. 26, no. 220, pp. 1753–1760, 1983, doi: 10.1299/JSME1958.26.1753.

[163] C. Hasse, "Scale-resolving simulations in engine combustion process design based on a systematic approach for model development," *Spec. Issue Artic. Int. J Engine Res.*, vol. 17, no. 1, pp. 44–62, 2016, doi: 10.1177/1468087415597842.

[164] H. Richter and J. B. Howard, "Formation of polycyclic aromatic hydrocarbons and their growth to soot — a review of chemical reaction pathways," *Prog. Energy Combust. Sci.*, vol. 26, no. 4–6, pp. 565–608, 2000, doi: 10.1016/S0360-1285(00)00009-5.

[165] COSILAB, "1-D and Counterflow Flames." www.rotexo.com, Bochum, 2018.

[166] U. Burke *et al.*, "An ignition delay and kinetic modeling study of methane, dimethyl ether, and their mixtures at high pressures," *Combust. Flame*, vol. 162, no. 2, pp. 315–330, Feb. 2015, doi: 10.1016/J.COMBUSTFLAME.2014.08.014.

[167] "Chemical Mechanism: Combustion Research Group at UC San Diego." https://web.eng.ucsd.edu/mae/groups/combustion/mechanism.html (accessed Sep. 07, 2021).

[168] R. W. Bilger, "A mixture fraction framework for the theory and modeling of droplets and sprays," *Combust. Flame*, vol. 158, no. 2, pp. 191–202, Feb. 2011, doi: 10.1016/J.COMBUSTFLAME.2010.08.008.

[169] B. H. Chao and C. K. Law, "Asymptotic theory of flame extinction with surface radiation," *Combust. Flame*, vol. 92, no. 1–2, pp. 1–24, 1993, doi: 10.1016/0010-2180(93)90195-9.

[170] J. Gau, D. Das, C. McEnally, D. Giassi, N. Kempema, and M. Long, "Yale Coflow Diffusion Flames," 2017. http://guilford.eng.yale.edu/yalecoflowflames/steady_burner.html (accessed May 25, 2021).

[171] C. Letty, E. Mastorakos, A. R. Masri, M. Juddoo, and W. O'Loughlin, "Structure of igniting ethanol and n-heptane spray flames with and without swirl," *Exp. Therm. Fluid Sci.*, vol. 43, pp. 47–54, Nov. 2012, doi: 10.1016/J.EXPTHERMFLUSCI.2012.03.020.

[172] Multi-lab, "EN07 - standard clear quartz glass," 2018. https://multi-lab.co.uk/quartz/en07/ (accessed Feb. 16, 2023).

[173] A. H. Lefebvre and D. R. Ballal, "Gas Turbine Combuston Alternative Fluels and Emmisions," *Tohoku J. Exp. Med.*, vol. 141, no. 2, pp. 247–248, 1983.

[174] W. D. Bachalo *et al.*, "Development of the Laser-Induced Incandescence Method for the Reliable Characterization of Particulate Emissions," *Int. Symp. Appl. Laser Tech. to Fluid Mech.*, 2002, Accessed: Feb. 27, 2023. [Online]. Available: https://www.researchgate.net/publication/44090360.

[175] R. J. Santoro, H. G. Semerjian, and R. A. Dobbins, "Soot Particle Measurements in Diffusion Flames," *Combust. Flame*, vol. 51, no. C, pp. 203–218, 1983, doi: 10.1016/0010-2180(83)90099-8.

[176] S. Will, S. Schraml, and A. Leipertz, "Two-dimensional soot-particle sizing by time-resolved laser-induced incandescence," *Opt. Lett. Vol. 20, Issue 22, pp. 2342-2344*, vol. 20, no. 22, pp.

2342–2344, Nov. 1995, doi: 10.1364/OL.20.002342.

[177] P. Roth and A. V. Filippov, “In situ ultrafine particle sizing by a combination of pulsed laser heatup and particle thermal emission,” *J. Aerosol Sci.*, vol. 27, no. 1, pp. 95–104, 1996, doi: 10.1016/0021-8502(95)00531-5.

[178] R. Hadef, K. Peter, and D. R. Snelling, “The concept of 2D gated imaging for particle sizing in a laminar diffusion flame,” pp. 395–408, 2013, doi: 10.1007/s00340-013-5507-1.

[179] “LIFBASE Spectroscopy Tool - SRI International.” https://www.sri.com/platform/lifbase-spectroscopy-tool/ (accessed Jun. 16, 2023).

[180] T. Metz, X. Bai, F. Ossler, and M. Aldén, “Fluorescence lifetimes of formaldehyde (H2CO) in the Ã1A2 → X̃1A1 band system at elevated temperatures and pressures,” *Spectrochim. Acta - Part A Mol. Biomol. Spectrosc.*, vol. 60, no. 5, pp. 1043–1053, Apr. 2004, doi: 10.1016/S1386-1425(03)00335-4.

[181] LaVision, “Davis 8.1 Software -Product Manual,” *https://www.lavision.de/en/*. 2013.

[182] “Tunable Narrow Bandwidth Pulsed Lasers - Sirah Lasertechnik.” https://www.sirah.com/lasers/he/narrow-bandwidth/ (accessed May 31, 2022).

[183] C. Dasch, “One-dimensional tomography: a comparison of Abel, onion-peeling, and filtered backprojection methods,” *Opt. Publ. Gr.*, vol. 31, no. 8, pp. 1146–1152, 1992, Accessed: Feb. 25, 2023. [Online]. Available: https://opg.optica.org/view_article.cfm?pdfKey=aafedfb1-4fa2-499a-962fa267e298ff5d_39408.

[184] R. Yuan, “Measurements in Swirl-stabilised Spray Flames at Blow-off,” PhD Thesis, University of Cambridge, 2015.

[185] R. Hadef, K. P. Geigle, W. Meier, and M. Aigner, “Soot characterization with laser-induced incandescence applied to a laminar premixed ethylene-air flame,” *Int. J. Therm. Sci.*, vol. 49, no. 8, pp. 1457–1467, Aug. 2010, doi: 10.1016/j.ijthermalsci.2010.02.014.

[186] G. J. Smallwood, “A Critique of Laser-Induced Incandescence for the Measurement of Soot,” PhD Thesis, Cranfield University, 2008.

[187] K. A. Thomson, D. R. Snelling, G. J. Smallwood, and F. Liu, “Laser induced incandescence measurements of soot volume fraction and effective particle size in a laminar co-annular non-premixed methane/air flame at pressures between 0.5-4.0 MPa,” *Appl. Phys. B Lasers Opt.*, vol. 83, no. 3, pp. 469–475, 2006, doi: 10.1007/s00340-006-2198-x.

[188] B. J. McCoy and C. Y. Cha, “Transport phenomena in the rarefied gas transition regime,” *Chem. Eng. Sci.*, vol. 29, no. 2, pp. 381–388, 1974, doi: 10.1016/0009-2509(74)80047-3.

[189] L. A. Melton, “Soot diagnostics based on laser heating,” *Appl. Opt. Vol. 23, Issue 13, pp. 2201-2208*, vol. 23, no. 13, pp. 2201–2208, Jul. 1984, doi: 10.1364/AO.23.002201.

[190] Ansys Fluids, “Fluent Theory Guide, Release 21.1.” ANSYS Inc, 2021.

[191] S. J. Brookes and J. B. Moss, “Predictions of soot and thermal radiation properties in confined turbulent jet diffusion flames,” *Combust. Flame*, vol. 116, no. 4, pp. 486–503, Mar. 1999, doi: 10.1016/S0010-2180(98)00056-X.

[192] Z. Wen, S. Yun, M. J. Thomson, and M. F. Lightstone, “Modeling soot formation in turbulent kerosene/air jet diffusion flames,” *Combust. Flame*, vol. 135, no. 3, pp. 323–340, Nov. 2003, doi: 10.1016/S0010-2180(03)00179-2.

[193] E. Jia Chiet Choo, X. Cheng, H. Kiat Ng, S. Gan, and G. Scribano, “Development and validation of a new n-dodecane-n-butanol-PAH reduced mechanism under diesel engine-relevant conditions,” *Fuel*, vol. 319, Jul. 2022, doi: 10.1016/J.FUEL.2022.123829.

[194] K. M. Pang, H. K. Ng, and S. Gan, “Simulation of temporal and spatial soot evolution in an automotive diesel engine using the Moss-Brookes soot model,” *Energy Convers. Manag.*, vol. 58, pp. 171–184, Jun. 2012, doi: 10.1016/J.ENCONMAN.2012.01.015.

[195] U. Vandsburger, I. Kennedy, and I. Glassman, “Sooting Counterflow Diffusion Flames with Varying Oxygen Index,” *Combust. Sci. Technol.*, vol. 39, no. 1–6, pp. 263–285, Aug. 1984, doi: 10.1080/00102208408923792.

[196] K. M. Leung, R. P. Lindstedt, and W. P. Jones, “A simplified reaction mechanism for soot formation in nonpremixed flames,” *Combust. Flame*, vol. 87, no. 3–4, pp. 289–305, 1991, doi: 10.1016/0010-2180(91)90114-Q.

[197] K. M. Pang, M. Jangi, X.-S. Bai, and J. Schramm, “Investigation of Chemical Kinetics on Soot Formation Event of n-Heptane Spray Combustion,” *SAE Tech. Pap.*, 2014, doi: 10.4271/2014-01-1254.

[198] S. C. Kong, Y. Sun, and R. D. Rietz, “Modeling Diesel Spray Flame Liftoff, Sooting Tendency, and NOx Emissions Using Detailed Chemistry With Phenomenological Soot Model,” *J. Eng. Gas Turbines Power*, vol. 129, no. 1, pp. 245–251, Jan. 2007, doi: 10.1115/1.2181596.

[199] K. M. Pang, M. Jangi, X.-S. Bai, and J. Schramm, “Evaluation and optimisation of phenomenological multi-step soot model for spray combustion under diesel engine-like operating conditions,” *Combust. Theory Model.*, vol. 19, no. 3, pp. 279–308, 2015, doi: 10.1080/13647830.2015.1019929.

[200] M. Bolla, Y. M. Wright, K. Boulouchos, G. Borghesi, and E. Mastorakos, “Soot Formation Modeling of n-Heptane Sprays Under Diesel Engine Conditions Using the Conditional Moment Closure Approach,” 2013, doi: 10.1080/00102202.2012.752362.

[201] M. A. Chishty, M. Bolla, E. R. Hawkes, Y. Pei, and S. Kook, “Soot formation modelling for n-dodecane sprays using the transported PDF model,” *Combust. Flame*, vol. 192, pp. 101–119, Jun. 2018, doi: 10.1016/J.COMBUSTFLAME.2018.01.028.

[202] G. Vishwanathan and R. D. Reitz, “Development of a practical soot modeling approach and its application to low-temperature diesel combustion,” *Combust. Sci. Technol.*, vol. 182, no. 8, pp. 1050–1082, Aug. 2010, doi: 10.1080/00102200903548124.

[203] C. S. McEnally *et al.*, “Computational and experimental study of soot formation in a coflow, laminar diffusion flame,” *Combust. Flame*, vol. 117, no. 1–2, pp. 117–139, 1999, doi: 10.1016/S0010-2180(98)00096-0.

[204] M. Kozubková *et al.*, “The Effect of Nitrogen and Argon Dilution on Methane Oxidation in Laminar Flames,” *Procedia Eng.*, vol. 42, pp. 1826–1839, Jan. 2012, doi: 10.1016/J.PROENG.2012.07.578.

[205] F. G. Roper, “The prediction of laminar jet diffusion flame sizes: Part I. Theoretical model,” *Combust. Flame*, vol. 29, no. C, pp. 219–226, 1977, doi: 10.1016/0010-2180(77)90112-2.

[206] L. Chen, S. Ding, H. Liu, Y. Lu, Y. Li, and A. P. Roskilly, “Comparative study of combustion and emissions of kerosene (RP-3), kerosene-pentanol blends and diesel in a compression ignition engine,” *Appl. Energy*, vol. 203, pp. 91–100, Oct. 2017, doi: 10.1016/J.APENERGY.2017.06.036.

[207] B. Zhmud, “Viscosity Blending Equations,” *The European Lubricants Industry Magazine*, no. 121, pp. 22–27, 2014.

[208] L. Grunberg and A. H. Nissan, “The energies of vaporisation, viscosity and cohesion and the structure of liquids,” *Trans. Faraday Soc.*, vol. 45, no. 0, pp. 125–137, 1949, doi: 10.1039/TF9494500125.

[209] J. Dechoz and C. Rozé, “Surface tension measurement of fuels and alkanes at high pressure under different atmospheres,” *Appl. Surf. Sci.*, vol. 229, no. 1–4, pp. 175–182, May 2004, doi: 10.1016/J.APSUSC.2004.01.057.

[210] J. Thangaraja, K. Anand, and P. S. Mehta, “Predicting surface tension for vegetable oil and biodiesel fuels,” *RSC Adv.*, vol. 6, no. 88, pp. 84645–84657, 2016, doi: 10.1039/c6ra17948g.

[211] A. K. Agarwal and K. Rajamanoharan, “Experimental investigations of performance and emissions of Karanja oil and its blends in a single cylinder agricultural diesel engine,” *Appl. Energy*, vol. 86, no. 1, pp. 106–112, Jan. 2009, doi: 10.1016/J.APENERGY.2008.04.008.

[212] N. Hashimoto, H. Nishida, and Y. Ozawa, “Fundamental combustion characteristics of Jatropha oil as alternative fuel for gas turbines,” *Fuel*, vol. 126, pp. 194–201, Jun. 2014, doi: 10.1016/J.FUEL.2014.02.057.

[213] M. C. Chiong *et al.*, “Liquid biofuels production and emissions performance in gas turbines: A review,” *Energy Convers. Manag.*, vol. 173, pp. 640–658, Oct. 2018, doi: 10.1016/J.ENCONMAN.2018.07.082.

[214] A. P. Kelley, A. J. Smallbone, D. L. Zhu, and C. K. Law, “Laminar flame speeds of C5 to C8 n-alkanes at elevated pressures: Experimental determination, fuel similarity, and stretch sensitivity,” *Proc. Combust. Inst.*, vol. 33, no. 1, pp. 963–970, Jan. 2011, doi: 10.1016/J.PROCI.2010.06.074.

[215] R. C. Wilhot and B. J. Zwolinski, *Physical and thermodynamic properties of aliphatic alcohols*. American Chemical Society and the American Institute of Physics, 1973.

[216] E. Reynolds, “Boiling points of n-heptane and 2,2,4-trimethylpentane over the range 100- to 1,500-millimeter pressure,” *J. Res. Natl. Bur. Stand. (1934).*, vol. 24, pp. 229–234, 1940.

[217] B. M. Crosland, M. R. Johnson, and K. A. Thomson, “Analysis of uncertainties in instantaneous soot volume fraction measurements using two-dimensional, auto-compensating, laser-induced incandescence (2D-AC-LII),” *Appl. Phys. B Lasers Opt.*, vol. 102, no. 1, pp. 173–183, 2011, doi: 10.1007/s00340-010-4130-7.

[218] H. A. Michelsen, P. O. Witze, D. Kayes, and S. Hochgreb, “Time-resolved laser-induced incandescence of soot: the influence of experimental factors and microphysical mechanisms,” *Appl. Opt.*, vol. 42, no. 27, p. 5577, 2003, doi: 10.1364/ao.42.005577.

[219] D. R. Snelling, K. A. Thomson, F. Liu, and G. J. Smallwood, “Comparison of LII derived soot temperature measurements with LII model predictions for soot in a laminar diffusion flame,” *Appl. Phys. B Lasers Opt.*, vol. 96, no. 4, pp. 657–669, 2009, doi: 10.1007/s00340-009-3614-9.

[220] F. Migliorini, S. De Iuliis, S. Maffi, F. Cignoli, and G. Zizak, “Investigation on the influence of soot size on prompt LII signals in flames,” *Appl. Phys. B Lasers Opt.*, vol. 96, no. 4, pp. 637–643, 2009, doi: 10.1007/s00340-009-3524-x.

[221] R. Yuan *et al.*, “Evaluation of in-cylinder endoscopic two-colour soot pyrometry of diesel combustion,” *Combust. Flame*, vol. 242, p. 112207, 2022, doi: 10.1016/j.combustflame.2022.112207.

[222] M. Reddy, A. De, and R. Yadav, “Effect of precursors and radiation on soot formation in turbulent diffusion flame,” *Fuel*, vol. 148, pp. 58–72, 2015, doi: 10.1016/j.fuel.2015.01.080.

[223] J. A. M. Sidey and E. Mastorakos, “Simulations of laminar non-premixed flames of methane with hot combustion products as oxidiser,” *Combust. Flame*, vol. 163, pp. 1–11, 2016, doi: 10.1016/j.combustflame.2015.07.034.

[224] D. O. Lignell, J. H. Chen, and H. A. Schmutz, “Effects of Damköhler number on flame extinction and reignition in turbulent non-premixed flames using DNS,” *Combust. Flame*, vol. 158, no. 5, pp. 949–963, 2011, doi: 10.1016/j.combustflame.2010.10.027.

[225] M. Mofijur, M. G. Rasul, J. Hyde, A. K. Azad, R. Mamat, and M. M. K. Bhuiya, “Role of biofuel and their binary (diesel-biodiesel) and ternary (ethanol-biodiesel-diesel) blends on internal combustion engines emission reduction,” *Renewable and Sustainable Energy Reviews*, vol. 53. Elsevier Ltd, pp. 265–278, Jan. 2016, doi: 10.1016/j.rser.2015.08.046.

[226] K. J. Hughes, M. Pourkashanian, and C. W. Wilson, “OH CONCENTRATION MEASUREMENTS IN A JET ENGINE EXHAUST,” in *9th Conference on Energy for a Clean Environment*, 2007, no. July.